



Université  
de Toulouse

# THÈSE

En vue de l'obtention du

## DOCTORAT DE L'UNIVERSITÉ DE TOULOUSE

**Délivré par :**

Institut National Polytechnique de Toulouse (INP Toulouse)

**Discipline ou spécialité :**

Energétique et Transferts

---

**Présentée et soutenue par :**

M. CESAR BECERRIL AGUIRRE

le mardi 19 septembre 2017

**Titre :**

Simulation of noise emitted by a reactive flow

---

**Ecole doctorale :**

Mécanique, Energétique, Génie civil, Procédés (MEGeP)

**Unité de recherche :**

Centre Européen de Recherche et Formation Avancées en Calcul Scientifique (CERFACS)

**Directeur(s) de Thèse :**

M. LAURENT GICQUEL

M. STÉPHANE MOREAU

**Rapporteurs :**

Mme AIMEE MORGANS, IMPERIAL COLLEGE OF SCIENCE LONDRES

M. SÉBASTIEN DUCRUIX, CENTRALESUPELEC GIF SUR YVETTE

**Membre(s) du jury :**

M. FRANCK NICOUD, UNIVERSITE DE MONTPELLIER, Président

M. FRIEDRICH BAKE, INST DE TECHNOLOGIE DE PROPULSION BERLIN, Membre

M. LAURENT GICQUEL, CERFACS, Membre

M. MAXIME HUET, ONERA, Membre

M. STÉPHANE MOREAU, UNIVERSITE DE SHERBROOKE, Membre







## Abstract

Combustion noise is increasing its relative contribution to aircraft noise, while other sources are being reduced and new low-NO<sub>x</sub> emission combustion chambers being built. Two mechanisms are responsible for this noise source: direct noise in which acoustic waves are generated by the flame and propagate to the outlet of the aero-engine, and indirect noise, where entropy waves generate noise as they are accelerated and decelerated in the turbine stages. In this work, the analytical models used for the propagation of waves through non-homogeneous flows, including the generation of indirect noise, are revised and extended. In the first part, the quasi-1D case is studied, extending the analytical method to non-zero frequencies and validating the results with numerical methods and experimental data. In the second part, the 2D method for the case of compact turbine blades is studied and validated using numerical simulations of a rotating blade and of a complete turbine stage. Finally, in the third part of this thesis, these models are combined with reactive and compressible Large Eddy Simulations (LES) of combustion chambers to build a hybrid approach, named CHORUS, able to predict combustion noise.

**Keywords:** Combustion noise, indirect noise, aero-acoustics, analytical methods.

## Résumé

Le bruit émis par les nouvelles architectures de moteurs aéronautiques a été considérablement réduit dans les dernières années. Les différentes sources de bruit ont été identifiées et pour la plupart réduites. Cependant, la contribution relative du bruit de combustion au bruit global a augmenté progressivement avec la décroissance des autres sources. Deux mécanismes de génération de bruit de combustion ont été identifiés : le bruit direct qui est produit par des fluctuations du dégagement de chaleur dû à la combustion, et le bruit indirect qui est généré par l'accélération des spots d'entropie. Dans ce travail, les mécanismes de génération et propagation du bruit entropique sont étudiés par des simulations numériques aux grandes échelles (en anglais LES) et par des modèles analytiques. Dans un premier temps, une configuration simplifiée du phénomène est étudiée : des spots d'entropie sont créés par des résistances chauffantes et ensuite accélérés par une tuyère pour générer du bruit indirect. Cette configuration a été simulée et ses résultats validés par des campagnes expérimentales. Ensuite, la simulation numérique est utilisée pour mieux comprendre les mécanismes de génération du bruit indirect et ses interactions avec des effets visqueux et non visqueux. Dans une seconde partie, une configuration de turbine haute pression à un seul étage est utilisée pour étudier le bruit indirect d'une façon plus réaliste. Dans les deux parties de cette thèse, les résultats numériques sont comparés à des théories analytiques pour mieux comprendre les avantages et inconvénients d'une méthode par rapport à l'autre.

**Mot clés:** Bruit de combustion, bruit indirect, aéro-acoustique, mécanique des fluides numérique.









# Acknowledgements

I would like to start expressing my gratitude to the entire committee of the defense: Mrs. Aimée MORGANS, Mr. Sébastien DUCRUIX, Mr. Friedrich BAKE and Mr. Maxime HUET, for accepting to evaluate my work and for all their fruitful observations, comments and discussions during the defense.

I would like to thank all the people that contributed one way or another in this PhD work, but there are so many people involved that I would not even know by whom start with and I cannot cite every one of them. I suppose that I should begin with thanking the person that allowed me to start working with this big family that is the CERFACS, so I am very grateful to Thierry POINSOT for this opportunity and his guidance since my internship and during my PhD. I would also like to address special thanks to my PhD advisors: Laurent GICQUEL and Stéphane MOREAU. Laurent, thank you very much for going along with me during this four years of work, for all your advises and the time that you have spent correcting/reviewing my work, especially for the written papers and oral presentations. Stéph, I am very grateful to you; even though you were not physically present, you have always taken the time (at least once per week) to keep a constant update of my work. Thank you very much for your guidance, your advices and for your support until the very end.

The completion of this PhD work was also possible thanks to the European project “REsearch on Core nOise ReDuction” RECORD which has financed this thesis. I would like to particularly acknowledge Mr. Friedrich BAKE and Mr. Maxime HUET for sharing experimental and numerical data but also for the very interesting discussions on technical and scientific topics.

I would like to express my sincere gratitude to some former PhD students that helped me a lot with theoretical and practical advices, especially to Ignacio DURAN, Mattieu LEYKO, Michael BAUERHEIM, Thomas JARAVEL, Dimitris PAPADOGIANNIS, Lucas ESCLAPEZ and my first co-worker Pierre QUILLATRE.

I am also very grateful to all the senior researchers team for their advice, especially to Gabriel STAFFELBACH and Olivier VERMOREL who helped me a lot with all the coding part in AVBP. Thank you also to all the CSG team, for all the technical

assistance during these four years. Besides, I would like to acknowledge the work of the administration team. Thank you Michèle, Marie, Nicole and Chantal for your support with all the administrative part (visa, flights, trains, hotels, insurance, ...); thanks to you we can really save a lot of time and it is always pleasant sharing discussions with you.

Thanks also to all my friends and colleagues for all the shared moments, scientific and much less scientific discussions, the time that we have spent together was really pleasant. I particularly think of you Majd, Romain, Dario, Aicha, Franchine, Luis and of course the best of the best co-workers Melissa (I have really enjoyed being in the same office as you).

Finally and of course, I am very grateful to my family who has completely supported me in each of the steps and decisions of my life, and in my family, you Marie SWIATEK are of course included. Thank you very much to you all for your encouragements and your unconditional support.





# Contents

Glossary	xvii
List of Figures	xxi
List of Tables	xxx
<b>1 General introduction</b>	<b>1</b>
1.1 Noise sources in aero-engines . . . . .	3
1.2 Combustion noise . . . . .	5
1.2.1 Direct combustion noise . . . . .	5
1.2.2 Indirect noise . . . . .	6
1.3 Objectives and organisation of this thesis . . . . .	8
<b>I Towards a better understanding of combustion noise: Study of noise generation in nozzle flows</b>	<b>11</b>
Introduction	15
<b>2 Analytic and reduced models: state-of-the-art for combustion noise prediction</b>	<b>17</b>
2.1 The compact theory . . . . .	20
2.2 The invariant method . . . . .	28
<b>3 The Entropy Wave Generator experiment</b>	<b>37</b>
<b>4 Analytical study of the EWG</b>	<b>43</b>
4.1 The heating device model . . . . .	44
4.2 Propagation of waves through the nozzle . . . . .	47
4.3 Chocked nozzle test case . . . . .	48
4.4 Subsonic nozzle test case . . . . .	55
4.5 Conclusion . . . . .	59

<b>5</b>	<b>Numerical compressible simulation of the EWG</b>	<b>63</b>
5.1	The baseline flow . . . . .	65
5.2	The entropy forced flow . . . . .	82
5.2.1	The heating device model . . . . .	82
5.2.2	Numerical simulation of the forced EWG subsonic test case . . . . .	86
5.2.3	Conclusion . . . . .	101
5.3	Evaluation of the nozzle transfer functions by CFD . . . . .	104
5.3.1	The forcing signal . . . . .	104
5.3.2	Euler forced simulations . . . . .	106
5.3.2.1	Entropy forced simulation . . . . .	109
5.3.2.2	Upstream acoustic forcing simulation . . . . .	120
5.3.2.3	Downstream acoustic forcing simulation . . . . .	123
5.3.2.4	Euler nozzle transfer functions . . . . .	127
5.3.2.5	Conclusion . . . . .	132
5.3.3	Navier-Stokes nozzle transfer functions . . . . .	135
5.3.3.1	Acoustic forcing Navier-Stokes simulations . . . . .	135
5.3.3.2	Entropy forcing Navier-Stokes simulation . . . . .	143
5.3.3.3	Application of the LES nozzle transfer functions into an analytical model . . . . .	154
5.4	Conclusions . . . . .	160
<b>II</b>	<b>Towards a better understanding of combustion noise: Study of noise generation in a turbine stage</b>	<b>165</b>
<b>6</b>	<b>Study of indirect combustion noise in a high-pressure turbine stage</b>	<b>169</b>
6.1	Introduction . . . . .	169
6.2	The MT1 turbine stage indirect combustion noise analysis . . . . .	171
6.2.1	Numerical methodology . . . . .	172
6.2.2	The MT1 baseline flow simulation . . . . .	174
6.2.3	The MT1 entropy forced simulation . . . . .	186
6.2.4	Comparison of the numerical results to the analytical compact actuator disk theory . . . . .	199
6.3	Conclusions . . . . .	210
	<b>General conclusions and perspectives</b>	<b>213</b>
	<b>Appendices</b>	<b>219</b>
<b>A</b>	<b>Characteristic Boundary Conditions</b>	<b>221</b>
A.1	NSCBC general formalism . . . . .	221
A.2	NSCBC extension for forcing waves . . . . .	223

A.2.1	Upstream acoustic forcing methodology . . . . .	224
A.2.2	Downstream acoustic forcing methodology . . . . .	224
A.2.3	Entropy forcing methodology . . . . .	225
<b>B</b>	<b>Spectral and modal decomposition</b>	<b>227</b>
B.1	Spectral decomposition . . . . .	227
B.2	Azimuthal mode decomposition . . . . .	228
B.3	Radial mode decomposition . . . . .	228
<b>C</b>	<b>Numerical dissipation/dispersion of the entropy wave</b>	<b>231</b>
<b>D</b>	<b>Conservation of the entropy wave through a nozzle flow</b>	<b>239</b>
	<b>Bibliography</b>	<b>243</b>





# Glossary

## Roman Symbols

$\mathcal{I}$	Identity matrix
$\mathcal{K}^{\pm}$	Acoustic wave number
$\mathcal{K}^s$	Entropy wave number
$\mathcal{P}$	Acoustic power [W]
$\dot{m}$	Mass flow rate [kg/s]
$\dot{Q}$	Global volumetric heat release [ $W.m^{-3}$ ]
$\dot{Q}$	Volumetric power source term introduced in the energy equation [ $W.m^{-3}$ ]
$A$	Duct cross section [ $m^2$ ]
$A^{\pm}$	Acoustic waves
$c_p$	Specific heat at constant pressure per mass unit [ $J.kg^{-1}.K^{-1}$ ]
$d$	Characteristic slope length of the heating device (energy deposition model) [ $m$ ]
$E_0$	Energy deposited by the energy deposition model [ $J$ ]
$h$	Specific enthalpy [ $J.Kg^{-1}$ ]
$He$	Helmholtz number
$i$	Imaginary unit
$k$	Thermal conductivity [ $W.m^{-1}.K^{-1}$ ]
$L_n$	Nozzle length [ $m$ ]
$L_t$	Characteristic flame length [ $m$ ]
$L_{HD}$	Heating Device length [ $m$ ]
$M$	Mach number

$n_r$	Number of rings of the heating device.
$p$	Pressure [ $Pa$ ]
$Q$	Global heat release [ $W$ ]
$R$	Reflection coefficient
$r$	Specific perfect gas constant [ $J.kg^{-1}.K^{-1}$ ]
$s$	Entropy per mass unit [ $J.kg^{-1}.K^{-1}$ ]
$St$	Strouhal number
$T$	Temperature [ $K$ ]
$t_n$	Triggering time of the $n^{th}$ ring (energy deposition model) [ $s$ ]
$T_p$	Temperature pulse duration (energy deposition model) [ $s$ ]
$X$	Dimensionless axial coordinate
$x$	Axial coordinate [ $m$ ]

### Greek Symbols

$\Delta x_R$	Spacing between heating rings [ $m$ ]
$\delta_f$	Flame thickness [ $m$ ]
$\eta$	Kolmogorov length scale [ $m$ ]
$\gamma$	Specific heats ratio $[-]$
$\lambda$	Characteristic acoustic wave length [ $m$ ]
$\lambda$	Thermal conductivity [ $W.m^{-1}.K^{-1}$ ]
$\nu$	Dimensionless velocity fluctuation
$\Omega$	Dimensionless angular frequency
$\omega$	Angular frequency [ $rad$ ]
$\rho$	Density [ $kg/m^3$ ]
$\rho_e$	Excess density [ $kg/m^3$ ]
$\sigma$	Entropy wave

$\tau_i$	Time delay of the $i^{\text{th}}$ heated ring introduced in the energy deposition model [s]
$\tau_1$	Relaxation time of the ascendant exponential phase (energy deposition model) [s]
$\tau_2$	Relaxation time of the descendant exponential phase (energy deposition model) [s]
$\varphi$	Dimensionless pressure fluctuation

### Superscripts

$(-)$	Time average
$( )'$	Fluctuating variables

### Subscripts

$( )_0$	Upstream position
$( )_1$	Downstream position
$( )_{HD}$	Heating Device
$( )_{mic}$	Microphone
$( )_{N_{in}}$	Nozzle inlet
$( )_{N_{out}}$	Nozzle outlet
$( )_{N_{th}}$	Nozzle throat
$( )_s$	Shock
$( )_{th}$	Thermocouple
$( )_{vib}$	Vibrometer

### Acronyms

<i>ACARE</i>	Advisory Council for Aviation Research and Innovation in Europe
--------------	---

<i>Btu</i>	British Thermal Unit (1 Btu $\approx$ 1055 J)
<i>CFD</i>	Computational Fluid Dynamics
<i>DFT</i>	Discrete Fourier Transform
<i>DLR</i>	German Aerospace Centre (Deutsches Zentrum für Luft und Raumfahrt)
<i>ECBC</i>	Euler Characteristic Boundary Conditions
<i>EIA</i>	The United States Energy Information Administration
<i>EWG</i>	Entropy Wave Generator
<i>HAT</i>	Hot Acoustic Test rig
<i>HHV</i>	Higher Heat Value
<i>ICAO</i>	International Civil Aviation Organisation
<i>LEE</i>	Linearised Euler Equations
<i>LES</i>	Large Eddy Simulation
<i>LNSE</i>	Linearised Navier-Stokes Equations
<i>MISCOG</i>	Multi Instances Solver Coupled on Overlapping Grids
<i>NIST</i>	National Institute of Standards and Technology
<i>NS</i>	Navier-Stokes
<i>NS – TF</i>	Navier-Stokes Transfer Functions
<i>NSCBC</i>	Navier-Stokes Characteristic Boundary Conditions
<i>OTRF</i>	Oxford Turbine Research Facility
<i>RECORD</i>	REsearch on Core nOise ReDuction
<i>TATEF – II</i>	Turbine Aero-Thermal External Flows 2
<i>TDIBC</i>	Time Domain Impedance Boundary Conditions
<i>VWG</i>	Vortex Wave Generator
<i>WP</i>	Work Package

# List of Figures

1.1	Energy production and consumption statistics of the United States delivered by the Energy Information Administration (EIA) in British thermal units (1 Btu $\approx$ 1055 J). . . . .	2
1.2	Certification points for noise emissions. . . . .	3
1.3	Illustration of noise sources in a turbo-engine. . . . .	4
2.1	Sketch of a converging diverging nozzle and waves propagation direction. .	20
2.2	Sketch of a supersonic nozzle with a shock. . . . .	24
2.3	Sketch of the acoustic and entropy waves in a converging-diverging choked nozzle. . . . .	34
3.1	Entropy Wave Generator test rig configuration. . . . .	38
3.2	Normalized entropy noise over nozzle Mach number measured at the EWG test rig from <a href="#">Bake et al. (2009)</a> . . . . .	41
4.1	Domain considered for the analytical study of the EWG. . . . .	44
4.2	Interaction of entropy and acoustics waves through a subcritical nozzle. .	47
4.3	Temperature fluctuations produced by considering $n_r = 1$ or 4 heated rings extracted at the thermocouple position $x_{th} = -72.5$ mm. Parameters of the model: $\Delta T_{exp} = 9.1$ K, $\tau_1 = 8$ ms, $\tau_2 = 8$ ms, $t_0 = 0.1$ s and $T_p = 0.1$ s. . . . .	50
4.4	Direct noise generated by the heating device plotted at the thermocouple position for three inlet reflection coefficients: $R_{in} = -1, 0, 1$ . . . . .	51
4.5	Pressure fluctuation traces recorded at the first microphone position $x_{mic_1} = 350$ mm. . . . .	52
4.6	Discrete Fourier Transform of incoming disturbances at the thermocouple position $x_{th} = -72.5$ mm. . . . .	53
4.7	Nozzle transfer functions of the choked test case. Modulus(—): left axis. Phase(- - -): right axis. . . . .	54
4.8	Modulus of indirect over direct noise ratio $\ \eta\  = \ A_{1,e}^+/A_{1,a}^+\ $ . . . . .	54
4.9	Pressure fluctuation recorded at the fourth microphone position $x_{mic_4} = 1150.5$ mm for an inlet reflexion coefficient $R_{in} = -1$ . . . . .	55

4.10	Temperature fluctuation produced by the heating device extracted at the vibrometer position $x_{vib} = -58.5$ mm. Parameters of the model: $\Delta T_{exp} = 13.4$ K, $n_r = 1$ , $\tau_1 = 3.5$ ms, $\tau_2 = 7$ ms, $t_0 = 0.1$ s and $T_p = 0.1$ s. . . . .	56
4.11	Pressure traces recorded at the outlet of the EWG ( $x_{out} = 2100$ mm) for different inlet reflection coefficients $R_{in}$ and a partially reflecting outlet reflection coefficient $R_{out}$ ( $K_{out} = 160$ s $^{-1}$ ). . . . .	57
4.12	Pressure traces recorded at the outlet of the EWG ( $x_{out} = 2100$ mm) for a partially reflecting inlet and outlet reflection coefficients ( $K_{in} = 100$ and $K_{out} = 160$ s $^{-1}$ ). . . . .	58
4.13	Discrete Fourier Transform of incoming disturbances at the vibrometer position $x_{vib} = -58.5$ mm. . . . .	59
4.14	Nozzle transfer functions of the subsonic test case. Modulus(—): left axis. Phase(---): right axis. . . . .	60
4.15	Modulus of indirect over direct noise ratio $\ \eta\  = \ A_{1,e}^+/A_{1,a}^+\ $ . . . . .	61
4.16	Evolution of the noise peak pressure at the outlet of the EWG as a function of the throat Mach number. . . . .	61
5.1	Sketch of the EWG complete geometry. . . . .	65
5.2	Vortex shedding produced inside the settling chamber. . . . .	66
5.3	Numerical grids for the baseline flow of the EWG. (Distances indicated in millimetres). . . . .	67
5.4	Temporal and azimuthal average of the wall variables $Y^+$ and $\tau_w$ represented against the axial coordinate. M1 (—). M2 (---). M3 (---). . . . .	69
5.5	Streamlines traced from an instantaneous solution of the flow computed in M3. . . . .	70
5.6	Radial profiles of azimuthal averaged vorticity with respect to $\theta$ ( $\xi_\theta$ ) close to the nozzle throat. . . . .	71
5.7	Bulk quantities computed from the LES and compared with the isentropic theory. . . . .	72
5.8	Temporal and azimuthal average of the axial axial velocity versus the radius. M1 (—). M2 (---). M3 (---). . . . .	75
5.9	Temporal and azimuthal average of the Mach number versus the radius. M1 (—). M2 (---). M3 (---). . . . .	76
5.10	Temporal and azimuthal average of the temperature versus the radius. M1 (—). M2 (---). M3 (---). . . . .	77
5.11	Temporal and azimuthal average of the static pressure versus the radius. M1 (—). M2 (---). M3 (---). . . . .	78
5.12	Azimuthal average of the radial pressure gradient at different positions of the diffuser. . . . .	79
5.13	Azimuthal average of the streamwise component of the vorticity ( $\xi_x$ ) at different positions of the diffuser. . . . .	80
5.14	Azimuthal average of the radial component of the vorticity ( $\xi_r$ ) at different positions of the diffuser. . . . .	81

5.15	Picture of one heating resistances module. . . . .	82
5.16	Representation of the spatial (left) and the temporal law (right) of the heating device model, $\phi(x)$ and $\xi(t)$ respectively. . . . .	84
5.17	Simplified domain: Cylindrical duct with adiabatic walls. . . . .	85
5.18	Upstream duct: Bulk temperature and mean temperature of the LES compared with the experimental measurement at vibrometer position ( $x_{vib} = -58.5$ mm). . . . .	86
5.19	Reflection coefficients imposed in the entropy forced simulation of the subsonic nozzle test case. Left axis (—): modulus of the reflection coefficient. Right axis (---): phase of the reflection coefficient. . . . .	88
5.20	Volumetric power deposited in the numerical simulation for the two different deposition models. . . . .	89
5.21	Azimuthal average of the axial velocity versus the radius. Baseline flow simulation mean profiles on M1 (+++). $t_1 = 0.1$ s - beginning of the energy introduction (—). $t_2 = 0.2$ s - end of the energy introduction (---). . . . .	90
5.22	Azimuthal average of the Mach number versus the radius. Baseline flow simulation mean profiles on M1 (+++). $t_1 = 0.1$ s - beginning of the energy introduction (—). $t_2 = 0.2$ s - end of the energy introduction (---). . . . .	91
5.23	Azimuthal average of the temperature versus the radius. Baseline flow simulation mean profiles on M1 (+++). $t_1 = 0.1$ s - beginning of the energy introduction (—). $t_2 = 0.2$ s - end of the energy introduction (---). . . . .	92
5.24	Azimuthal average of the pressure versus the radius. Baseline flow simulation mean profiles on M1 (+++). $t_1 = 0.1$ s - beginning of the energy introduction (—). $t_2 = 0.2$ s - end of the energy introduction (---). . . . .	93
5.25	Zoom over the first instants of the energy deposition. . . . .	94
5.26	Zoom over the first instants of the energy deposition. Comparison with the introduction of a hot slug by the inlet boundary condition simulation. . . . .	95
5.27	Norm of the temperature gradient of the forced flow divided by the mean temperature of the non forced flow ( $\ \nabla(T - \bar{T}_0)\ /\bar{T}_0$ ). Only a part of the EWG geometry is represented ( $x \in [-0.15 : 0.5]$ ). . . . .	96
5.28	Comparison of the isentropic mean flow and the bulk quantities computed from the time averaged baseline flow LES. . . . .	98
5.29	Azimuthal average of the dimensionless temperature $T_{dimless} = (T_{bulk} - T_{0,bulk})/T_{0,bulk}$ . Shaded region: Heating Device location. Vertical lines: separation between the inlet duct, the convergent, the diffuser and the outlet duct. . . . .	100
5.30	Azimuthal average of the dimensionless bulk temperature $T_{dimless} = (T_{bulk} - T_{0,bulk})/T_{0,bulk}$ at the different positions of the nozzle against time. . . . .	102
5.31	Relative magnitude of $T_{dimless}$ (compared to its value taken at the vibrometer position) as it is convected through the EWG nozzle. . . . .	103
5.32	Forcing signal with and without phase shift for each harmonic. . . . .	105
5.33	Sketch of the reduced domain of the EWG used to compute the nozzle transfer functions. . . . .	106

5.34	Isentropic quasi-1D variables compared with bulk quantities extracted from the Euler numerical simulation. . . . .	108
5.35	Schematic view of entropy and acoustic waves formed by an entropy forcing with non-reflective boundary conditions. . . . .	109
5.36	Temperature fluctuation extracted from the numerical simulation compared with the forcing signal. . . . .	110
5.37	Entropy wave phase compared with particle-lines traced from the inlet of the baseline flow. . . . .	111
5.38	Entropy flux ratio of different points (inlet and outlet of the nozzle and outlet of the domain) to the inlet of the domain. . . . .	112
5.39	Amplitude of the entropy plane wave $\sigma$ in the upstream and downstream ducts of the EWG. (Only harmonics 1, 10, 20 and 25 are presented). . . .	112
5.40	Entropy-entropy transmission coefficient $T_{ee}$ . . . . .	114
5.41	Ratio of entropy fluxes between the outlet of the nozzle and the inlet of the CFD domain. . . . .	117
5.42	Acoustic wave $A^+$ in the upstream and downstream ducts of the nozzle. (Only harmonics 1, 10, 20 and 25 are presented). . . . .	117
5.43	Acoustic wave $A^-$ in the upstream and downstream ducts of the nozzle. (Only harmonics 1, 10, 20 and 25 are presented). . . . .	118
5.44	Reflection coefficient computed from the extracted waves at the inlet boundary condition of the simulation. . . . .	118
5.45	Reflection coefficient computed from the extracted waves at the outlet boundary condition of the simulation. . . . .	119
5.46	Schematic view of acoustic waves formed by an upstream acoustic forcing with non-reflective boundary conditions. . . . .	120
5.47	Axial velocity extracted at the inlet boundary condition compared with the forcing signal. . . . .	121
5.48	Acoustic wave $A^+$ in the upstream and downstream ducts of the EWG. (Only harmonics 1, 10, 20 and 25 are presented). . . . .	122
5.49	Acoustic wave $A^-$ in the upstream and downstream ducts of the EWG. (Only harmonics 1, 10, 20 and 25 are presented). . . . .	122
5.50	Reflection coefficient computed from the extracted waves at the outlet boundary condition of the simulation. . . . .	123
5.51	Schematic view of acoustic waves formed by a downstream acoustic forcing with non-reflective boundary conditions. . . . .	123
5.52	Static pressure extracted at the outlet boundary condition compared with the forcing signal. . . . .	124
5.53	Acoustic wave $A^+$ in the upstream and downstream ducts of the EWG. (Only harmonics 1, 10, 20 and 25 are presented). . . . .	125
5.54	Acoustic wave $A^-$ in the upstream and downstream ducts of the EWG. (Only harmonics 1, 10, 20 and 25 are presented). . . . .	125
5.55	Reflection coefficient computed from the extracted waves at the inlet boundary condition of the simulation. . . . .	126



5.56	Upstream reflecting coefficient $R_{aa}^+$ filtered from the boundary conditions reflections. . . . .	129
5.57	Upstream transmission coefficient $T_{aa}^+$ filtered from the boundary conditions reflections. . . . .	129
5.58	Downstream reflecting coefficient $R_{aa}^-$ filtered from the boundary conditions reflections. . . . .	130
5.59	Downstream transmission coefficient $T_{aa}^-$ filtered from the boundary conditions reflections. . . . .	130
5.60	Entropy-acoustic transmission coefficient $T_{ea}$ filtered from the boundary conditions reflections. . . . .	132
5.61	Entropy-acoustic reflection coefficient $R_{ea}$ filtered from the boundary conditions reflections. . . . .	132
5.62	Azimuthal vorticity fluctuations generated in the entropy forced Euler simulation for different harmonics (only harmonics 1, 10, 20 and 25 are presented). . . . .	133
5.63	Entropy-acoustic transfer function associated to the generated acoustic wave from a vorticity forcing. . . . .	133
5.64	Reconstruction of the forced signal from the information at the boundary conditions for the acoustic forced simulations. . . . .	136
5.65	Inlet acoustic forcing: Acoustic wave $A^+$ in the upstream and downstream ducts of the EWG. Navier-Stokes simulation (lines), Euler simulations (lines with symbols). (Only harmonics 1, 10, 20 and 25 are presented). . .	136
5.66	Inlet acoustic forcing: Acoustic wave $A^-$ in the upstream and downstream ducts of the EWG. Navier-Stokes simulation (lines), Euler simulations (lines with symbols). (Only harmonics 1, 10, 20 and 25 are presented). . .	137
5.67	Outlet acoustic forcing: Acoustic wave $A^+$ in the upstream and downstream ducts of the EWG. Navier-Stokes simulation (lines), Euler simulations (lines with symbols). (Only harmonics 1, 10, 20 and 25 are presented). .	137
5.68	Outlet acoustic forcing: Acoustic wave $A^-$ in the upstream and downstream ducts of the EWG. Navier-Stokes simulation (lines), Euler simulations (lines with symbols). (Only harmonics 1, 10, 20 and 25 are presented). .	138
5.69	Upstream transmission coefficient $T_{aa}^+$ without the contribution of reflections. . . . .	140
5.70	Upstream reflecting coefficient $R_{aa}^+$ without the contribution of reflections. . . . .	140
5.71	Downstream transmission coefficient $T_{aa}^-$ without the contribution of reflections. . . . .	141
5.72	Downstream reflecting coefficient $R_{aa}^-$ without the contribution of reflections. . . . .	141
5.73	Modulus of the azimuthal vorticity fluctuation $  \xi'_\theta  $ for different harmonics along the axial coordinate. . . . .	142
5.74	Modulus of the radial vorticity fluctuation $  \xi'_R  $ for different harmonics along the axial coordinate. . . . .	142
5.75	Temperature fluctuation extracted from the numerical simulation compared with the forcing signal. . . . .	143

5.76	Entropy wave real part compared with particle-lines traced from the inlet of the baseline flow. . . . .	144
5.77	Particles traced from the inlet of the baseline flow for two time lapses: 1 and 18.5 ms. . . . .	145
5.78	Entropy flux ratio between different sections of the EWG (inlet and outlet of the nozzle and outlet of the domain) to the inlet of the domain. . . . .	148
5.79	Entropy flux of different modes at the outlet of the nozzle compared with the plane mode introduced at the inlet. . . . .	148
5.80	Entropy wave $\sigma$ in the upstream and downstream ducts of the EWG. Navier-Stokes simulation (lines). Euler simulation (lines with symbols). (Only harmonics 1, 10, 20 and 25 are presented). . . . .	149
5.81	Entropy-entropy transfer function $T_{ee}$ . . . . .	150
5.82	Entropy-acoustic transmission coefficient $T_{ea}$ filtered from boundary condition reflections. . . . .	151
5.83	Entropy-acoustic reflection coefficient $R_{ea}$ filtered from the boundary conditions reflections. . . . .	152
5.84	Amplitude of the azimuthal vorticity wave ( $  \xi'_t  $ ) along the stream-wise coordinate for different harmonics. . . . .	153
5.85	Amplitude of the radial vorticity wave ( $  \xi'_r  $ ) along the stream-wise coordinate for different harmonics. . . . .	153
5.86	Interpolated Navier-Stokes upstream acoustic-acoustic transmission coefficient $T_{aa}^+$ . . . . .	155
5.87	Interpolated Navier-Stokes upstream acoustic-acoustic reflection coefficient $R_{aa}^+$ . . . . .	155
5.88	Interpolated Navier-Stokes downstream acoustic-acoustic transmission coefficient $T_{aa}^-$ . . . . .	156
5.89	Interpolated Navier-Stokes downstream acoustic-acoustic reflection coefficient $R_{aa}^-$ . . . . .	156
5.90	Interpolated Navier-Stokes upstream entropy-acoustic transmission coefficient. $T_{ea}$ . . . . .	157
5.91	Interpolated Navier-Stokes upstream entropy-acoustic reflection coefficient $R_{ea}$ . . . . .	157
5.92	Pressure traces measured at the fourth microphone ( $x_{mic_4} = 1150.5$ mm) for the different analytical approaches, the numerical LES simulation and the experimental data. . . . .	158
5.93	Contribution of direct/indirect noise on the pressure traces measured at the fourth microphone ( $x_{mic_4} = 1150.5$ mm). . . . .	158
5.94	Evaluation of the noise peak pressure at the outlet of the EWG as a function of the throat Mach number. . . . .	159
6.1	Sketch of the Oxford Turbine Research Facility. . . . .	171
6.2	Numerical domains corresponding to each AVBP instance. . . . .	174
6.3	MT1 elements positions. . . . .	175

6.4	Mean profiles extracted at 50% span: LES predictions compared with the numerical simulations of Wang et al. (2013, 2014a) and experimental data.	176
6.5	Azimuthal mean profiles. LES predictions (—). Wang et al. (2013, 2014a) predictions (---). Experimental data (*).	177
6.6	Iso-surface of the Q criterion coloured by the absolute Mach number.	178
6.7	Field of $  \nabla\rho  /\rho$ of an instantaneous field at $R = 0.284$ mm.	178
6.8	Temperature fluctuations instantaneous fields. Radial cut at $r_0 = 0.284$ m.	179
6.9	Temperature fluctuations registered at different probes inside the MT1 baseline flow simulation.	179
6.9	Temperature fluctuations registered at different probes inside the MT1 baseline flow simulation.	180
6.10	DMD spectra of the velocity magnitude and the temperature inside the stator and rotor wakes.	181
6.11	Strongest velocity fluctuation modes in the DMD analysis of the stator wake extracted in plane $P_{int}$ .	182
6.12	Strongest temperature fluctuation modes in the DMD analysis of the stator wake extracted in plane $P_{int}$ .	183
6.13	Strongest velocity fluctuation (relative velocity) modes in the DMD analysis of the rotor wake extracted in plane $P_{near}$ .	184
6.14	Strongest temperature fluctuation modes in the DMD analysis of the rotor wake extracted in plane $P_{near}$ .	185
6.15	Instantaneous fields of $  \nabla\rho  /\rho$ at $r_0 = 0.284$ m.	189
6.16	Temperature fluctuations registered at different probes inside the MT1 domain.	190
6.17	DMD spectra of the velocity magnitude and the temperature inside the stator and rotor wakes. (—) Forced flow. (---) Baseline flow.	191
6.18	DFT of the MT1 instantaneous fields computed for different run time lengths. Extraction of the fundamental forcing frequency: 100 Hz. Radial cut at $r_0 = 0.284$ m.	195
6.19	DFT of the MT1 instantaneous fields computed for different run time lengths. Extraction of the harmonic at 1500 Hz. Radial cut at $r_0 = 0.284$ m.	196
6.20	DFT of the MT1 instantaneous fields computed for different run time lengths. Extraction of the harmonic at 3000 Hz. Radial cut at $r_0 = 0.284$ m.	197
6.21	DFT in the stator reference frame, extraction of the fundamental frequency: 100 Hz. Axial cuts at positions $x_{P_{Sin}}$ and $x_{P_{int}}$ for different run time lengths.	198
6.22	DFT in the rotor reference frame, extraction of the fundamental forcing frequency: 100 Hz. Axial cuts at positions: (a) $x_{P_{Sin}}$ , (b) $x_{P_{rot}}$ and (c) $x_{P_{near}}$ for different run time lengths.	198
6.23	DFT in the stator reference frame, extraction of the harmonic at 1500 Hz. Axial cuts at positions $x_{P_{Sin}}$ and $x_{P_{int}}$ for different run time lengths.	199

6.24	DFT in the rotor reference frame, extraction of the harmonic frequency: 1500 Hz. Axial cuts at positions: (a) $x_{P_{S_{in}}}$ , (b) $x_{P_{rot}}$ and (c) $x_{P_{near}}$ for different run time lengths. . . . .	199
6.25	DFT in the stator reference frame, extraction of the harmonic at 3000 Hz. Axial cuts at positions $x_{P_{S_{in}}}$ and $x_{P_{int}}$ for different run time lengths. . . .	200
6.26	DFT in the rotor reference frame, extraction of the harmonic frequency: 3000 Hz. Axial cuts at positions: (a) $x_{P_{S_{in}}}$ , (b) $x_{P_{rot}}$ and (c) $x_{P_{near}}$ for different run time lengths. . . . .	200
6.27	Axial evolution of the entropy wave at frequency $f = 100$ Hz. . . . .	201
6.28	Axial evolution of the entropy wave at frequency $f = 1500$ Hz. . . . .	201
6.29	Axial evolution of the entropy wave at frequency $f = 3000$ Hz. . . . .	202
6.30	Comparison of the entropy-entropy transmission coefficient between the analytical model (CHORUS), the numerical simulation using different run times and <a href="#">Papadogiannis et al. (2016)</a> entropy forced simulation. . . . .	205
6.31	MT1 baseline mean flow streamlines coloured by the elapsed time of a particle over the streamline. . . . .	206
6.32	MT1 elapsed time spatial distribution at the outlet of the MT1 sub-domains (function $t_d(r, \theta)$ ). . . . .	207
6.33	Attenuation functions of each MT1 sub-domain. . . . .	207
6.34	Entropy-acoustic transmission coefficient computed numerically compared with CHORUS and <a href="#">Papadogiannis et al. (2016)</a> 3D MT1 simulation. . . .	209
6.35	Acoustic power at the outlet of the MT1 turbine. . . . .	209
A.1	NSCBC waves decomposition for a subsonic inflow and outflow. . . . .	222
C.1	Numerical dissipation and dispersion introduced by the different numerical schemes of AVBP computed with a CFL=0.1. . . . .	232
C.2	Numerical dissipation and dispersion introduced by the different numerical schemes of AVBP computed with a CFL=0.7. . . . .	232
C.3	Wavelengths of the disturbances at 250 Hz along the EWG numerical domain. . . . .	233
C.4	Temperature fluctuations extracted at the central line ( $R=0$ ) of the cylindrical duct domain with and without artificial viscosity. . . . .	235
C.5	Axial velocity profiles along the axial coordinate of the cylindrical test case with a velocity profile. . . . .	236
C.6	Real part of the entropy wave of the cylindrical test case with a velocity profile. . . . .	237
C.7	Attenuation functions of the entropy wave based on the mean flow compared with the entropy attenuation extracted from the numerical simulation. . . .	238
C.8	Convection of an entropy impulsion along a straight cylindrical duct by a non-homogeneous flow. . . . .	238
D.1	Progression of the entropy pulse through a nozzle viscous and inviscid flow. . . .	240
D.2	Variation of $T'/T_0$ along the EWG configuration against time. . . . .	241

D.3	Absolute value axial velocity radial gradient ( $  \partial U_x/\partial R  $ ) computed from the baseline flow of the numerical simulations. . . . .	241
D.4	Relative magnitude of the temperature fluctuation as it is advected through the EWG configuration. . . . .	242



# List of Tables

1.1	Heat of combustion of some commonly used fuels. . . . .	1
2.1	Waves to impose and to determine to compute the nozzle transfer functions.	22
2.2	Response of a compact subsonic nozzle to acoustic and entropy unitary disturbances. . . . .	23
2.3	Response of a compact supersonic nozzle to acoustic and entropy unitary disturbances. . . . .	23
2.4	Response of a shock wave to acoustic and entropy unitary disturbances. .	27
3.1	Summary of the axial positions of the different elements of the EWG. . .	39
3.2	Summary of geometric, flow and excitation parameters of the EWG test cases. . . . .	40
5.1	Numerical set-up of the simulations. . . . .	67
5.2	Comparison of parameters of the unperturbed flow between the numerical simulation and the experiment. . . . .	73
5.3	Computational costs of the different numerical simulations for the baseline flow. . . . .	75
5.4	Numerical set-up for the entropy forced simulation. . . . .	87
5.5	List of parameters for each deposition model test case. . . . .	89
5.6	Numerical set-up for the Euler computation of the nozzle transfer functions.	107
5.7	Modulus of the entropy wave extracted at the inlet plane of the nozzle ( $x_{N_{in}}$ ). . . . .	115
5.8	Modulus of the entropy wave extracted at the outlet plane of the nozzle ( $x_{N_{out}}$ ). . . . .	116
5.9	Modulus of the entropy wave modal decomposition extracted at the inlet plane of the nozzle ( $x_{N_{in}}$ ). $m$ : order of the azimuthal mode, $\mu$ : order of the radial mode. . . . .	146
5.10	Modulus of the entropy wave modal decomposition extracted at the outlet plane of the nozzle ( $x_{N_{out}}$ ) ordered by the importance of its module. $m$ : order of the azimuthal mode, $\mu$ : order of the radial mode. . . . .	147
6.1	MT1 operating conditions. . . . .	172
6.2	Numerical set-up of the MT1 numerical simulations. . . . .	173

6.3	Summary of the axial positions of the different elements of the MT1 numerical domain. . . . .	176
6.4	List of values for the energy deposition model of the MT1 entropy forced simulation. . . . .	188
C.1	Wave numbers and wavelengths to obtain less than 5% error in the phase velocity. . . . .	233



# Chapter 1

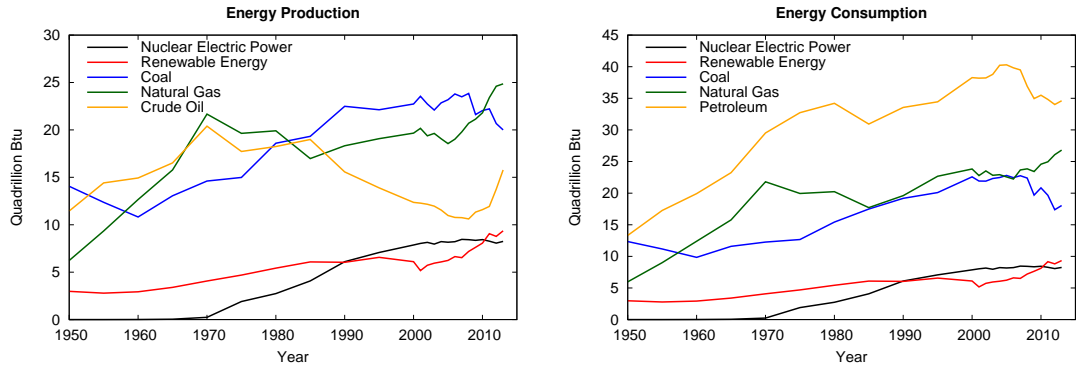
## General introduction

Combustion has always been a very important part of society, where it is used for the very simple objective of heating and cooking as well as very sophisticated processes like propulsion of space ships, rockets, missiles and aeroplanes. Nowadays, despite the growth and development of green and renewable energies, combustion produces approximately ninety percent of the total energy in the world. The United States Energy Information Administration publishes a Monthly Energy Review [EIA \(2016\)](#) containing statistics of the energy production, consumption, trade and energy prices. [Figure 1.1](#) shows the amount of different energy sources produced or consumed by the United States per year and out of which one notices that in 2015 the renewable and nuclear energy production/consumptions represent only 20% of the total energy. The fact that combustion remains the most common energy source, is mainly explained by the large energy release per unit mass ratio (called heat of combustion or higher heat value HHV) stored in fossil fuels. Fossil fuels are indeed very suitable for lots of industrial applications, where weight is a key constraint of the design process. [Table 1.1](#) regroups a short list of combustion heat released per unit of mass of common fuels extracted from [NIST](#).

Fuel	HHV (MJ/Kg)
Hydrogen	141.8
Methane	55.5
Kerosene	46.2
Diesel	44.8
Gasoline	47.3
Coal	$\approx 25$
Wood	21

**Table 1.1** Heat of combustion of some commonly used fuels.

In the aviation industry (which is the main matter of the present work), the Airbus A380 has become the reference commercial aeroplane for its energetic performances. This particular super-jumbo has a maximal fuel capacity of 250 tonnes of kerosene



(a) Energy production of the United States per quadrillion of British Thermal Unit (Btu). (b) Energy consumption of the United States per quadrillion of British Thermal Unit (Btu).

**Figure 1.1** Energy production and consumption statistics of the United States delivered by the Energy Information Administration (EIA) in British thermal units (1 Btu  $\approx$  1055 J).

and can travel up to 15 000 km, transporting up to 540 passengers (cf. [A380 2017](#)). For this aeroplane the fuel consumption per passenger per km has reduced to 0.033 kg/km/passenger, and according to [Tab. 1.1](#), the corresponding energy consumed to transport one passenger over one Km is approximatively 2 MJ/Km/passenger. The principal difficulty for the aviation industry is that it is extremely difficult to store such an amount of energy per kilogram in other form than through the use of a fossil fuel. At the same time all combustion processes have an impact to the environment and health. Indeed, the main combustion products are water and carbon dioxide which are greenhouse gases. Nitric and sulphur oxides, which are also produced through the combustion process, contribute to the degradation of air quality and are at the origin of acid rains. Important technological efforts have been deployed to reduce the use of fossil fuels, which is the case of the A380. Combustion products are not the only pollutants released by an aeronautical engine, noise emissions are a new problem and the heart of this thesis. To limit the damages caused to the environment and health, multiple organisations have appeared. The Advisory Council for Aviation Research and Innovation in Europe (ACARE), provides technical and institutional guidance to the European Commission. Likewise, the International Civil Aviation Organisation (ICAO) codifies the principles and techniques of international air navigation to ensure safe and orderly growth. Both of these organisations regulate present pollutant emissions of aircraft engines and specify future targets to be reached for levels of emitted carbon dioxide, nitric oxides or even noise emission levels.

According to [ACARE \(2016\)](#), aviation is recognised as one of the top five advanced technology sectors in Europe. Providing close to nine million of skilled jobs and contributing to 600 billion Euros to Europe's Gross Domestic Product. Aviation sector welcomes close to 450 airlines and over 700 airports. Air traffic has grown by 50% in the

last ten years, yet the needs for fuel has only risen by 3% thanks to the technological advances. To keep improving designs and pressure on engines manufacturers, ACARE has set out challenging objectives for future decades in the new Europe Vision for Aviation. In terms of pollutants emissions, some targets for 2050 are:

1. Reduction of  $CO_2$  emissions by 75% relative to year 2000.
2. Reduction of  $NO_x$  emissions by 90% relative to year 2000.
3. Reduction of perceived noise by 65% relative to year 2000.
4. Aircraft movements emission-free when taxiing.

In terms of noise emissions, which is a big concern in urban zones near the airports, ICAO (2013) defines maximum overall noise levels emitted by the aircraft (no particular noise source is aimed, but the overall noise emissions) for three different certification points showed in Fig. 1.2. In this process, the aircraft manufacturer performs his own noise measurements and sends the data to organisms that approve the results before sending it to ICAO. If the data is approved, it is added to the noise certification database and the aircraft is certified.

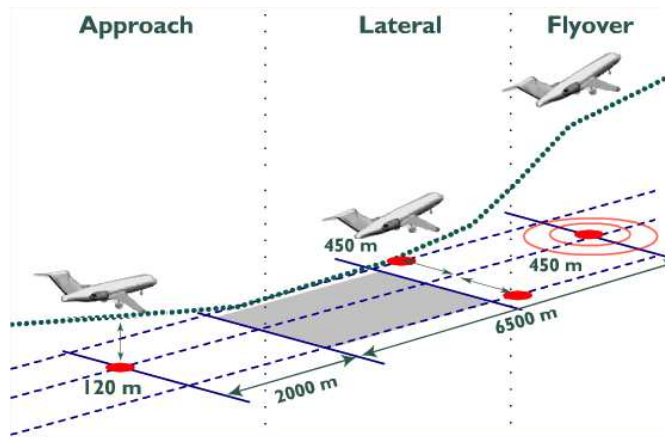


**Figure 1.2** Certification points for noise emissions.

## 1.1 Noise sources in aero-engines

Sound radiated from an aircraft is the result of many individual and separate noise sources, some tonal and other broadband. Noise can be separated roughly in two main contributors:

1. Airframe noise generated by the fuselage, nacelle, landing gear, wings and other surfaces.

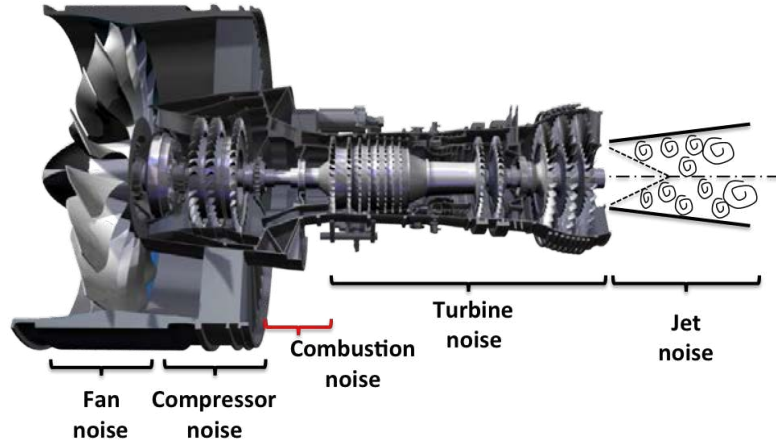


**Figure 1.3** Illustration of noise sources in a turbo-engine.

2. Engine-core noise generated by fan, compressor, combustor, turbine and jet exhaust.

A remarkable work reviewing the noise emitted by an aero-engine is [Ihme \(2017\)](#), which summarizes the state of the art on combustion and core noise. In this present PhD work, we will only focus on the core noise contribution.

A turbo-engine can be decomposed into four main components: compressor, combustor, turbine and nozzle (cf. [Fig. 1.3](#)). Noise emission from rotating tubomachinery components (compressor and turbine), is tonal and results from the rotor and harmonics of the blade passing frequency. Superimposed onto this tonal noise, broadband noise is generated by the scattering of the flow boundary layers, turbulence at the trailing edge of the blades ([Tyler and Sofrin 1962](#); [Griffiths 1964](#)). However, not all this noise produced is transmitted through all the stages. For example, only low frequencies (wavelengths larger than the cord of the stages) and perturbations noise at the last compressor stages require consideration as potential noise mechanism inside the combustor. Indeed, broadband perturbations entering the combustor are typically outweighed by turbulent mixing and combustion processes. Inside the combustor, fluctuations of heat release generate broadband noise known as combustion noise which was first studied by [Strahle \(1972\)](#), [Chiu and Summerfield \(1974\)](#), [Hassan \(1974\)](#), [Marble and Candel \(1977b\)](#) and [Cumpsty and Marble \(1977a\)](#). However, at this time, its relative contribution to global aircraft acoustic emissions was still low. Earlier, [Lighthill \(1952\)](#) showed the importance of jet noise in the overall noise emissions, demonstrating that jet noise scales with the eighth power of the jet-exhaust speed. Since then, new technologies have emerged. The turbofan, where the bypass ratio is increased by a secondary flow and the jet speed is diminished, is one example. The introduction of the turbofan decreased the jet noise but also added the non-negligible contribution of fan noise. As a consequence, core noise, fan and airframe noise became the leading contributors to the overall noise emissions

of the aircraft. At the same time, fuel costs and environmental concerns lead to further investigation on consumption reduction. As a result, lean pre-vaporized combustion and associated lean injection systems, and other low-emission combustion technologies (Hultgren 2011 and Chang et al. 2013) were developed. Despite all these progresses and new technologies, noise emissions increased due to two facts: turbulence levels present in the engine increased and the heat release fluctuations of the now partially premixed turbulent flame also increased as the mixture got closer to the lean extinction point. With years and the reduction of different airframe noise sources, noise contributions from the engine core became increasingly important and combustion noise, which had no important role in the overall noise contributions, started to gain in importance with a clear increasing share in the overall noise signature of new engines.

## 1.2 Combustion noise

Combustion noise is known to be a low frequency broadband noise (cf. Hassan 1974). Nevertheless, the importance of combustion noise in the overall radiated noise is so far not well-known. Indeed, engine manufacturers are not able to discriminate combustion noise from exhaust noise and it is often called "core-noise". Combustion noise has been estimated using scaling laws (cf. Harper-Bourne et al. 2008) based on previous engine data out of which all known noise sources had been removed (jet, fan, turbomachinery, and others) out of the engine sound pressure spectra. In terms of physics, combustion noise finds its roots inside the combustion chamber and is then propagated through the combustor-downstream engine components before radiating to the far field. Propagation of acoustic waves through accelerating flows was first studied by Tsien (1952) in a rocket engine combustion instability framework. But it was Marble and Candel (1977b), who included the propagation of entropy waves through subsonic as well as supersonic nozzles. It resulted the definition of two types of combustion noise:

**Direct combustion noise:** Generation of acoustic waves in the combustor due to the unsteady heat release.

**Indirect combustion noise:** Generation of acoustic waves after the combustor due to the interaction of inhomogeneities in velocity, temperature and mixture composition with the mean flow and pressure gradients in the turbine and nozzle (Marble and Candel 1977b, Cumpsty and Marble 1977a,b and Magri et al. 2016).

### 1.2.1 Direct combustion noise

Direct combustion noise was first studied in open flame configurations. The first experimental studies were carried out by Smith and Kilham (1963) who investigated the influence of the burner geometry, mass-flow rate and fuel mixture on the generation of noise of an open premixed turbulent flame. Hurle et al. (1968) and Price et al. (1969) evaluated with chemiluminescence of  $C_2$  and  $CH$  (representative radicals of the reaction zone of a flame) the heat-release fluctuations and their link to sound generation.

Kumar's (1975) work showed that noise sources in premixed flames are associated with unsteady fluctuations in the flame surface area, whereas in non-premixed flames they are associated with dilatational effects generated by mixing and turbulence. All of these experimental studies showed the monopolar character of direct combustion noise.

The study of direct combustion noise was carried out analytically by Strahle (1971, 1972, 1973) employing the acoustic analogy of Lighthill (1952) to propagate the noise sources in the open space. Later on, Chiu and Summerfield (1974) as well as Kotake (1975) extended Phillips' analogy to reactive flows in the limit of low Mach numbers and again illustrated the monopole nature of direct combustion noise.

Direct combustion noise is the major source of noise in lab-scale combustion chambers, where no acceleration of entropy wave exists. Entropy noise for example, appears when studying the entropy propagation equation with a source term representing any heat release:

$$\frac{\partial s}{\partial t} + u \cdot \nabla s = \frac{\dot{Q}}{\rho T} \quad \text{with} \quad s = c_v \ln \left( \frac{P}{\rho^\gamma} \right) = c_p \ln \left( \frac{P^{1/\gamma}}{\rho} \right). \quad (1.1)$$

Linearisation of Eq. (1.1) yields:

$$\frac{\partial s'}{\partial t} + u \cdot \nabla s' = \frac{\dot{Q}'}{\rho T} - \frac{\dot{Q}}{\rho T} \left[ \frac{p'}{p} + \frac{u'}{u} \right], \quad (1.2)$$

where the primed variables ( $x'$ ) represent fluctuations and the non primed variables are mean steady quantities around which the system has been linearised. Equation (1.2) shows that fluctuations of entropy can be generated by two mechanisms : first the fluctuations of heat release ( $\dot{Q}'$ ) and second through the interaction of acoustic fluctuations with the mean heat release (second term of the equation). Equation (1.2) also shows that in regions far from the flame ( $\dot{Q}$  and  $\dot{Q}' = 0$ ), entropy fluctuations are only convected and no sound is generated. Therefore, the generation of acoustic waves takes place in the flame region which is called direct noise. However, the large acceleration of entropy waves through turbine stages usually makes indirect combustion noise a non negligible noise source, as demonstrated by Leyko et al. (2008) with a 1D model combustor followed by a choked nozzle.

### 1.2.2 Indirect noise

Unlike direct combustion noise, indirect noise cannot be generated in open flame configurations as described in §1.2.1. Indirect combustion noise is generated by the interaction of inhomogeneities in temperature and eventually mixture composition (cf. Sinai 1980 and Magri et al. 2016) with the mean flow and pressure gradients.

From Eq. (1.2), one can see a coupling between entropy and acoustics. The mechanism that describes this coupling was first identified by [Marble and Candel \(1977b\)](#) using the linearised quasi-1D Euler equations for an adiabatic flow, neglecting heat release and diffusion for compact nozzles. The set of equations satisfying these hypotheses are:

$$\frac{D}{Dt} \left( \frac{P'}{\gamma P} \right) + u \frac{\partial}{\partial x} \left( \frac{u'}{u} \right) = 0 \quad (1.3a)$$

$$\frac{D}{Dt} \left( \frac{u'}{u} \right) + \frac{c^2}{u} \frac{\partial}{\partial x} \left( \frac{P'}{\gamma P} \right) = \left[ \frac{s'}{c_p} + (\gamma - 1) \frac{P'}{\gamma P} - 2 \frac{u'}{u} \right] \frac{du}{dx} \quad (1.3b)$$

$$\frac{D}{Dt} \left( \frac{s}{c_p} \right) = 0 \quad (1.3c)$$

in which the coupling between acoustics and entropy appears in Eq. (1.3b). The entropy wave acts as a source term of acoustics only if there is an acceleration of the flow ( $du/dx \neq 0$ ). Other authors extended the acoustic analogies for sound propagation to take into account direct and indirect combustion noise sources. This is the case of [Bailly et al. \(2010\)](#), who introduced the excess density (initially defined by [Morfey 1973](#) as  $\rho_e = (\rho - \rho_\infty) - (P - P_\infty)/c_\infty^2$ ) into [Lighthill](#) and [Phillips's](#) analogies to compute and propagate the combustion noise source terms. Indeed, the excess density is associated to entropy variations and is an important source term which is often neglected in aeroacoustic applications.

Following these theoretical developments, experiments have been carried out to study the indirect combustion noise generation, the firsts ones being realised by [Zukoski and Auerbach \(1976\)](#) and [Bohn \(1976, 1977\)](#) within the simplified framework of nozzles. In these experiments the amplitude of the upstream induced temperature fluctuation was very small ( $\approx 1$  K). Furthermore, due to technical restrictions at this time a post-processing of the acquired data in the time domain was not possible (only a time period of 0.1 s could be stored). More recently, [Bake et al. \(2009\)](#), [Knobloch et al. \(2011, 2015a,b\)](#) and [Kings et al. \(2012\)](#) conceived a series of nozzle experiments in which temperature, acoustic and vorticity disturbances were introduced to study the sound radiated by the acceleration of the different perturbations. One of these experiments, the Entropy Wave Generator (EWG) will be used as a reference test case for this PhD work. After such nozzle test cases, the scientific community developed turbine test cases, in which acoustic and entropy disturbances were introduced to study indirect combustion noise. In the work of [Gaetani et al. \(2015\)](#), strokes of hot/cold air are introduced by 11 injectors into a High-Pressure (HP) turbine stage, in which the pressure fluctuations are measured afterwards to quantify the amount of indirect noise generated. The same year, [Schuster et al. \(2015\)](#) studied indirect combustion noise in a Honeywell TECH977 engine, pressure and temperature fluctuations were measured at different positions in the engine to study the propagation of sound and the dissipation of the entropy wave along the different stages of the machine.



Analytical studies in combustion noise have also been carried out by different authors. Williams and Howe (1975) and Howe (2010) studied the convection of an entropy slug by a non homogeneous mean flow, showing that indirect combustion noise acts as a dipole source term. They also developed a model in which when the flow separates in the diffuser, vortex sound and entropy noise correlate and can reduce the overall sound level. In terms of flow physics, the deformation of the hot slug through the nozzle reduces the entropy gradients and therefore the amount of noise generated. Dependency on the operating conditions was addressed by Leyko et al. (2011) and Duran et al. (2013b) by the use of the compact theory of Marble and Candel (1977b) to study the radiated sound of an entropy perturbation convected through a subsonic and a supersonic nozzle with a shock. To finish, Dowling and Mahmoudi (2015) studied the effect of heat release fluctuations (frequency and mode number) in the generation of indirect and direct noise in the limit of low Mach numbers.

More recently, the use of Computational Fluid Dynamics (CFD) started to appear in this specific context. However, the study of combustion noise by numerical simulations requires to take into account different length scales such as the characteristic acoustic wave length  $\lambda$  (in a flow at  $2000K$ ,  $\lambda \approx m$ ), the characteristic flame length  $L_t$  ( $\approx mm$ ), the Kolmogorov length scale  $\eta$  ( $\approx \mu m$ ) and the flame thickness  $\delta_f$  ( $\approx \mu m$ ). The separation of these scales depends on the spatial structure of the turbulent flow, the flame structure and the spatial extent of the acoustic source terms. This wide range of length scales is the reason why numerical simulation is often used to compute first noise sources which are then fed to acoustic analogies, Computational Aero-Acoustics (CAA) or analytical methods for the propagation phase (Ihme et al. 2005, Ihme and Pitsch 2012, Ullrich et al. 2015, Livebardon et al. 2016 and Férand et al. 2016).

### 1.3 Objectives and organisation of this thesis

New technologies of aeronautical combustion chambers have the objective of reducing pollutant emissions and fuel consumption. Nevertheless, these technologies create unwanted effects like unstable combustion, extinction of flame and generation of broadband noise at low frequency. In order to achieve the greening of the European air transport, new technologies need the development of reliable prediction tools. This task requires extensive research with experimental test cases and sophisticated numerical as well as analytical modelling to increase the physical understanding of the core noise generation mechanisms. In this context, the project called "Research on Core Noise Reduction" (RECORD) was initiated, in which the major aero-engine manufacturers, laboratories and Universities of five different European countries collaborate to enable the design of low core noise aero-engines.

In the RECORD project, theory, experiments and numerical methods are used together to better understand the different noise sources of a real engine and its transmis-



sion through turbine stages. Four different Work Packages (WP) were created, each one with a particular objective:

**WP1 - Nozzle flow test cases:** Different test-rigs were built to study the generation and transmission of entropy, vorticity and acoustic waves individually, covering different operating points for a nozzle (subsonic, transonic and supersonic).

**WP2 - Combustor test case:** Noise generation mechanisms in a combustion chamber.

**WP3 - Turbine test cases:** Introduction of acoustic and entropy waves separately into a high-pressure turbine stage.

**WP4 - Exploitation to full scale:** Take advantage of the developments and validation steps done in the other work packages.

In the framework of this PhD thesis, which inscribes itself in the RECORD project, a considerable amount of work is focused on the study of generation and propagation of combustion noise in nozzle flows within WP1. Afterwards, the generation of combustion noise is also studied in a high pressure turbine stage (WP3). The methodology adopted relies on full compressible simulations and comparison to analytical models of the literature. This manuscript is divided into two main parts:

- **Part I:** Study of noise generation in nozzle flows.  
Generation and transmission of combustion noise in nozzles is addressed in this first part. The first chapter describes the state of the art of this specific problem, starting with the analytical and reduced models. In the second chapter, a canonical nozzle test case is extensively studied by means of compressible Large Eddy Simulation (LES). Throughout this study, analytical models, LES results and experimental data are compared. Results obtained from the study of this canonical test case were published and presented in the 22nd AIAA/CEAS Aero-Acoustics Conference, [Becerril et al. \(2016\)](#). Afterwards, to give a better insight into the physical phenomena of direct and indirect generation of combustion noise, the nozzle response to ingoing acoustic and entropy disturbances is assessed through LES and compared to analytical models.
- **Part II:** Study of noise generation in a turbine stage.  
Generation and transmission of combustion noise in a turbine stage is addressed in this second part. This specific application adds two supplementary problems absent in the nozzle case: a strong azimuthal flow deviation induced by the turbine blades and interactions between a fix and a rotating part. To investigate the generation and transmission of combustion noise, harmonic fluctuations of temperature are introduced in LES by a fluctuating energy source term. Noise produced by this fluctuating source term, as well as the noise generated by the acceleration of

the temperature spot downstream of the turbine are then compared with an analytical methodology for combustion noise applications called CHORUS developed at CERFACS ([Leyko 2010](#), [Duran 2013](#) and [Livebardon 2015](#)).

All along this work, multiple comparisons between the numerical simulations and analytical methods are done to obtain a better insight of the different phenomena neglected in the models. Furthermore, the different studies are complemented by validation test cases and further description of the employed tools in specifically dedicated appendices.

## Part I

# Towards a better understanding of combustion noise: Study of noise generation in nozzle flows



# Table of Contents

---

<b>Introduction</b>	<b>15</b>
<b>2 Analytic and reduced models: state-of-the-art for combustion noise prediction</b>	<b>17</b>
2.1 The compact theory . . . . .	20
2.2 The invariant method . . . . .	28
<b>3 The Entropy Wave Generator experiment</b>	<b>37</b>
<b>4 Analytical study of the EWG</b>	<b>43</b>
4.1 The heating device model . . . . .	44
4.2 Propagation of waves through the nozzle . . . . .	47
4.3 Choked nozzle test case . . . . .	48
4.4 Subsonic nozzle test case . . . . .	55
4.5 Conclusion . . . . .	59
<b>5 Numerical compressible simulation of the EWG</b>	<b>63</b>
5.1 The baseline flow . . . . .	65
5.2 The entropy forced flow . . . . .	82
5.2.1 The heating device model . . . . .	82
5.2.2 Numerical simulation of the forced EWG subsonic test case . . . .	86
5.2.3 Conclusion . . . . .	101
5.3 Evaluation of the nozzle transfer functions by CFD . . . . .	104
5.3.1 The forcing signal . . . . .	104
5.3.2 Euler forced simulations . . . . .	106

5.3.3	Navier-Stokes nozzle transfer functions . . . . .	135
5.4	Conclusions . . . . .	160

---

# Introduction

Today and this will remain for a long time, it is still too difficult to study combustion noise generation and transmission in a complex machine like a full aero-engine. One still requires to simplify such a complex systems into more fundamental problems. Direct combustion noise for example was first studied in open flame configurations, for which [Lighthill \(1952\)](#) analogy was reformulated by [Bailly et al. \(2010\)](#) and was applied to reacting flows. Since indirect combustion noise is generated by the acceleration of flow inhomogeneities it cannot exist in open flame configurations. Although studying indirect combustion noise in an accelerated flow through multiple turbine stages is the subject of the second part of this work, the description of the flow is very complex due to the stator/rotor blades, wakes, mixing, shocks and other complex phenomena. It is therefore easier to first describe and apprehend the fundamental generation as well as transmission of indirect combustion noise in a simpler configuration: i.e. a nozzle, where the flow is almost axisymmetric. This simpler objective is the focus of this specific part where analysis and computation is primarily devoted to indirect combustion noise inside this simpler configuration.

All along [Part I](#), nozzle flow configurations will be studied. First, different types of modelling are compared, from reduced analytical models (most of the time the isentropic quasi-1D theory is used), 3D numerical simulation without the effect of viscosity (Euler equations) to the full compressible Navier-Stokes (NS) simulations (LES in the present study). The comparison between these types of modelling will allow evaluating the influence of different parameters in the generation and transmission of combustion noise; from the importance of the geometry (passage from quasi-1D theory to the 3D Euler simulation) to the influence of viscous effects (Euler to NS simulation). [Part I](#) is organized as follows: first, different analytic models for one dimensional axisymmetric flow configurations are presented in [Chapter 2](#). This chapter intends to underline the physics of indirect combustion noise generation. Then, in [Chapter 3](#), the Entropy Wave Generator (EWG) experiment, which is a nozzle test rig located at the German Aerospace Center (DLR) is described and taken as experimental reference case for analytical and numerical comparisons. [Chapter 4](#) details the use of the analytical methodologies of [Chapter 2](#) to study two reference test cases of the EWG: one supersonic and one subsonic flow configuration. Finally, [Chapter 5](#) presents a complete study of a subcritical operating point of the EWG using full compressible 3D LES.





## Chapter 2

# Analytic and reduced models: state-of-the-art for combustion noise prediction

In this chapter, an overview of analytic methods for the prediction of combustion noise through a non-uniform quasi-1D flow are reviewed. The starting point (before studying acoustics or perturbations) is the mean flow through the nozzle. This flow is ultimately supposed to obey the NS equations, namely:

$$\frac{\partial \rho}{\partial t} + \nabla \cdot (\rho u) = 0, \quad (2.1a)$$

$$\frac{\partial (\rho u)}{\partial t} + \nabla \cdot (\rho u u) = \nabla \cdot (-pI + \tau), \quad (2.1b)$$

$$\rho T \left( \frac{\partial s}{\partial t} + u \cdot \nabla s \right) = \nabla \cdot (k \nabla T) + \Phi_v. \quad (2.1c)$$

[Equations \(2.1a–2.1c\)](#), respectively, stand for mass, momentum and energy conservation. The primitive variables are the density  $\rho$ , the pressure  $p$  and the velocity  $u$ .  $I$  is the identity matrix,  $\tau$  the viscous stress tensor,  $k$  the thermal conductivity, and  $\Phi_v$  the Rayleigh dissipation function.  $s$  stands for the specific entropy, which is related to the state variables through the equation  $ds = c_p \frac{dT}{T} - r \frac{dp}{p}$  for a perfect gas, with  $c_p$  the specific heat capacity at constant pressure,  $T$  the temperature and  $r$  the specific perfect gas constant.

For the present study, some assumptions can be made to simplify this set of equations:

- No heat exchange through the fluid and at boundaries (i.e. adiabatic flow) is considered.
- Viscous effects are neglected.

- The flow transformations are reversible (combined with the adiabatic and inviscid conditions, the flow becomes isentropic).
- The gas is ideal and thermodynamically perfect (i.e.  $\gamma$ ,  $c_p$  and  $c_v$  are constants).
- The flow/geometry is considered to be quasi-1D.

With these assumptions, the quasi 1D-Euler equations are obtained, reading:

$$\frac{1}{\rho} \left[ \frac{\partial \rho}{\partial t} + u \frac{\partial \rho}{\partial x} \right] + \frac{\partial u}{\partial x} = - \frac{u}{A} \frac{dA}{dx}, \quad (2.2a)$$

$$\frac{\partial u}{\partial t} + u \frac{\partial u}{\partial x} + \frac{1}{\rho} \frac{\partial p}{\partial x} = 0, \quad (2.2b)$$

$$\frac{\partial s}{\partial t} + u \frac{\partial s}{\partial x} = 0, \quad (2.2c)$$

where  $A$  is the duct cross section and is supposed to vary with the axial coordinate  $x$  ( $A = A(x)$ ).

In the general case, the flow resulting from this last set of simplified equations needs to be solved numerically. Likewise and under specific constraints (linearisation), an expression for the disturbed quantities can be found. To linearise Eqs. (2.2a–2.2c), the flow variables must be split into two contributions:  $\varphi = \bar{\varphi} + \varphi'$ , a mean part ( $\bar{\varphi}$ ) and a fluctuating part  $\varphi'$ . Linearisation is possible if the fluctuating contribution is small compared to its mean value ( $\frac{\varphi'}{\bar{\varphi}} \ll 1$ ). In this case, the Linearised Euler Equations (LEE) for a quasi-1D flow can be recast into:

$$\left[ \frac{\partial}{\partial t} + u \frac{\partial}{\partial x} \right] \left( \frac{p'}{\gamma p} \right) + u \frac{\partial}{\partial x} \left( \frac{u'}{u} \right) = 0, \quad (2.3a)$$

$$\left[ \frac{\partial}{\partial t} + u \frac{\partial}{\partial x} \right] \left( \frac{u'}{u} \right) + \frac{c^2}{u} \frac{\partial}{\partial x} \left( \frac{p'}{\gamma p} \right) + \left[ \frac{2u'}{u} - (\gamma - 1) \frac{p'}{\gamma p} \right] \frac{du}{dx} = \frac{s'}{c_p} \frac{du}{dx}, \quad (2.3b)$$

$$\left[ \frac{\partial}{\partial t} + u \frac{\partial}{\partial x} \right] \left( \frac{s'}{c_p} \right) = 0, \quad (2.3c)$$

where for simplicity the symbol  $(-)$  has been dropped.

If the flow is homogeneous (i.e.  $\frac{du}{dx} = 0$ ), Eq. (2.3b) can be further simplified. Furthermore, manipulating the term  $u \frac{\partial}{\partial x} \left( \frac{u'}{u} \right)$  to make appear the sound speed,

$$u \frac{\partial}{\partial x} \left( \frac{u'}{u} \right) = u \frac{\partial}{\partial x} \left( \frac{u'}{Mc} \right) = \frac{1}{M} \left[ \frac{\partial}{\partial x} \left( \frac{u'}{c} \right) - \frac{u'}{u} \frac{\partial M}{\partial x} \right], \quad (2.4)$$

the system of LEE can be rearranged into:

$$\left[ \frac{\partial}{\partial t} + u \frac{\partial}{\partial x} \right] \left( \frac{p'}{\gamma p} \right) + c \frac{\partial}{\partial x} \left( \frac{u'}{c} \right) = 0. \quad (2.5a)$$

$$\left[ \frac{\partial}{\partial t} + u \frac{\partial}{\partial x} \right] \left( \frac{u'}{c} \right) + c \frac{\partial}{\partial x} \left( \frac{p'}{\gamma p} \right) = 0, \quad (2.5b)$$

$$\left[ \frac{\partial}{\partial t} + u \frac{\partial}{\partial x} \right] \left( \frac{s'}{c_p} \right) = 0. \quad (2.5c)$$

Finally, Eq. (2.5a)±Eq. (2.5b) can be recast into a new pair of equations so the LEE system is rewritten into a system of characteristic equations that read:

$$\left[ \frac{\partial}{\partial t} + (u + c) \frac{\partial}{\partial x} \right] A^+ = 0, \quad (2.6a)$$

$$\left[ \frac{\partial}{\partial t} + (u - c) \frac{\partial}{\partial x} \right] A^- = 0, \quad (2.6b)$$

$$\left[ \frac{\partial}{\partial t} + u \frac{\partial}{\partial x} \right] \sigma = 0, \quad (2.6c)$$

where,

$$A^+ = \frac{1}{2} \left[ \frac{p'}{\gamma p} + \frac{u'}{c} \right], \quad A^- = \frac{1}{2} \left[ \frac{p'}{\gamma p} - \frac{u'}{c} \right] \quad \text{and} \quad \sigma = \frac{s'}{c_p} = \frac{p'}{\gamma p} - \frac{\rho'}{\rho} \quad (2.7)$$

are the so called characteristic variables. In this form, they are associated to the progressive acoustic wave  $A^+$ , the retrograde acoustic wave  $A^-$  and the entropy wave  $\sigma$ . Note that  $A^+$  and  $A^-$  are affected by a  $1/2$  coefficient to be in accordance with the work of [Marble and Candel \(1977b\)](#). In terms of physics or mathematical properties, each wave is propagated at its own velocity: acoustic waves are propagated at the velocity  $(u + c)$  or  $(u - c)$ , whereas the entropy wave  $\sigma$  is propagated at the velocity of the flow  $u$ . The propagation direction of the acoustic waves depends on the nature of the flow (subsonic or supersonic). For a subsonic flow, where the velocity of the sound is greater than the velocity of the fluid, the acoustic wave  $A^+$  propagates downstream, whereas the acoustic wave  $A^-$  propagates upstream. When the flow is supersonic, the sound velocity is greater than the velocity of the fluid. As a consequence, the propagation direction of  $A^-$  changes, making both acoustic waves propagate downstream, as shown by [Fig. 2.1](#).

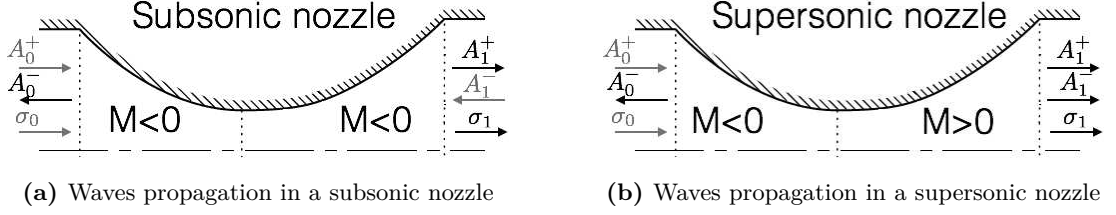


**Figure 2.1** Sketch of a converging diverging nozzle and waves propagation direction.

When the flow is non-homogeneous (inside the nozzle), the acoustic and entropy waves are coupled by the velocity gradient ( Eq. (2.3b)) and the characteristic solution proposed in Eqs. (2.5a–2.5c) and (2.7) cannot describe the propagation of waves. Other methodologies like the ones introduced in this chapter need to be used. The simpler one is to consider the nozzle as an interface. The disturbances wavelengths are hence considered to be big compared to the nozzle characteristic length ( $\lambda \gg l_n$ ). This theory was proposed by Marble and Candel (1977b) and is the basis of multiple subsequent theories and extensions in the acoustic wave propagation through a non-homogeneous flow. In the following, the compact theory is explained and rederived in order to understand the fundamental equations that govern the propagation of acoustic waves in a non-homogeneous flow. Then, the analytical theory of Duran and Moreau (2013a), that solves the LEE in the frequency domain is introduced and explained. This theory is used later to compute the response of a nozzle to acoustic and entropy disturbances and study the generation of entropy noise.

## 2.1 The compact theory

Marble and Candel (1977b) were the first to propose a theory that introduces the notion of entropy generated noise. In their pioneering work, they also provide for the first time the acoustic response of a nozzle to acoustic and entropy perturbations relying on the so called compact assumption. This specific assumption requires that the acoustic and entropy wave lengths  $\lambda$  are big compared to the characteristic length of the nozzle  $l_n$ . If the wave length is considered to be big, it also means that this method only works for near zero frequencies. In other words, the temporal dependency of the balance equations is dropped and no phase shift is induced by the nozzle. For example, the compact assumption applied to the continuity equation gives:

$$\frac{\partial \rho A}{\partial t} + \frac{\partial \rho u A}{\partial x} = 0, \quad (2.8)$$

$$\lambda \gg l_n, \quad t \equiv f^{-1} \rightarrow \infty \quad \text{and} \quad x \equiv l_n, \text{ so,}$$

$$\frac{\partial \rho A}{\partial t} + \frac{\partial \rho u A}{\partial x} = 0 \Rightarrow \boxed{\frac{\partial \rho u A}{\partial x} = 0}.$$

The compactness of the nozzle makes that the different disturbances see the nozzle as an interface. Therefore, matching conditions can be applied between the inlet (indexed by the subscript  $(\cdot)_0$ ) and the outlet (indexed by the subscript  $(\cdot)_1$ ) of the nozzle choosing the variables that are conserved:

- Conservation of the mass flow rate  $\dot{m}$  (continuity equation),
- Conservation of the stagnation temperature  $T_T$  (adiabatic condition),
- Conservation of entropy  $s$  (isentropic condition).

Note that to fullfill the isentropic condition, no shock waves are considered in this part and they should be treated separately. Linearising the conserved quantities across the nozzle to obtain jump conditions for fluctuations, one obtains:

$$\left(\frac{\dot{m}'}{\dot{m}}\right)_0 = \left(\frac{\dot{m}'}{\dot{m}}\right)_1, \quad (2.9a)$$

$$\left(\frac{T_T'}{T_T}\right)_0 = \left(\frac{T_T'}{T_T}\right)_1, \quad (2.9b)$$

$$\left(\frac{s'}{c_p}\right)_0 = \left(\frac{s'}{c_p}\right)_1. \quad (2.9c)$$

Equations (2.9a–2.9c) show the conservation of the reduced mass flow rate, the stagnation temperature and the entropy along the nozzle. These quantities are called "flow invariants" and the relations that link them to the primitive variables read:

$$\left(\frac{\dot{m}'}{\dot{m}}\right) = \varphi + \nu - \sigma, \quad (2.10a)$$

$$\left(\frac{T_T'}{T_T}\right) = \frac{\gamma - 1}{1 + \frac{\gamma - 1}{2}M^2} \left[ M^2\nu + \varphi + \frac{\sigma}{\gamma - 1} \right], \quad (2.10b)$$

$$\left(\frac{s'}{c_p}\right) = \sigma, \quad (2.10c)$$

where  $\varphi = \frac{p'}{\gamma p}$ ,  $\nu = \frac{u'}{u}$  and  $\sigma = \frac{s'}{c_p}$  are the dimensionless fluctuating pressure, velocity and entropy respectively.

With this formalism, the problem to be solved is the response of the nozzle in terms of outgoing waves and ingoing waves. This is usually retrieved by the so called nozzle transfer functions. This means that ingoing waves are boundary conditions of the problem (variables to be imposed) while outgoing waves (unknowns) are the response of the nozzle to the ingoing perturbation. The number of ingoing and outgoing waves depends on the nature of the flow, as shown in Fig. 2.1. Table 2.1 summarizes the number of boundary conditions to impose and the number of unknowns to determine when a nozzle is subsonic or choked.

Subsonic		Chocked	
Boundary conditions	Unknowns	Boundary conditions	Unknowns
$A_0^+$	$A_1^+$	$A_0^+$	$A_0^-$
$A_1^-$	$A_1^-$	$\sigma_0$	$A_1^+$
$\sigma_0$	$\sigma_1$		$A_1^-$
			$\sigma_1$

**Table 2.1** Waves to impose and to determine to compute the nozzle transfer functions.

The transfer functions of the nozzle (ratio of an outgoing to an ingoing wave) are obtained by imposing one ingoing wave at a time (setting the others to zero) and combining Eq. (2.7) with the flow invariants of Eqs. (2.10a–2.10c). For a chocked nozzle the problem is not closed: four waves need to be determined for only three jump conditions. One supplementary relation is needed. Usually, the particular point of the nozzle throat, where the nozzle Mach number is equal to one, is used based upon the relationship:

$$\dot{m} (M = 1) = A P_T \left( \frac{\gamma}{r T_T} \right)^{1/2} \left( \frac{\gamma + 1}{2} \right)^{\frac{\gamma+1}{2(\gamma-1)}} = \rho u A. \quad (2.11)$$

Both parts of the equation can be linearised, which yields:

$$\frac{(\dot{m} (M = 1))'}{\dot{m} (M = 1)} = \frac{\dot{m}'}{\dot{m}} \Rightarrow \nu + \frac{1 - \gamma}{2} \varphi - \frac{1}{2} \sigma = 0. \quad (2.12)$$




It should be noted that Eq. (2.12) also states that Mach fluctuation at the nozzle throat is zero. In other words, the nozzle throat Mach number cannot be different from one ( $M'/M = 0$ ), which holds for the compact nozzle at any point in the nozzle.

Rearranging Eq. (2.12) to make appear the linearised mass flow rate and entropy conservation invariant equations, Eqs. (2.10a) and (2.10c), it can be shown that for a supersonic nozzle,  $\nu$ ,  $\varphi$  and  $\sigma$  are constant through the nozzle:



$$\underbrace{\varphi + \nu - \sigma}_{\left( \frac{\dot{m}'}{\dot{m}} \right) = \text{cst}} + \frac{1}{2} \underbrace{\sigma}_{\left( \frac{s'}{c_p} \right) = \text{cst}} - \frac{\gamma + 1}{2} \varphi = 0. \quad (2.13)$$

$$\Rightarrow \varphi = \text{cst}, \quad \nu = \text{cst}.$$

Finally the transfer functions of the nozzle, which are written as the ratio of the transmitted/reflected wave over the unitary forced wave, can be expressed and are summarized in Tab. 2.2 and Tab. 2.3.

	Subsonic nozzle	
	$A_0^-$	$A_1^+$
Response to 	$\frac{M_1 - M_0}{1 - M_0} \frac{1 + M_0}{M_0 + M_1} \frac{1 - \frac{\gamma-1}{2} M_0 M_1}{1 + \frac{\gamma-1}{2} M_0 M_1}$	$\frac{2M_1}{1 - M_1} \frac{1 + M_0}{M_0 + M_1} \frac{1 + \frac{\gamma-1}{2} M_1^2}{1 + \frac{\gamma-1}{2} M_0 M_1}$
Response to 	$-\frac{M_1 - M_0}{1 - M_0} \frac{\frac{1}{2} M_0}{1 + \frac{\gamma-1}{2} M_0 M_1}$	$\frac{M_1 - M_0}{1 + M_1} \frac{\frac{1}{2} M_1}{1 + \frac{\gamma-1}{2} M_0 M_1}$
Response to 	$\frac{2M_0}{1 - M_0} \frac{1 - M_1}{M_0 + M_1} \frac{1 + \frac{\gamma-1}{2} M_0^2}{1 + \frac{\gamma-1}{2} M_0 M_1}$	$-\frac{M_1 - M_0}{1 + M_1} \frac{1 - M_1}{M_0 + M_1} \frac{1 - \frac{\gamma-1}{2} M_0 M_1}{1 + \frac{\gamma-1}{2} M_0 M_1}$

**Table 2.2** Response of a compact subsonic nozzle to acoustic and entropy unitary disturbances.

	Supersonic nozzle		
	$A_0^-$	$A_1^+$	$A_1^-$
Response to 	$\frac{1 - \frac{\gamma-1}{2} M_0}{1 + \frac{\gamma-1}{2} M_0}$	$\frac{1 + \frac{\gamma-1}{2} M_1}{1 + \frac{\gamma-1}{2} M_0}$	$\frac{1 - \frac{\gamma-1}{2} M_1}{1 + \frac{\gamma-1}{2} M_0}$
Response to 	$-\frac{M_0}{2(1 + \frac{\gamma-1}{2} M_0)}$	$\frac{M_1 - M_0}{4(1 + \frac{\gamma-1}{2} M_0)}$	$-\frac{M_1 + M_0}{4(1 + \frac{\gamma-1}{2} M_0)}$

**Table 2.3** Response of a compact supersonic nozzle to acoustic and entropy unitary disturbances.

The transfer functions for subsonic and choked nozzles have now been established under the compact assumption. It is however important to note that the flow does not always leave the nozzle as supersonic and a shock can be formed in the diffuser. In this case, the nozzle can be split into two regions (cf. [Fig. 2.2](#)): an upstream supersonic nozzle which can be solved using the transfer functions presented in [Tab. 2.3](#) and a downstream subsonic nozzle where the relations of [Tab. 2.2](#) are applicable. To link both nozzles, jump conditions across the shock need to be supplied. [Stow et al. \(2002\)](#), [Moase et al. \(2007\)](#), [Goh and Morgans \(2011b\)](#) and [Duran and Moreau \(2013a\)](#) described a methodology to obtain the response of a shock to acoustic and entropy perturbations.

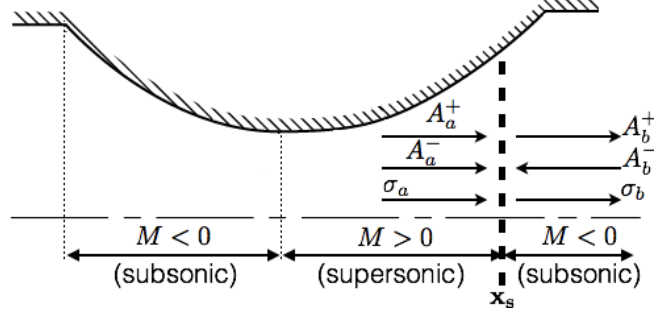


**Figure 2.2** Sketch of a supersonic nozzle with a shock.

To do so, the shock is considered to be an infinitesimally small interface located at the position  $x_s = \bar{x}_s + x'_s$ , where the fluctuating part  $x'_s$  is caused by the acoustic and entropic perturbations impinging the shock. At this position, four waves travel towards the shock, namely  $A_a^+$ ,  $A_a^-$ ,  $\sigma_a$  (from the supersonic part) and  $A_b^-$  (from the subsonic part), while only two waves propagate in the outward direction in the subsonic part, namely  $A_b^+$  and  $\sigma_b$  as shown by Fig. 2.2.

Rankine-Hugoniot shock relations for normal shock waves are then used to link the upstream and downstream states of the shock wave, so that:

$$M_b^2 = \frac{1 + \frac{\gamma-1}{2} M_a^2}{\gamma M_a^2 - \frac{\gamma-1}{2}}, \quad (2.14a)$$

$$\frac{p_b}{p_a} = \frac{2\gamma M_a^2 - \gamma + 1}{\gamma + 1}, \quad (2.14b)$$

$$\frac{\rho_b}{\rho_a} = \frac{u_a}{u_b} = \frac{\frac{\gamma+1}{2} M_a^2}{1 + \frac{\gamma-1}{2} M_a^2}. \quad (2.14c)$$

Linearising these relations in the shock reference frame  $(\ )_{sh}$  yields:

$$\frac{p'_{b,sh}}{\gamma p_b} - \frac{p'_{a,sh}}{\gamma p_a} = \frac{4M_a^2}{\gamma + 1} \left( \frac{p_a}{p_b} \right) \left( \frac{M'_{a,sh}}{M_a} \right), \quad (2.15a)$$

$$\frac{\rho'_{b,sh}}{\rho_b} - \frac{\rho'_{a,sh}}{\rho_a} = \frac{4}{M_a^2 (\gamma + 1)} \left( \frac{u_a}{u_b} \right) \left( \frac{M'_{a,sh}}{M_a} \right), \quad (2.15b)$$

$$\frac{u'_{b,sh}}{u_b} - \frac{u'_{a,sh}}{u_a} = \frac{-4}{M_a^2 (\gamma + 1)} \left( \frac{u_a}{u_b} \right) \left( \frac{M'_{a,sh}}{M_a} \right), \quad (2.15c)$$

where the fluctuating pressure and density in the reference frame of the shock can be decomposed into two contributions: 1) the absolute fluctuation in the reference frame of the shock; 2) a fluctuation generated by the motion of the shock wave inside the nozzle multiplied by the gradient of the mean pressure/density (this step can be seen as



a Taylor expansion up to first order at the shock position):

$$p'_{sh} = p' + x'_s \frac{dp}{dx}, \quad (2.16a)$$

$$\rho'_{sh} = \rho' + x'_s \frac{d\rho}{dx}. \quad (2.16b)$$

Similarly, assuming that fluctuations are harmonic in time,  $\exp(i\omega t)$ , velocity and Mach number fluctuations in the vicinity of the shock read:

$$u'_{sh} = u' + x'_s \frac{du}{dx} - \frac{dx'_s}{dt} = u' + x'_s \left( \frac{du}{dx} - i\omega \right), \quad (2.17a)$$

$$M'_{sh} = M' + x'_s \frac{dM}{dx} - \frac{1}{c} \frac{dx'_s}{dt} = M' + x'_s \left( \frac{dM}{dx} - \frac{i\omega}{c} \right). \quad (2.17b)$$

To close the system, expressions for the mean density, mean pressure, mean velocity and mean Mach number are needed. First, the conservation of mass flow rate through the shock wave can be established, allowing to write a relation linking the Mach numbers behind and ahead of the shock with the Mach gradients:

$$\frac{M_b^2 - 1}{M_b \left( 1 + \frac{\gamma-1}{2} M_b^2 \right)} \frac{dM_b}{dx} = \frac{M_a^2 - 1}{M_a \left( 1 + \frac{\gamma-1}{2} M_a^2 \right)} \frac{dM_a}{dx}. \quad (2.18)$$

From the definition of the Mach number, a relation for the gradient of velocity can be written:

$$\frac{du}{dx} = \frac{d(Mc)}{dx} = c \frac{dM}{dx} + M \frac{dc}{dx} = \frac{c}{1 + \frac{\gamma-1}{2} M^2} \frac{dM}{dx}. \quad (2.19)$$

To express the gradients of pressure and density, the isentropic relations are used:

$$\frac{1}{\gamma p} \frac{dp}{dx} = \frac{1}{\rho} \frac{d\rho}{dx} = - \frac{-M}{1 + \frac{\gamma-1}{2} M^2} \frac{dM}{dx}. \quad (2.20)$$

Writing mean pressure, mean velocity and mean density gradients as functions of the Mach gradient upstream of the shock wave using Eqs. (2.18–2.20) and replacing Eqs. (2.16) and (2.17) in Eq. (2.15), the equations for the fluctuating primitive variables upstream and downstream of the shock wave read:

$$\frac{p'_b}{\gamma p_b} - \frac{p'_a}{\gamma p_a} = \frac{4M_a^2}{\gamma + 1} \left( \frac{p_a}{p_b} \right) \left[ \frac{M'_a}{M_a} + \Gamma_p x'_s \right], \quad (2.21a)$$

$$\frac{\rho'_b}{\rho_b} - \frac{\rho'_a}{\rho_a} = \frac{4}{M_a^2 (\gamma + 1)} \left( \frac{u_a}{u_b} \right) \left[ \frac{M'_a}{M_a} + \Gamma_\rho x'_s \right], \quad (2.21b)$$

$$\frac{u'_b}{u_b} - \frac{u'_a}{u_a} = \frac{-4}{M_a^2 (\gamma + 1)} \left( \frac{u_a}{u_b} \right) \left[ \frac{M'_a}{M_a} + \Gamma_u x'_s \right], \quad (2.21c)$$

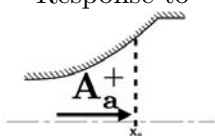
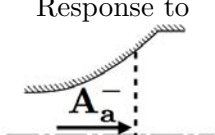
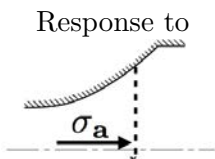
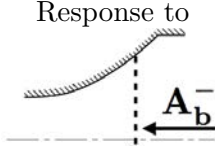
where the expression for  $\Gamma_x$  are:

$$\Gamma_p = \frac{1}{M_a} \left[ 1 - \frac{M_b^2 - M_a^2}{2M_a^2 M_b^2 (M_b^2 - 1)} \right] \frac{dM_a}{dx} - \frac{i\omega}{M_a c_a}, \quad (2.22a)$$

$$\Gamma_\rho = \frac{1}{2M_a} \left[ 1 + \frac{M_a^2 - 1}{M_b^2 - 1} \right] \frac{dM_a}{dx} - \frac{i\omega}{M_a c_a}, \quad (2.22b)$$

$$\Gamma_u = \frac{1}{2M_a} \left[ 1 + \frac{M_a^2 - 1}{M_b^2 - 1} \right] \frac{dM_a}{dx} - \left( \frac{M_a^2 + 1}{2} \right) \frac{i\omega}{M_a c_a}. \quad (2.22c)$$

Only two jump conditions are needed since there are only two outgoing waves issuing from the shock ( $A_b^+$  and  $\sigma_b$ ). Hence, the dependency on  $x'_s$  can be dropped if [Eq. \(2.21\)](#) is combined to yield only two jump conditions. Finally, to compute the response of the shock front to the arriving disturbances, the wave formulation of [Eqs. \(2.21a–2.21c\)](#) is used. This is done knowing that the Mach number fluctuation in a supersonic nozzle is given by [Eq. \(2.12\)](#) and that the density fluctuation can be computed using the definition of the entropy wave  $\rho'/\rho = \varphi - \sigma$ . Hence, the jump relations for a normal shock are obtained and summarized in [Tab. 2.4](#). It should be noted that the acoustic-entropy transfer functions differ from [Duran and Moreau \(2011\)](#) by a factor 2 and the entropy-acoustic transfer function by a factor  $1/2$ . This is due to the definition of the acoustic waves employed in this manuscript (cf. [Eq. \(2.7\)](#)).

	$\mathbf{A}_b^+$	$\sigma_b$
Response to 	$\frac{\alpha^+}{\psi^+}$	$2 \left[ \phi \left( \frac{\alpha^+}{\psi^+} - 1 \right) - \Lambda \left( 1 - \frac{\gamma-1}{2} M_a \right) \right]$
Response to 	$\frac{\alpha^-}{\psi^+}$	$2 \left[ \phi \left( \frac{\alpha^-}{\psi^+} - 1 \right) + \Lambda \left( 1 + \frac{\gamma-1}{2} M_a \right) \right]$
Response to 	$\frac{1}{2} M_a^2 M_b^2 \frac{\delta}{\psi^+}$	$1 + \phi M_a^2 M_b^2 \frac{\delta}{\psi^+} + M_a \Lambda$
Response to 	$-\frac{\psi^-}{\psi^+}$	$2\phi \left( 1 - \frac{\psi^-}{\psi^+} \right)$

$$\Lambda = \frac{1 - \left( \frac{\Gamma_\rho}{\Gamma_p} \right)}{M_a \left( 1 + \frac{\gamma-1}{2} M_a^2 \right)} \quad \delta = \frac{2 \left( 1 - \frac{\Gamma_u}{\Gamma_p} \right)}{1 + \frac{\gamma-1}{2} M_a^2}$$

$$\alpha^\pm = \frac{\Gamma_u}{\Gamma_p} \pm M_a^2 M_b^2 \left[ 1 - \delta \left( 1 \mp \frac{\gamma-1}{2} M_a \right) \right]$$

$$\phi = \frac{1}{2} \left[ 1 - \frac{1}{M_a^2 M_b^2} \left( \frac{\Gamma_\rho}{\Gamma_p} \right) \right] \quad \psi^\pm = \left( \frac{\Gamma_u}{\Gamma_p} \pm M_a^2 M_b \right)$$

**Table 2.4** Response of a shock wave to acoustic and entropy unitary disturbances.

The shock transfer functions were derived for the general case. It is important to notice that the obtained shock relations are frequency dependent which is in agreement with the analyse of [Stow et al. \(2002\)](#) or [Goh and Morgans \(2011b\)](#) obtained using an asymptotic expansion of the LEE.

The supersonic part of the nozzle is solved applying directly the transfer functions of [Tab. 2.3](#). To solve the downstream subsonic nozzle, the inlet waves must be computed correctly. Indeed, the acoustic and entropy inlet waves for this nozzle will be the sum of

the different responses of the shock, therefore:

$$A_b^+ = \underbrace{\left[ \frac{A_b^+}{A_a^+} \right] A_a^+ + \left[ \frac{A_b^+}{A_a^-} \right] A_a^- + \left[ \frac{A_b^+}{\sigma_a} \right] \sigma_a}_{A_{b,f}^+} + \underbrace{\left[ \frac{A_b^+}{A_b^-} \right] A_b^-}_{R_{in}}, \quad (2.23)$$

$$\sigma_b = \underbrace{\left[ \frac{\sigma_b}{A_a^+} \right] A_a^+ + \left[ \frac{\sigma_b}{A_a^-} \right] A_a^- + \left[ \frac{\sigma_b}{\sigma_a} \right] \sigma_a}_{\sigma_{b,f}} + \underbrace{\left[ \frac{\sigma_b}{A_b^-} \right] A_b^-}_{R'_s}. \quad (2.24)$$

The first contribution, here denoted by the subscript  $f$  (for forced) results from the transmitted waves through the shock. The second contribution, called "reflected" is the result of the reflection of the upstream-propagating wave coming from the outlet of the nozzle. From here on, the downstream subsonic nozzle can be easily solved applying the transfer functions of [Tab. 2.2](#).

The analytic transfer functions of a compact subsonic and choked nozzle with and without a shock have been rederived following the work of [Marble and Candel \(1977b\)](#). From this work, multiple extensions to the compact theory have been developed. For example, the compact non-linear nozzle of [Huet and Giauque \(2013\)](#) and [Huet \(2016\)](#), proposes analytical second order transfer functions to take into account the non-linear effects produced by a high amplitude entropy forcing. The work of [Stow et al. \(2002\)](#); [Goh and Morgans \(2011b\)](#) proposes an asymptotic expansion of the LEE that corrects the phase of the choked nozzle transfer functions introducing an equivalent nozzle length (by definition the compact nozzle is an interface and therefore there is no phase shift between the waves through the nozzle). Afterwards, and to study the response of the nozzle to non-zero frequencies, [Giauque et al. \(2012\)](#) proposed the introduction of a linear mean velocity profile method. This methodology considers that the nozzle is represented as a series of smaller nozzles, each nozzle being governed by a linear mean velocity profile forming a piece-wise velocity profile for the entire nozzle. With these assumptions, a hypergeometric differential equation coupled to the adjacent intervals needs to be solved to compute the complete solution of the nozzle.

## 2.2 The invariant method

In this section the analytical non-compact solution of the quasi-1D LEE in the frequency domain developed by [Duran and Moreau \(2013a\)](#) is presented. This solution allows to study the acoustic response of a nozzle for all frequencies. Indeed, even if combustion noise is known to radiate broadband noise in the low frequency limit, it is important to know that the compactness limit (and therefore the validity of the compact solution) is reached rapidly (cf. [Leyko et al. 2010](#)) and that the nozzle transfer functions depend strongly on frequency (cf. [Leyko et al. 2009](#) and [Duran et al. 2013b](#)).

The analytical methodology developed by [Duran and Moreau \(2013a\)](#) does not use the compact hypothesis for the nozzle and solves the LEE for every point in the nozzle. The methodology consists in introducing [Marble and Candel's](#) flow invariants (dimensionless mass flow rate, total temperature and entropy of [Eqs. \(2.9a–2.9c\)](#)) into [Eqs. \(2.3a–2.3c\)](#) to obtain a linear ordinary differential equation system of the form  $d[I]/dX = \mathcal{A}(X)I$ , where  $I$  is the invariant vector and  $\mathcal{A}$  is a matrix.

To do so, the first step is to write the one dimensional LEE ([Eqs. \(2.3a–2.3c\)](#)) into a dimensionless form. [Duran and Moreau](#) have chosen to take as reference state the inlet of the nozzle (referenced by the subscript 0) to reduce velocity variables. Therefore, dimensionless space  $X = x/L_n$ , dimensionless time  $\tau = tf'$  (here  $f'$  is the characteristic frequency of the flow), dimensionless frequency  $\Omega = fL_n/c_0$ , dimensionless velocity  $\bar{u} = u/c_0$ , dimensionless speed of sound  $\bar{c} = c/c_0$  and dimensionless primitive variables fluctuations ( $\varphi$ ,  $\nu$  and  $\sigma$ ) are introduced into the LEE to yield the following set of equations:

$$\left[ \Omega \frac{\partial}{\partial \tau} + \bar{u} \frac{\partial}{\partial X} \right] \varphi + \bar{u} \frac{\partial \nu}{\partial X} = 0, \quad (2.25a)$$

$$\left[ \Omega \frac{\partial}{\partial \tau} + \bar{u} \frac{\partial}{\partial X} \right] \nu + \frac{\bar{c}^2}{\bar{u}} \frac{\partial \varphi}{\partial X} + [2\nu - (\gamma - 1)\varphi - \sigma] \frac{d\bar{u}}{dX} = 0, \quad (2.25b)$$

$$\left[ \Omega \frac{\partial}{\partial \tau} + \bar{u} \frac{\partial}{\partial X} \right] \sigma = 0. \quad (2.25c)$$

The method consists then in writing the transport equations for the three flow invariants  $I_A = \dot{m}'/\dot{m}$ ,  $I_B = T'_T/T_T$  and  $I_C = \sigma$  instead of solving the conventional LEE. Let us start with the dimensionless mass flow rate fluctuation invariant transport equation. [Eq. \(2.25a\)](#) is subtracted from [Eq. \(2.25c\)](#) to yield:

$$\frac{D}{D\tau}(I_A) = \Omega \frac{\partial \nu}{\partial \tau}, \quad (2.26)$$

where the substantial derivative is defined as  $D/D\tau = \Omega \partial/\partial \tau + \bar{u} \partial/\partial X$ .

Invariant  $I_B$  is introduced using the linearised dimensionless momentum equation, [Eq. \(2.25b\)](#), but first the dependency on the velocity gradient needs to be dropped and expressed as a function of the Mach number (like the flow invariants),

$$\frac{d\bar{u}}{dX} = \frac{d(M\bar{c})}{dX} = \left( \frac{\bar{c}}{1 + \frac{\gamma-1}{2}M^2} \right) \frac{dM}{dX}. \quad (2.27)$$

Then using [Eq. \(2.27\)](#) and multiplying [Eq. \(2.25a\)](#) by  $M^2$ , the following expression for  $I_B$  is obtained:

$$\Omega \frac{\partial (M^2 \nu)}{\partial \tau} + \bar{u} \left( \frac{1 + \frac{\gamma-1}{2}M^2}{\gamma - 1} \right) \frac{\partial I_B}{\partial X} - \bar{u} \frac{\partial}{\partial X} \left( \frac{\sigma}{\gamma - 1} \right) = 0. \quad (2.28)$$

Subtracting Eq. (2.25c) from Eq. (2.28) the transport equation for  $I_B$  becomes:

$$\frac{D}{D\tau}(I_B) = \Omega \left( \frac{\gamma-1}{1 + \frac{\gamma-1}{2}M^2} \right) \frac{\partial \varphi}{\partial \tau}. \quad (2.29)$$

The transport equation for the entropy fluctuation invariant  $I_C$  is obtained directly.

To close the system, expressions for  $\partial\nu/\partial\tau$  and  $\partial\varphi/\partial\tau$  are needed, which is done by using Eq. (2.25a) and Eq. (2.28) to obtain the system:

$$\frac{D}{D\tau}(I_A) = \frac{\bar{u}}{M^2(\gamma-1)} \left[ \frac{\partial}{\partial X}(I_C) - \left( 1 + \frac{\gamma-1}{2}M^2 \right) \frac{\partial}{\partial X}(I_B) \right], \quad (2.30a)$$

$$\frac{D}{D\tau}(I_B) = -\frac{\bar{u}(\gamma-1)}{1 + \frac{\gamma-1}{2}M^2} \left[ \frac{\partial}{\partial X}(I_A + I_C) \right], \quad (2.30b)$$

$$\frac{D}{D\tau}(I_C) = 0. \quad (2.30c)$$

If the invariants are assumed to be harmonic, the system can be written as a linear differential equation system,

$$[\mathcal{E}(X)] \frac{d}{dX}[I] = 2\pi i \Omega I, \quad (2.31)$$

where the invariant vector is  $I = [I_A; I_B; I_C]$  and  $\mathcal{E}$  is a 3x3 matrix,

$$\mathcal{E}(X) = -\bar{u} \begin{bmatrix} 1 & \frac{1 + \frac{\gamma-1}{2}M^2}{M^2(\gamma-1)} & -\frac{1}{M^2(\gamma-1)} \\ \frac{\gamma-1}{1 + \frac{\gamma-1}{2}M^2} & 1 & \frac{\gamma-1}{1 + \frac{\gamma-1}{2}M^2} \\ 0 & 0 & 1 \end{bmatrix}. \quad (2.32)$$

When the determinant of  $\mathcal{E}$  is non-zero ( $M \neq 1$ ), the matrix can be inverted leading to:

$$\frac{d}{dX}[I] = \mathcal{A}(X) I, \quad (2.33)$$

where  $\mathcal{A}$  is the complex matrix

$$\mathcal{A}(X) = -\frac{2\pi\Omega i}{u(M^2-1)} \begin{bmatrix} M^2 & -\frac{1 + \frac{\gamma-1}{2}M^2}{\gamma-1} & \frac{\gamma}{\gamma-1} \\ -\frac{M^2(\gamma-1)}{1 + \frac{\gamma-1}{2}M^2} & M^2 & -\frac{M^2(\gamma-1)+1}{1 + \frac{\gamma-1}{2}M^2} \\ 0 & 0 & M^2-1 \end{bmatrix}. \quad (2.34)$$

Note that for choked nozzles, where the nozzle throat Mach number is unity  $M_{N_{th}} = 1$ , the determinant of  $\mathcal{E}$  is zero and it cannot be inverted. This particular case needs therefore to be treated separately.

To solve the differential system of Eq. (2.33), which is a set of homogeneous first order differential equations, Duran et al. (2013b) used the Magnus expansion (Magnus 1954; Blanes et al. 2009). In this approach, the solution of the system in matrix form can be written:

$$I(X) = [\mathcal{C}(X)] I_0, \quad \text{with} \quad \mathcal{C}(X) = \exp(\mathcal{B}(X)), \quad (2.35)$$

where  $I_0$  is the invariant vector at the inlet. The asymptotic expansion is performed in terms of  $\mathcal{B}$  (around  $\Omega \rightarrow 0$ ) instead of expanding  $I$  directly. In the particular case where the Mach number is constant (e.g. a straight duct),  $\mathcal{A}(X)$  commutes for any value of  $X_1$  and  $X_2$  ( $\mathcal{A}(X_1)\mathcal{A}(X_2) - \mathcal{A}(X_2)\mathcal{A}(X_1) = 0$ ). In this case,  $\mathcal{B}(X)$  does not need to be expanded and can be integrated directly term by term,

$$\mathcal{B}(X) = \int_0^X \mathcal{A}(X_1) dX_1. \quad (2.36)$$

However, if the Mach number inside the nozzle is not constant, then  $\mathcal{A}(X_1)\mathcal{A}(X_2) - \mathcal{A}(X_2)\mathcal{A}(X_1) \neq 0$ . Therefore,  $\mathcal{B}(X)$  is obtained using the Magnus expansion:

$$\mathcal{B}(X) = \sum_{k=1}^{\infty} \mathcal{B}^{(k)}(X). \quad (2.37)$$

The first three terms of the series are (as described by Blanes et al. 2009):

$$\mathcal{B}^{(1)}(X) = \int_0^X \mathcal{A}(X_1) dX_1, \quad (2.38a)$$

$$\mathcal{B}^{(2)}(X) = \frac{1}{2} \int_0^X dX_1 \int_0^{X_2} dX_2 [\mathcal{A}(X_1), \mathcal{A}(X_2)], \quad (2.38b)$$

$$\mathcal{B}^{(3)}(X) = \frac{1}{6} \int_0^X dX_1 \int_0^{X_1} dX_2 \int_0^{X_2} dX_3 ( [\mathcal{A}(X_1), [\mathcal{A}(X_2), \mathcal{A}(X_3)]] + [\mathcal{A}(X_3), [\mathcal{A}(X_2), \mathcal{A}(X_1)]] ), \quad (2.38c)$$

where  $[\mathcal{A}, \mathcal{A}]$  is the matrix commutator. One should notice that if  $[\mathcal{A}, \mathcal{A}] = 0$  the first order of the Magnus expansion is the exact solution of Eq. (2.36) and the other terms are zero.

To obtain the final solution,  $\mathcal{C} = \exp(\mathcal{B})$  is needed. Duran and Moreau (2013a) proposed to use a Taylor series to expand the exponential, namely:

$$\mathcal{C} = \exp(\mathcal{B}) = \mathcal{I} + \mathcal{B} + \frac{(\mathcal{B})^2}{2!} + \dots + \frac{(\mathcal{B})^n}{n!} \quad (2.39)$$

The advantage of this method is that the Taylor series and the Magnus expansion can be truncated at the same order. One can verify that at the inlet  $\mathcal{B}(0) = 0$ , and therefore  $\mathcal{C}(0) = \mathcal{I}$ , the identity matrix.

As explained before, the Magnus expansion of the solution  $I(X)$  is done around 0. Therefore, the convergence of the series will be limited by the condition (as shown by [Moan and Niesen 2006](#)):

$$\int_0^{X_{crit}} \|\mathcal{A}(X)\|_2 dX < \pi, \quad (2.40)$$

where  $\|\cdot\|_2$  stands for the 2-norm, which for a square matrix is equal to the spectral norm and can be calculated as  $\|\mathcal{A}\|_2 = \sqrt{\lambda_{max}(\mathcal{A}^* \mathcal{A})}$ , where  $\lambda_{max}$  is the largest singular value and  $\mathcal{A}^*$  is the complex conjugate of matrix  $\mathcal{A}$ . The critical length  $X_{crit}$  ( $< X = 1$ ) depends on the maximal frequency to be resolved  $\Omega_{max}$ . Below this critical value, the convergence of the series only needs a few terms<sup>1</sup>, otherwise the series may diverge. To compute analytically the complete solution of the nozzle (from  $X = 0$  to  $X = 1$ ), the nozzle is divided into different sub-parts, each one bounded between  $X_{n-1}$  and  $X_n$  ( $= X_{crit}$ ). The analytical solution of each part  $n$  then reads,

$$I(X_n) = \exp(\mathcal{B}(X_n, X_{n-1})) I(X_{n-1}), \quad (2.41)$$

where  $I(X_{n-1})$  is the invariant vector at the "inlet" of the sub-part. Then, the concatenation of all  $N$  parts of the nozzle, i.e. the solution from the inlet to the outlet provides the nozzle solution which hence reads:

$$I(X_N) = [\exp(\mathcal{B}(X_N)) \cdot \exp(\mathcal{B}(X_{N-1})) \cdot \dots \cdot \exp(\mathcal{B}(X_1))] I_0. \quad (2.42)$$

The analytical approximation of the exact solution of the LEE in the frequency domain is obtained relating the acoustic and entropy perturbations of each point inside the nozzle to the perturbations at the inlet through the relation  $I(X) = [\mathcal{C}(X)] I_0$ , where  $[\mathcal{C}] = \exp(\int [\mathcal{A}] dX)$ . Note that this new expansion produces a solution dependent on the nozzle length and shape when the analytical solution of [Marble and Candel \(1977b\)](#) (i.e. the compact solution) indicates that the nozzle has no length, and therefore corresponds to  $[\mathcal{C}] = \mathcal{I}$  and  $I(X) = I_0$ .

The last step of the methodology is to impose correctly the inlet invariant vector  $I_0$ , which represents the boundary conditions of the system. To do so, it is necessary to have a representation of this vector in a propagating wave formulation, in which only the ingoing waves should be imposed.

Considering a straight duct of constant section, the harmonic invariant vector can be written as:

$$I = \hat{I} \exp\left(-i \int_0^X \mathcal{K}(\zeta) d\zeta\right) \quad (2.43)$$

$$\mathcal{K}^\pm = \frac{2\pi\Omega}{\bar{u} \pm \bar{c}} \quad \text{and} \quad \mathcal{K}^s = \frac{2\pi\Omega}{\bar{u}}$$

---

<sup>1</sup>[Duran and Moreau \(2013a\)](#): using the EWG subsonic nozzle going up to the third or fifth order of the Magnus expansion is sufficient for the convergence of the series.



where  $\mathcal{K}$  are the wave numbers of the acoustic and entropy perturbations and are the eigenvalues of the system obtained introducing Eq. (2.43) into Eq. (2.33). The associated eigenvectors read,

$$\hat{I} = \mathcal{D}W = \begin{bmatrix} \eta^+ & \eta^- & -1 \\ \beta^+ & \beta^- & \zeta \\ 0 & 0 & 1 \end{bmatrix} \begin{pmatrix} A^+ \\ A^- \\ \sigma \end{pmatrix}, \quad (2.44)$$

where  $W$  is the wave vector and  $\eta^\pm = 1 \pm 1/M$ ,  $\beta^\pm = (\gamma - 1)(1 \pm M)\zeta$  and  $\zeta = \left(1 + \frac{(\gamma-1)}{2}M^2\right)^{-1}$ .

In the case of a subsonic flow, the waves to be imposed at the inlet of the nozzle are the downstream propagating acoustic wave  $A_0^+$  and the entropy wave  $\sigma_0$  while at the outlet the upstream propagating acoustic wave  $A_1^-$  needs to be prescribed. The different waves can be imposed directly imposing a value, or indirectly through a reflection coefficient. The different ingoing waves can hence be written as:

$$A_0^+ = A_{0,f}^+ + R_0 A_0^-, \quad (2.45a)$$

$$A_1^- = A_{1,f}^- + R_1 A_1^+ + R_s \sigma_1, \quad (2.45b)$$

$$\sigma_0 = \sigma_{0,f} + R'_s A_0^-, \quad (2.45c)$$

where subscript 0 indicates the inlet position, 1 the outlet and terms with the subscript  $f$  denote the forcing terms while  $R$  are reflection coefficients. The reflection coefficient  $R_s$  is an additional term accounting for the acoustic generation due to an entropy wave in a choked flow and  $R'_s$  is the ratio of the transmitted entropy wave through a shock wave over the incident upstream propagating acoustic wave to the shock  $[\sigma_v/A_b^-]$  as shown by Eq. (2.24) in the shock relations for the compact theory of §2.1.

Finally, writing the solution of Eq. (2.35) between the inlet and outlet of the nozzle, namely  $I_1 = \mathcal{C}I_0$ , replacing  $I_1$  and  $I_0$  by relation Eq. (2.44) and introducing the additional reflection coefficients and forced waves, the system can be written as:

$$\mathcal{D}_1 \begin{bmatrix} A^+ \\ A^- \\ \sigma \end{bmatrix}_1 = \mathcal{C}_1 \mathcal{D}_0 \begin{bmatrix} A_f^+ \\ A^- \\ \sigma_f \end{bmatrix}_0, \quad (2.46)$$

with

$$\mathcal{D}_0 = \begin{bmatrix} \eta_0^+ & \eta_0^- + R_0 \eta_0^+ - R'_s & -1 \\ \beta_0^+ & \beta_0^- + R_0 \beta_0^+ - \zeta_0 R'_s & \zeta_0 \\ 0 & R'_s & 1 \end{bmatrix}, \quad (2.47)$$

$$\mathcal{D}_1 = \begin{bmatrix} \eta_1^+ + R_1 \eta_1^- & \eta_1^- & -1 + R_s \eta_1^- \\ \beta_1^+ + R_1 \beta_1^- & \beta_1^- & \zeta_1 + R_s \beta_1^- \\ 0 & 0 & 1 \end{bmatrix}. \quad (2.48)$$

This system is solved moving all the forced waves to the right hand side of the equation and the non forced waves to the left to rewrite the system into:

$$\left[ (\mathcal{D}_1)_{(i,1)} ; -(\mathcal{C}_1 \mathcal{D}_0)_{(i,2)} ; (\mathcal{D}_1)_{(i,3)} \right] \begin{pmatrix} A_1^+ \\ A_0^- \\ \sigma_1 \end{pmatrix} = \left[ (\mathcal{C}_1 \mathcal{D}_0)_{(i,1)} ; -(\mathcal{D}_1)_{(i,2)} ; (\mathcal{C}_1 \mathcal{D}_0)_{(i,3)} \right] \begin{pmatrix} A_{1,f}^+ \\ A_{0,f}^- \\ \sigma_{1,f} \end{pmatrix}. \quad (2.49)$$

Note that the second column of matrices  $\mathcal{D}_1$  and  $\mathcal{C}_1 \mathcal{D}_0$  have been exchanged in Eq. (2.49) so that the system can be inverted and then solved.

The case of a choked nozzle needs to be treated separately, since Eq. (2.32) cannot be inverted. In this specific case, the choked condition (i.e.  $M_{th} = 1$ ) is treated as a boundary condition. In the case of a compact nozzle, as done by Marble and Candel (1977b); Stow et al. (2002); Goh and Morgans (2011a), the condition  $M'/M = 0$  holds everywhere in the nozzle and in particular at the outlet (the nozzle is considered to have no length). In the present case, this condition cannot be imposed at the outlet but can be imposed at the nozzle throat. At this singular point, the upstream propagating wave in the convergent  $A_u^-$  changes its propagation direction to become in the nozzle diffuser  $A_d^-$  (as shown in Figure 2.3). The methodology to compute a choked nozzle is hence split in two parts: First, the subsonic part is computed solving the system of Eq. (2.49), afterwards, matching conditions at the nozzle throat are applied to compute the supersonic part.

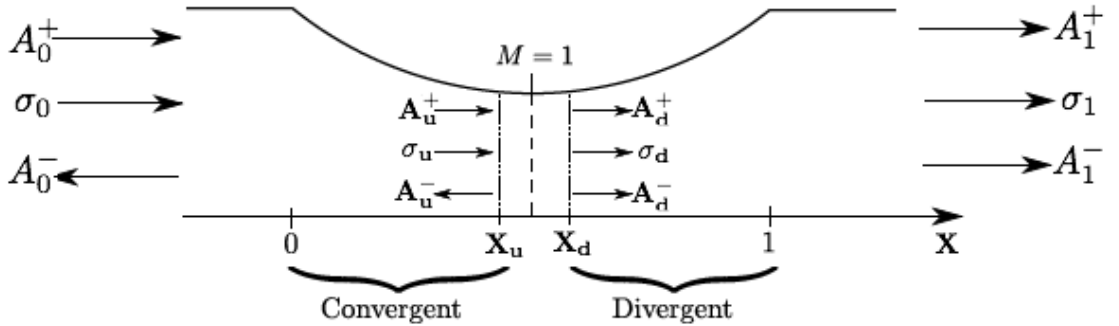


**Figure 2.3** Sketch of the acoustic and entropy waves in a converging-diverging choked nozzle.

The matching conditions at the nozzle throat are applied considering the nozzle throat as a compact element of infinitesimally small length as done by Moase et al. (2007), where

$M_u = 1 - \epsilon$ ,  $M_d = 1 + \epsilon$  and subscript  $u$  stands for the upstream part of the chocked throat and  $d$  for the downstream part of the chocked throat.

Imposing the condition  $M'/M = 0$  (cf. Eq. (2.12)) at  $X_u$  and assuming  $\epsilon \rightarrow 0$  (i.e.  $M_u \rightarrow 1$ ) allows to write the acoustic and entropy waves as  $A_u^+ = 1/2[\phi + \nu]$ ,  $A_u^- = 1/2[\phi - \nu]$  and  $\sigma_u$ . Therefore, the upstream propagating acoustic wave  $A_u^-$  can be computed as a function of the two incoming waves:

$$A_u^- = R_u A_u^+ + R_s \sigma_u, \quad (2.50)$$

with

$$R_u = \frac{3 - \gamma}{1 + \gamma} \quad \text{and} \quad R_s = -\frac{1}{1 + \gamma}. \quad (2.51)$$

$R_u$  and  $R_s$  must be imposed at the nozzle throat to allow the resolution of the subsonic half of the chocked nozzle written in Eq. (2.49). For the supersonic half of the nozzle, three waves have to be imposed at the nozzle throat. This is done knowing that  $I_u = I_d$  and using Eq. (2.44). Afterwards, only the supersonic half is needed to be solved via the relation  $I_1 = C_{\text{divergent}} I_d$ .

The last case to be treated corresponds to the supersonic nozzle with a shock wave. In this case, only the upstream propagation of waves has to be taken into account. The transmitted waves through the shock are expressed by Eqs. (2.23) and (2.24), and the upstream reflection coefficients for the shock are taken from Table 2.4. Afterwards, the system is solved similarly to the subsonic nozzle case.

For the study of indirect combustion noise, an experimentally well parametrised configuration is needed. The characteristics of the mean flow and the acoustic impedances must be well defined and the measurement of the different acoustic and entropy waves well managed. To do so, the Entropy Wave Generator (EWG) facility, described in Chapter 3, has been created and already studied extensively using different methodologies. In this PhD work, the generation and propagation of entropy noise in this nozzle configuration is studied analytically using the invariants methodology of Duran and Moreau (2013a) in Chapter 4. Different operating points, shapes of entropy disturbances and the influence of the acoustic impedances at the boundary conditions are analysed. It should be pointed out that an extension of the invariants methodology has been developed by Duran and Morgans (2015), where the azimuthal velocity fluctuations are taken into account and used as a fourth invariant. The introduction of an azimuthal velocity component allows therefore to compute circumferential modes and vorticity waves, which generate acoustic waves by the same mechanism as the entropy waves (indirect noise generation). However, the analytical study conducted in the present work will only be focused in the study of plane waves and the formalism developed by Duran and Moreau (2013a) is retained.



## Chapter 3

# The Entropy Wave Generator experiment

Indirect combustion noise was first studied experimentally by [Zukoski and Auerbach \(1976\)](#) and [Bohn \(1976\)](#) in a nozzle accelerated flow heated by electrical resistances. In these experiments the amplitude of the induced temperature fluctuation was kept very low. Furthermore, due to technical restrictions at the time, a post-processing of the acquired data in the time domain was not possible (only a time period of 0.1 s could be stored). Three decades later, [Harper-Bourne et al. \(2008\)](#) analysed combustion noise in a turbofan demonstrator engine using cross-correlations and scaling laws. The results of this work showed that direct combustion noise is dominant at low frequencies (below 100 Hz) while entropy noise peaks at 200 Hz and appears to dominate the combustor noise at higher frequencies. [Eckstein et al. \(2004\)](#) evaluated the importance of entropy noise in a combustor test rig with a self excited combustion instability (rumble) varying the outlet condition (open or choked nozzle). The investigation showed in the case of the choked outlet nozzle a clear contribution of entropy noise to the emitted noise spectrum. Finally, in the study carried out by [Leyko et al. \(2009\)](#), a relation to predict the ratio between indirect and direct noise for compact frequencies based on [Marble and Candel \(1977a\)](#) is proposed. This relation is only dependent on the inlet and outlet nozzle Mach numbers and shows that for laboratory scale experiments, this ratio is very small and direct noise is the dominant source. It also shows that for modern aero-engines indirect noise is one order of magnitude greater than direct noise confirming that indirect noise should be taken into account in the overall noise spectra of real applications. However, these results are only valid in the low frequency limit and a more complete study should be carried out considering their dependence on the frequency. In the present work, the methodology proposed by [Duran et al. \(2013b\)](#) to solve the LEE in the frequency domain is used to remove the compact limitation.

In an attempt to better characterize the entropy noise generation phenomena, a test rig called the Entropy Wave Generator (EWG) has been built by [Bake et al. \(2009\)](#) at the German Aerospace Centre (DLR). The main characteristics of this test rig have been

defined to have:

- A well defined flow,
- Well defined boundary conditions,
- The possibility of inducing specifically controlled entropy waves,
- The detection of the subsequently generated entropy noise.

The set-up of the EWG basically consists of two straight circular ducts connected by a convergent-divergent nozzle (cf. Fig. 3.1). The upstream duct is equipped with a heating module composed of six rings, each of them with ten heating wires covering the apparatus cross section. Thanks to an electronic circuit, the activation of each heating ring can be delayed or not, therewith different shapes of entropy waves can be produced. The upstream duct is equipped with a fast thermocouple and a vibrometer to measure the temperature fluctuations generated by the heating device. Finally, four wall-flushed mounted microphones are disposed at different axial positions of the downstream duct to measure the pressure fluctuations generated by the heating and acceleration of the entropy wave. Setting the origin of the coordinate system at the nozzle throat plane, Tab. 3.1 summarizes the axial locations of the different elements of the EWG.

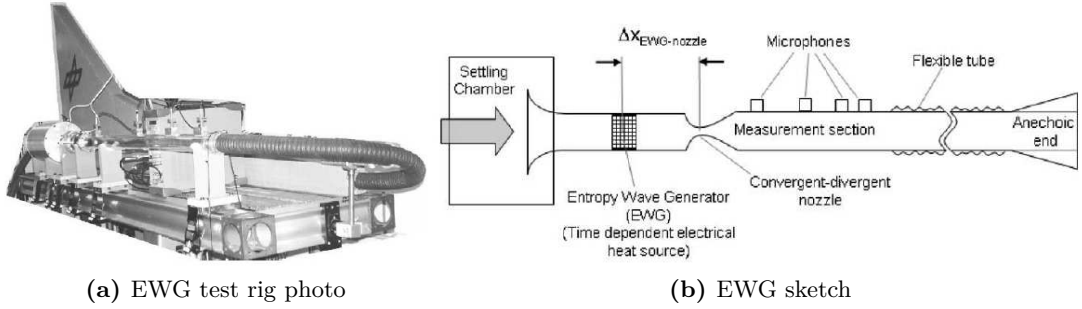


**Figure 3.1** Entropy Wave Generator test rig configuration.

The flow that feeds the EWG is supplied by the laboratory compressed air system monitored through a mass flow controller. This air enters the set-up through a settling chamber with a honeycomb flow straightener before arriving into the upstream duct. Different operating points from subsonic to supersonic can be reached by the test rig. Only two of them are documented in detail in [Bake et al. \(2009\)](#):

**Case No. 1:** Supersonic operating point.

The mass flow rate is set at 42 kg/h. The entropy wave is generated by the simultaneous activation of four heating rings (from 3 to 6) for a pulse duration of 100 ms. This pulse excitation is repeated once per second to enable a phase averaging over 300 pulse events. The temperature fluctuation (entropy wave) is measured by a wire thermocouple (R-type) achieving an amplitude of 9.1 K.

Element	Symbol	Axial position
Inlet	$x_{in}$	-250 mm
1st heated ring	$x_{HD_1}$	-145.5 mm
Spacing between heating rings	$\Delta x_R$	8 mm
Thermocouple	$x_{th}$	-72.5 mm
Vibrometer	$x_{vib}$	-58 mm
Convergent inlet	$x_{N_{in}}$	-13 mm
Nozzle throat	$x_{N_{th}}$	0 mm
Diffuser outlet	$x_{N_{out}}$	250 mm
Microphone 1	$x_{mic_1}$	350.5 mm
Microphone 2	$x_{mic_2}$	730.5 mm
Microphone 3	$x_{mic_3}$	975.5 mm
Microphone 4	$x_{mic_4}$	1150.5 mm
Outlet	$x_{out}$	2250 mm

**Table 3.1** Summary of the axial positions of the different elements of the EWG.

**Case No. 2:** Subsonic operating point.

The mass flow rate is set at 37 kg/h, which corresponds to a subcritical nozzle Mach number of  $M_{N_{th}} = 0.7$ . The six heating rings are activated but the activation is delayed according to the flow velocity in the tube and the distance between each heating ring. Note that, a larger temperature gradient is expected by the generation of this pulse. The associated temperature fluctuation is measured by a vibrometer, which evaluates the change of the optical path length through the tube resulting from the density change in the flow induced by the temperature fluctuation. For this case, the averaged amplitude of the temperature fluctuation is measured to reach 13.4 K. The pulse duration is 100 ms and is triggered every second.

The different geometric, flow and excitation parameters of the two test cases of interest are summarized in [Tab. 3.2](#).

The EWG is one of the first experiments that showed conclusively the generation of indirect noise and so the resulting interest in combustion noise grew and different laboratories computed the EWG test cases analytically and numerically. The supersonic test case was computed analytically and numerically by [Leyko et al. \(2011\)](#). Its analytical approach assumes a quasi-1D flow field and a compact nozzle (cf. [Marble and Candel 1977a](#)). The LES compressible solver AVBP ([Schönfeld and Rudgyard 1999](#)) has been used for the numerical simulations. However, only Euler equations on a 10° azimuthal periodic sector have been solved for this study. Results show that the compact assumption and the knowledge of the acoustic outlet boundary condition are sufficient to obtain satisfactory results for this test case. [Duran et al. \(2011; 2013b\)](#) computed the subsonic test case using the same approach as [Leyko et al. \(2011\)](#) but added to

Parameter		Case No. 1	Case No. 2
Mass flow rate $\dot{m}$	$[kg/h]$	42	37
Nozzle Mach number $M_{N_{th}}$		1.0	0.7
Settling chamber pressure	$[Pa]$	111970	105640
Nozzle throat pressure	$[Pa]$	48090	68650
Bulk velocity in the upstream duct	$[m/s]$	12.18	11.39
Pulse duration	$[s]$	0.1	0.1
Pulse repetition rate	$[s^{-1}]$	1	1
Temperature increase $\Delta T$	$[K]$	9.1	13.4
Heating electrical power	$[W]$	143.7	192.7
Heating power $Q$ (determined with $\Delta T$ )	$[W]$	106.8	138.2
Heated rings		From 3 to 6	From 1 to 6
Activation time delay of the heated rings	$[ms]$	no	0.702

**Table 3.2** Summary of geometric, flow and excitation parameters of the EWG test cases.

the analytical method the resolution of non zero frequencies by solving the LEE in the frequency domain. [Duran et al.](#) found that the nozzle can be considered as compact, finding the same result using the compact and non-compact nozzle transfer functions. In this study, direct noise is found to be dominant over indirect noise. The noise peak evolution as a function of the flow Mach number has also been computed, obtaining that the peak increases with the Mach number, which was not the case experimentally. In the experiment, the maximum noise generated reaches a plateau (cf. [Fig. 3.2](#)). To explain this phenomenon [Howe \(2010\)](#) suggested that in cases with flow separation inside the diffuser, vortex sound strongly correlates with entropy noise and can reduce the overall sound level. Furthermore, the strong deformation of the hot slug at the nozzle throat will reduce the entropy gradients within the front, decreasing the corresponding acoustic pressure level. [Muhlbauer et al. \(2009\)](#) computed the subsonic and supersonic test cases by means of URANS coupled to acoustic boundary conditions obtaining also very good results in comparison with the experiment. The peak for different Mach numbers has also been computed, obtaining good agreement with the experimental results. [Ullrich et al. \(2014; 2015\)](#) computed both the subsonic and the supersonic configurations of EWG by means of RANS simulations for the unforced flow and a Linearised Navier-Stokes Equations (LNSE) to determine the acoustic-acoustic and entropy-acoustic transfer functions of the nozzle. [Lourier et al. \(2014\)](#) used a new approach to treat the acoustic boundary conditions in the time domain (TDIBC) coupled with a URANS approach to solve the subsonic test case of the EWG. Good results have been found in comparison to the experimental data, maximal and minimal peaks of the pressure response are indeed well reproduced, although some overestimations of the signal and some time delays remain. Finally, this last work by [Lourier et al.](#) claimed that the indirect noise dominates direct noise (which somewhat contradicts previous results by [Duran et al. 2011; 2013b](#)).



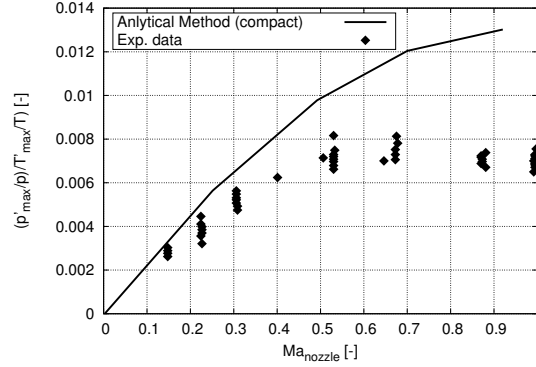


**Figure 3.2** Normalized entropy noise over nozzle Mach number measured at the EWG test rig from [Bake et al. \(2009\)](#).

Until this date, EWG experiment has been used as a reference test case for different studies and has clarified some interrogations concerning combustion noise. Nevertheless, some questions remain open or need to be studied in more details. For example, entropy noise cancellation due to flow separation and distortion of the temperature inhomogeneities in the nozzle ([Howe 2010](#)), entropy dispersion and dissipation ([Morgans et al. 2013](#)) as well as the presence of the plateau reached at high subsonic nozzle Mach number in the entropy noise measured by [Bake et al. \(2009\)](#) (cf. [Fig. 3.2](#)) are features that still remain to be either understood or clarified. More generally, analytic models fail to capture specific features for non-understood reasons today. All these points are the primary motivations for the generation of a full compressible LES of one subsonic test case of this configuration. This LES can indeed provide valuable information thanks to its well controlled design, which will be guided by analytical models all along this work. Once mastered such predictions can ultimately be compared to experimental findings as well as potential sources of improvement of analytical models.

In the following (i.e. [Chapter 4](#)), the subsonic and choked test cases of the EWG described in [Bake et al. \(2009\)](#) are computed analytically. The analytical methodology employed by [Duran et al. \(2013b\)](#) to model the subsonic operating point of the EWG is revisited to take into account the complete EWG heating device (which was modelled as a compact element) and its ignition sequence. Furthermore, the analytical solution of the LEE proposed by [Duran and Moreau \(2013a\)](#) is used to study the response of the EWG nozzle to acoustic and entropy disturbances for non-compact frequencies.



## Chapter 4

# Analytical study of the EWG

In this chapter, the analytical method developed by [Duran and Moreau \(2013a\)](#) is used to compute the transfer functions of the EWG for the operating points described in the work of [Bake et al. \(2009\)](#). A methodology is presented to predict the generated noise caused by the introduction and convection of a hot slug. The advantages of an analytic method over numerical simulations, are that each noise source (direct or indirect) can be computed separately to determine its contribution to the overall noise produced. The time of computation is furthermore negligible compared to numerical simulations, allowing to investigate the influence of different parameters. In particular, the influence of the acoustic boundary conditions, the consideration of each heating wire, the ignition sequence for the generation of the hot slug and the compactness of the nozzle are studied in this chapter. Note also that all obtained results issued by the above analysis are compared to results obtained in other studies.

The assumptions for the present study are recalled for clarity:

- The flow is adiabatic: heat exchanges through the nozzle and duct walls are neglected.
- Viscous effects are neglected.
- The undisturbed flow is supposed isentropic.
- Harmonic shape of small amplitude disturbances (linear acoustics).

The analytical modelling of the EWG used in this chapter is based on the works of [Leyko et al. \(2011\)](#) and [Duran et al. \(2013b\)](#). To compute the transfer functions of the nozzle and then compare them with the compact transfer functions, the chosen method relies specifically on the analytical resolution of the LEE proposed by [Duran and Moreau \(2013a\)](#). As the frequency is low, only plane waves are considered to propagate in the ducts. Furthermore, the positions of the different elements being known, they are treated with the introduction of time delays. Since the study is purely analytic, the

domain considered corresponds to the axisymmetric volume sketched in Fig. 4.1, where all relevant length scales and indices are provided.

The chapter is organised as follows: First, the model proposed by Leyko et al. (2011) is extended to take into account the ignition sequence and each heating ring of the experimental heating device in §4.1. Then, the construction of the system of waves to solve (ingoing and outgoing waves) is described in §4.2. Finally, in §4.3 and §4.4 the choked and subsonic nozzle test cases of Bake et al. (2009) are investigated analytically with the methodology described in this chapter.

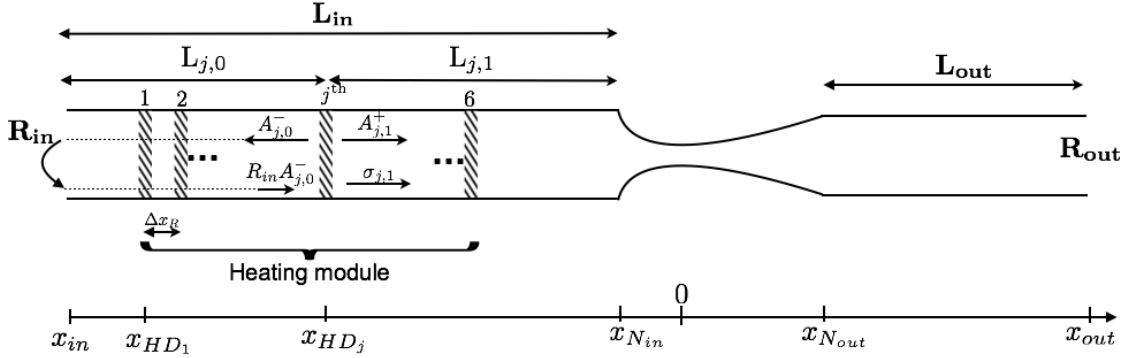


Figure 4.1 Domain considered for the analytical study of the EWG.

## 4.1 The heating device model

Compressible LES of a full 360° configuration of the subsonic test case of Bake et al. (2009) carried in §5.2 (which has been published in Becerril et al. 2016) shows that the modelling of the heating device has an important effect on the shape of the measured temperature fluctuation. Indeed, the ignition sequence of the heating device is seen to generate a time delay on the measured temperature and pressure signals. The analytical model considered in this study cannot take into account all the aspects of the LES, in particular the boundary layers, dissipation and distortion of the temperature fronts, flow separation and other phenomena. Nevertheless, an effort can be done to reproduce the different parameters of the experiment as accurately as possible. Among other things, the need for a reliable model to reproduce the heating device clearly appears.

The EWG heating device is composed of six heating wires. Here, rather than considering all the heating device as a compact element (as done by Leyko et al. 2011; Duran et al. 2013b), it will be represented by six compact heating modules. Balance equations can hence be written for each compact heated ring:

$$\left(\frac{\dot{m}'}{\dot{m}}\right)_{j,0} = \left(\frac{\dot{m}'}{\dot{m}}\right)_{j,1}, \quad (4.1a)$$

$$\left(\frac{T'_t}{T_t}\right)_{j,0} + q'_j \left(1 + \frac{\gamma - 1}{2} M_0^2\right)^{-1} = \left(\frac{T'_t}{T_t}\right)_{j,1}, \quad (4.1b)$$

$$\left(\frac{s'}{c_p}\right)_{j,0} + q'_j = \left(\frac{s'}{c_p}\right)_{j,1}, \quad (4.1c)$$

where subscript  $j$  indicates that the balance equation is applied to the  $j^{\text{th}}$  ring and subscripts 0 and 1 stand for upstream and downstream positions of the considered ring respectively;  $q'_j$  is the energy induced by the heating. It should be noticed that the balance equations for the heating module are written using the flow invariants formulation of Eqs. (2.10a–2.10c). Expressing the flow invariants as a function of the acoustic and entropy waves as done in Eq. (2.44), the system can be rewritten as:

$$\left(1 + \frac{1}{M_0}\right) A_{j,0}^+ + \left(1 - \frac{1}{M_0}\right) A_{j,0}^- - \sigma_{j,0} = \left(1 + \frac{1}{M_0}\right) A_{j,1}^+ + \left(1 - \frac{1}{M_0}\right) A_{j,1}^- - \sigma_{j,1}, \quad (4.2a)$$

$$(1 + M_0) A_{j,0}^+ + (1 - M_0) A_{j,0}^- + \frac{\sigma_{j,0} + q'_j}{\gamma - 1} = (1 + M_0) A_{j,1}^+ + (1 - M_0) A_{j,1}^- + \frac{\sigma_{j,1}}{\gamma - 1}, \quad (4.2b)$$

$$\sigma_{j,0} + q'_j = \sigma_{j,1}. \quad (4.2c)$$

Note that, before the introduction of the temperature fluctuation by the heating device, no acoustic or entropy disturbances are considered. Therefore, all incident waves to the heated ring may be considered to be zero ( $A_{j,0}^+ = A_{j,1}^- = \sigma_{j,0} = 0$ ), and the outgoing waves may be computed as a function of the introduced energy and Mach number (which is assumed to be constant through the heating device), that is,

$$\sigma_{j,1} = q'_j, \quad (4.3a)$$

$$A_{j,1}^+ = \frac{M_0}{2(1 + M_0)} q'_j, \quad (4.3b)$$

$$A_{j,0}^- = \frac{M_0}{2(1 - M_0)} q'_j. \quad (4.3c)$$

Waves generated by the compact  $j^{\text{th}}$  ring are represented in Fig. 4.1, where only the downstream travelling waves are needed and propagated through the nozzle. Therefore, the overall acoustic wave propagated downstream  $A_{\text{HD}}^+$  can be represented as the summation of the downstream travelling waves produced by the each heated ring  $A_{j,1}^+$  and the upstream travelling wave that has reached the boundary condition  $R_{in}$  and has been

reflected into a downstream travelling wave  $R_{in}A_{j,0}^-$ . These waves are written at the inlet of the nozzle,  $x_{N_{in}}$ :

$$A_{HD_j}^+(x_{N_{in}}) = A_{j,1}^+(x_{HD_j}) \exp\left(-i\omega \frac{L_{j,1}}{c_0(1+M_0)}\right) + \left(R_{in}A_{j,0}^-\right)(x_{HD_j}) \exp\left[-i\omega \left(\frac{2L_{j,0}}{c_0(1-M_0^2)} + \frac{L_{j,1}}{c_0(1+M_0)}\right)\right], \quad (4.4a)$$

$$\sigma_{HD_j}(x_{N_{in}}) = \sigma_{j,1}(x_{HD_j}) \exp\left(-i\omega \frac{L_{j,1}}{c_0 M_0}\right), \quad (4.4b)$$

where  $\omega$  is the angular frequency and the distances  $L_{j,0}$  and  $L_{j,1}$  represent the distance from the inlet  $x_{in}$  to the  $j^{\text{th}}$  ring and the distance from the  $j^{\text{th}}$  ring to the inlet of the nozzle  $x_{N_{in}}$  respectively, and expressed by:

$$L_{j,0} = x_{HD_1} + (j-1)\Delta x_R - x_{in}, \quad (4.5a)$$

$$L_{j,1} = x_{N_{in}} - x_{HD_1} - (j-1)\Delta x_R. \quad (4.5b)$$

where the subscript HD stands for Heating Device. The values of all the elements of the EWG configuration ( $x_{HD_1}$ ,  $x_{N_{in}}$  and  $\Delta x_R$ ) are summarised in [Tab. 3.1](#).

One last parameter needs to be defined: the energy provided by the heating device  $q'_j$ . This energy has been introduced in the above balance equations as an entropy perturbation source term. With the assumption of an isobaric entropy perturbation as done by [Huet and Giauque \(2013\)](#),  $q'_j = s'_{HD}/c_p$  can be expressed as a sole temperature perturbation, for which a delay  $\tau_j$  can be introduced to take into account the ignition sequence of the heating device:

$$q'_j = \frac{s'_{HD_j}}{c_p} = \frac{T'_{HD_j}}{T} \exp(i\omega\tau_j). \quad (4.6)$$

From this input, the acoustic and entropy waves generated by the whole heating device at the inlet of the nozzle are described as the summation of the acoustic and entropy waves generated by the individual rings,  $A_{HD_j}^+$  and  $\sigma_{HD_j}$ , and recast into:

$$A_{HD}^+ = \frac{M_0}{2(1-M_0^2)} \sum_j \frac{T'_{HD_j}}{T} \exp\left[-i\omega \left(\frac{L_{j,1}}{c_0(1+M_0)} - \tau_j\right)\right] \left[1 - M_0 + (1+M_0) R_{in} \exp\left(-i\omega \frac{2L_{j,0}}{c_0(1-M_0^2)}\right)\right], \quad (4.7a)$$

$$\sigma_{HD} = \sum_j \frac{T'_{HD_j}}{T} \exp\left[-i\omega \left(\frac{L_{j,1}}{c_0 M_0} - \tau_j\right)\right]. \quad (4.7b)$$

## 4.2 Propagation of waves through the nozzle

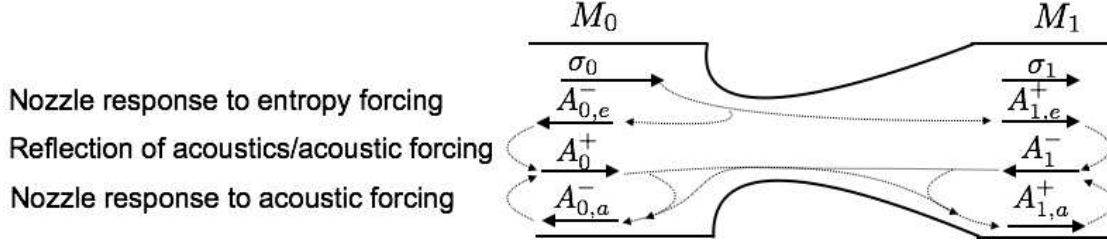


**Figure 4.2** Interaction of entropy and acoustics waves through a subcritical nozzle.

The response of a nozzle to an incoming entropy disturbance is a complex coupling problem involving entropy and acoustics. [Figure 4.2](#) describes this coupling in a subcritical nozzle configuration: First, the entropy wave is accelerated by the nozzle generating two acoustic waves  $A_{0,e}^-$  and  $A_{1,e}^+$  produced by the indirect noise mechanism. If boundary conditions are non-reflective, the process ends here and acoustic waves leave the domain. If not, boundary conditions reflect the incident acoustic waves. Reflected waves  $A_0^+$  and  $A_1^-$  as well as acoustic forced waves (in the studied case it will be  $A_{HD}^+$ ) can be considered as waves produced by the same mechanism: boundary condition interaction. Afterwards, the passage of such acoustic waves through the nozzle will generate additional noise via the direct noise mechanism, producing two supplementary acoustic waves  $A_{0,a}^-$  and  $A_{1,a}^+$ . Finally, these waves will be reflected once again by the boundary conditions. Writing the coupling of waves into a mathematical formulation, assuming linear acoustics and the transport of waves inside the nozzle using the invariants method of [Duran et al. \(2013b\)](#) (expressing transfer functions between the inlet and outlet of the nozzle as the ratio of the resulting wave over the forcing wave), the following set of equations for upstream and downstream acoustic and entropy waves are obtained:

$$A_0^- = A_{0,e}^- + A_{0,a}^- = \underbrace{\left[ \frac{A_{0,e}^-}{\sigma_0} \right]}_{R_{ea}} \sigma_0 + \underbrace{\left[ \frac{A_{0,a}^-}{A_0^+} \right]}_{R_{aa}^+} A_0^+ + \underbrace{\left[ \frac{A_{0,a}^-}{A_1^-} \right]}_{T_{aa}^-} A_1^-, \quad (4.8a)$$

$$A_0^+ = A_0^- R_{in}(x_{N_{in}}) + A_{HD}^+, \quad (4.8b)$$

$$A_1^- = A_1^+ R_{out}(x_{N_{out}}), \quad (4.8c)$$

$$A_1^+ = A_{1,e}^+ + A_{1,a}^+ = \underbrace{\left[ \frac{A_{1,e}^+}{\sigma_0} \right]}_{T_{ea}} \sigma_0 + \underbrace{\left[ \frac{A_{1,a}^+}{A_0^+} \right]}_{T_{aa}^+} A_0^+ + \underbrace{\left[ \frac{A_{1,a}^+}{A_1^-} \right]}_{R_{aa}^-} A_1^-, \quad (4.8d)$$

$$\sigma_0 = \sigma_{HD} = \sigma_1, \quad (4.8e)$$

where the nozzle transfer functions are divided into transmission  $T$  and reflection  $R$  coefficients, obtained with the different analytical methods presented in [Chapter 2](#). Subscripts  $ea$  and  $aa$  stand for entropy-acoustic and acoustic-acoustic interactions respec-

tively; subscripts  $^+$  and  $^-$  indicate the nature of the ingoing disturbance (an acoustic wave  $A^+$  or  $A^-$ ). Note that waves described by Eqs. (4.8a–4.8e) are only valid for a subcritical flow. For a supercritical flow,  $A_1^- = \left[ \frac{A_1^-}{A_0^+} \right] A_0^+$  and in the case of a supercritical flow with a shock, the shock relations of Table 2.4 are needed.

Finally, in order to close the system, boundary conditions are specified as upstream and downstream reflection coefficients  $R_{in}(x_{in})$  and  $R_{out}(x_{out})$ . In Eqs. (4.8b) and (4.8c), boundary conditions are written at the inlet and outlet of the nozzle ( $x_{N_{in}}$  and  $x_{N_{out}}$ ), they have therefore to be shifted to the correct axial position through:

$$R_{in}(x_{N_{in}}) = R_{in}(x_{in}) \exp \left[ -i\omega \left( \frac{2L_{in}}{c_0(1-M_0^2)} \right) \right], \quad (4.9a)$$

$$R_{out}(x_{N_{out}}) = R_{out}(x_{out}) \exp \left[ -i\omega \left( \frac{-2L_{out}}{c_1(1-M_1^2)} \right) \right]. \quad (4.9b)$$

Note that Eqs. (4.8a–4.8e) can be rearranged to obtain the following matrix system to be solved:

$$\begin{bmatrix} -1 & R_{aa}^+ & T_{aa}^- & 0 \\ R_{in} & -1 & 0 & 0 \\ 0 & 0 & -1 & R_{out} \\ 0 & T_{aa}^+ & R_{aa}^- & -1 \end{bmatrix} \begin{pmatrix} A_0^- \\ A_0^+ \\ A_1^- \\ A_1^+ \end{pmatrix} = \begin{pmatrix} -R_{ea} \sigma_{HD} \\ -A_{HD}^+ \\ 0 \\ -T_{ea} \sigma_{HD} \end{pmatrix}. \quad (4.10)$$

The resolution of this system allows knowing the upstream and downstream acoustic waves, from which the pressure fluctuations  $p'$  generated by the forced perturbations  $\sigma_{HD}$  and  $A_{HD}^+$  can be computed using Eq. (2.7):

$$p' = \gamma \bar{p} (A^+ + A^-) \quad (4.11)$$

Finally, one should note that direct combustion noise alone can be computed setting  $\sigma_{HD}$  to zero and indirect combustion noise is obtained by setting  $A_{HD}^+$  to zero in the right hand side of Eq. (4.10).

### 4.3 Chocked nozzle test case

In previous studies of the EWG (Leyko et al. 2011; Duran et al. 2013b), the heating device was considered as a whole and as a compact element for analytical studies. In some cases it was modelled by the use of a cylindrical source term, including all individual activated heated rings in numerical simulations (numerical simulation of Muhlbauer et al. 2009 discretized each heating wire of the heating device). In the experiment, the supersonic test case ignition sequence activates simultaneously rings from 3 to 6, generating a temperature fluctuation of  $\Delta T_{exp} = 9.1$  K measured by a thermocouple located at the axial position  $x_{th} = -58$  mm from the nozzle throat. To reproduce



the shape of the temperature fluctuation recorded by the thermocouple, while avoiding to simulate the activation sequence, [Leyko et al. \(2011\)](#) introduced a temporal function using two exponentials. The stiffness of the rising and decreasing phases of the respective functions are controlled with a unique relaxation parameter noted  $\tau$ . In the present study, which follows the same strategy, one relaxation coefficient is used for the rising phase  $\tau_1$  and a second one for the decreasing phase  $\tau_2$ :

$$\xi(t) = \begin{cases} 0 & \text{if } t < t_0, \\ 1 - \exp\left(-\frac{t-t_0}{\tau_1}\right) & \text{if } t \in [t_0; t_0 + T_p], \\ \left[1 - \exp\left(-\frac{T_p}{\tau_1}\right)\right] \exp\left(-\frac{t-t_0-T_p}{\tau_2}\right) & \text{if } t > t_0 + T_p, \end{cases} \quad (4.12)$$

where  $t_0$  is the triggering time of the heating device ignition sequence,  $\tau_1$  and  $\tau_2$  are the relaxation parameters to control the stiffness of the rising and decreasing phases and  $T_p$  is the pulse duration. As  $\Delta T_{exp}\xi(t)$  represents the total measurement of the thermocouple, the assumption of splitting uniformly the energy into  $n_r$  activated rings at once is implicitly made. Therefore, the temperature fluctuation delivered by each heated ring reads:

$$\frac{T'_{HD_j}}{T} = \xi(t) \frac{\Delta T_{exp}}{n_r T}. \quad (4.13)$$

In order to evaluate the influence of the ignition sequence and the discretisation of the individual heated rings on the temperature signal as well as the generated pressure fluctuations, two test cases are evaluated: The representation of the heating device as a single compact element ( $n_r = 1$ ) as done by [Leyko et al. \(2011\)](#) and [Duran et al. \(2013b\)](#), and the representation of all the individual rings composing the heating device while following the ignition sequence. In the supersonic test case, the time delay of activation of the rings is set to 0 (rings 3-6 are activated at the same time), meaning that each ring generated temperature front arrives at the thermocouple position at different times (temperature front coming from  $x_{HD_3}$  in [Fig. 4.1](#) being the last one to arrive). If the heating device is considered as a single compact element as done by [Leyko et al. \(2011\)](#), the position of the compact heating device should be located at  $x_{HD_6}$  to respect the time delays of convection of the temperature front. [Figure 4.3](#) shows the effect of considering 1 or 4 heated rings on the temperature fluctuation measured at the thermocouple position  $x_{th} = -72.5$  mm. Both temperature signals start their rising and decreasing phases at the same instant ( $t_0$  and  $t_0 + T_p$  respectively). However, when considering 4 heated rings instead of 1, a temperature fluctuation profile with smoother raising and decreasing phases is created. This is due to the summation of the different temperature signals produced by the different heated rings. Despite all these observations and possible modelling approaches, the shapes of the temperature fluctuations are very similar and should not have an important effect on the transmitted noise.

Focusing on the effects of the boundary conditions on noise generation, several points need specific attention. [Leyko et al. \(2011\)](#) addressed the influence of acoustic boundary

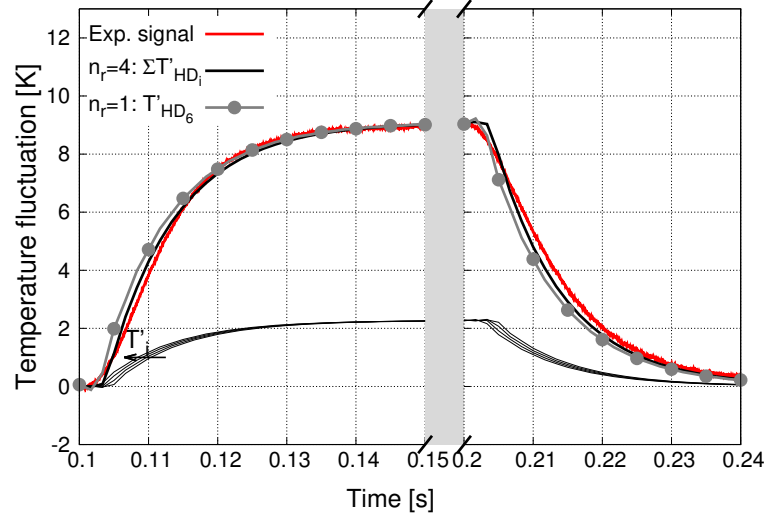


**Figure 4.3** Temperature fluctuations produced by considering  $n_r = 1$  or 4 heated rings extracted at the thermocouple position  $x_{th} = -72.5$  mm. Parameters of the model:  $\Delta T_{exp} = 9.1$  K,  $\tau_1 = 8$  ms,  $\tau_2 = 8$  ms,  $t_0 = 0.1$  s and  $T_p = 0.1$  s.

conditions, showing that for the choked case, the upstream boundary condition does not have an important influence on the propagated noise after the nozzle due to choked conditions at the nozzle throat. The inlet acoustic boundary condition can however have an important effect on direct noise generation (wave  $A_{HD}^+$  considered in this work). To assess this specific point, three different inlet reflection coefficients ( $R_{in} = -1, 0, 1$ ) have been tested to evaluate their influence on the value of  $A_{HD}^+$ . Figure 4.4 shows the pressure traces extracted at the thermocouple position resulting from the temperature fluctuation induced by the heating device. The pressure fluctuations produced by a single ring ( $n_r = 1$  in Fig. 4.4) and the ones generated by the activation of multiple rings ( $n_r = 4$ ) are all superimposed irrespectively of the inflow acoustic boundary condition. This is due to the time delay associated with the convection of the acoustic wave through the total length of the heating device  $\Delta\tau \approx \frac{L_{HD}}{c} \approx 0.1$  ms. According to this time delay evaluation, the acoustic wave travels merely instantaneously across the heating device, which is not the case of the entropy wave. The heating device may therefore be considered as compact for acoustics but not for entropy (in agreement with results from Fig. 4.3). More importantly, the inlet reflection coefficient is observed to have (as expected) a crucial influence on the amplitude of the measured noise. The question then becomes how much of this generated noise remains downstream of the nozzle?

Before going further in this study, the downstream boundary condition has to be set. Leyko et al. (2011) showed the importance of this boundary condition (which has been measured experimentally) and fitted it numerically to obtain the best compromise on the basis of the experimental findings. This was obtained using the NSCBC formulation

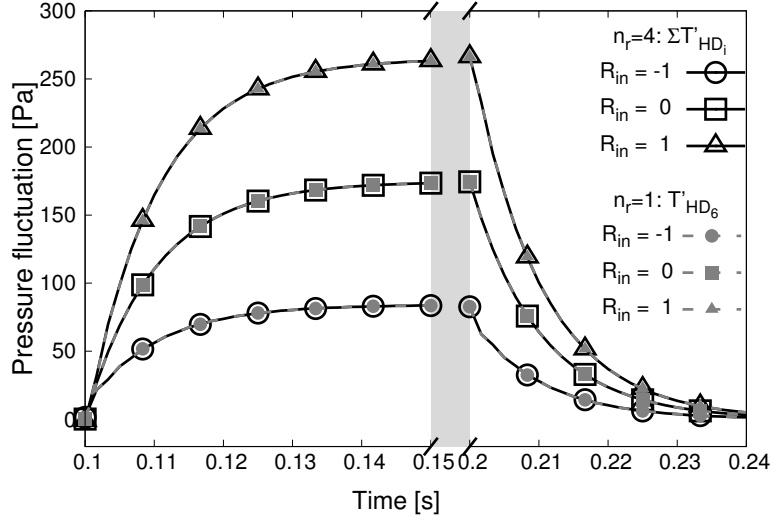


**Figure 4.4** Direct noise generated by the heating device plotted at the thermocouple position for three inlet reflection coefficients:  $R_{in} = -1, 0, 1$ .

of Selle et al. (2004):

$$R_{out} = -\frac{1}{1 + i\frac{\omega}{K_{out}}}, \quad (4.14)$$

where  $K_{out} = 160 \text{ s}^{-1}$  is found to be the most satisfactory value. This outlet reflection coefficient is hereafter left unchanged.

Figure 4.5 shows the influence of (a) the consideration of  $n_r = 4$  or 1, the compact/non-compact transfer functions of the nozzle and (b) the effect of the inlet boundary condition, on the pressure fluctuation traces recorded at the first microphone location  $x_{mic_1} = 350 \text{ mm}$ . In Fig. 4.5a, the same inlet reflection coefficient  $R_{in} = -1$  is used for all cases. First of all, the results of the heating model with  $n_r = 1$  and the compact transfer functions are compared to Leyko et al.'s (2011) results. The difference in the pressure signals between the analytical model using  $n_r = 1$  considered in this study and the case of Leyko et al. comes from the choice of the relaxation coefficients  $\tau_1$  and  $\tau_2$ . In the present study, coefficients  $\tau_1$  and  $\tau_2$  have been chosen to fit better the experimental temperature measurement if compared to Leyko et al.'s expression. This result indicates that the choice of the relaxation parameters  $\tau_1$  and  $\tau_2$  has an important role on the shape and amplitude of the recorded pressure signals. Analysing the influence of the discretisation of the heating device with  $n_r = 4$  or  $n_r = 1$ , both pressure signals are seen to start their rising phase at the same time (like the temperature fluctuation in Fig. 4.3). However, a time delay of about 2 ms between the peak values is observed. This time delay in the pressure signals comes from the time delay of the different temperature fronts of each heated ring to arrive to the nozzle. Indeed, the temperature front arriving from  $x_{HD_3}$  takes about 2 ms longer to arrive to the nozzle than the temperature

front arriving from  $x_{HD6}$  (i.e. individual temperature signals from Fig. 4.3). Concerning the influence of the non-compact/compact nozzle transfer functions, a small time delay between obtained pressure signals is observed, which is attributed to the phase shift present in the non-compact transfer functions. Figure 4.5b shows the influence of the inlet reflection coefficient, for which the non-compact nozzle transfer functions and  $n_r = 4$  modelling have been used. Results obtained with  $R_{in} = -1$  and  $R_{in} = 0$  are very similar (as already observed by Leyko et al. 2011). However, setting  $R_{in} = 1$  doubles the amplitude of the pressure signal. In order to understand these results, one should look at two different parameters: 1) the spectra of the incident acoustic  $A_{HD}^+$  as well as entropy  $\sigma_{HD}$  perturbations, and 2) the transfer functions of the nozzle.

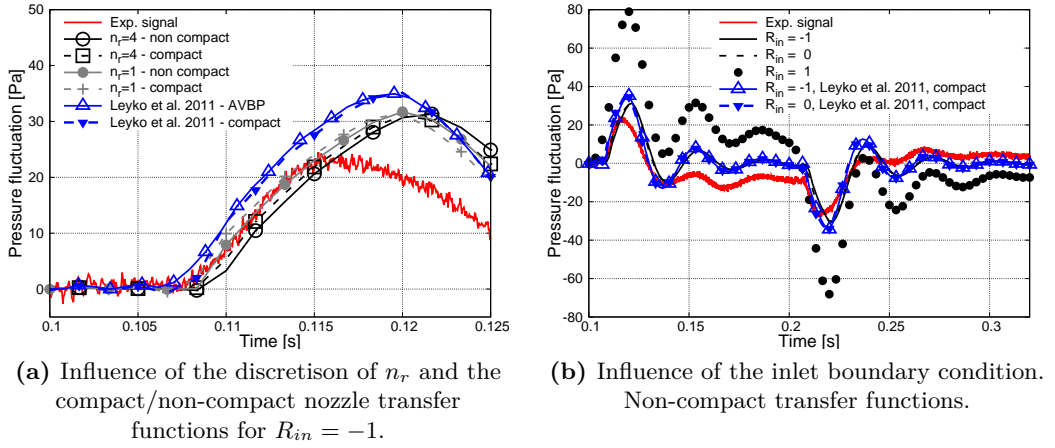


**Figure 4.5** Pressure fluctuation traces recorded at the first microphone position  $x_{mic_1} = 350$  mm.

Figure 4.6 shows the modulus of the Discrete Fourier Transform (DFT) of the temperature and pressure disturbances (only direct noise) recorded at the thermocouple axial position  $x_{th} = -72.5$  mm. As evidenced by the distributions, the inflow impedance has an important influence on the generated pressure signals (as already shown by Fig. 4.4). It is furthermore noticed that almost all the energy of the generated disturbances in the upstream duct is contained in the band 0-10 Hz (very low frequencies), allowing to show why the non-compact and compact transfer functions give the same result. To confirm the compactness of the nozzle, the non-compact transfer functions are displayed in Fig. 4.7. Up to 50 Hz the modulus and phase of the different transfer functions is almost constant, showing that the compact assumption is valid up to at least 50 Hz. This result, in addition with Fig. 4.6 justifies why the pressure fluctuations obtained by the compact and non-compact nozzle transfer functions are almost equal in Fig. 4.5a. Figures 4.7a and 4.7b display acoustic-acoustic upstream transfer functions (acoustic waves generated by the forcing of  $A_0^+$  in Fig. 4.2). Almost all the incident wave  $A^+$  is seen to be reflected by the nozzle ( $R_{aa}^+ \approx 1$ ) and only  $\approx 7\%$  is transmitted to the

downstream duct. On the contrary, the transmitted and reflected acoustic waves due to entropy-acoustic interaction (Figs. 4.7c and 4.7d respectively) remain at the same level. Finally, the time delay observed in Fig. 4.5a between the pressure fluctuations obtained by the compact and non-compact transfer functions may be explained by the entropy-acoustic transmitted acoustic wave phase, which is not constant, as shown by Fig. 4.7c.

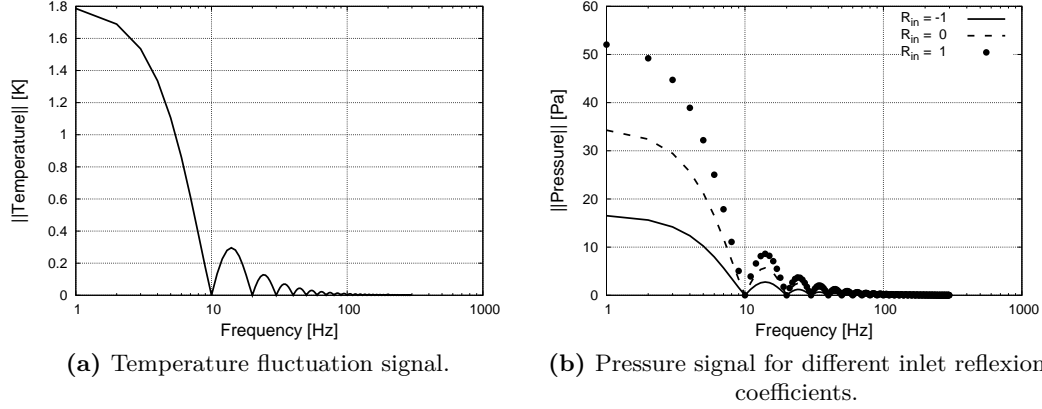


**Figure 4.6** Discrete Fourier Transform of incoming disturbances at the thermocouple position  $x_{th} = -72.5$  mm.

The amount of direct noise produced by the temperature fluctuation is shown to be strongly dependent on the inlet acoustic impedance (cf. Figs. 4.4 and 4.6). It is therefore normal to expect that the ratio of indirect to direct noise  $\eta = A_{1,e}^+ / A_{1,a}^+$  changes drastically with the inlet acoustic impedance. The modulus of the indirect over direct noise ratio  $||\eta||$  is displayed in Fig. 4.8 for the three inlet reflection coefficients tested. In cases where  $R_{in} \leq 0$ , indirect noise is dominant over the whole spectrum, especially for frequencies lower than 10 Hz. At these very low frequencies, where the temperature fluctuation is found to be the most energetic, indirect noise is at least 10 times greater than direct noise. Setting  $R_{in} = 1$  makes direct noise dominant in the very low frequency range (0-10 Hz). However, the indirect noise contribution remains non-negligible and becomes the largest contribution for frequencies higher than 30 Hz. This allows to conclude that indirect noise generation is the dominant noise source for almost all the inlet acoustic impedances.

Up to now all results were analysed at an axial position where numerical, analytical and experimental data are available. This position is however found to be close to the nozzle, at a location where the effects of the nozzle jet could play a role deforming the pressure signals. Figure 4.9 proposes a view of the pressure fluctuations at the fourth microphone position  $x_{mic_4} = 1150.5$  mm instead. The discretisation of the 4 heated rings and/or the non-compact transfer functions of the nozzle are seen to have only a

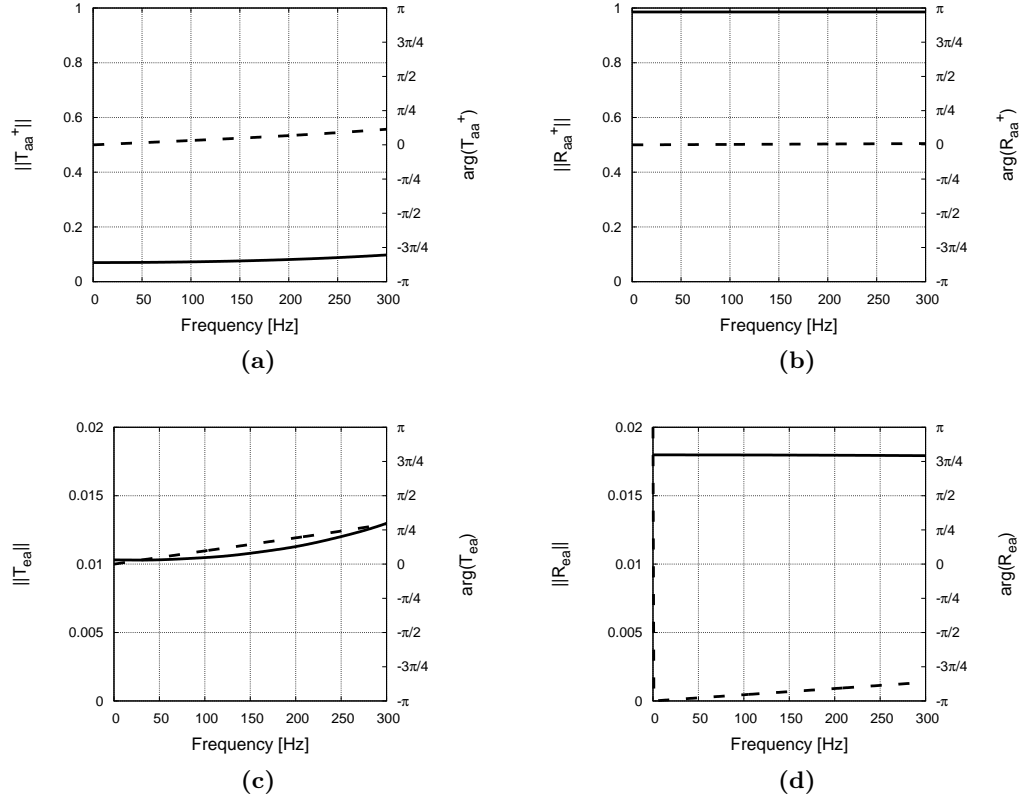


**Figure 4.7** Nozzle transfer functions of the choked test case. Modulus(—): left axis. Phase(---): right axis.

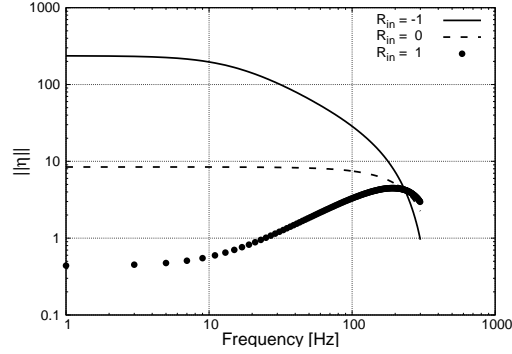


**Figure 4.8** Modulus of indirect over direct noise ratio  $\|\eta\| = \|A_{1,e}^+/A_{1,a}^+\|$ .

marginal influence in this case. The most notable change appears in the shape of the temperature fluctuation, controlled by the relaxation coefficients  $\tau_1$  and  $\tau_2$ . In terms of recommendation, it seems that the inlet reflection coefficient value must approach -1 in agreement with the observed predictions and the presence of a sudden contrac-

tion between the tranquillisation chamber and the inlet duct. Its exact value remains however unknown and is a clear source of uncertainty since it has not been evaluated experimentally.

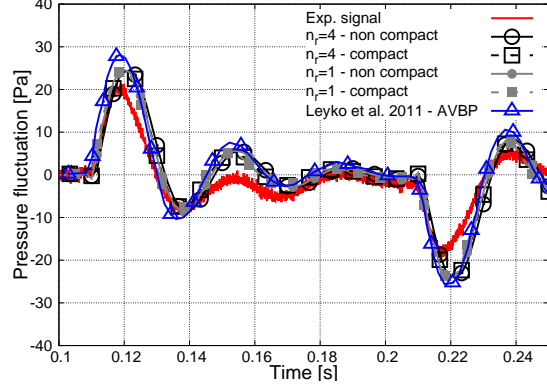


**Figure 4.9** Pressure fluctuation recorded at the fourth microphone position  $x_{mic_4} = 1150.5$  mm for an inlet reflexion coefficient  $R_{in} = -1$ .

## 4.4 Subsonic nozzle test case

In this section, the subsonic case of [Bake et al. \(2009\)](#), referenced as "Case No. 2" in [Tab. 3.2](#) is studied using the same analytical approach described in [§4.3](#). However, besides the nature of the flow (in the present case subsonic), the ignition sequence as well as the number of activated rings have changed. Concerning the ignition sequence, a time delay is used for the activation of six heated rings in order to create a sharper temperature gradient. Note also that for this specific test case the temperature fluctuation is no longer measured by a thermocouple (local measurement) but by a vibrometer<sup>1</sup> which also allows having access to a mean temperature value in the duct.

The ignition sequence applied in the subsonic test case activates each heating ring one after the other, starting by the one located at the axial position  $x_{HD_1}$  (cf. [Fig. 4.1](#)). The delay between each ring activation corresponds to the time that one temperature front takes to reach the next ring. Therefore, it can be simply written for each  $j^{\text{th}}$  ring as:

$$\tau_j = -(j - 1) \frac{\Delta x_R}{M_0 c_0}, \quad (4.15)$$

so [Eq. \(4.7b\)](#) can be reduced to:

$$\sigma_{HD} = \xi(t) \frac{\Delta T_{exp}}{T} \exp \left[ -i\omega \left( \frac{x_{N_{in}} - x_{HD_1}}{c_0 M_0} \right) \right], \quad (4.16)$$

<sup>1</sup>Non-intrusive measurement that provides the change in the optical path length caused by the change of density in the flow.

which is the same expression as the compact expression for the most upstream heated ring ( $x_{HD_1}$ ). Moreover, since the heating device can be considered as compact for acoustics (as showed in §4.3), it can be modelled as a compact element located at the axial position  $x_{HD_1}$  and will therefore be modelled as such hereafter.

Similarly to the previous test case, the relaxation coefficients  $\tau_1$  and  $\tau_2$  are chosen to fit at best the experimental measurement of the vibrometer. In Fig. 4.10 the temperature fluctuation modelled analytically is compared with the experimental measurement as well as with the results published in Duran et al. (2013b) at the vibrometer position  $x_{vib} = -58.5$  mm. Note that, at the time, Duran et al. did not study in details the heating device and located it at the axial position  $x_{HD_{Duran}} = -100$  mm which induces a time delay of 3.6 ms in the signals. Temperature and pressure signals have therefore been shifted by 3.6 ms for proper comparisons of the temperature fluctuation profiles.

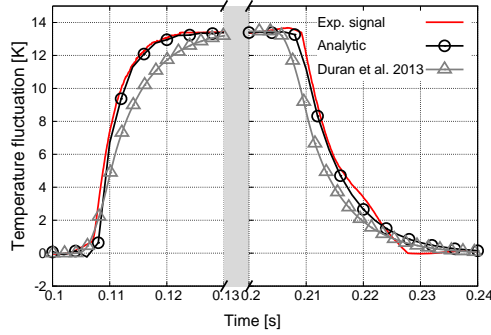


**Figure 4.10** Temperature fluctuation produced by the heating device extracted at the vibrometer position  $x_{vib} = -58.5$  mm. Parameters of the model:  $\Delta T_{exp} = 13.4$  K,  $n_r = 1$ ,  $\tau_1 = 3.5$  ms,  $\tau_2 = 7$  ms,  $t_0 = 0.1$  s and  $T_p = 0.1$  s.

Pressure fluctuations issued by the temperature hot slug are shown in Fig. 4.11 for the three inlet reflection coefficients studied in the supersonic case  $R_{in} = [-1, 0, 1]$ . Duran et al. (2013b) considered an inlet reflection coefficient close to 1. Clearly from Fig. 4.11, none of the results is close to the analytical result obtained by Duran et al. However, it should be noted that for reflection coefficients different from zero ( $R_{in} \neq 0$ ), the pressure fluctuations obtained with the non-compact transfer functions differ from the ones obtained with the compact transfer functions, especially the ones obtained for  $R_{in} = -1$ . This result shows that the nozzle is not compact for this operating point, which is in disagreement with the results found by Duran et al. (2013b). In an attempt to retrieve the results obtained by Duran et al. (2013b), the impedances of the numerical simulation of Duran et al. are approached using the low-pass filter formulation of the NSCBC boundary conditions derived by Selle et al. (2004) (i.e. Eq. (4.14)). In this specific case, relaxation coefficients for the inlet and outlet of the configuration are set to  $K_{in} = 100$  s<sup>-1</sup> and  $K_{out} = 160$  s<sup>-1</sup>. As done before, the inlet reflection coefficient



is tested for a negative and positive value. Pressure fluctuations obtained by partially reflective inlet and outlet boundary conditions are shown in Fig. 4.12. Compact and non-compact results are almost the same. Considering however the case of  $R_{in} > 0$ , the pressure fluctuation signal is almost superimposed with the result obtained by Duran et al. The variance in the results from Figs. 4.11 and 4.12 shows the great influence of the inlet impedance in the generated pressure fluctuations. Therefore, without the precise value of the inlet impedance the comparison of the pressure fluctuations with the experimental ones can only be inexact or at least not mastered.

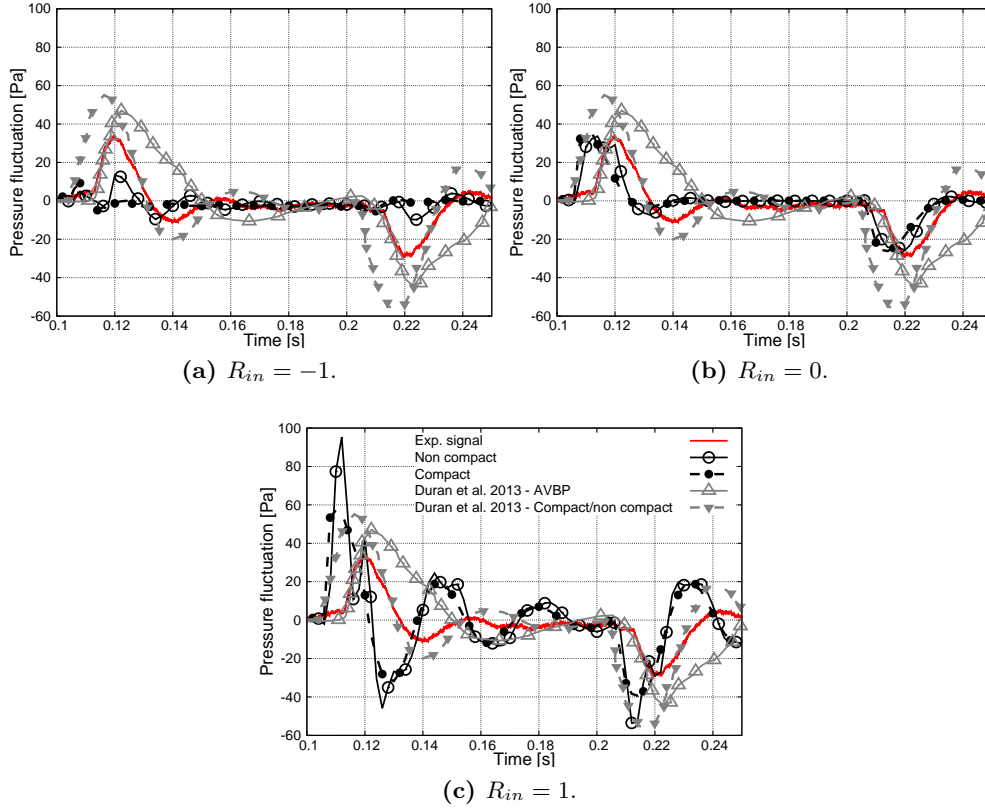


**Figure 4.11** Pressure traces recorded at the outlet of the EWG ( $x_{out} = 2100$  mm) for different inlet reflection coefficients  $R_{in}$  and a partially reflecting outlet reflection coefficient  $R_{out}$  ( $K_{out} = 160 \text{ s}^{-1}$ ).

As done in the study of the supersonic test case described in §4.3, the spectrum of the upstream temperature and pressure disturbances (only direct noise -  $A_{HD}^+$ ) in the upstream duct are analysed for the different inlet reflection coefficients studied. Figure 4.13 shows the modulus of the DFT of these variables extracted at the vibrometer position  $x_{vib} = -58.5$  mm. The obtained spectra are very similar to the ones obtained in the supersonic test case (cf. Fig. 4.6), where almost all the energy is contained in

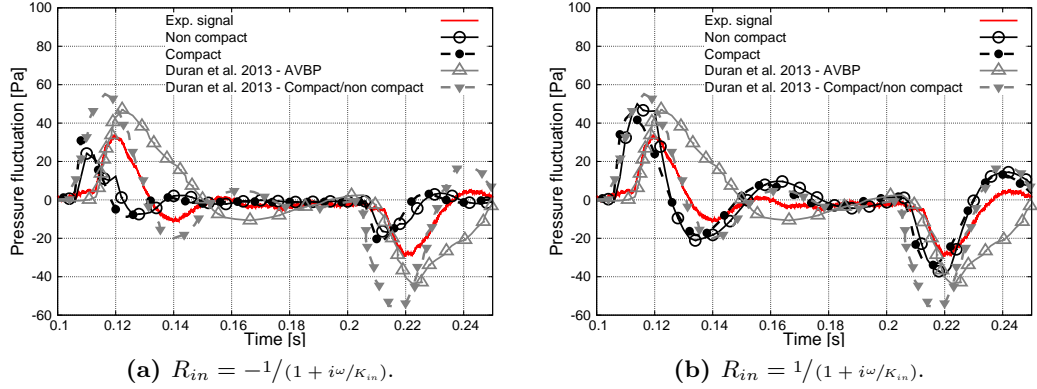


**Figure 4.12** Pressure traces recorded at the outlet of the EWG ( $x_{out} = 2100$  mm) for a partially reflecting inlet and outlet reflection coefficients ( $K_{in} = 100$  and  $K_{out} = 160$  s<sup>-1</sup>).

frequencies lower than 10 Hz. However, the case with the negative partially reflective inlet boundary condition shows that for frequencies  $\leq 80$  Hz, the harmonic amplitudes of the generated pressure fluctuation remain of the same magnitude, which may question the compactness of the nozzle (as already observed in Fig. 4.11a). To confirm this, the transfer functions of the nozzle are displayed in Fig. 4.14. In comparison with the supersonic nozzle transfer functions (cf. Fig. 4.7), the subsonic transfer functions modulus and phase are observed to change drastically with frequency, which confirms that the nozzle cannot be considered as compact for the subsonic operating point. According to the upstream acoustic-acoustic transfer functions (cf. Figs. 4.14a and 4.14b), at least 30% of the amplitude of  $A_{HD}^+$  is transmitted to the downstream duct, while frequencies  $\geq 100$  Hz, are almost fully reflected by the nozzle into the upstream duct. Concerning the generation of indirect noise and according to Figs. 4.14e and 4.14f, its generation is greater with an increasing frequency. Therefore, direct noise is transmitted by the lowest frequencies, while indirect noise is produced by higher frequencies attenuating direct noise (cf. Fig. 4.14a for the transmission of direct noise, Figs. 4.14e and 4.14f for the generation of indirect noise). Then, the ratio of indirect to direct noise  $\eta$  is computed and shown in Fig. 4.15. Indirect noise generation increases with frequency as well as with a decreasing inlet reflection coefficient, which is in agreement with previous results (maximal generation of direct noise for  $R_{in} = 1$  and its transmission is greater in the lowest frequencies). The dominant noise source for almost all the inlet reflection coefficients tested here seems to be the direct noise, contrarily to the supersonic test case. However, in the particular case of  $R_{in} = -1$ , a dominant noise source cannot be determined and the value of  $\|\eta\|$  oscillates between 0.5 and 3.

Finally, using the different inlet reflection coefficients tested and the analytical method presented in this section, the evolution of the peak pressure at the outlet of the EWG can be computed as a function of the nozzle Mach number. This result is shown in Fig. 4.16. The evolution of the peak noise is increasing monotonously, except for the

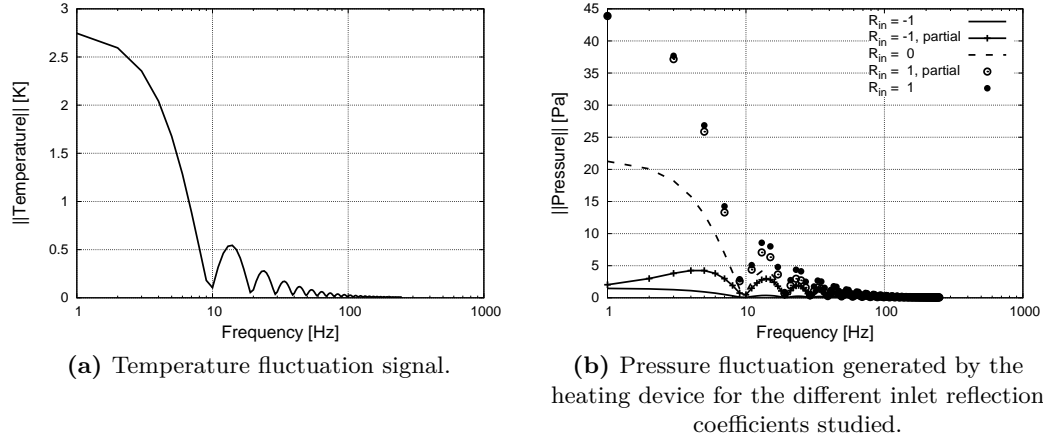


**Figure 4.13** Discrete Fourier Transform of incoming disturbances at the vibrometer position  $x_{vib} = -58.5$  mm.

partially reflecting case with  $R_{in} = -1$ , which has the same trend as the experimental values (reaching a maximum value and then decreasing). This result shows, once again the strong dependency of the peak noise to the inlet reflection coefficient. Without its experimental value, no conclusion can in fact be drawn in terms of shape or amplitude of the generated pressure disturbances within the system.

## 4.5 Conclusion

In this chapter, the analytical methodology proposed by [Duran et al. \(2013b\)](#) has been revisited introducing a model to take into account the entire heating device and non-compact transfer functions of the nozzle. The model for the heating device considers each heated ring of the device as a compact element. Therefore each ring generates its own acoustic and entropy waves. Note also that a time delay has been introduced to take into account the ignition sequence of the subsonic test case. Results show that the heating device may be considered as compact for acoustics, and when no time delay is considered, the overall entropy front is smoothed by the convective process taking place when each front is transported from its origin to the next heating ring.

The supersonic test case shows that the nozzle can be considered as compact for the range of frequencies studied, which confirms the results of [Leyko et al. \(2011\)](#). In this case, the shape of the pressure signal at the fourth microphone is in agreement with the experimental measurements and the peak pressure is slightly overestimated. The inlet reflection coefficient is finally found to have an important role in the determination of the total direct noise generated. When the value of  $R_{in}$  is between -1 and 0, indirect noise is at least 10 times higher than the direct noise production. Indeed, a value for the reflection coefficient equivalent to -1 produces a destructive interaction between

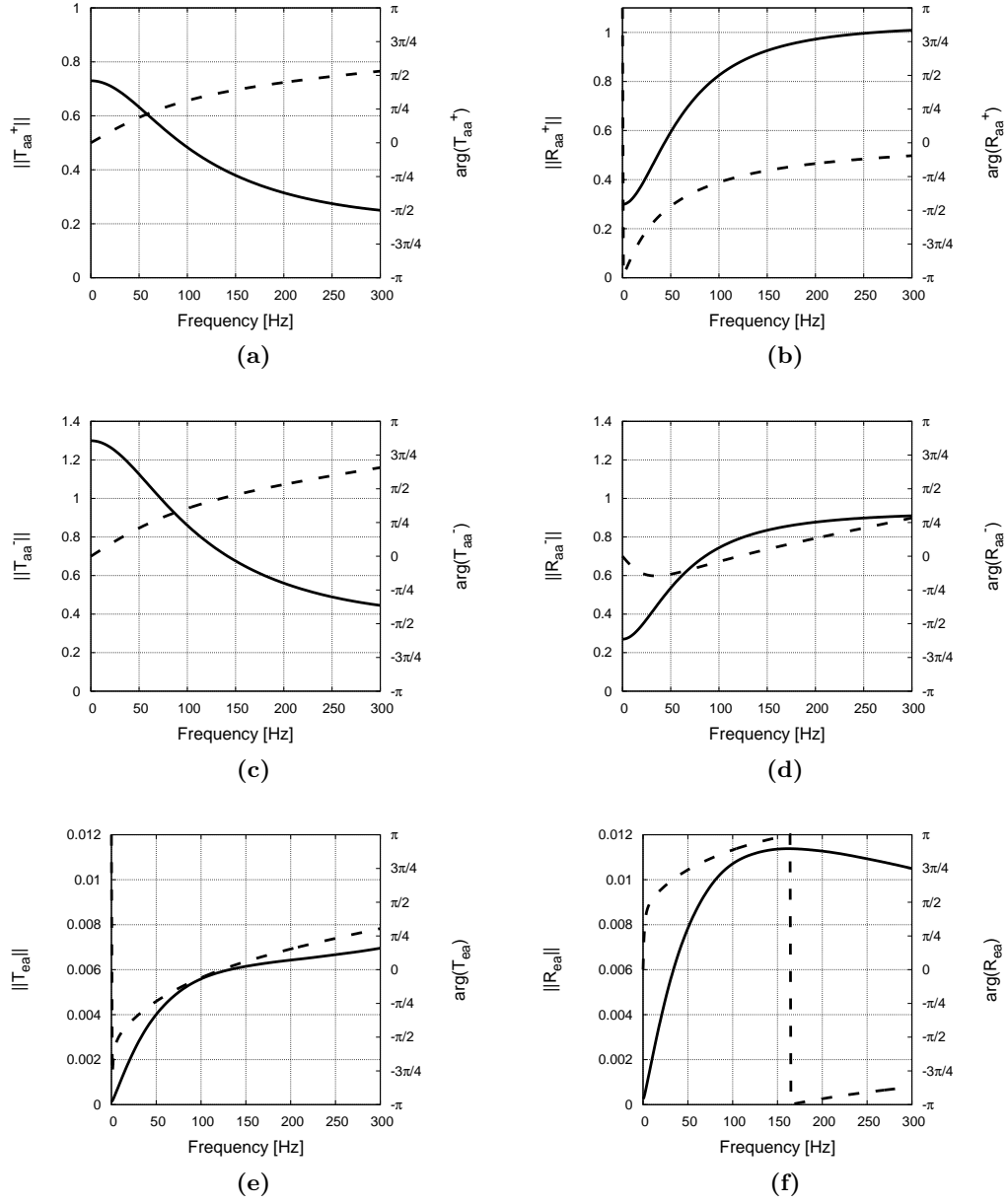


**Figure 4.14** Nozzle transfer functions of the subsonic test case. Modulus(—): left axis. Phase(---): right axis.

incident and reflected wave, whereas with  $R_{in} = 0$  no acoustic wave is introduced. It is also noted that only  $\approx 10\%$  of the incident acoustic wave is transmitted through the nozzle (as shown by Fig. 4.7c). Therefore, acoustic waves in the upstream duct can be attenuated by the destructive interaction controlled by the inlet boundary condition

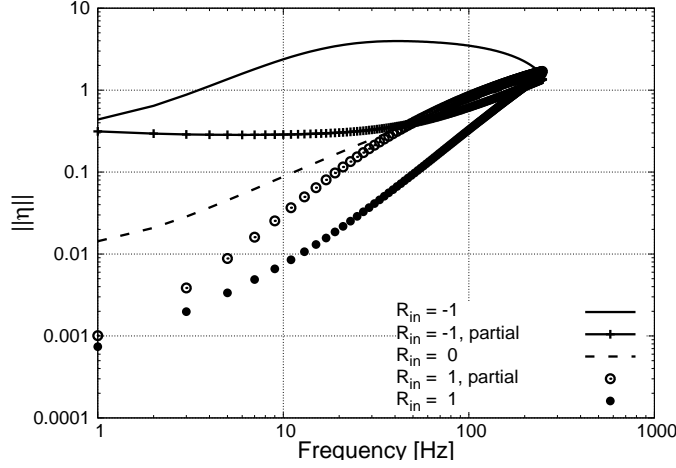


**Figure 4.15** Modulus of indirect over direct noise ratio  $\|\eta\| = \|A_{1,e}^+/A_{1,a}^+\|$ .

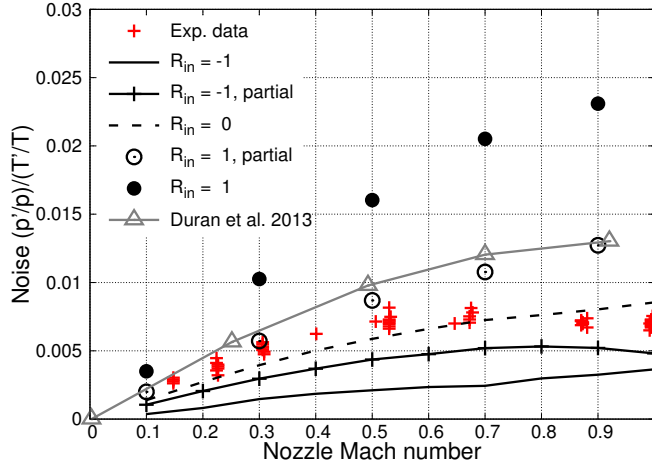


**Figure 4.16** Evolution of the noise peak pressure at the outlet of the EWG as a function of the throat Mach number.

( $R_{in} = -1$ ) or evacuated ( $R_{in} = 0$ ). Afterwards, the only sound transmitted is the one produced by the entropy wave. When  $R_{in} = 1$ , indirect to direct noise ratio is almost equal to one for the most energetic frequencies ( $< 10$  Hz). This is because the inlet boundary condition produces a constructive interaction between the incident and the reflected wave. Acoustic waves in the upstream duct cannot leave the domain by the boundary condition and direct noise becomes a non negligible noise source.

In the subsonic case, the heating device may be considered as a compact element (no need to represent each of the six heated rings) thanks to the delay in the activation of the heated rings. The nozzle transfer functions show however that the nozzle cannot be considered as compact. Results published by [Duran et al. \(2013b\)](#) were partially re-

trieved using a partially reflecting inlet and outlet reflection coefficients. Regarding the dominant noise source, it has been found that it is strongly dependent on the inlet reflection coefficient but it is mostly direct noise. However, cases with  $R_{in} = -1$  (partially and fully reflective) show that indirect noise is not negligible.

To conclude with this initial analysis, two parameters are found to strongly modify the generated noise induced by the temperature fluctuation: the shape of the hot slug (modulated by relaxation parameters  $\tau_1$  and  $\tau_2$ ) controls the peak pressure generated, and the inlet reflection coefficient modifies the shape of the generated acoustic pressure signal. This inlet reflection coefficient, linked to the relaxation chamber upstream of the inlet duct of the EWG seems to be close to -1. Nevertheless, no experimental data about this inlet impedance is available and this parameter remains unknown. It should be however noted that the use of a partially reflective condition seems sufficient to recover the experimental variation of the noise peak pressure at the outlet of the EWG (cf. [Fig. 4.16](#)).

This analytical study of the EWG test cases allowed to assess the influence of different parameters in the transmitted entropy noise. However, the analytical results of the subsonic test case have not shown satisfactory results between the experimental and the analytical ones. Therefore, to have a better insight of the phenomenology generating and transmitting the so called indirect combustion noise, this subsonic test case is chosen to be simulated by a full compressible LES in the following chapter.

## Chapter 5

# Numerical compressible simulation of the EWG

In this chapter, the subsonic test case of the EWG studied analytically in §4.4 is analysed by means of Large Eddy Simulation (LES). A simulation of this kind requires to solve a large range of characteristic length scales. In particular, the acoustic and entropy wavelengths ( $\lambda_{ac} \sim \mathcal{O}(\text{m})$  and  $\lambda_\sigma \sim \mathcal{O}(\text{mm})$  respectively) as well as the characteristic length of the heating device ( $L_{\text{HD}} \sim \mathcal{O}(\text{mm})$ ) and the Kolmogorov length scale for turbulence ( $\eta \sim \mathcal{O}(\mu\text{m})$ ) are all to be considered for an adequate quality simulation.

The analytical modelling of the EWG has shown that the inlet acoustic impedance has a great impact on the propagated noise and that without the knowledge of the experimental value, the comparison between the models/simulations and the experiment can be misleading (at least for the subsonic case). Nevertheless, LES still remains a valuable tool that further increases our capacity to more and more accurately understand the mechanisms at the origin of the generation of noise (i.e. Brès et al. 2012, Giret et al. 2012, 2013, Sanjose et al. 2014 and Wang et al. 2016). Indeed it can provide some useful information that cannot be captured through Euler simulations or analytical methods about the generation and transport mechanisms of combustion noise. For example, it is only through the use of such approaches that one will adequately quantify the effects of dissipation and dispersion of a hot slug, as done by Morgans et al. (2013), Giusti et al. (2016) and Hosseinalipour et al. (2017) in the framework of a turbulent channel flow, or by Papadogiannis et al. (2016) in the framework of a high pressure turbine stage. The effects of flow separation on indirect combustion noise as described by Howe (2010) can also be studied further within this specific numerical context. All of these effects have not been studied in previous works concerning the EWG, which are based on the coupling of RANS simulations with CAA methodologies (Ullrich et al. 2014, 2015), URANS simulations (Muhlbauer et al. 2009 and Lourier et al. 2014), Euler simulations and even analytical modelling (Leyko et al. 2011 and Duran et al. 2013b). LES seems therefore a good candidate to provide further insight into the physical phenomena of indirect combustion noise generation and transmission.

The EWG subsonic test ( $M_{Nth} = 0.7$ ) case has been chosen to be analysed in LES due to the non compactness of the nozzle and the amount of direct and indirect (none of the noise sources can be neglected) noise in the overall noise generated. Furthermore, the analytical results obtained in §4.4 partly disagree with the experimental data, which can be explained by their inherent simplifications and the actual flow physics. LES (if properly conducted) can thus help understanding the weaknesses of the analytical methods and eventually be at the source of model improvements.

The numerical tool used for the simulations detailed in this chapter is the LES compressible solver AVBP (Schönfeld and Poinso 1999). AVBP is based on a cell-vertex formulation, and the commonly used numerical schemes are Lax-Wendroff<sup>1</sup> (LW), Two step-Taylor-Galerkin '4A'<sup>2</sup> and 'C'<sup>2</sup> (TTG4A and TTGC) along with an explicit time-advancement and a linear-preserving artificial viscosity model solve the filtered NS equations. These numerical techniques allow to control numerical dissipation and to properly capture acoustic waves. In this framework, AVBP has shown its capability to compute acoustics in complex geometries, for example Truffin and Poinso (2005); Martin et al. (2006); Selle et al. (2006) which used AVBP to study acoustic instabilities or the works of Giret et al. (2012, 2013), Sanjose et al. (2014) and Salas and Moreau (2016) for the study of aero-acoustics. When studying acoustics, boundary conditions are a crucial matter. In the studies of thermo-acoustic instabilities in combustion chambers, the propagation of acoustic and entropy waves through the inlet and the outlet of the chamber determines the coupling of acoustics and the flame, producing or not an unstable mode. At these inflow/outflow boundary conditions, AVBP uses Navier-Stokes Characteristic Boundary Conditions (NSCBC) to decompose flow variables on the boundaries into ingoing and outgoing waves (cf. Poinso and Lele 1992).

This chapter is organised as follows: §5.1 discusses and compares the unperturbed flow computed by LES with the experimental measurements. In §5.2, the methodology used to reproduce the experimental conditions and requirements for the forced flow (in particular the modelling of the heating device and the acoustic impedances) is explained and compared with the experimental measurements and analytical models. In §5.3 a methodology to compute the nozzle transfer functions from LES is detailed. The methodology is first validated computing the transfer functions of the nozzle using Euler equations. Then, the obtained transfer functions are compared to the analytical theory of Duran et al. (2013b) in §5.3.2. The same process is then used to compute the nozzle transfer functions on the basis of LES and results are presented in §5.3.3. This specific step intends to give a better understanding of the real behaviour of the nozzle when subject to acoustic and entropy disturbances, taking into account the effects neglected by the analytical models. To finish, the LES transfer functions are directly used in the analytical modelling of §4.4 to evaluate their impact on the propagation of combustion noise.

---

<sup>1</sup>Finite-volume scheme, precise at the order two in space and time.

<sup>2</sup>Finite-element scheme, precise at the order three in space and time.



## 5.1 The baseline flow

The study of a flow with acoustic or entropy disturbances requires at first a well statistically converged flow to investigate only the effect of the disturbances and avoid any interaction issued from the transient flow and statistically unsteady base flow. This is valid for numerical simulations as well as for experiments. Therefore, in this section the unperturbed flow is first analysed.

The complete domain of the EWG (illustrated in Fig. 5.1) includes a settling chamber with a plate installed at the inlet to avoid the formation of a jet generated by the sudden expansion. In addition to the plate, a honeycomb flow straightener (hatched section in Figure 5.1) has been installed to minimize lateral velocity components and obtain a straight plug flow entering the nozzle.

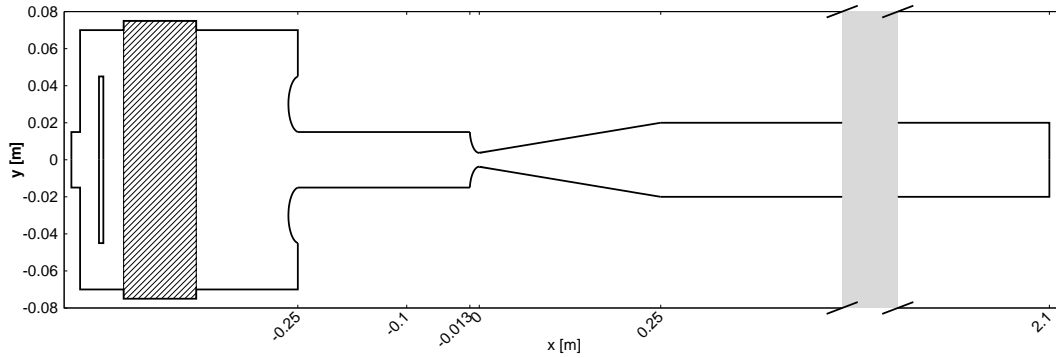


**Figure 5.1** Sketch of the EWG complete geometry.

Considering the whole EWG configuration without a model describing the honeycomb flow straightener, big vortical structures are detached from the plate (Q criterion shown in Fig. 5.2), generating unwanted acoustic perturbations. Therefore, the complexity of the flow inside the settling chamber, the lack of model to represent the honeycomb and the uncertainty issued by the corresponding upstream acoustic reflection coefficient, inferred to trim the settling chamber from the numerical domain.

For the base flow computation, three numerical meshes were created and then used to study the indirect combustion noise generation within nozzle flows, each one with a different purpose. A coarse mesh (M1) is used to reproduce numerically the experiment carried by [Bake et al. \(2009\)](#), a finer mesh (M2) is then used to compute the nozzle transfer functions and a very fine mesh (M3) intends to comply with wall resolved (dimensionless distance to the wall  $Y^+ < 5$ ) LES. M1 and M3 cover the entire EWG configuration, from the inlet of the upstream duct ( $x = -250$  mm) to the outlet of the downstream duct ( $x = 2100$  mm). Since the computation of the transfer functions of the

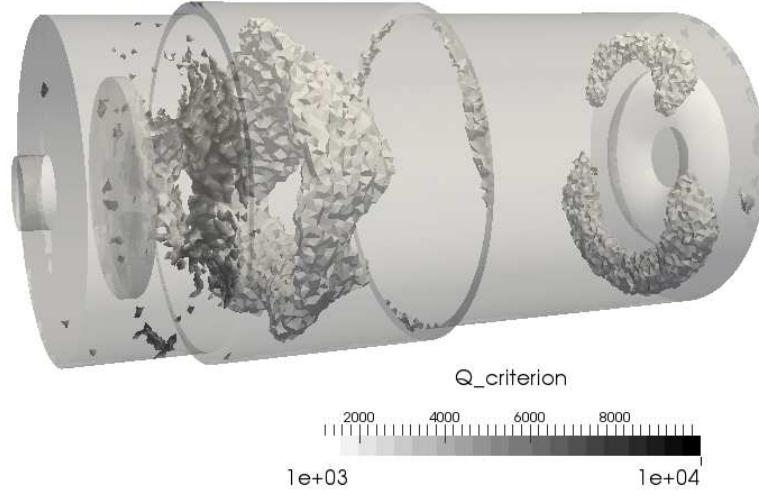


**Figure 5.2** Vortex shedding produced inside the settling chamber.

nozzle does not require to mesh the entire EWG configuration, the domain considered is smaller (from  $x = -100$  mm to  $x = 400$  mm). Although, calculations carried with M3 are very consuming in terms of CPU and storage, they comply with recommended academic LES modelling, so this simulation intends to be the reference point of the others. However, at the time of this document compilation, the computation of the unperturbed flow on M3 was not statistically fully converged in the entire domain (especially in the downstream duct) and can be only partially exploited. All meshes are multi-elements composed of prisms at the walls to improve the resolution of the flow boundary layers and tetrahedral elements elsewhere. M1 is composed of  $\approx 6$  M cells ( $\approx 1.5$  M nodes) with four prism layers, M2  $\approx 22$  M cells ( $\approx 5.4$  M nodes) with five prism layers and M3 contains  $\approx 300$  M cells ( $\approx 80$  M nodes) with six prism layers. The different numerical domains and associated meshes are illustrated in [Fig. 5.3](#).

The baseline flow is obtained by initialising and imposing a mass flow rate and a static temperature at the inlet and a static pressure at the outlet (cf. specifications in [Tab. 3.2](#)). Note that, the static pressure at the outlet of M1 and M2 have been corrected to obtain the appropriate mean operating point. Indeed, in the case of M1, the outlet pressure needs to be increased to recover the operating point fixed by the nozzle-throat (indicated by the experimentalist  $M_{N_{th}} = 0.7$ ). This adaptation is due to the lack of resolution near the wall region inside the convergent of M1. The boundary layers are not well resolved, which results in a smaller effective section of the nozzle. As a consequence, the flow is more accelerated than in the real nozzle. M2 has a smaller domain than M1 and M3, therefore the outlet pressure of M2 was chosen to be extracted from the other computations for full equivalence. The numerical set-up for the simulations is summarized in [Table 5.1](#), where a two-step Taylor–Galerkin (TTG) finite-element numerical scheme developed by [Colin and Rudgyard \(2000\)](#) with the Wall-Adapting Local

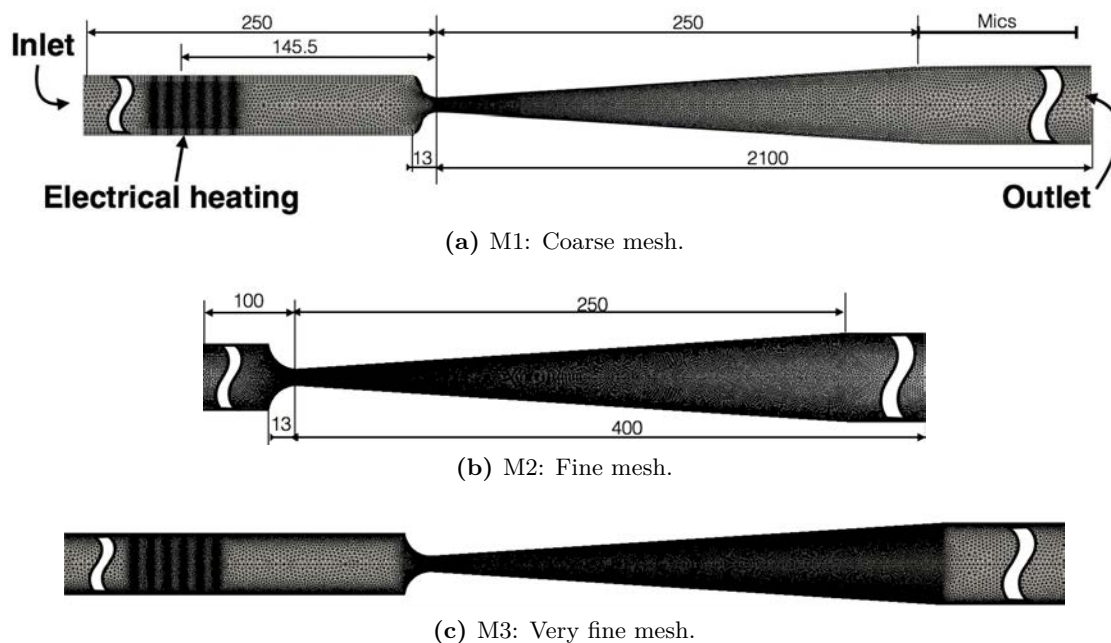


**Figure 5.3** Numerical grids for the baseline flow of the EWG.  
(Distances indicated in millimetres).

Eddy-viscosity (WALE) subgrid-scale model developed by [Ducros et al. \(1998\)](#) and a CFL adaptive time-step were used.

#### Boundary conditions

Inlet	NSCBC Mass flow rate and static temperature
Outlet	NSCBC Static pressure
Walls	Non slip adiabatic

#### Numerical parameters

Governing equations	Navier-Stokes
Numerical scheme	TTGC
LES model	WALE
CFL	0.7

**Table 5.1** Numerical set-up of the simulations.

To evaluate the quality of the LES simulations, their ability to resolve the boundary layers is analysed. To do so, mean profiles of the dimensionless distance to the wall  $Y^+$  and wall shear stress  $\tau_w$  are extracted. Then, bulk quantities issued by all simulations are compared with the isentropic quasi-1D theory. For each prediction, experimental diagnostics are reproduced on the basis of the LES predictions for comparisons with available data. Finally, axial velocity, Mach number, temperature and pressure mean

simulation profiles are compared to assess potential sources of differences issued by the three different meshes.

First, mean flow quantities are detailed and discussed. To do so, a temporal average followed by an azimuthal average of the flow fields are computed. Mean resulting axial profiles of  $Y^+$  and  $\tau_w$  are displayed in Fig. 5.4. Values of  $Y^+$  are represented in Fig. 5.4a for the three meshes. M1 pictures a maximal  $Y^+ \approx 35$  in the convergent zone and  $Y^+$  greater than 10 in the upstream and downstream ducts, indicating that the boundary layer is not well resolved: i.e. not satisfying the requirements of a wall resolved LES (Jiménez and Moin 1991). M2 reaches its maximum  $Y^+$  value of 25 in the convergent. However, in the other zones (diffuser and upstream and downstream duct)  $Y^+$  values are always smaller than 6, indicating that wall resolved LES is reached almost everywhere with M2. Finally, for M3, the value of  $Y^+$  is below 2 almost everywhere and never exceeds 5, reflecting a fully wall resolved simulation only for this mesh. Mean wall shear stress  $\tau_w$  axial evolution is displayed in Fig. 5.4b for the three different meshes.  $\tau_w$  is proportional to the normal gradient of the velocity to the wall and representative of the friction of the flow to the wall. For example, in the particular case of flow separation, the separation point can be identified by  $\tau_w = 0$ . According to  $\tau_w$  profiles shown in Fig. 5.4b, no flow separation (in the temporal averaged mean flow) is captured in the LES simulations. In the inlet duct,  $\tau_w$  is almost constant for  $x \leq -40$  mm, where the streamlines are straight, then the area constriction of the convergent makes the streamlines bend and a recirculation zone is formed at the inlet of the convergent. This recirculation zone is not visible in the temporal averaged mean flow but can be visualised in the instantaneous velocity field displayed in Fig. 5.5a. This recirculation zone is responsible for the decrease of  $\tau_w$  at the inlet of convergent in the temporal averaged mean flow. Then, in the first millimetres of the divergent (near the nozzle throat), the transition to turbulence is triggered and a vortex sheet is created. In this zone  $\tau_w$  decreases rapidly and in M2, the flow is found to be on the verge of separation (cf. Fig. 5.4b). Instantaneous streamlines are displayed for the first millimetres of the diffuser in Fig. 5.5b to visualise this transition. To estimate the intensity of the transition to turbulence in the different meshes, profiles of mean vorticity with respect to  $\theta$  are computed, azimuthally averaged and presented in Fig. 5.6. The azimuthal vorticity profiles are almost equivalent between meshes and the only differences are found to be inside the boundary layer, where only the most resolved meshes (M2 and M3) capture an inflection point in the azimuthal vorticity profiles. In M2, where the flow is on the verge of separation, the azimuthal vorticity intensity in the boundary layer is smaller than the other calculations, but catches the same profile shape afterwards.

Global mean flow quantities are now analysed. To do so, bulk velocity, bulk temperature, bulk Mach number and mean pressure are computed and compared with the results of the quasi-1D isentropic theory. The definition of the different computed quantities

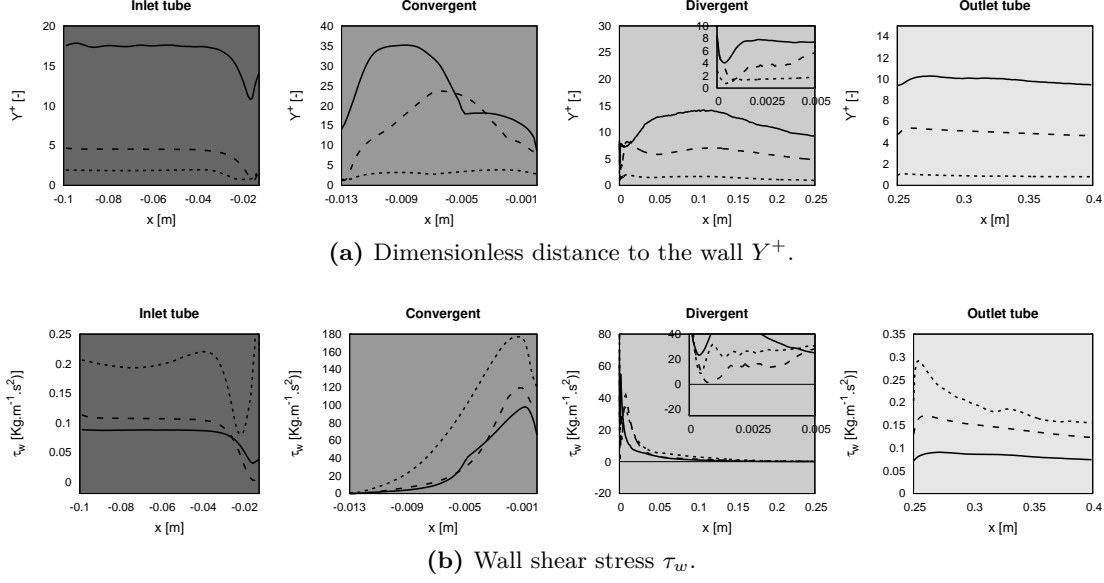


**Figure 5.4** Temporal and azimuthal average of the wall variables  $Y^+$  and  $\tau_w$  represented against the axial coordinate. M1 (—). M2 (---). M3 (···).

follows:

$$u_b = \frac{\int \rho u dA}{\int \rho dA}, \quad T_b = \frac{\int \rho u T dA}{\int \rho u dA},$$

$$M_b = \frac{u_b}{\sqrt{\gamma r T_b}}, \quad p = \frac{1}{A} \int p dA.$$

The isentropic operating point used for comparison respects the operating point No. 2 of Tab. 3.2. Figure 5.7 shows the three baseline flow axial evaluations obtained with the different meshes and compares them to the isentropic quasi-1D theory results. Clearly, computations on M1 and M2 appear very similar (almost superimposed). However, it is important to remember that the outlet pressure has been adapted to match the operating point in M1 and M2, whereas the value at the outlet of M3 uses the atmospheric pressure (without correction). Furthermore, the total pressure measured in M3 is very close to the measured one, which confirms the better resolution of the pressure losses. Concerning the bulk Mach number at the nozzle throat, M1 and M2 are in agreement with the experimental value, whereas M3 overestimates it slightly. Note however that in the experiment, the Mach number and the inlet duct bulk velocity are determined by the use of correlations and are not measured. Therefore, to make a fair comparison with the experimental data, the same methodology is used to compute the bulk velocity and the nozzle Mach number on the basis of the LES data. In this approach the bulk velocity is computed based on measured data that are the inlet duct temperature, pressure and mass flow rate:

$$u_{bulk} = \dot{m} \frac{rT}{pA}, \quad (5.1)$$

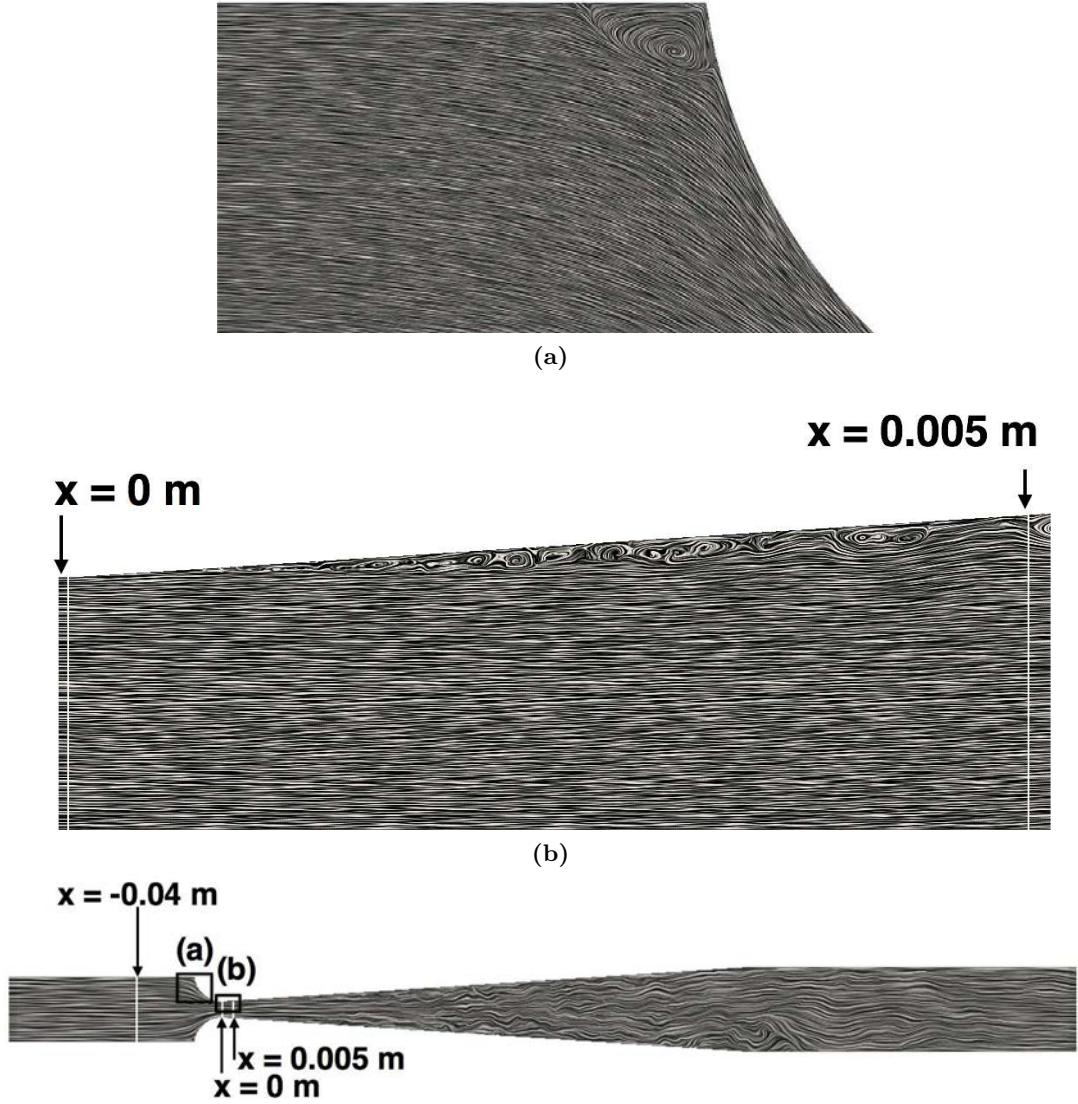


**Figure 5.5** Streamlines traced from an instantaneous solution of the flow computed in M3.

where  $T$  and  $p$  are the temperature and pressure measured by a thermocouple or a vibrometer in the inlet duct and a pressure probe in the settling chamber (assumed to be constant due to the low Mach number in the settling chamber and inlet duct) respectively. The nozzle-throat Mach number  $M_{N_{th}}$  is estimated then in the experiment using an iterative method described by [Knobloch et al. \(2015b\)](#). The methodology consists in computing a first value of  $M_{N_{th}}$  using the static pressure measured at the nozzle-throat and the total pressure measured in the settling chamber. Afterwards, a correction due to the curvature of the streamlines inside the nozzle (related to the flow

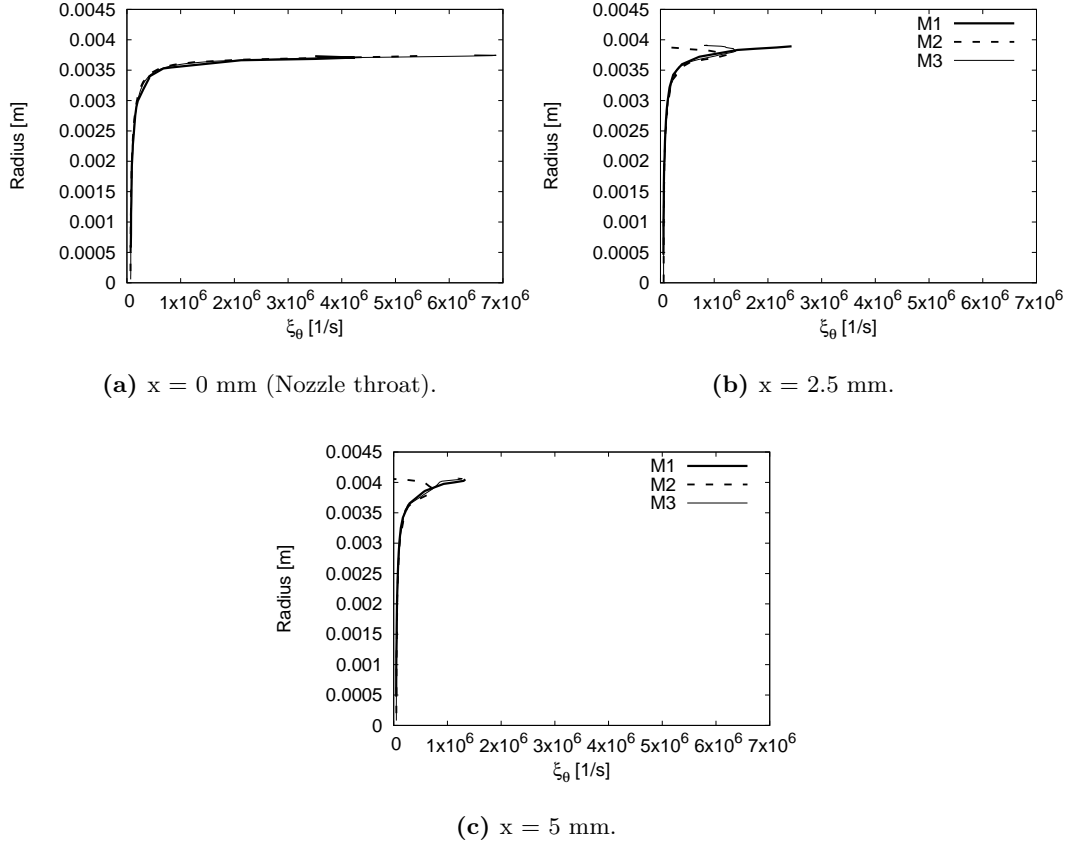


**Figure 5.6** Radial profiles of azimuthal averaged vorticity with respect to  $\theta$  ( $\xi_\theta$ ) close to the nozzle throat.

radial equilibrium hypothesis) is applied to the total pressure, as detailed hereafter:

$$M_{N_{th}} = \sqrt{\frac{2}{\gamma - 1} \left[ \left( \frac{p_T}{p} \right)^{\frac{\gamma-1}{\gamma}} - 1 \right]}, \quad (5.2)$$

$$p_{T,corr} = p_T + \frac{dp}{dn} dn = p_T - \frac{\rho u^2}{R_c} dn = p_T - \frac{M^2 P \gamma}{R_c} dn, \quad (5.3)$$

where  $R_c = 13$  mm is the nozzle curvature radius and  $dn$  the normal to a streamline set to 1.875 mm ( $1/4$  of the nozzle-throat diameter). Eqs. (5.2) and (5.3) are solved iteratively until convergence of the Mach number. The measured values of the static pressure at the nozzle-throat, the total pressure (settling chamber), ambient pressure and the estimations of the bulk velocity in the upstream duct and nozzle-throat Mach number are summarized in Tab. 5.2.



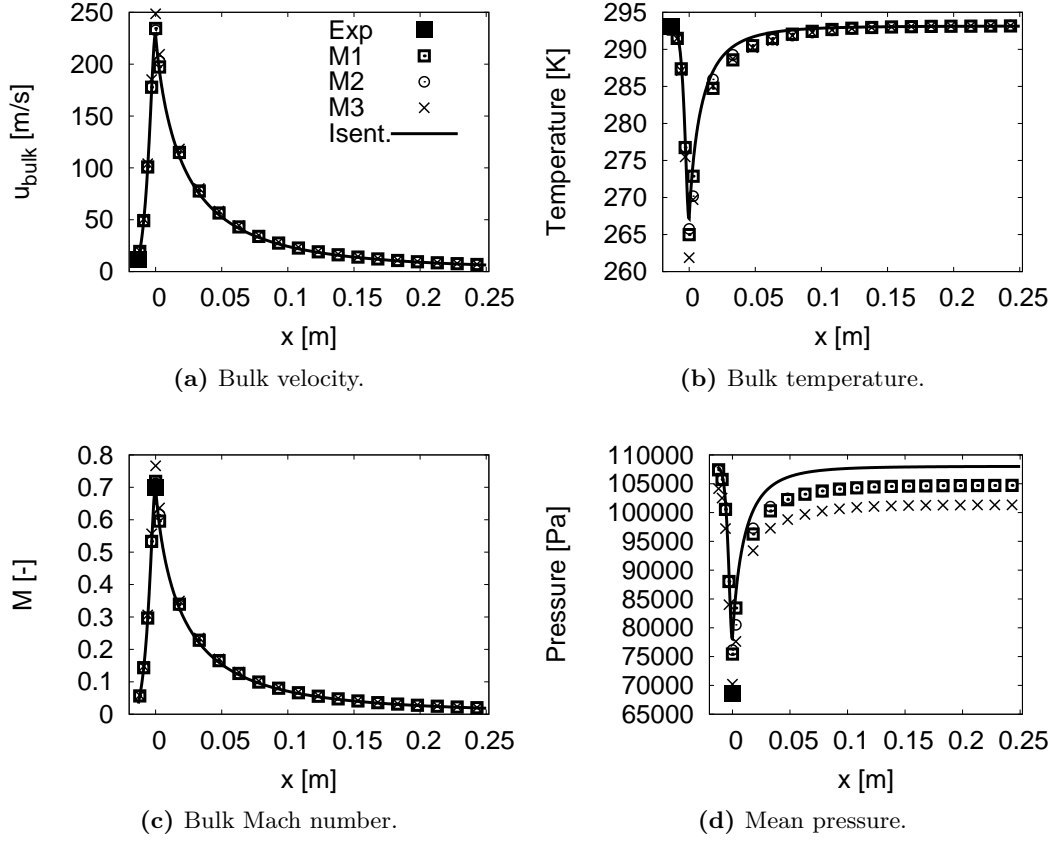


**Figure 5.7** Bulk quantities computed from the LES and compared with the isentropic theory.

Mean values obtained from the LES's and in the experiment are in overall good agreement, in particular for the simulation on M3 whose values of total and static pressure are the closest to the experimental values. The nozzle Mach number computed using the experimental methodology seems to be very close to the experimental value for all the simulations, which is not the case when comparing the bulk Mach number at the nozzle throat in the fully resolved LES. This variability in the bulk Mach number seems to indicate that the resolution of boundary layer has an important influence on the nozzle Mach number determination that is not taken into account in the experimental model used to compute the nozzle Mach number. The low variability in the isentropic vs bulk profiles shown in Fig. 5.7 as well as the good comparison with the experimental measurements of Tab. 5.2 allow to conclude that the operating point has been retrieved in all the simulations.

Up to now, mean profiles of  $Y^+$ ,  $\tau_w$  and bulk quantities have been compared (only 1D information). In the following, axial velocity, Mach number, temperature and pressure at different axial key points in the domain are detailed: (1) at the inlet of the nozzle  $x_{N_{in}} =$



Parameter	Experimental value	Isentropic	LES		
			M1	M2	M3
Mass flow rate	37 Kg/hr	37 Kg/hr	37 Kg/hr	37 Kg/hr	37 Kg/hr
Total pressure	105640 Pa	108025 Pa	107840 Pa	107730 Pa	104620 Pa
Pressure nozzle	68650 Pa	78050 Pa	69100 Pa	71900 Pa	66640 Pa
Nozzle Mach number (bulk value)	0.7	0.7	0.688	0.712	0.77
Nozzle Mach number (exp. methodology)	0.7	0.7	0.72	0.685	0.725
Bulk velocity (upstream duct)	11.39 m/s	11.33 m/s	11.34 m/s	11.34 m/s	11.67 m/s
Outlet pressure (boundary condition)	101300 Pa	100800 Pa	104700 Pa	104715 Pa	101300 Pa

**Table 5.2** Comparison of parameters of the unperturbed flow between the numerical simulation and the experiment.

−13 mm, (2) at the nozzle-throat  $x_{N_{th}} = 0$  mm, (3) inside the diffuser at  $x = 50$  mm and (4) at the outlet of the diffuser  $x_{N_{out}} = 250$  mm. Profiles at these four locations are shown in Figs. 5.8–5.11, and are found very much alike for all computations. Figure 5.8 shows the evolution of the axial velocity, as well as a flow boundary layer up to the nozzle throat (where the acceleration of the flow is the strongest) which seems to be well captured in the three simulations. A stronger acceleration along the axis is also seen on the finest mesh. At the outlet of the diffuser, the boundary layer is however clearly thickened by the coarsest mesh. Figure 5.9 shows the evolution of the Mach number, whose evolution is the same as the axial velocity. To complement these purely aerodynamic quantities, the evolution of the temperature is displayed in Fig. 5.10. The thermal boundary layer thickness at the nozzle throat seems to be the same for the three calculations and the same temperature value is retrieved at the exit of the nozzle. Finally, pressure profiles are shown in Fig. 5.11, which are observed to be shifted due to the augmentation of the pressure at the outlet of the M1 and M2. Despite this drawback issued by the wall resolution, the shapes and especially the ranges of variations remain of the same order of magnitude in all the simulations. Indeed, such a pressure profile is generated at the nozzle throat and is produced by the curvature of the streamlines at this specific location. A consequence of this flow curvature is the generation of a transverse pressure gradient that generates an unsteady azimuthal velocity in the divergent section. This specific effect is described by the local radial equilibrium equation (already used by the experimentalist to compute the nozzle Mach number), which in its simplified form reads:

$$\frac{1}{\rho} \frac{\partial p}{\partial r} \approx \frac{u_\theta^2}{r}. \quad (5.4)$$

This equation stands for the momentum conservation in the radial direction for an axisymmetric flow without radial velocity, which is only strictly valid at the nozzle

throat. Yet, the radial velocity remains small in the present slowly-varying divergent. Note also that the mean tangential velocity remains zero in the present axisymmetric set-up. The generation of  $u_\theta$  means that vorticity is generated in the axial and radial directions ( $\xi_x$  and  $\xi_r$  respectively) by the radial pressure gradient. Such vortices are then stretched and deformed by the flow acceleration through the nozzle and are a sound generation mechanism that contributes to the indirect noise generation. To study the axial evolution of the radial pressure gradient ( $\frac{\partial P}{\partial r}$ ) and the vorticity intensity in the different calculations, azimuthally averaged radial profiles of these magnitudes are extracted at different axial locations and shown in Figs. 5.12–5.14. The maximal radial pressure fluctuation is located at the nozzle throat (where the streamlines curvature is the strongest). At this location the stream-wise and radial vorticity values have also their maximal intensity. The radial pressure gradient is found to be very similar in the fine mesh computations (M2 and M3), where a very thin boundary layer is captured, which is not the case for the computation on M1. Then, further in the diffuser, the radial pressure gradients of all the simulations get closer, become of the same order of magnitude and almost flat at the outlet of the diffuser. Figures 5.13 and 5.14 show that the stream-wise and radial vorticity decreases with the pressure radial gradient (as described in the radial equilibrium Eq. (5.4)). Vorticity captured by M3 is greater than in the other meshes. Note that a mesh is only capable of transporting vortices bigger than its characteristic element length. Therefore, the vorticity generated at the nozzle throat will decrease as a function of the mesh element size increase, indicating that M3 should depict a stronger vorticity intensity at the outlet of the diffuser. Once again, comparison of all three predictions confirms that flow activity is better resolved with M2 and M3 (fully resolved mesh), and M3 depicts a stronger vorticity intensity at the outlet of the diffuser.

The different results shown in this section, from 1D results like the bulk quantities and the azimuthally averaged wall variables to the 2D azimuthally averaged profiles of different flow variables prove that the three numerical simulations are representative of the same operating point. The biggest differences between the different computations are at the nozzle throat, where the number of points used to describe the boundary layers is also very different. Despite these observations at the nozzle throat, all the other quantities compared at different sections (except for the pressure) are found to be very similar. Due to the huge differences in the computational costs and return time of simulations with M3 (details of the computational costs are summarised in Table 5.3), and the small differences in the computed profiles in comparison with the other meshes, it is concluded that M1 and M2 are well suited for the study of the entropy forced case of the EWG as well as the nozzle transfer functions. However, it should be kept in mind that the operating point computed with M1 and M2 is adjusted by modifying the outlet static pressure and that only the simulation carried with M3 strictly respects the experimental data.

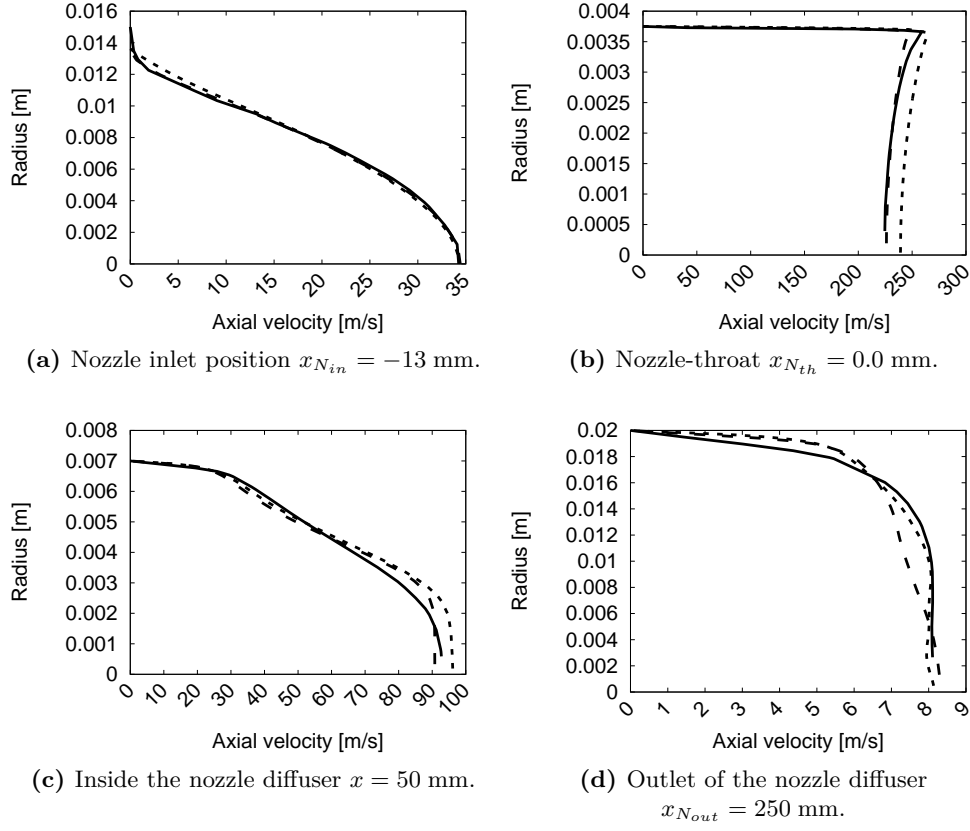
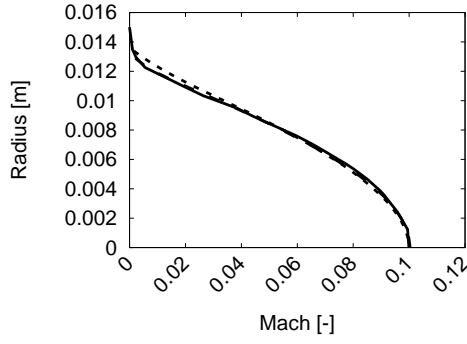


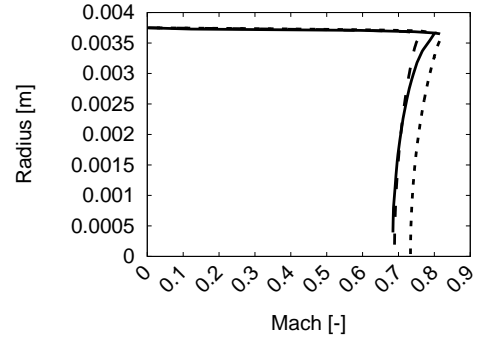
**Figure 5.8** Temporal and azimuthal average of the axial axial velocity versus the radius. M1 (—). M2 (---). M3 (---).

Numerical mesh	Number of cores and machine	Computed physical time	Computational cost
M1	360 - Nemo	0.4 s	150 000 hrs
M2	256 - Neptune	0.4 s	1 500 000 hrs
M3	8192 - Turing 1024 - Ada 3600 - Occigen 360 - Nemo 1200 - Nemo	0.4 s	20 000 000 hrs

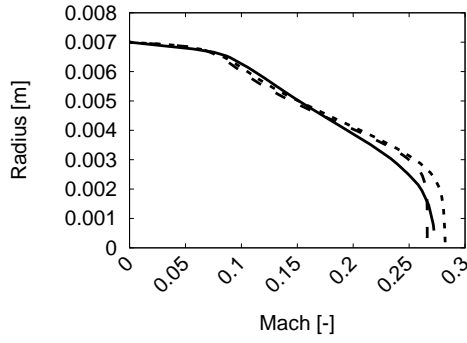
**Table 5.3** Computational costs of the different numerical simulations for the baseline flow.



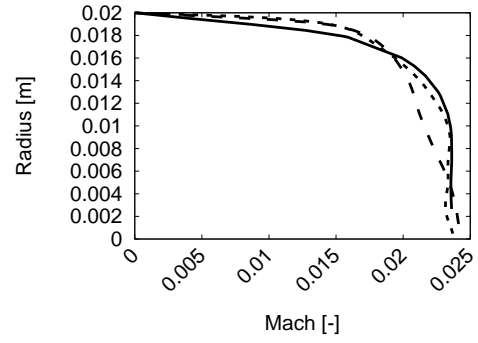
(a) Nozzle inlet position  $x_{N_{in}} = -13$  mm.



(b) Nozzle-throat  $x_{N_{th}} = 0.0$  mm.

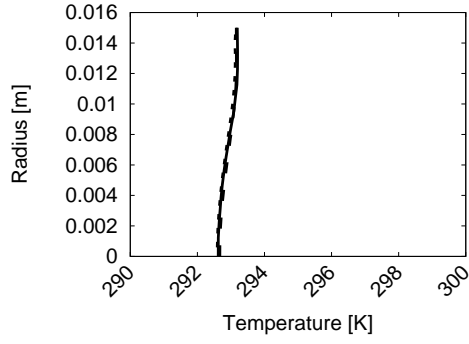


(c) Inside the nozzle diffuser  $x = 50$  mm.

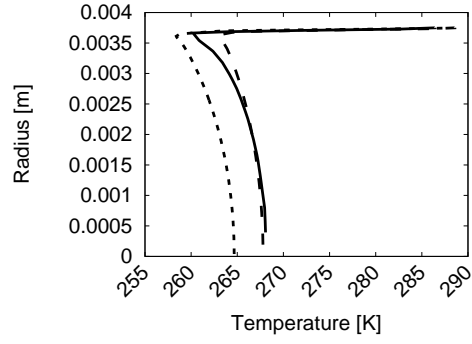


(d) Outlet of the nozzle diffuser  
 $x_{N_{out}} = 250$  mm.

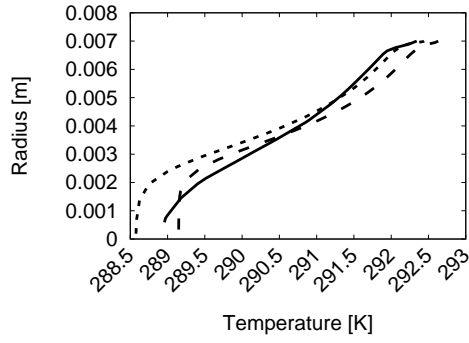
**Figure 5.9** Temporal and azimuthal average of the Mach number versus the radius. M1 (—). M2 (---). M3 (---).



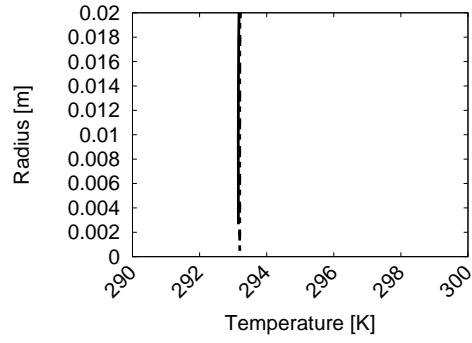
(a) Nozzle inlet position  $x_{N_{in}} = -13$  mm.



(b) Nozzle-throat  $x_{N_{th}} = 0.0$  mm.

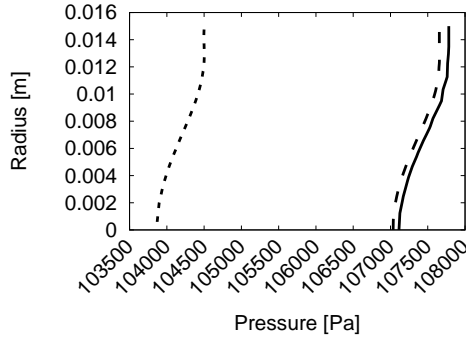


(c) Inside the nozzle diffuser  $x = 50$  mm.

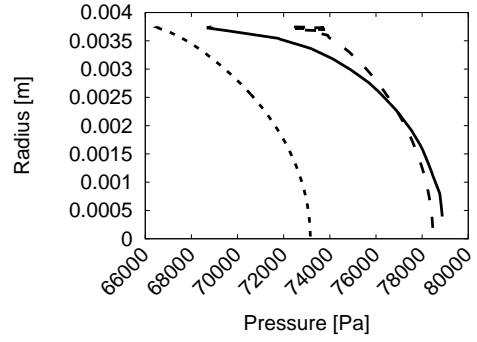


(d) Outlet of the nozzle diffuser  
 $x_{N_{out}} = 250$  mm.

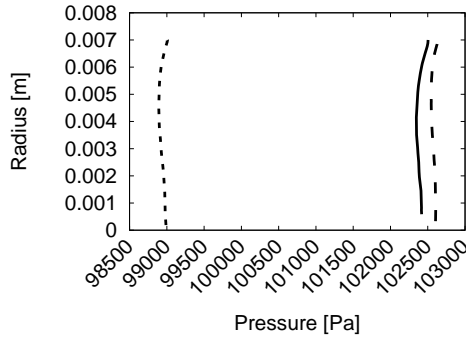
**Figure 5.10** Temporal and azimuthal average of the temperature versus the radius. M1 (—). M2 (---). M3 (···).



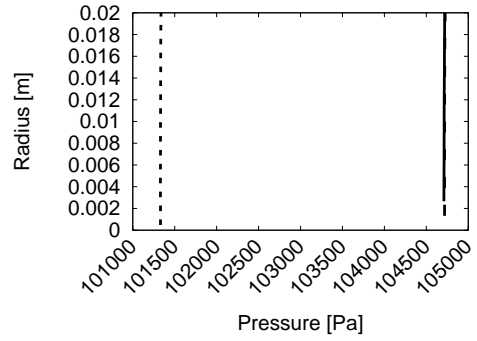
(a) Nozzle inlet position  $x_{N_{in}} = -13$  mm.



(b) Nozzle-throat  $x_{N_{th}} = 0.0$  mm.



(c) Inside the nozzle diffuser  $x = 50$  mm.



(d) Outlet of the nozzle diffuser  
 $x_{N_{out}} = 250$  mm.

**Figure 5.11** Temporal and azimuthal average of the static pressure versus the radius.  
M1 (—). M2 (---). M3 (···).

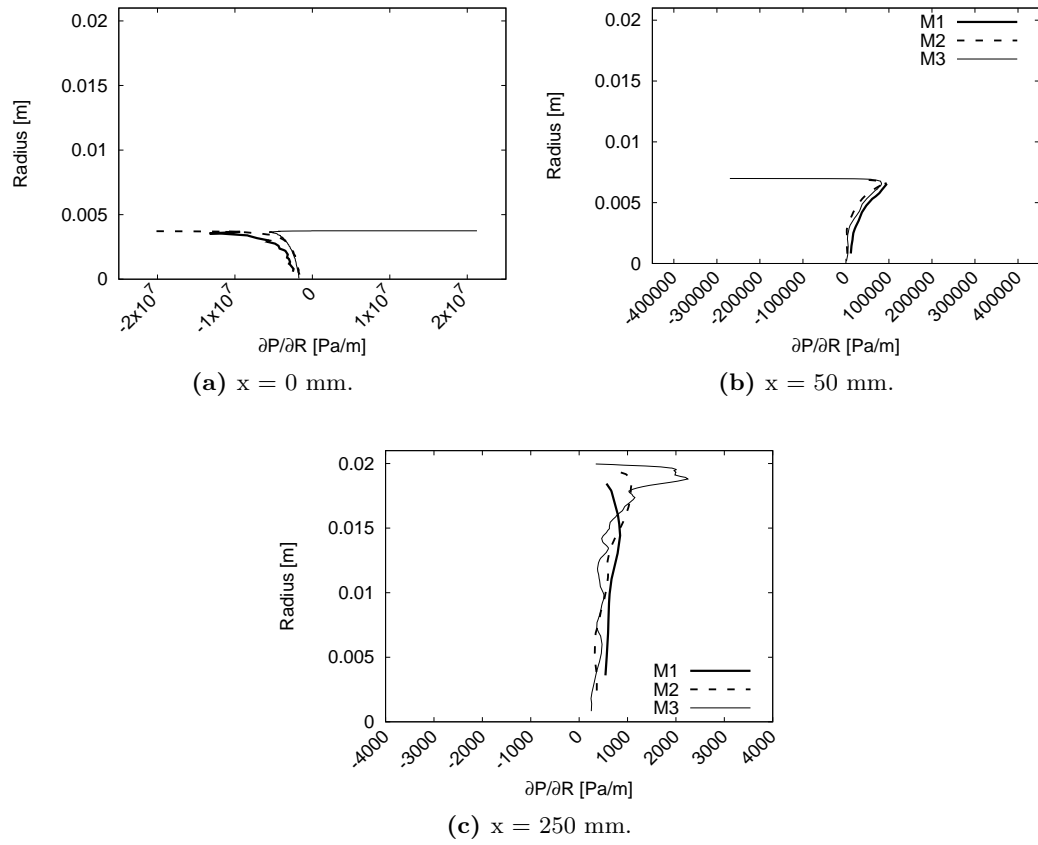


**Figure 5.12** Azimuthal average of the radial pressure gradient at different positions of the diffuser.

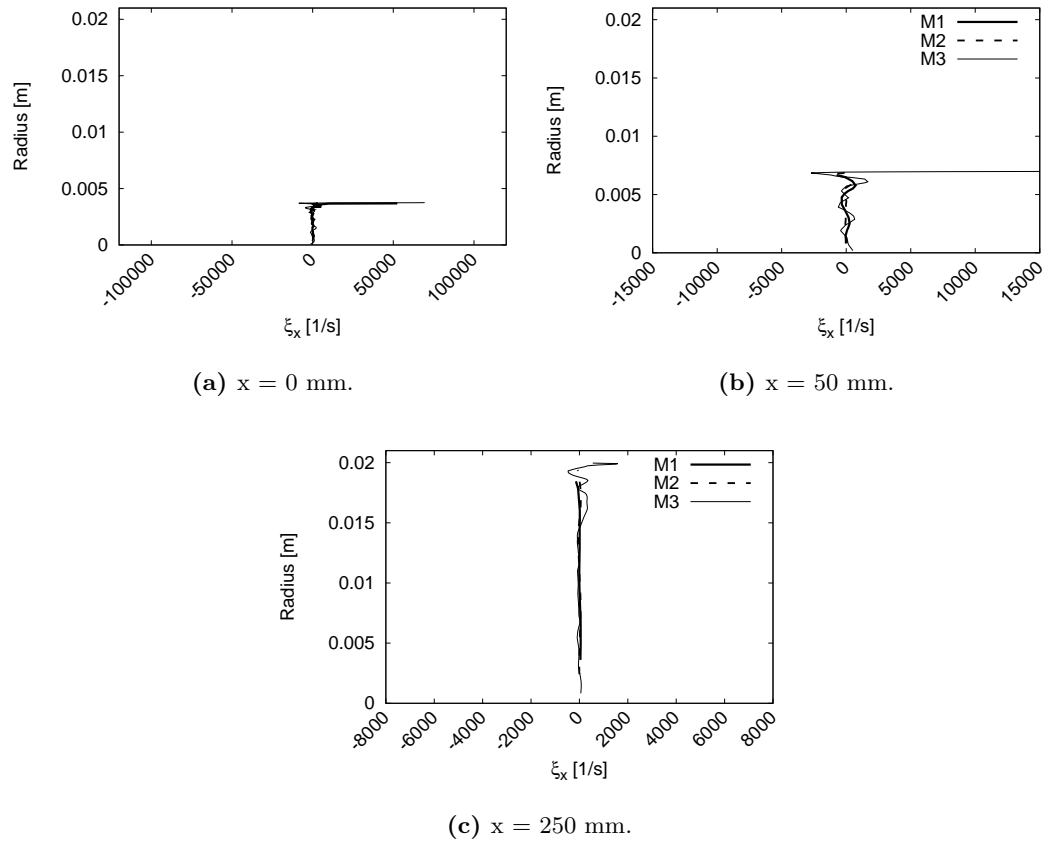


**Figure 5.13** Azimuthal average of the streamwise component of the vorticity ( $\xi_x$ ) at different positions of the diffuser.



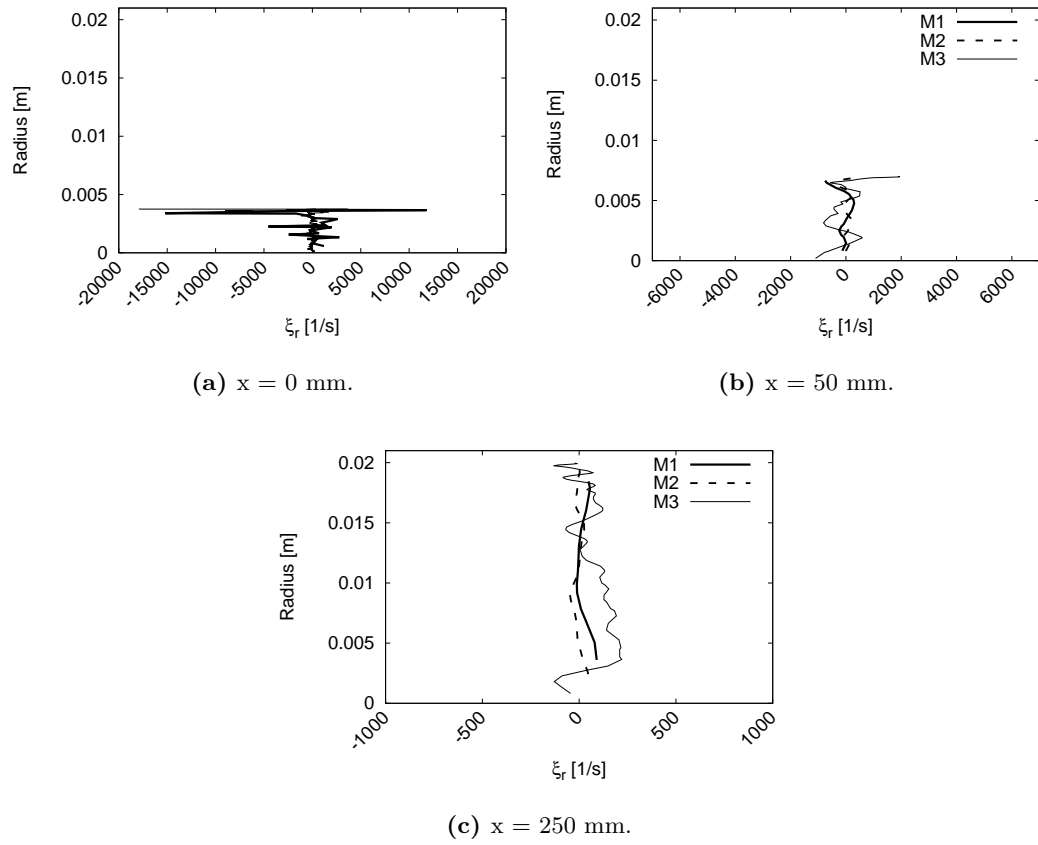


**Figure 5.14** Azimuthal average of the radial component of the vorticity ( $\xi_r$ ) at different positions of the diffuser.

## 5.2 The entropy forced flow

In this section the Entropy Wave Generator operated in subsonic forced conditions described by [Bake et al. \(2009\)](#) is simulated using the baseline flow computed with M1 in §5.1. For this exercise, particular attention is taken to the modelling of the heating device. Indeed, the preliminary analytical study carried in [Chapter 4](#) showed that the ignition sequence of the heating device and the shape of the generated temperature fluctuation have an effect on the generated pressure signals. Therefore, the experimental heating device ignition sequence, the modelling of the six heating rings as well as the gap presented in the experiment between the heated rings and the duct wall are taken into account. A reliable parametrised model of the heating device is hence first described. Based on this model, the introduction of the entropy disturbance is simulated by LES and analysed in terms of noise transmitted through the nozzle.

### 5.2.1 The heating device model

In terms of real hardware, the heating device of the EWG is composed of six modules themselves composed of electric resistances (a picture of one module is shown in [Fig. 5.15](#)), each module being separated from its neighbours by 8 mm. The most upstream heating module is located at  $x_{HD_1} = -145.5$  mm from the nozzle-throat. Note that experimentally a gap of 1.8 mm separates the electrical resistances from the duct wall to prevent overheating and fusion of the wires. This implies that only part of the boundary layer and flow are heated, an effect which has to be accounted for in the model to describe the heating device as accurately as possible in LES.



**Figure 5.15** Picture of one heating resistances module.

[Leyko et al. \(2011\)](#), [Muhlbauer et al. \(2009\)](#) and [Lourier et al. \(2014\)](#) have proposed different models to describe the heating device of the experiment. Usually the model consists in the introduction of a volumetric power source term in the energy equation. In this expression, the source term  $\dot{Q}$  is the result of the product of one temporal function  $\xi(t)$  and a spatial function  $\phi(x)$  (in the analytical analysis of the EWG of [Chapter 4](#), only the temporal function is used). In order to take into account the gap between the

heating wires and the duct wall, another function  $\varphi(r)$  is introduced here to restrain the energy deposition to a cylinder of radius  $R_{dep}$ . Furthermore, and for this particular experimental test case, each heating module is activated one after the other with a delay corresponding to the convective time of the flow for a distance equal to the module separation distances (8 mm). Hence, the model proposed here to describe the heating device follows:

$$\dot{Q}(x, r, t) = \frac{E_0}{n_r} \sum_{j=1}^{n_r} \frac{\phi(x) \cdot \varphi(r) \cdot \xi(t)}{\iint_{-\infty}^{\infty} \phi(x) \cdot \varphi(r) dV \int_0^{\infty} \xi(t) dt}, \quad (5.5)$$

$$\phi(x) = \frac{1}{2} \left[ 1 + \tanh \left( \frac{x - x_j + L_j/2}{d} \right) \tanh \left( -\frac{x - x_j - L_j/2}{d} \right) \right], \quad (5.5a)$$

$$\xi(t) = \begin{cases} 0 & \text{if } t < t_j \\ 1 - \exp \left( -\frac{t-t_j}{\tau_1} \right) & \text{if } t \in [t_j; t_j + T_p] \\ \phi(t_j + T_p) \exp \left( -\frac{t-t_j-T_p}{\tau_2} \right) & \text{if } t > t_j + T_p \end{cases} \quad (5.5b)$$

$$\varphi(r) = \begin{cases} 1 & \text{if } r \in [0; R_{dep}] \\ 0 & \text{if } r > R_{dep} \end{cases} \quad (5.5c)$$

where  $n_r$  is the number of activated rings;  $x_j$  and  $t_j$  are the position and the triggering time of the  $j^{\text{th}}$  heating ring, while  $T_p$  is the duration of the energy deposition.  $E_0$  is the total energy introduced by the model;  $L_j$  is the length of heating ring;  $\tau_1$  and  $\tau_2$  are the relaxation times of the temporal function  $\xi$  and  $d$  is the characteristic slope of the spatial function  $\phi$ . Here,  $t_j$  is controlled by a time delay  $\Delta\tau$  in the activation of each ring:  $t_j = t_0 + (j-1)\Delta\tau$ . Note that [Eq. \(5.5b\)](#) is the same as the one used for the analytical modelling (cf. [Eq. \(4.12\)](#)), but the activation time corresponding to each heating module  $t_j$  is directly taken into account in the expression. [Figure 5.16](#) shows an example of spatial and temporal distributions of energy obtained by the heating device functions for three activated heating rings.

This model of energy deposition is believed to be generic, being able to introduce different energy distributions both in time and space. For instance, this model can reproduce (1) the energy deposition of [Leyko et al. \(2011\)](#) and [Duran et al. \(2013b\)](#) where all the energy is deposited into a single cylinder that covers the entire length covered by all the heating rings, (2) the model of [Lourier et al. \(2014\)](#) where the energy is distributed in six different heating modules, each zone being activated at a different instant (the delay being based on the convective time of the mean flow).

In the experiment, once the heating device is activated, a hot spot is convected by the flow and the temperature fluctuation produced by this energy deposition is measured by a vibrometer located at  $x_{vib} = -58.5$  mm from the nozzle-throat. The vibrometer measures the temperature along a line of sight (in this case the diameter of the

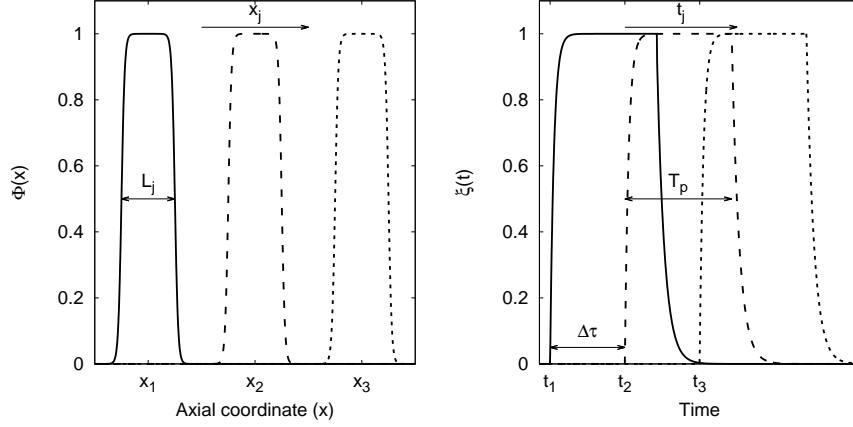


**Figure 5.16** Representation of the spatial (left) and the temporal law (right) of the heating device model,  $\phi(x)$  and  $\xi(t)$  respectively.

duct). Therefore, the temperature measured by this element can be described as a mean temperature over the diameter,

$$T_{vib} = T_{mean} = \frac{1}{2R} \int_{y=-R}^R T(y) dy. \quad (5.6)$$

Ideally, a relation between the energy introduced by the model and the induced temperature fluctuation must be found to give an estimation of the energy needed to obtain the temperature fluctuation measured by the vibrometer. This relationship clearly comes from the flow energy equation without chemical reactions, which reads:

$$\rho \frac{Dh}{Dt} = \frac{DP}{Dt} + \frac{\partial^2 \lambda T}{\partial x_i^2} + \tau_{ij} \frac{\partial u_i}{\partial x_j} + \dot{Q}, \quad (5.7)$$

where  $\frac{D}{Dt} = \frac{\partial}{\partial t} + u_i \frac{\partial}{\partial x_i}$  is the particular derivative,  $h$  is the specific enthalpy,  $\rho$  the density,  $P$  the pressure,  $T$  the temperature,  $u_i$  the different components of the velocity vector,  $\lambda$  the thermal conductivity,  $\tau_{ij}$  the viscous tensor and  $\dot{Q}$  a volumetric source term. To derive an expression linking the energy deposition  $E_0$  to the temperature fluctuation, a simplified axisymmetric domain is assumed (i.e. Fig. 5.17). The mean flow is hence assumed to only depend on the radial coordinate  $\vec{U} = U_x(r)\vec{x}$ . Additional assumptions are: an established regime ( $\partial/\partial t = 0$ ), no viscous losses ( $\tau_{ij} = 0$ ), adiabatic walls ( $\partial T/\partial \vec{n}|_{wall} = 0$ ), to finish with small temperature fluctuations ( $c_p \approx \text{constant}$  and  $\rho \approx \text{constant}$ ). With these assumptions, the energy balance can be recast into:

$$\rho U_x c_p \frac{\partial T}{\partial x} = \lambda \frac{\partial^2 T}{\partial x_i^2} + \dot{Q}. \quad (5.8)$$



**Figure 5.17** Simplified domain: Cylindrical duct with adiabatic walls.

To easily integrate Eq. (5.8) in space and time, two magnitudes are introduced: the bulk velocity and the bulk temperature defined as:

$$U_{bulk} = \frac{\int_{r=0}^R \int_{\theta=0}^{2\pi} U_x(r) r dr d\theta}{A}, \quad T_{bulk}(x) = \frac{\int_{r=0}^R \int_{\theta=0}^{2\pi} U_x(r) T(x, r, \theta) r dr d\theta}{A U_{bulk}}, \quad (5.9)$$

where  $A$  is the duct cross-section and  $R$  stands for the duct radius. Note that the bulk velocity is assumed to be constant in the duct, while the bulk temperature is dependent on the axial coordinate. Now, Eq. (5.8) can be integrated in the duct volume and between the energy deposition triggering time  $t_0$  and the total energy deposition time  $t_0 + T_P$ , yielding the identification of the energy to be introduced in the simulation  $E_0$ :

$$E_0 = \dot{m} c_p \Delta T_{bulk} \left[ T_p + (\tau_2 - \tau_1) \left( 1 - \exp \left( -\frac{T_p}{\tau_1} \right) \right) \right]. \quad (5.10)$$

Using the experimental data, the values of the specific heat at constant pressure  $c_p = 1004 \text{ J.kg}^{-1}.\text{K}^{-1}$  and the deposition duration time  $T_p = 0.1 \text{ s}$ . The best compromise for the two relaxation times of the heating device  $\tau_1$  and  $\tau_2$  found in the analytical evaluation of the EWG subsonic test case are 3.5 ms and 7 ms respectively. Finally, assuming that  $\Delta T_{bulk} = \Delta T_{mean} = 13.4 \text{ K}$  (which in the particular case of a 1D flow is true but not in the LES), the total energy  $E_0$  to be introduced in the simulation is 14.25 J (which is very close to the 13.82 J estimated by the experimentalist, cf. Table 3.2). However, it is important to underline that the model is constructed to use the bulk temperature fluctuation to estimate the deposition energy  $E_0$ , whereas the experimental input is the mean temperature fluctuation. Therefore a correction in  $E_0$  is expected if the bulk and mean temperature are different.

To study the accuracy of the model in obtaining the desired bulk temperature fluctuation and its difference with the mean temperature, a LES simulating only the duct upstream of the nozzle is produced using the above analytical value of  $E_0$ . Figure 5.18 shows the resulting evolution of the bulk and mean temperature when extracted from this numerical simulation and compared with the experimental reported mean temperature at the vibrometer position. The analytical model is seen to be very accurate. The bulk temperature of the simulation indeed collapses onto the experimental mean temperature value, whereas the corresponding mean temperature issued by LES shows a lower value. This specific difference is due to the thermal boundary layers developed in the flow. The bulk temperature results from the temperature weighted by the velocity

profile, therefore, temperature fluctuations inside the boundary layer have less weight than the ones in the center of the duct. Contrarily, the weight of the temperature is the same in the mean temperature formulation regardless of the flow velocity profile. In order to correct the value of the mean temperature obtained from the LES to the value reported by the experimental data, a linear correction between the energy and the mean temperature is done, obtaining the new value of  $E_0 = 16.24$  J, yielding a mean temperature profile in full agreement with the experimental data.

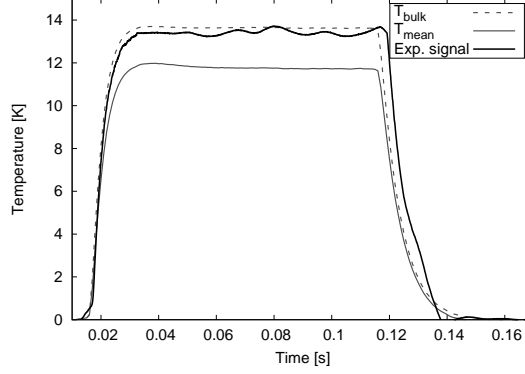


**Figure 5.18** Upstream duct: Bulk temperature and mean temperature of the LES compared with the experimental measurement at vibrometer position ( $x_{vib} = -58.5$  mm).

### 5.2.2 Numerical simulation of the forced EWG subsonic test case

To simulate the forced EWG experiment, three parameters need to be controlled numerically:

- A statistically converged baseline flow,
- The energy deposition model,
- The impedances of the boundary conditions.

The statistically converged mean flow and the energy deposition model have been analysed and presented in §5.1 and §5.2.1. Complemented by the analytical analysis of the EWG subsonic test case of §4.4, the following two parameters are now known to have a significant influence on the generation of combustion noise: the heating device and the acoustic impedances. The heating device is shown to be compact acoustically but it is not the case for entropy. It is also of note to highlight that the analytical study could not provide information about the shape of the slug and its influence on the generated noise, so the numerical simulations will be an important asset on such shortcomings. Concerning the acoustic impedances, Leyko et al. (2011) numerically fitted the outlet impedance of the EWG as close as possible to the experimental value. The analytical analysis, showed that the inlet impedance has also an important impact on the amount

of direct noise generated, showing that it must be close to -1 due to the sudden expansion between the upstream duct and the settling chamber.

Numerical implementation of the baseline flow needed a mass flow rate to be imposed to agree with the experimental data. However, acoustically, imposing the mass flow rate at the inlet of the configuration corresponds to imposing a positive reflection coefficient, whereas imposing a pressure results in a negative reflection coefficient. This effect can be simply shown by the direct definition of the reflection coefficient: the ratio of the reflected wave over the incident wave:

$$R = \frac{A^+}{A^-} = \frac{\frac{p'}{\gamma p} + \frac{u'}{c}}{\frac{p'}{\gamma p} - \frac{u'}{c}}, \quad (5.11)$$

$$R \xrightarrow[u'=0]{u=cst} 1 \quad ; \quad R \xrightarrow[p'=0]{p=cst} -1.$$

Ideally, a pressure should be imposed at the inlet of the EWG to obtain a negative reflection coefficient as recommended previously. In order to avoid numerical instabilities while imposing a pressure at the inlet and at the outlet (no degree of freedom left), a total pressure is preferred at the inlet. To do so, the total pressure is computed for the inlet plane of the baseline flow simulation and imposed as target value for the total pressure boundary condition of the entropy forced simulation. Note that, the new simulation was verified to have the same mass flow rate and nozzle Mach number as the baseline flow analysed in §5.1. Furthermore, using the expression of [Selle et al. \(2004\)](#) to determine the value of the reflection coefficient against frequency, a relaxation parameter  $K_{in} = 50000 \text{ s}^{-1}$  is chosen to impose a fully reflective inlet. [Figure 5.19](#) shows the theoretical reflection coefficients imposed in the simulation while [Tab. 5.4](#) summarizes the numerical set-up.

#### Boundary conditions

Inlet	NSCBC Total pressure and total temperature, $K_{in} = 50000 \text{ s}^{-1}$ .
Outlet	NSCBC Static pressure, $K_{out} = 160 \text{ s}^{-1}$ .
Walls	Non slip adiabatic

#### Numerical parameters

Governing equations	Navier-Stokes
Numerical scheme	TTGC
LES model	WALE
CFL	0.7

**Table 5.4** Numerical set-up for the entropy forced simulation.

The influence of the shape of the hot slug can be studied modifying the characteristic lengths, delays and times of the energy deposition model presented in §5.2.1. Two energy

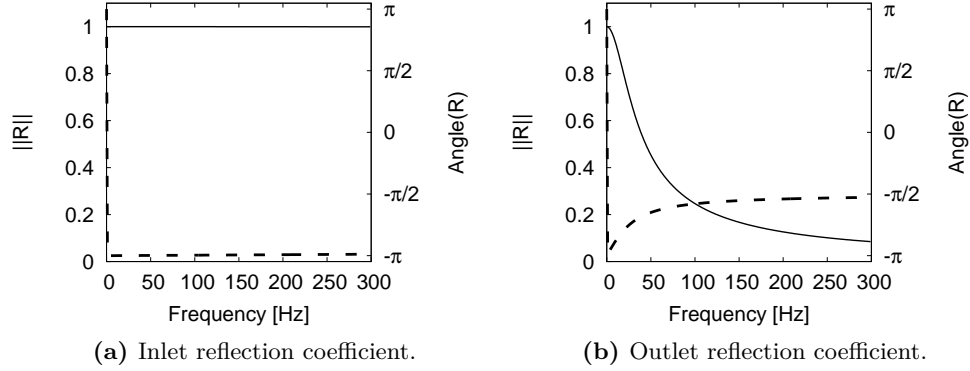


**Figure 5.19** Reflection coefficients imposed in the entropy forced simulation of the subsonic nozzle test case.

Left axis (—): modulus of the reflection coefficient. Right axis (---): phase of the reflection coefficient.

deposition shapes will be studied in this work: the one derived from [Leyko et al. \(2011\)](#), called "Block model" and the one proposed in this manuscript called hereafter "Delayed model". The main differences between both energy depositions are:

**Block** : The energy is deposited within a unique cylinder that overlaps the six heating wire modules activated at the same time. The difference with [Leyko et al.](#)'s model is that the volume of deposition is restrained by a radius  $R_{dep} = 13.2$  mm (smaller than the duct). This is because boundary layers are present in the LES and not in the Euler computation of [Leyko et al.](#)

**Delayed**: The energy is spread over six cylinders of length  $L_n = 1$  mm (5 mesh cells resolution), and a time delay of activation  $\Delta\tau = 0.702 \mu s$  between each cylinder is introduced to closely reproduce the experimental ignition sequence.

According to [Eq. \(5.5\)](#) the values of the different parameters of the deposition model for the two different test cases are listed in [Tab. 5.5](#).

To illustrate the main difference in both energy depositions, [Fig. 5.20](#) shows a planar cut normal to the "Z" coordinate displaying the instantaneous volumetric power introduced by the heating device at time  $t = 200$  ms (end of the energy deposition). This figure illustrates how the energy is distributed into the different rings. Note that when the deposition volume is smaller, more energy per unit volume is introduced, leading to a more brutal and shorter heating, which has an impact on the temperature gradients of the hot slug and therefore the generated direct noise.

To study the influence of the energy deposition on the different flow variables, instantaneous profiles of axial velocity, Mach number, temperature and pressure at two



Parameter	Block	Delayed
$n_r$	1	6
$E_0$	16.24 J	16.24 J
$x_0$	-125.5 mm	-145.5 mm
$\Delta x_r$	0 mm	8 mm
$L_n$	40 mm	1 mm
$R_{dep}$	13.2 mm	13.2 mm
$d$	1 $\mu m$	1 $\mu m$
$t_0$	0.1 s	0.1 s
$\Delta \tau$	0 s	0.702 ms
$T_p$	0.1 s	0.1 s
$\tau_1$	3.5 ms	3.5 ms
$\tau_2$	7 ms	7 ms

**Table 5.5** List of parameters for each deposition model test case.

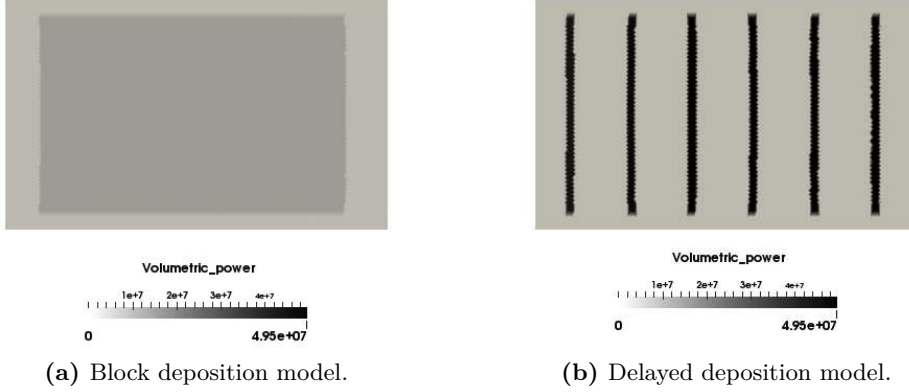


**Figure 5.20** Volumetric power deposited in the numerical simulation for the two different deposition models.

different instants ( $t_1 = 100$  ms and  $t_2 = 200$  ms) of the "Delayed model" simulation are compared with the mean profiles extracted from the baseline flow simulation computed on M1 (cf. §5.1) and showed in Figs. 5.21–5.24. Recall that  $t_1$  corresponds to the time when the deposition starts and  $t_2$  when the energy deposition stops. All profiles from the inlet of the nozzle ( $x_{N_{in}}$ ) to the nozzle throat ( $x_{N_{th}}$ ) are found to be equivalent at  $t_1$  to the mean profiles from the baseline flow simulation. This is due to the fact that upstream of the nozzle throat, the flow is "laminar" (confirmed by the streamlines in Fig. 5.5); there is no effect of vortices or any flow perturbation before the nozzle throat. In the divergent, the effects of the unsteady nozzle jet are visible in the instantaneous solution profiles, where the profiles are affected by the convection of vortices generated at the nozzle throat (cf. Figs. (5.21–5.24)(c,d)). Profiles at  $t_2$  show the evolution of the different variables when the temperature is increased by the energy deposition. The

elevation of the measured temperature in the upstream duct is 13.4 K, which is not significant enough to modify the velocity or the Mach number profiles. However, this temperature increase affects slightly the pressure profiles by about 20 Pa. It is worth noting that at the chosen instants, there is no sound generation by the entropy wave, at  $t_1$  the hot slug has not reached the nozzle and at  $t_2$  the first temperature front has already traversed the nozzle generating a steady state after its passage (the temperature between  $t_1$  and  $t_2$  reaches a constant value, cf. Fig. 4.10). Therefore, pressure fluctuations are only the result of boundary condition reflections (cf. Fig. 4.11) and vortex sound.

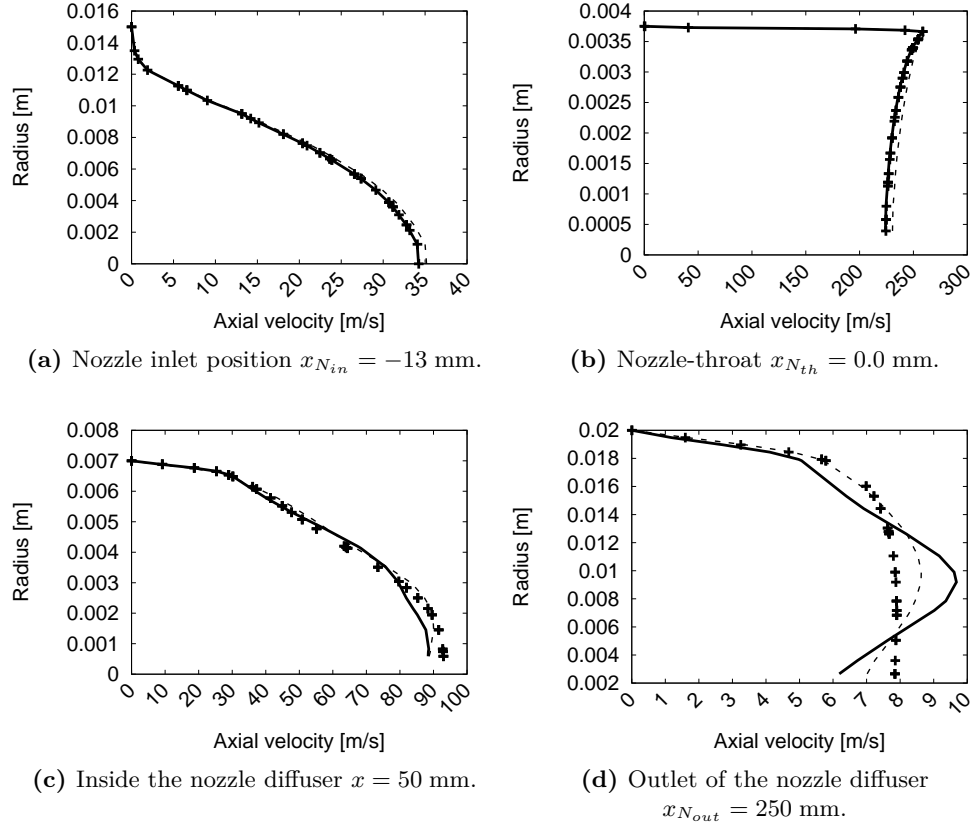


**Figure 5.21** Azimuthal average of the axial velocity versus the radius. Baseline flow simulation mean profiles on M1 (+++).  $t_1 = 0.1$  s - beginning of the energy introduction (—).  $t_2 = 0.2$  s - end of the energy introduction (---).

The first instants of the energy deposition are compared with the experimental data. To do so, only the first 35 ms of the energy deposition are shown in Fig. 5.25, where the spatially averaged temperature (according to Eq. (5.6)) and pressure fluctuation traces obtained in the numerical simulations are compared with the analytical results

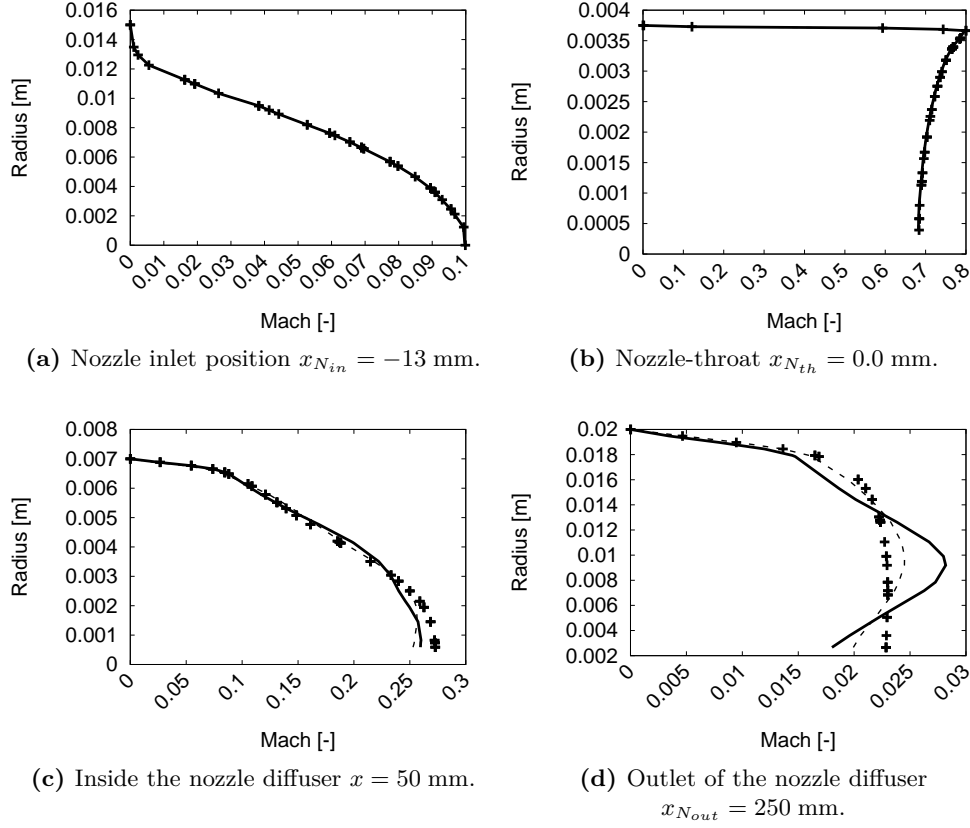


**Figure 5.22** Azimuthal average of the Mach number versus the radius. Baseline flow simulation mean profiles on M1 (+++).  $t_1 = 0.1$  s - beginning of the energy introduction (—).  $t_2 = 0.2$  s - end of the energy introduction (---).

obtained in §4.4 (invariants with  $R_{in} = -1$ , Fig. 4.11a) as well as with the experimental measurements. As already highlighted in the analytical evaluation of the EWG, the simultaneous activation of all the heating rings (block deposition model) induces a time delay in the temperature and pressure signals of about 3 ms due to the convection time of the temperature front between each heating ring. This time delay is taken into account in the delayed model, and is computed using the mean values reported by the experimentalist (cf. Bake et al. 2009): the bulk velocity in the upstream duct  $U_{bulk} \approx 11.4$  m/s and the spacing between each heating ring  $\Delta x_r = 8$  mm, yield a value of  $\Delta\tau = 0.702$  ms. This time delay multiplied by the number of heated modules minus one (number of intervals) provides the total time delay found to be about 3.5 ms. Figure 5.25a shows the spatially averaged temperature evolution at the vibrometer position. As expected, a very good agreement between the delayed ignition model, the analytical modelling and the experiment is found, while the block deposition model exhibits a time delay with respect to the others signals. The overlapping of the

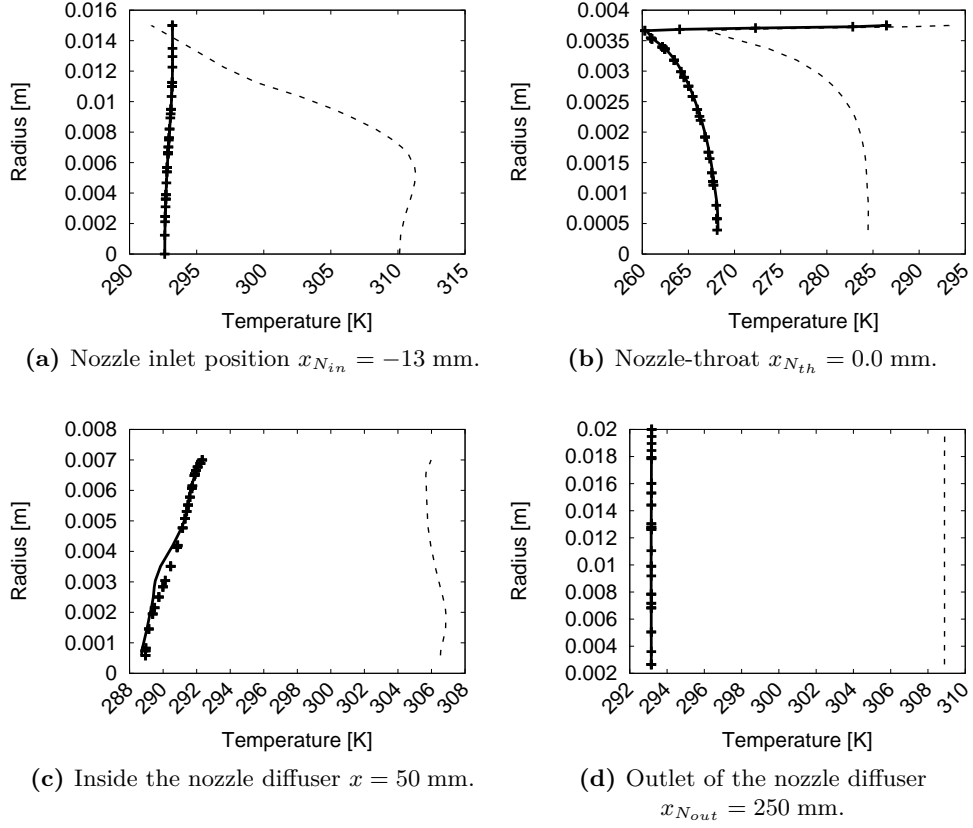


**Figure 5.23** Azimuthal average of the temperature versus the radius. Baseline flow simulation mean profiles on M1 (+++).  $t_1 = 0.1$  s - beginning of the energy introduction (—).  $t_2 = 0.2$  s - end of the energy introduction (---).

temperature signal produced by the delayed model and the vibrometer measurement allows verifying two things: first, the parameters chosen to describe the hot slug shape with the delayed model reproduce the shape of the temperature fluctuation measured by the vibrometer well; and second, the delay of activation of each heating module as well as the right convection velocity of the hot slug provides the correct operating point of the simulation (the hot slug arrives at the proper time at the vibrometer position). Concerning the pressure fluctuations generated by the heating and the acceleration of the hot slug through the nozzle, a sliding average has been applied to the numerical signals to obtain a better signal-to-noise ratio. Indeed, the experimental pressure signals are the result of a phase average of several hundreds of repetitions of the same pulse, when only one ignition sequence has been simulated by LES. The time delays of the different noise sources (direct and indirect) in the pressure signals have been analysed by [Lourier et al. \(2014\)](#). According to [Lourier et al. \(2014\)](#), the first direct noise signal (noise produced by the fluctuating heat release of the heating device) starts at about 4

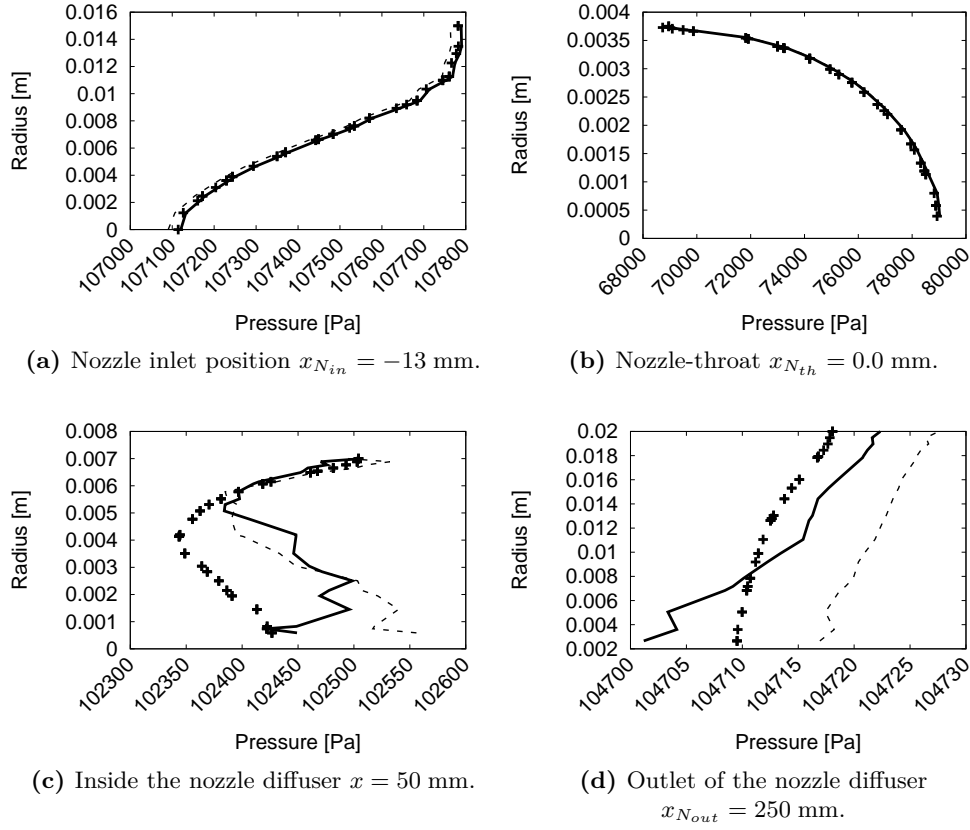


**Figure 5.24** Azimuthal average of the pressure versus the radius. Baseline flow simulation mean profiles on M1 (+++).  $t_1 = 0.1$  s - beginning of the energy introduction (—).  $t_2 = 0.2$  s - end of the energy introduction (---).

ms after the triggering of the energy deposition and the first indirect noise signal (due to the acceleration of the hot spot through the nozzle) arrives at about 12.5 ms. Pressure fluctuations generated by the heating and convection of the hot slug through the nozzle are represented in Fig. 5.25b at the fourth microphone position ( $x_{mic_4} = 1150.5$  mm), where time delays computed by [Lourier et al.](#) are also depicted. The heating device is found to be compact for the acoustic waves of interest (cf. [Chapter 4](#)) and direct noise signals arrive at the same time for both models ( $t \approx 103.5$  ms). Indirect noise contribution is seen to start earlier for the block deposition model (about 3.5 ms earlier) compared with the delayed model. Therefore, between  $t \approx 103.5$  and  $t \approx 109.1$  ms only direct noise is recorded by the microphone. However, here due to the noise present in the numerical results and the small window of time for purely direct noise contribution, one cannot conclude which model produces more or less direct noise. Nevertheless, the overall noise produced by the block deposition model is more spread and reaches a lower peak value. This result is somehow expected, as the same amount of energy is introduced

by both models and only the volume of deposition differs. The path followed by the flow in the block deposition approach during the ignition sequence is smoother and more continuous compared with the delayed deposition. Furthermore, when comparing the delayed model pressure results with the analytical ones, the shape of the signals is very similar (cf. Fig. 5.25b) and the starting point of indirect noise signals matches very well (slightly after [Lourier et al. 2014](#) prediction). In the zone where direct and indirect noise interact together, the analytical model appears to underestimate the pressure signal by half when LES seems to overestimate only the peak value, obtaining a better agreement with the experimental measurement. The differences between the analytical pressure signal and the numerical one can be attributed to different elements: the vortex shedding produced in the diffuser and the vortex sound generated at this occasion, the possible excitation of the nozzle jet by the entropy disturbance, and viscous effects. To better understand the impact of these effects on the generated noise, the computation of the nozzle transfer functions by a numerical simulation is presented in §5.3.

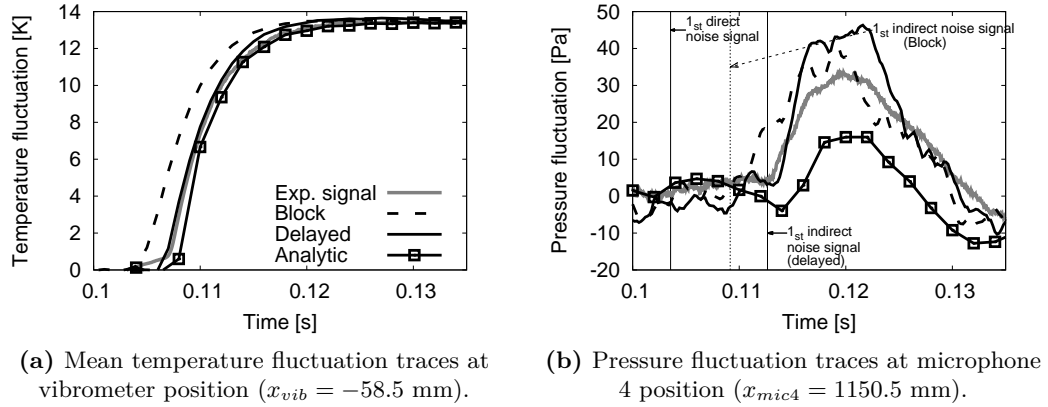


**Figure 5.25** Zoom over the first instants of the energy deposition.

Prior to the LES simulations dedicated to the nozzle transfer functions (cf. §5.3), another numerical simulation in which a temperature fluctuation with the same characteristics as the ones generated by the heating device is introduced in the domain without the generated direct noise. In such a simulation, one attempts to estimate the amount of indirect noise generated in the LES. To do so, a plane next to the heating device ( $x = -100$  mm) is extracted from the forced simulation discussed above to obtain a 2D temperature field that depends on time only. Afterwards, the inlet boundary condition used in the block and delayed models are modified so as to impose the extracted 2D temperature fluctuation signal. Figure 5.26 represents the result of this simulation and compares it to the delayed deposition model and the experimental results. The temperature and pressure fluctuations of the "only indirect noise" simulation have been shifted by 10 ms (convection time of the flow to reach the heating device) to make a fair comparison. The first phenomenon seen in the temperature fluctuation traces of the

latter simulation is an attenuation of the maximum value reached. This is due to the longer path followed by the hot slug to reach the nozzle. Pressure traces indicate that there is no direct noise (which is one of the principal objectives of this simulation) in the zone targeted where only direct noise exists. Furthermore, and despite the smaller maximum temperature fluctuation reached, the amount of indirect noise generated is observed to be almost the same as the overall contribution of both noise sources, indicating that direct noise has a very small contribution and that indirect noise generation is the dominant source in this experiment (in agreement with the work of [Lourier et al. 2014](#)).

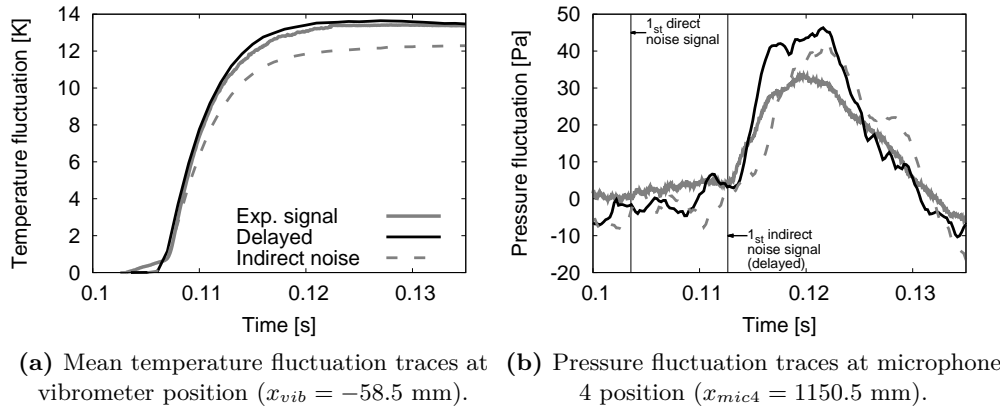


**Figure 5.26** Zoom over the first instants of the energy deposition. Comparison with the introduction of a hot slug by the inlet boundary condition simulation.

Up to now, the results of LES were compared to the experimental data. Thereafter and until the end of this section, the deformation of the entropy spot will be studied. Indeed, the convection of entropy fluctuations through a non homogeneous flow is responsible for the so called indirect noise. Therefore, it is important to study how the entropy spot generated by the heating device is distorted through the nozzle and how it is convected through the downstream duct. This process is similar to the one observed in real aeronautical engines, where the entropy fluctuations generated in the combustion chamber are first distorted by the outlet guide vane (replaced by the nozzle in this study) before being convected to a rotor row. Between the outlet guide vane and the rotor row, the entropy spots are only convected by the flow (as in the downstream duct of the EWG), where the entropy wave seems to be attenuated (as described by the studies conducted by [Morgans et al. 2013](#) and [Giusti et al. 2016](#)). To visualise the deformation of the entropy fronts, the norm of the temperature gradient is computed. In [Fig. 5.27](#), the numerical simulations of the two energy deposition models are compared. The block deposition simulation is showed in the upper half and the delayed deposition in the lower half of each instant. The field represented in this figure is the norm of the gradient of the temperature  $T$  minus the mean temperature of the baseline flow  $T_0$  normalized by

the mean temperature of the baseline flow  $\frac{\|\nabla(T-\bar{T}_0)\|}{\bar{T}_0}$ . This variable allows tracking the position and form of the entropy front generated by each energy deposition model. In the first instant ( $t = 0.105$  s) represented in this figure, the entropy spot is located in the upstream duct. The block deposition model front is in advance by almost 40 mm (length of the heating device). Steep gradients of temperature are formed near the wall due to the local energy deposition and the flow boundary layers. At the second instant ( $t = 0.115$  s), the entropy front arrives inside the nozzle diffuser and its front shape is already completely distorted by the jet and nozzle geometry. In the last instant ( $t = 0.145$  s), the front has reached the outlet duct and a "stationary state" has been reached in the upstream duct. At this stage, the entropy front has been distorted by the mean flow, where different authors explain that the entropy planar mode is scattered into higher modes affecting the production of entropy noise. The 2D analytical model proposed by [Zheng et al. \(2015\)](#), predicts the impact on indirect noise of the entropy front distortion through a nozzle. The model proposed by [Leyko et al. \(2010\)](#), [Duran and Moreau \(2012\)](#), [Livebardon et al. \(2016\)](#) and [Bauerheim et al. \(2016\)](#), introduces an attenuation function to describe this distortion and the conversion of the entropy plane wave into higher modes are examples of this effect.

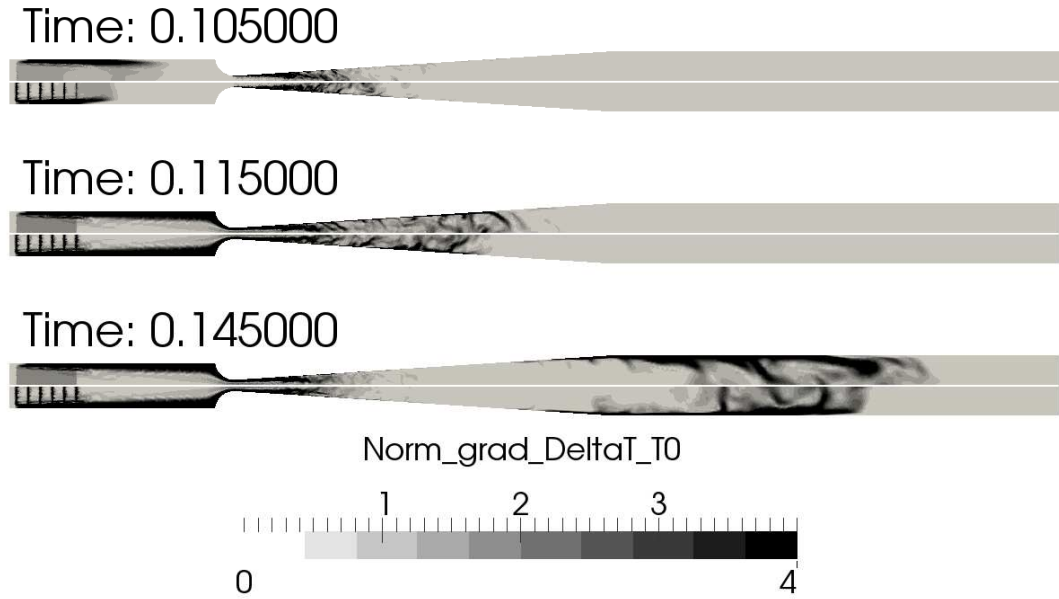


**Figure 5.27** Norm of the temperature gradient of the forced flow divided by the mean temperature of the non forced flow ( $\|\nabla(T - \bar{T}_0)\|/\bar{T}_0$ ). Only a part of the EWG geometry is represented ( $x \in [-0.15 : 0.5]$ ).

Instantaneous fields shown in [Fig. 5.27](#) are important to visualise the location of the entropy gradients and therefore, according to [Morgans et al. \(2013\)](#) and [Giusti et al.](#)

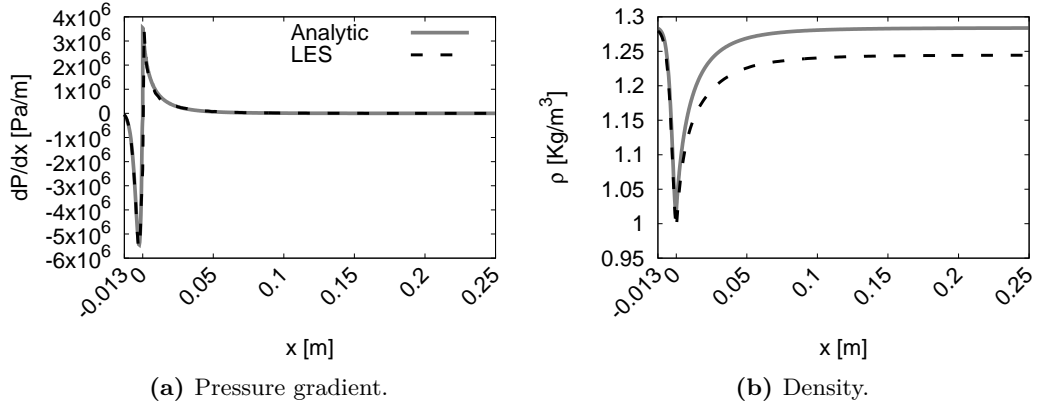


(2016), where the entropy wave is more attenuated. However, it remains only a qualitative information of the problem. In order to quantify the amount of remaining entropy, another parameter must be found to better represent the entropy attenuation phenomena. At the beginning of this numerical study, two definitions of planar average (integration within a plane normalized by the section of the plane) of the temperature have been introduced: the mean temperature  $T_{mean}$  (cf. Eq. (5.6)), which is the temperature accessible by the experimental measurements, and the bulk temperature  $T_{bulk}$  (cf. Eq. (5.9)), introduced to estimate the amount of energy needed to reach the temperature fluctuation measured in the experiment. One can show that the bulk temperature is energy conservative by construction (integration of the energy balance, Eq. (5.8)), and should be used to compare the 1D theory to the 3D simulation. Therefore, the bulk temperature field is computed for the two entropy forced simulations (block and delayed deposition representations of the heating device) to construct the dimensionless temperature 1D field  $T_{dimless}(x) = \frac{(T_{bulk}(x) - \bar{T}_{0,bulk}(x))}{\bar{T}_{0,bulk}(x)}$ , where  $\bar{T}_{0,bulk}(x)$  is the time-averaged bulk temperature of the baseline flow. Both LES are compared with the resolution of the quasi-1D advection of a hot spot generated by an energy source term  $\dot{Q}$  with the properties of the block deposition model. For this specific 1D problem, the advection equation is used to transport the temperature, for which the temperature fluctuation and the transport in the nozzle are modelled by source terms:  $\dot{Q}$  introduces the temperature fluctuation and  $u \frac{\partial p}{\partial x}$  the transport inside the nozzle, leading to the expression:

$$\begin{cases} \frac{\partial T(t,x)}{\partial t} + u(x) \frac{\partial T(t,x)}{\partial x} = \frac{1}{\rho(x)c_p} \left[ u(x) \frac{\partial p(x)}{\partial x} + \dot{Q}(t,x) \right] \\ T(t=0, x) = T(x) \end{cases} \quad (5.12)$$

where  $u(x)$ ,  $\rho(x)$ ,  $T(0, x)$  and  $\frac{\partial p(x)}{\partial x}$  are extracted from the isentropic mean flow computed in §5.1. Note that Eq. (5.12) is a simplified form of the energy conservation equation (cf. Eq. (5.7)) assuming an adiabatic inviscid flow. This equation satisfies the conservation of the entropy fluctuations through the nozzle, which is the assumption done in the analytical model of Duran and Moreau (2013a) (cf. Eqs. (2.25c) and (2.30c)) for the entropy perturbations. The pressure gradient  $\frac{\partial p(x)}{\partial x}$  and the density  $\rho$  fields issued from the isentropic calculation are compared with the numerical simulation in Fig. 5.28. Good agreement is found for the pressure gradient between the analytical model and the simulation. The density is however overestimated by the isentropic theory in the nozzle diffuser. This is due to the pressure loss neglected (inviscid flow) by the isentropic theory. Velocity, temperature and pressure profiles have been shown in the analysis of the baseline flow in Fig. 5.7. To respect the perfect gas law and keep the velocity and temperature constant, an increase of the pressure is compensated by an increase of density.

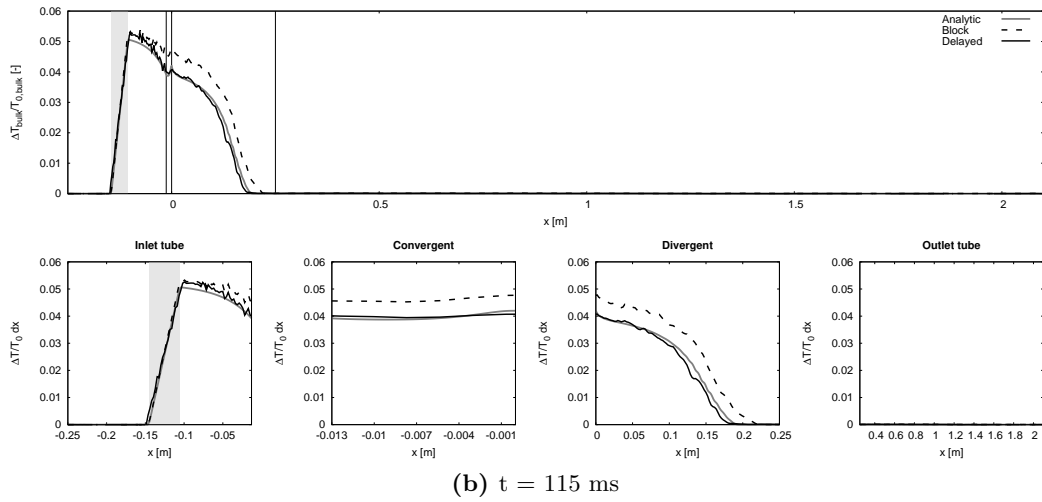
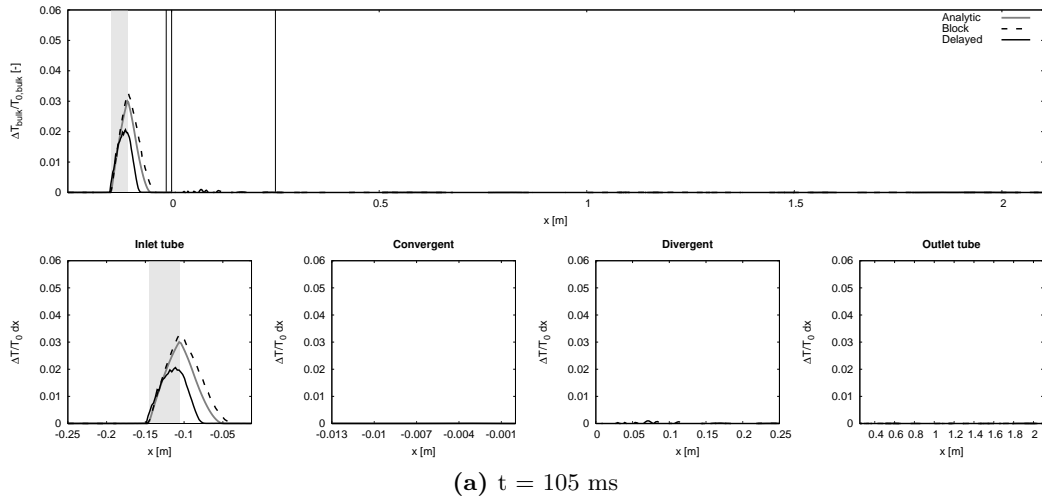
Figure 5.29 shows  $T_{dimless}$  fields computed from Eq. (5.12) and extracted from the numerical simulations. The position of the heating device is represented by the shaded region, whereas the vertical lines represent the separation between the different components of the geometry: inlet duct, convergent and diffuser of the nozzle, and outlet duct.

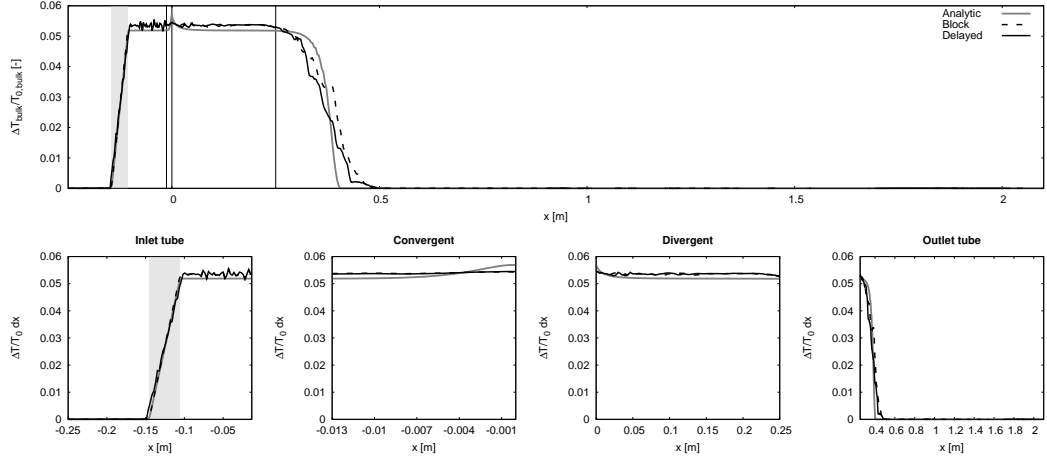


**Figure 5.28** Comparison of the isentropic mean flow and the bulk quantities computed from the time averaged baseline flow LES.

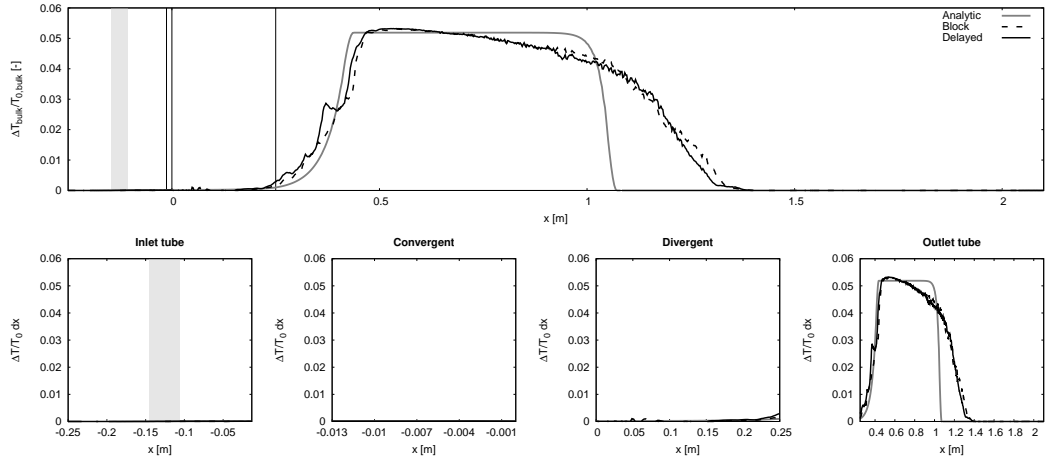
Each sub-figure (a, b, c, d and e) shows a different physical time and is divided in two parts: the overall evolution of  $T_{dimless}$  along the EWG configuration (upper part), and a zoom over each element of the nozzle (lower part). In Fig. 5.29a, only 5 ms elapsed since the energy deposition started. The analytical convection of the entropy spot proposed by Eq. (5.12) correctly predicts the rise and decay of the temperature through the heating device region compared with the LES block deposition model. However, the analytical convection of temperature spot is seen to differ from the LES using the block deposition model, where the spot seems to be convected with a smaller velocity. The delayed model takes more time to reach the heating device zone as shown by Fig. 5.27. In Fig. 5.29b, energy has been deposited during 15 ms and the entropy front is located inside the nozzle. At this point, the mean flow accelerates the temperature front along the centreline of the nozzle (as showed by Zheng et al. 2015). This effect should be taken into account by the definition of the bulk temperature since it is weighted by the velocity. The analytical model predicts a smaller maximum temperature fluctuation and a shorter distance is travelled by the front (the temperature front moves slowly in the divergent compared with the LES and no temperature diffusion is present in the analytical model). The delayed model follows the same shape as the block model but with a time delay. In Fig. 5.29c, the entropy leading front has reached the outlet duct and a stationary state has been reached in the nozzle and the upstream duct. At this point, the hot spot from LES has suffered from dispersion arising from the mean velocity profile as explained by Morgans et al. (2013), Giusti et al. (2016) and Hosseinalipour et al. (2017). In these studies, DNS and LES simulations were carried out to study the dissipation and dispersion of an entropy fluctuation along a fully-developed turbulent flow. Furthermore, the attenuation of the entropy spot has also been studied by Leyko et al. (2010), Duran and Moreau (2012), Livebardon et al. (2016) and Bauerheim et al. (2016) in the framework of turbine configurations. All these works arrived to the conclusion that the entropy wave is attenuated mostly by shear dispersion generated by the

velocity profile. Up to the divergent, the numerical simulations and the analytical model show the same behaviour: the entropy wave seems to be convected without dissipation through the nozzle, even if the leading entropy front has been deformed by the flow. Afterwards, the shape of the hot spot given by the analytical convection model is not attenuated and remains unchanged, while the shape of the hot spot in the numerical simulations is dispersed. In Fig. 5.29d the energy deposition is finished and the hot slug has traversed the nozzle entirely. At this point, the leading front of the hot slugs from the simulations have been deformed (dispersed and attenuated by the mean flow) and both energy deposition models follow the same shape. Finally, from Fig. 5.29d to Fig. 5.29e, the entropy spot has only been convected through a straight circular duct, where it suffers from bigger deformations and attenuation than at its passage through the nozzle.

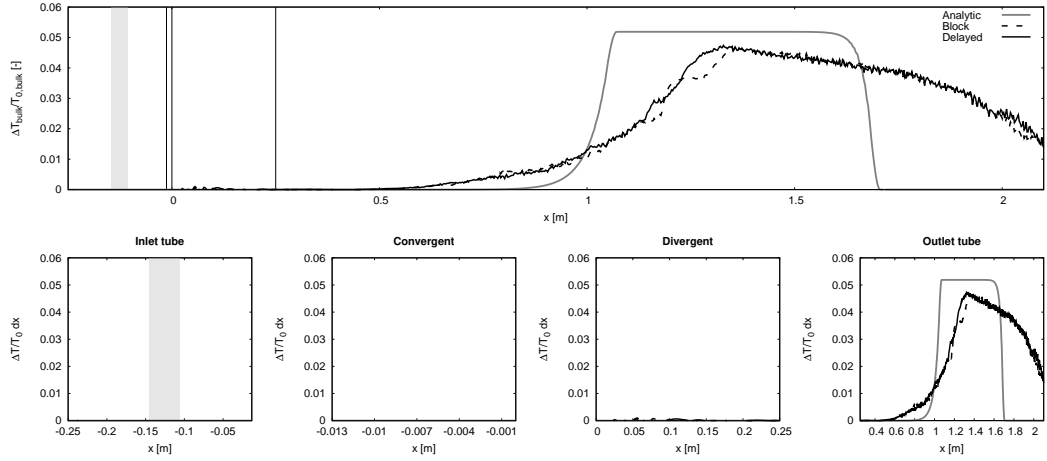




(c)  $t = 145$  ms



(d)  $t = 250$  ms



(e)  $t = 350$  ms

**Figure 5.29** Azimuthal average of the dimensionless temperature  $T_{dimless} = (T_{bulk} - T_{0,bulk})/T_{0,bulk}$ . Shaded region: Heating Device location. Vertical lines: separation between the inlet duct, the convergent, the diffuser and the outlet duct.

In order to verify if the entropy fluctuations only suffer from dispersion and not dissipation (as explained by [Morgans et al. 2013](#) and [Giusti et al. 2016](#) in the framework of constant section turbulent channels flows) through the nozzle, profiles of  $T_{dimless}$  are extracted at different axial locations of the domain to look at the temporal evolution of the temperature fluctuations. [Figure 5.30](#) shows the evolution of  $T_{dimless}$  at the inlet and the outlet of the nozzle, and at  $x = 0.5$  m and  $x = 1$  m from the nozzle throat for the two LES and the analytical temperature convection model. It appears that the shape of the temperature fluctuation is conserved through the nozzle and it is only in the downstream duct where its shape is distorted and attenuated. The entropy hot slug needs almost one meter for its amplitude to be decreased by the effects of the mean flow. It is important to remember that the temperature fluctuation generated by the heating device is composed of almost only very low frequencies (cf. [Fig. 4.13](#)) and according to [Giusti et al. \(2016\)](#), the higher the frequency is, the higher the dispersion of the entropy perturbation is. However, [Giusti et al.](#)'s study was carried out in the framework of a constant section duct. In the present simulations, additional 3D effects are added with the presence of the nozzle. In order to estimate the dissipation of the entropy wave through the nozzle, the temporal relative integral (to the vibrometer position) of each extracted position is computed and showed in [Fig. 5.31](#), which help us conclude that the entropy fluctuation is only convected through the nozzle without dissipation.

### 5.2.3 Conclusion

In this subsection, the subsonic operating point of the EWG experiment (described by [Bake et al. \(2009\)](#)) has been computed numerically by LES. Particular attention has been taken to the modelling of the heating device, for which a model derived from [Leyko et al. \(2011\)](#) has been extended to take into account the experimental ignition sequence and geometry. Based on the analytical study of the EWG subsonic test case carried in [§4.4](#), it has been chosen to fix the inlet acoustic reflection coefficient to be fully reflective (most physical choice) for the range of frequencies studied to have a comparison point between the analytical theory and the numerical simulations.

Two energy deposition shapes have been studied using the model proposed in [§5.2.1](#): the one used by [Leyko et al. \(2011\)](#), and the delayed deposition proposed in this work. From the comparison between these two energy depositions, it has been found that it is necessary to take into account the time delay between the activation of the heating modules (as in the experiment) to retrieve the right time delay in the temperature signal measured at the vibrometer and pressure signals at the microphones. Furthermore, pressure signal extracted from the simulation at the fourth microphone using the delayed ignition model clearly reproduces well the experimental signal (even if the inlet acoustic impedance is not perfectly known). To complement previous findings, the temperature fluctuation generated by the delayed ignition model has been introduced in another simulation to estimate the contribution of indirect noise only. Analysis of the results allows to determine that the pressure fluctuations produced by the acceleration of the hot slug express almost entirely into indirect noise.

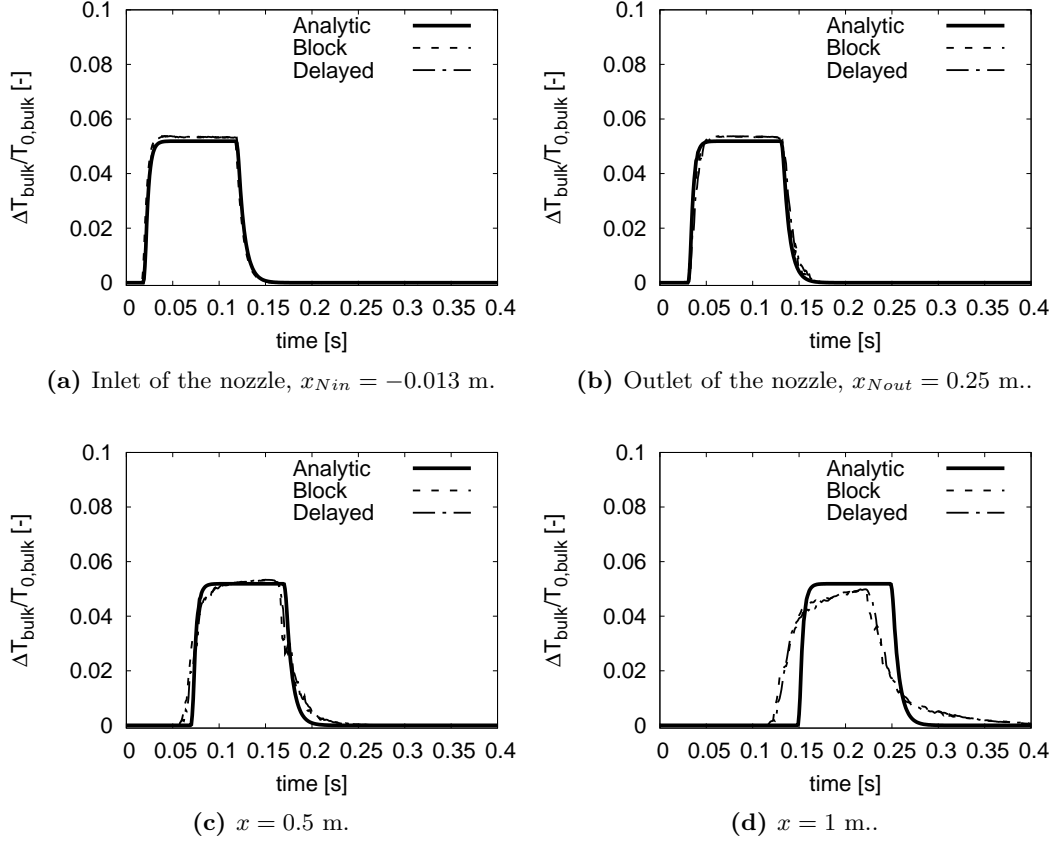


**Figure 5.30** Azimuthal average of the dimensionless bulk temperature  $T_{dimless} = (T_{bulk} - T_{0,bulk})/T_{0,bulk}$  at the different positions of the nozzle against time.

Finally, the convection of the hot spot has been studied and compared with a quasi-1D convection solution of a hot spot. To do so, the energy conservation equation has been reduced to a 1D advection equation with two source terms and has been used to transport the temperature through the nozzle. The source terms in this 1D advection equation take into account the convection in the nozzle and the introduction of the temperature fluctuation. This methodology allows to evaluate how the assumption of entropy conservation through the nozzle done in the analytical theory of [Duran and Moreau \(2013a\)](#) is valid. First, the convection of the entropy spot using a 1D advection equation has been validated computing the one dimensional field of the temperature fluctuations at different instants and comparing it to the numerical simulations. As expected by the analytical 1D convection of the entropy spot, the amplitude and shape of the entropy spot remains constant when it is convected through the constant section ducts, while the amplitude of the entropy spot decreases and its shape is dispersed in the numerical simulations. However, attenuation and distortion of the entropy spot in the simulation appears to be negligible through the nozzle and become important only when

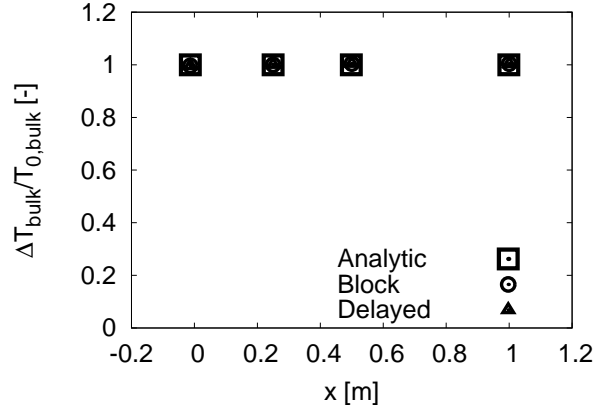


**Figure 5.31** Relative magnitude of  $T_{dimless}$  (compared to its value taken at the vibrometer position) as it is convected through the EWG nozzle.

convected over a long distance (about one metre): i.e. in the downstream duct. It is also noted that since in this experiment, the dominant frequencies of the entropy forcing are very low (higher frequencies are hidden by the importance of the low frequencies), the effects of dispersion due to the mean flow are weak.

Finally, the LES has shown its capability to reproduce the experimental results with success, while the analytical analysis carried in §4 did not. Therefore, the next sections are dedicated to the evaluation of the response of the EWG nozzle to incident acoustic and entropy disturbances. This will allow to understand the phenomenology missing in the analytical modelling, considering first a non-viscous flow to first study the effects of the nozzle geometry, and then the effect of viscosity in the determination of the nozzle transfer functions.

### 5.3 Evaluation of the nozzle transfer functions by CFD

The numerical simulation performed in the former section has shown results in good agreement with the experimental data, even though the exact experimental inlet impedance is unknown. Despite this shortcoming, identified also through the use of analytical models, the same analytical methodology does not show close agreement with the experimental or LES results. Indeed, the analytical evaluation of the subsonic test case underestimates by half the pressure fluctuations generated by the acceleration of the hot slug. One key in the analytic approach is the access or model of the nozzle transfer functions, which can be flawed and yield improper predictions. To further improve on this specific aspect, the subsonic nozzle transfer functions are computed in a full 360° compressible simulation on the shorter M2 mesh with the LES solver AVBP. To do so, a polychromatic harmonic forcing (sum of multiple frequencies) is introduced through the boundary conditions. Such a forcing consists in the introduction of acoustic or entropy disturbances using the NSCBC formalism described in [Appendix A](#). Afterwards, frequency analysis is done to separate each harmonic from the overall polychromatic fields and study the response of the nozzle to the individual ingoing disturbances.

First and to validate the proposed methodology, the nozzle transfer functions are computed using the Euler equations only. This validation step allows to compare the inviscid nozzle transfer functions to the quasi-1D analytical transfer functions obtained by the methodology of [Duran and Moreau \(2013a\)](#). In the case of the numerical Euler simulation, the flow is expected to be axisymmetric (2D), which is different from the quasi-1D assumption considered in the analytical approach. Based on this prediction, the influence of a 2D flow on the numerically computed transfer functions is evaluated. Once the methodology is validated, it is used to compute the acoustic response of the nozzle using the Navier-Stokes LES equations to evaluate the viscous effects on the different components of such transfer functions.

This section is therefore divided in different parts: [§5.3.1](#) describes how the multi-harmonic forced signal is constructed. [§5.3.2](#) discusses the validation of the acoustic/entropy response of the subsonic nozzle using Euler equations before applying the same methodology to compute the nozzle transfer functions with LES in [§5.3.3](#).

#### 5.3.1 The forcing signal

In order to study the nozzle response to different disturbances, a harmonic regime is considered. Assuming full linearity of the system, a polychromatic forcing allows reducing the computational cost of the simulations by running only one simulation with the sum of harmonics considered. The forcing signal is composed of a sum of sinus normalized by the maximum absolute value of the sum (this normalization allows to have a signal bounded between -1 and 1),  $f(t) = \frac{\sum_k^{N_{harm}} \sin(2\pi k f_0 t)}{\max \left| \sum_k^{N_{harm}} \sin(2\pi k f_0 t) \right|}$  as done by



Leyko et al. (2014). The fundamental frequency  $f_0$  in this study is equal to 10 Hz and 24 harmonics are employed, resulting in a signal composed of the sum of 25 sinus and a range of frequencies going from 10 to 250 by steps of 10 Hz. The choice of the frequency range is justified by the fact that the most energetic frequencies in the experiment are small, and beyond 100 Hz their contribution is negligible compared with that of the lower frequencies (as showed in Fig. 4.13).

The formulation proposed in Leyko et al. (2014) and used for the forcing  $f(t)$  has a main drawback: a peak that is 20 times larger than the individual harmonics. This will limit the amplitude  $\mathcal{A}$  of the forcing to remain in the linear acoustic regime. To solve this problem, a random phase  $\varphi_k$  is added to each harmonic (methodology already used by Duran (2013)), yielding the new formulation:

$$f_r(t) = \frac{\sum_k^{N_{harm}} \sin(2\pi k f_0 t + \varphi_k)}{\max \left| \sum_k^{N_{harm}} \sin(2\pi k f_0 t + \varphi_k) \right|}, \quad (5.13)$$

Both forcing formulations are compared in Fig. 5.32. As shown by Fig. 5.32a, both forcing signals are bounded between -1 and 1, but the oscillations of  $f_r(t)$  are more homogeneous than the ones in  $f(t)$ . Figure 5.32b shows the modulus of the DFT of both signals, where the amplitude of each harmonic of  $f_r(t)$  is 4 times greater than  $f(t)$ . This result shows that the random phase introduced in the formulation of  $f_r(t)$  allows higher amplitudes of each harmonic, obtaining a better signal-to-noise ratio and a higher limit before reaching a non linear regime induced by the initially proposed signal. For these reasons, in the following only  $f_r(t)$  is used as forcing for the acoustic and entropy forced simulations.

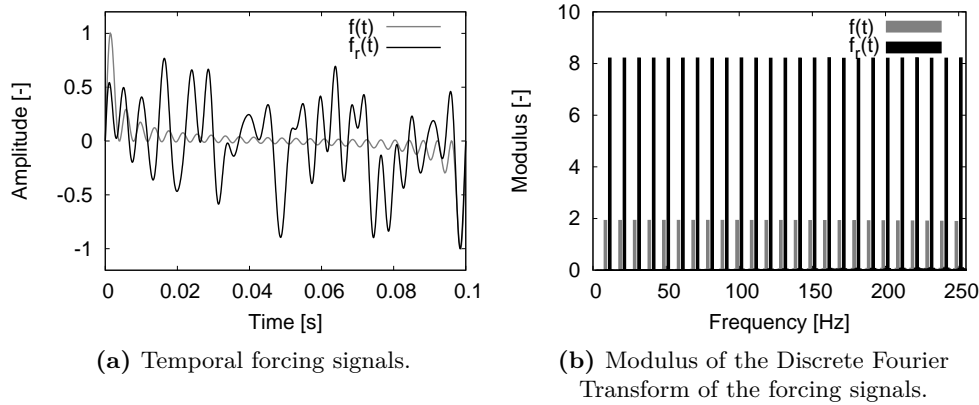


**Figure 5.32** Forcing signal with and without phase shift for each harmonic.

### 5.3.2 Euler forced simulations

The forcing methodology being introduced (cf. boundary conditions forcing is detailed in [Appendix A](#) and forcing signal in [§5.3.1](#)), acoustic and entropy disturbances are forced in the EWG configuration. In order to validate the methodology to compute the nozzle transfer functions (separation of each harmonic from the forced field, computing plane waves and the nozzle transfer functions), the acoustic and entropy disturbances are introduced in a reduced domain including only the nozzle of the EWG and small duct lengths. [Figure 5.33](#) shows a sketch of the reduced domain of the EWG used to compute the nozzle transfer functions. Note that the upstream and downstream ducts are used to study the convection of waves in circular ducts (characteristic acoustic and entropy waves defined in [Eq. \(2.7\)](#)).

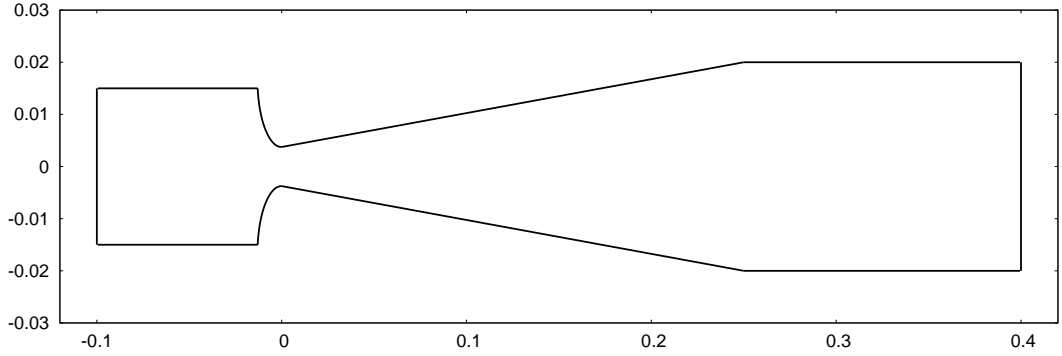


**Figure 5.33** Sketch of the reduced domain of the EWG used to compute the nozzle transfer functions.

The acoustic response of the nozzle to ingoing disturbances is studied in this section. The best practice is to impose non-reflecting boundary conditions to avoid the pollution of the signals by reflections. Nevertheless, a fully non-reflective boundary condition in the NSCBC formalism (in its relaxed form, it is equivalent to imposing  $K = 0$ ) does not ensure that the mean value at the boundary condition remains equal to the target value. To avoid this drift from the target value, a relaxation coefficient  $K$  should be different from zero, which results in a partially reflecting boundary condition. To avoid as much as possible the reflections, multiple values of  $K$  have been tested to be the less reflective as possible while maintaining the target values, obtaining  $K = 20 \text{ s}^{-1}$  as the better compromise. A direct consequence is that the boundary conditions of the domain are partially reflective and particular attention needs to be taken to separate the acoustic response of the nozzle from the overall acoustic waves polluted by reflections from the boundary conditions.

The characteristic element size of the numerical mesh for this study was based on the numerical dispersion and dissipation properties of AVBP schemes detailed in [Ap-](#)

pendix C. Indeed, it has been found that the limiting factor for the mesh construction is the entropy smallest wavelength. Therefore, a series of numerical test cases based on this wavelength have been carried out to ensure the capability of the AVBP numerical schemes to properly convect these entropy waves with minimal dispersion and dissipation by an induced inadequately designed mesh for a given numerical scheme (cf. Appendix C). Following these results, the mesh constructed for the nozzle test case has at least 20 points per identified wavelength, the rest of the numerical set-up being summarized in Tab. 5.6.

Boundary conditions	
Inlet	NSCBC velocity and static temperature, $K_{in} = 20 \text{ s}^{-1}$ .
Outlet	NSCBC Static pressure, $K_{out} = 20 \text{ s}^{-1}$ .
Walls	Slip adiabatic
Numerical parameters	
Governing equations	Euler
Numerical scheme	TTGC
LES model	none
CFL	0.7
Artificial viscosity sensor	Jameson et al.
Artificial viscosity coefficients <sup>1</sup>	$smu_2 = 0$ and $smu_4 = 0.007$

**Table 5.6** Numerical set-up for the Euler computation of the nozzle transfer functions.

To study the nozzle transfer functions, an unperturbed mean flow must first be computed. The bulk quantities of the computed mean flow are compared with the isentropic baseline flow described in §5.1 and showed in Fig. 5.34. A perfect match has been obtained between both numerical Euler simulation and isentropic theory. This result allows to use the operating point obtained in the simulation to be forced by acoustic and entropy disturbances and make a fair comparison to the analytical quasi-1D model of Duran and Moreau (2013a).

In the following, harmonic acoustic and entropy disturbances are introduced into the EWG reduced domain depicted in Fig. 5.33 to study the acoustic response of the nozzle to ingoing acoustic and entropy disturbances. First, in §5.3.2.1, entropy harmonic disturbances are introduced through the inlet boundary condition of the reduced EWG domain to study the generation of indirect noise through the nozzle. Then, in §5.3.2.2 and §5.3.2.3, harmonic acoustic waves are introduced through the inlet and outlet boundary conditions to analyse the acoustic response of the nozzle to ingoing acoustic disturbances. Finally in §5.3.2.4, the nozzle transfer functions are computed and compared with the analytical transfer functions computed with the model of Duran and Moreau (2013a).

<sup>1</sup>Minimal value found to have a stable simulation (cf. Appendix C).

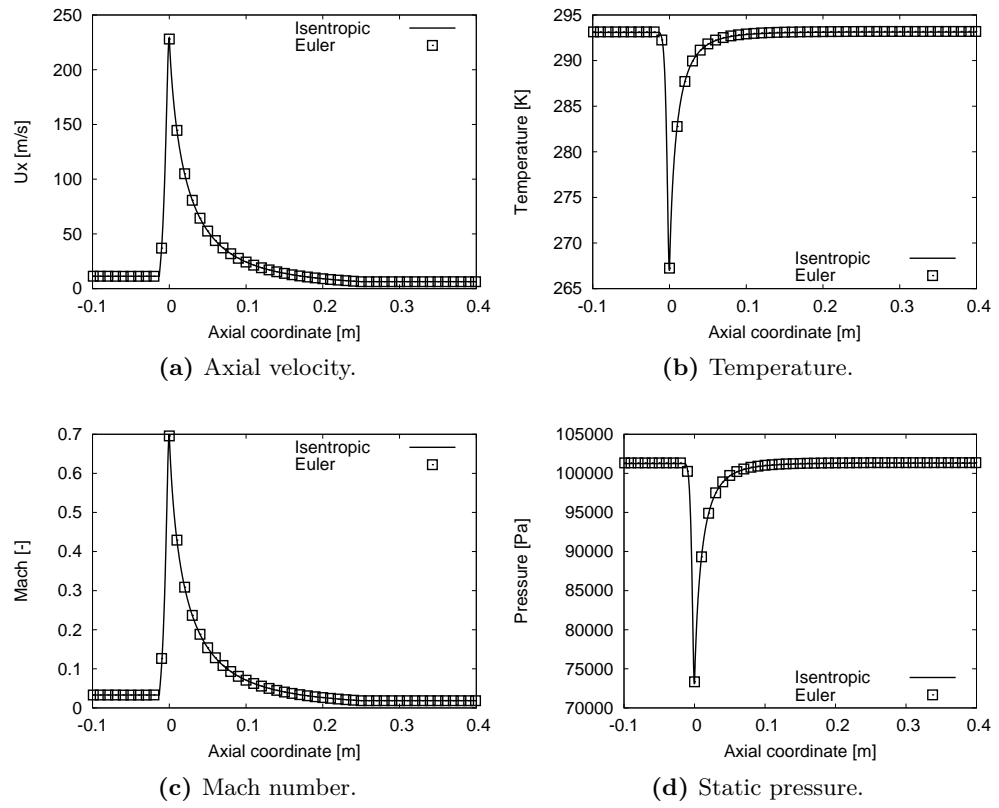


**Figure 5.34** Isentropic quasi-1D variables compared with bulk quantities extracted from the Euler numerical simulation.

### 5.3.2.1 Entropy forced simulation

The methodology to introduce an entropy disturbance through the inlet boundary condition is detailed in [Appendix A](#). It is emphasized here that the system of waves generated by such a forcing is more complicated than the one created by a sole acoustic excitation. Indeed, entropy-acoustic interactions are coupled to acoustic-acoustic interactions. The acoustic and entropy waves in such a system can be illustrated by [Fig. 5.35](#), in which acoustic waves produced by entropy-acoustic interactions are denoted by the subscript *ea*. In the absence of reflections, only the entropy waves and the entropy-acoustic generated acoustic waves remain. The reflected acoustic waves generate four supplementary acoustic waves (two transmitted and two reflected waves) due to acoustic-acoustic interactions with the nozzle.

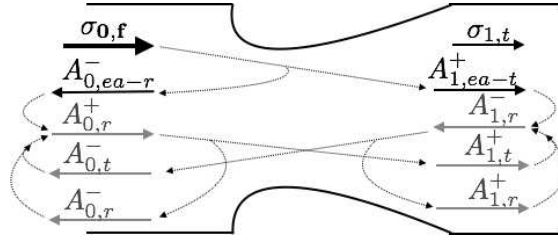


**Figure 5.35** Schematic view of entropy and acoustic waves formed by an entropy forcing with non-reflective boundary conditions.

In the following simulation, a polychromatic entropy forcing of 15 K amplitude (5% of the baseline flow temperature in the upstream duct) is introduced at the EWG's inlet. To ensure that the NSCBC entropy forcing methodology described in [Appendix A](#) works correctly, the temperature fluctuation extracted from the inlet boundary condition is compared with the polychromatic forcing signal in [Fig. 5.36](#). Unlike the acoustic waves, the entropy wave is not subject to reflections and therefore the temperature issued by the forcing should be equal to the temperature fluctuation extracted at the boundary condition and hence seen by the code, as confirmed by the superposition of both signals in [Fig. 5.36](#).

Since entropy waves are transported by the mean flow, they also undergo deformations issued by any change of the velocity field (as highlighted by [Zheng et al. 2015](#) within the framework of nozzle flows and by [Leyko et al. 2010](#), [Duran and Moreau 2012](#) and [Bauerheim et al. 2016](#) in the context of turbine rows). As a consequence, the entropy wave cannot be considered to remain a plane wave along the nozzle. To illustrate this, the entropy waves corresponding to each harmonic of the forcing signal are computed with a DFT (cf. [Appendix B](#)) using the 3D fields of the simulation. An instantaneous solution is saved every 0.5 ms during 0.1 s of simulation, obtaining a total of 200 solutions. The frequency step of such a sampling is 10 Hz and the maximal resolved frequency is 1000

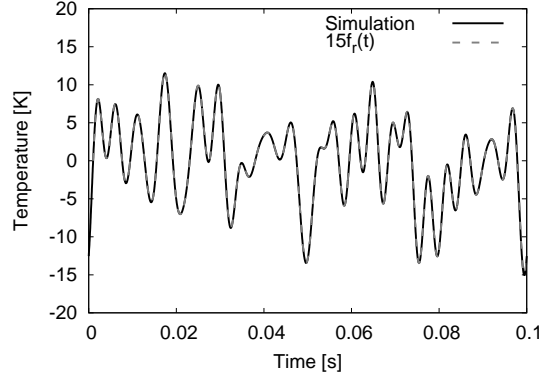


**Figure 5.36** Temperature fluctuation extracted from the numerical simulation compared with the forcing signal.

Hz (four points in the largest frequency of interest, that is 250 Hz). Note that, only the harmonics corresponding to the forced frequencies are kept (sum of 25 sinus composing the forced signal). Then, a plane normal to  $\vec{e}_z$  of the baseline flow is used to show the deformation of vertical particle-lines as they are convected by the flow through the configuration. Particle-lines and the real part of the entropy wave are compared and represented in Fig. 5.37. Very good agreement is found between the particle-lines and the real part of the entropy wave, showing that particle-lines are a very good indicator of the deformation of the entropy fronts and that for all frequencies. Figure 5.37 also shows that the entropy wave is strongly dispersed in the downstream duct for the high frequencies studied. Indeed, the curvature of the nozzle deforms the streamlines and a non-homogeneous velocity profile is established, which by shear dispersion attenuates the amplitude of the entropy plane waves (as already explained in the cylindrical test case with an imposed velocity profile in Appendix C).

To estimate the attenuation of the entropy waves, the entropy flux (cf. Huet 2017) is computed at different axial positions of the configuration:

$$W^s = \iint \rho u T c_p \|\sigma\|^2 dA. \quad (5.14)$$

Figure 5.38 shows the ratio of  $W^s$  between different axial positions of the domain (the inlet and outlet of the nozzle as well as the outlet of the domain) to the inlet value. In the inlet duct, the entropy flux is almost constant for all frequencies, the largest dissipation represents  $\approx 10\%$  of the inlet entropy plane wave for the largest frequency computed. In the nozzle, up to 100 Hz, at least 90% of the entropy flux is preserved, and decreases rapidly afterwards. Finally, in the downstream duct, only the very low frequencies reach the outlet. The highest frequencies being completely attenuated (as seen also in Fig. 5.37). This result shows that the strongest attenuation happens in the downstream duct. Indeed, as explained by Giusti et al. (2016) a smaller wavelength of the entropy perturbation (i.e. higher frequency) leads to stronger gradients, making

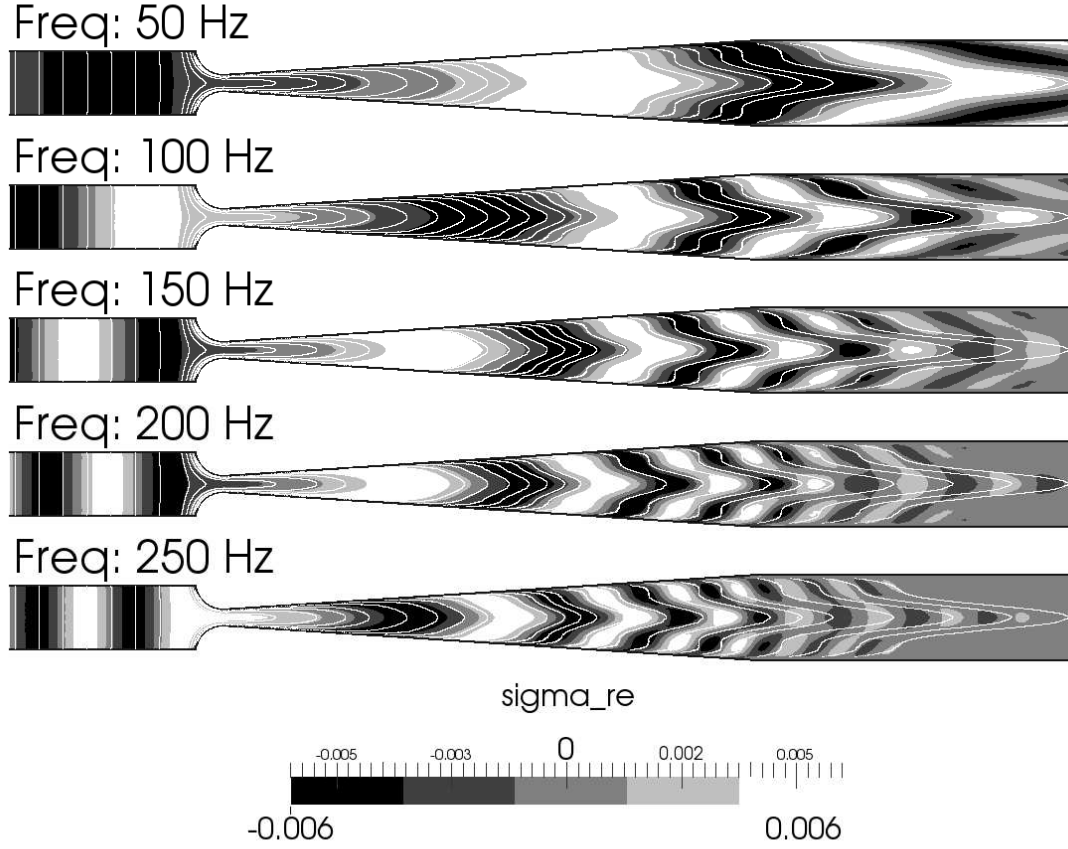


**Figure 5.37** Entropy wave phase compared with particle-lines traced from the inlet of the baseline flow.

the diffusion process faster. It is important to notice that in this section, the entropy wave is no longer submitted to the acceleration of the nozzle and therefore no more indirect noise is generated (the entropy wave is only convected by the flow). It is also worth noticing that even if the amplitude of the entropy plane wave is attenuated, it is only scattered spatially and no dissipation of the overall entropy wave is found (more information about the dissipation of the entropy wave can be found in [Appendix D](#)).

Finally, to compare the results from the simulation with the analytical method, a modal decomposition is done (more details about the modal decomposition can be found in [Appendix B](#)) and the entropy plane wave is plotted as a function of the axial coordinate in [Fig. 5.39](#). At the inlet of the configuration, all the waves are planar and introduced with the same amplitude. Afterwards, the entropy wave cannot remain planar due to the non-homogeneous acceleration of the flow produced by the nozzle and the entropy wave scatters into radial modes. This scattering of the planar mode energy produces a decay in the amplitude of the plane wave. The greater the frequency, the smaller the wavelength and the higher the attenuation of its amplitude is due to the sharper

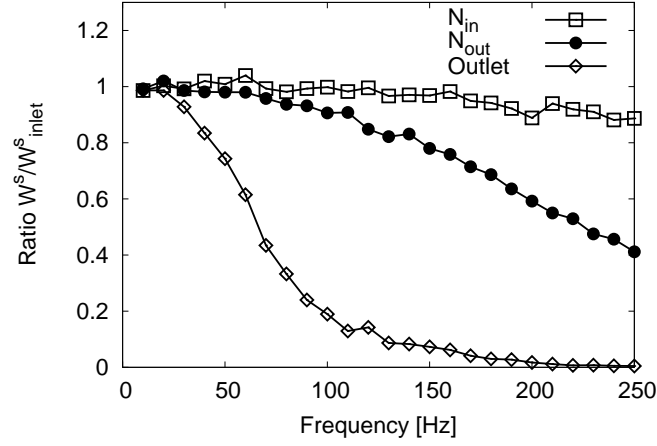


**Figure 5.38** Entropy flux ratio of different points (inlet and outlet of the nozzle and outlet of the domain) to the inlet of the domain.

gradients generated (cf. Fig. 5.37 and highlighted by Giusti et al. 2016). The attenuation of the plane entropy wave across the nozzle can be estimated analytically using only the mean flow as proposed by Leyko et al. (2010) (cf. Appendix C, Eq. (C.1b)). The ratio of the planar entropy wave through the nozzle can also be described through the entropy-entropy transmission coefficient:

$$T_{ee} = \frac{\sigma_1(x_{out})}{\sigma_0(x_{in})}. \quad (5.15)$$

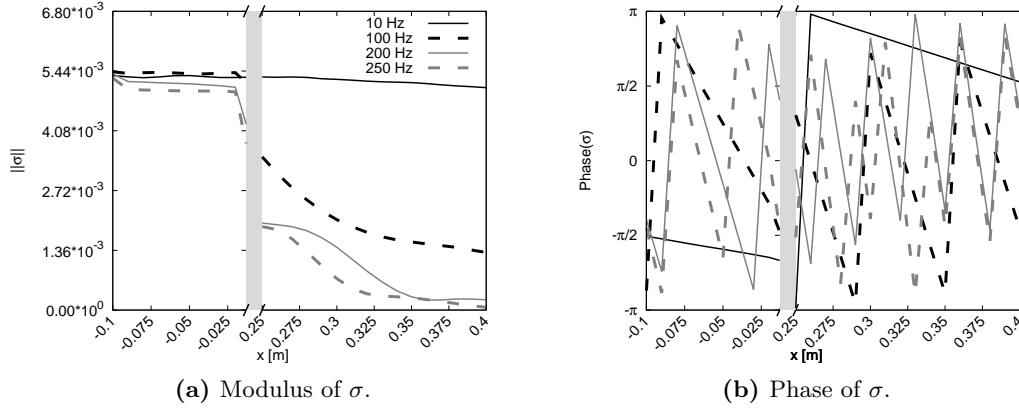


**Figure 5.39** Amplitude of the entropy plane wave  $\sigma$  in the upstream and downstream ducts of the EWG.

(Only harmonics 1, 10, 20 and 25 are presented).

It should be noticed that the attenuation of an entropy plane wave by models based only on the characteristics of the mean flow has also been addressed by Sattelmayer



(2003), Morgans et al. (2013) and Giusti et al. (2016). However, the attenuation expression of those models only deals with the convection of the entropy plane wave through a constant duct section. Models like the ones proposed by Leyko et al. (2010) and Zheng et al. (2015), which are based on the flow streamlines are capable of estimating the attenuation of the entropy wave through a nozzle or even multiple turbine stages (in the case of the model proposed by Leyko et al. (2010)). Figure 5.40 shows entropy-entropy transmission coefficient obtained in the simulation compared with the analytical invariants theory of Duran and Moreau (2013a) and the attenuation function of Leyko et al. (2010). The attenuation function based in the analytical solution of the convection of the entropy wave (cf. Leyko et al. 2010) has been computed in two cases: performing an azimuthal average of the mean flow to consider it axisymmetrical and using the full 3D mean flow. Both attenuation functions are very close to the numerical one. However, the attenuation functions computed using only the axisymmetrical flow hypothesis underestimates the attenuation of the entropy plane wave for some frequencies. This is due to the fact that the tangential velocity generated by the transverse pressure gradient (cf. radial equilibrium at the nozzle) has been neglected in the axisymmetrical flow hypothesis and clearly contributes to the attenuation of the entropy plane wave. Considering the full 3D field to compute the flow streamlines, a very good agreement between Leyko et al. (2010) attenuation function and the numerical simulation is found. Concerning the comparison with the analytical methodology of Duran and Moreau (2013a) for  $T_{ee}$ , the analytical method assumes a quasi-1D flow, where by definition, no radial or azimuthal velocity gradients can exist and no shear dispersion of the entropy wave can therefore be expected. This results in the conservation of the amplitude of the entropy plane wave through the nozzle. However, even if the amplitude of the plane entropy wave remains constant in the analytical model and cannot be compared with the numerical simulation, the convection velocity of each harmonic entropy wave (associated with the phase represented in Fig. 5.40b) is found to be in good agreement between the numerical simulation and the analytical model. Indeed, the bulk velocity of the flow is the convection velocity of the entropy wave, which has been verified to be the same between the numerical simulation and the isentropic relations that govern the mean flow associated to the analytical method (cf. Fig. 5.34).

Above results show that the entropy plane mode is attenuated as it is convected by the flow. However, Morgans et al. (2013), Giusti et al. (2016) and results obtained in Appendix D show that the entropy fluctuations are not dissipated but dispersed by the mean flow. To understand how the energy is distributed, a modal decomposition into azimuthal and radial modes (cf. Appendix B) is computed at the inlet and outlet planes of the nozzle. The amplitude of the planar and the first four radial modes (most energetic modes found by the modal decomposition) at the inlet and outlet of the nozzle are represented in Tables 5.7 and 5.8 respectively. Since the entropy wave at the inlet duct remains planar for almost the total length of the inlet duct (the velocity profile remains flat) as shown by Fig. 5.37, the modal decomposition at the inlet of the nozzle (cf. Tab. 5.7) is thus representative of the distortion of the entropy wave induced bending of

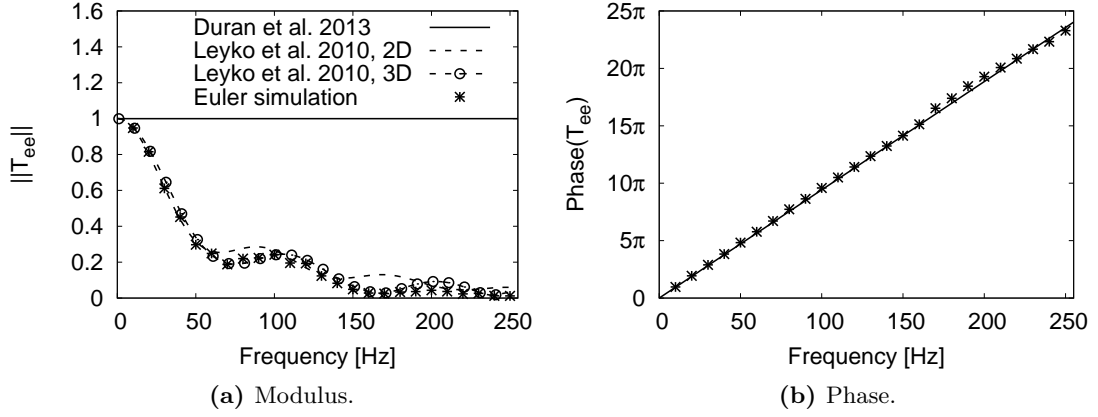


**Figure 5.40** Entropy-entropy transmission coefficient  $T_{ee}$ .

the streamlines at the convergent. Table 5.7 shows that almost all the energy is contained in the planar mode and the first two radial modes. At low frequencies, the planar mode dominates. For larger frequencies, the dominant mode becomes the first radial mode. The modal decomposition of the entropy wave at the outlet of the nozzle is represented in Tab. 5.8, where azimuthal modes are also found to be negligible compared to the planar and first four radial modes. At this point, the entropy wave has been distorted by the non-homogeneous mean flow produced by the nozzle. The planar mode is found to dominate only the very low frequencies and when the frequency increases, the order of the dominant mode increases as well.

Results from Table 5.8 are used to estimate the importance of each mode at the outlet of the nozzle when compared to the planar entropy mode introduced at the inlet using the definition of the entropy flux of Eq. (5.14) (as done in Fig. 5.38). The ratio of the entropy flux between nozzle outlet and inlet of the CFD domain is shown in Fig. 5.41. The planar mode is clearly not sufficient to represent the evolution of the entropy wave through the nozzle, as its amplitude decreases rapidly and higher modes gain in amplitude with the frequency. Few modes (for instance the planar mode and the first four radial modes) are however sufficient to describe the attenuation of the overall entropy wave. The attenuation of the entropy wave through the nozzle should be taken into account since the amount of indirect noise generated is directly related to the amplitude of the entropy wave. Clearly, based on this diagnostics, an analytical model as the one proposed by Zheng et al. (2015), where the radial deformation of the entropy wave is estimated using the mean flow, will be more effective to describe the convection of the entropy wave through a nozzle. It furthermore allows to consider this attenuation to compute the indirect generated noise.

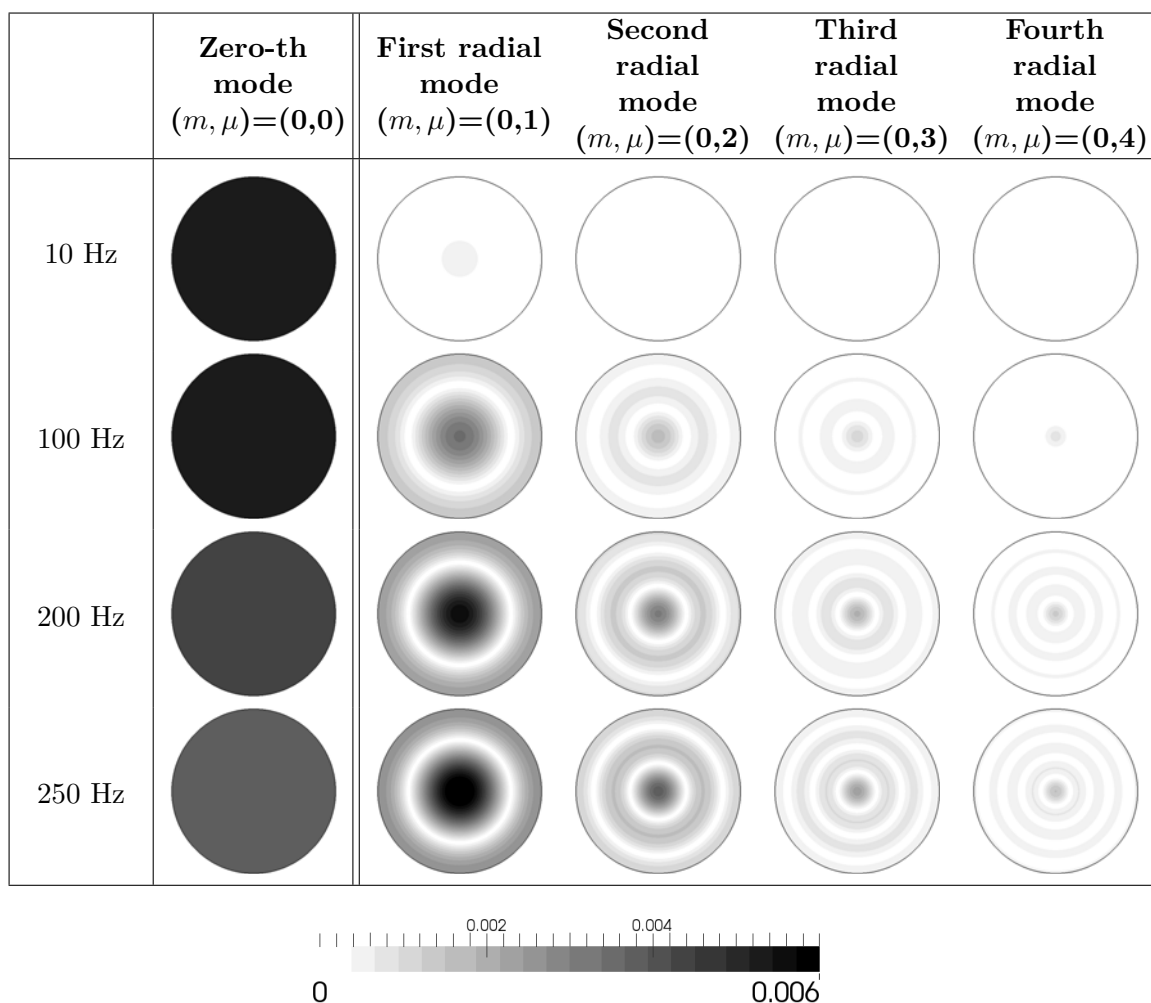


**Table 5.7** Modulus of the entropy wave extracted at the inlet plane of the nozzle ( $x_{N_{in}}$ ).

All the analysis made until now for the entropy forcing was concentrated solely on the entropy wave. Let's now study the acoustic waves generated when the entropy wave travels through the nozzle. Due to the huge difference between the flow and sound velocities in the upstream and downstream ducts, acoustic waves can be considered as planar (their propagation velocity is very close to the velocity of sound) and their propagation far from the nozzle can be described by a 1D advection equation. The progressive and retrograde acoustic plane waves,  $A^+$  and  $A^-$  respectively are computed using Eq. (2.7) and the DFT procedure described in the above paragraphs. It is important to notice that in the downstream duct, these definitions for the acoustic waves are not rigorously correct due to the vorticity waves generated by the radial entropy modes generated and accelerated through the nozzle (cf. [Duran and Morgans 2015](#) and [Emmanuelli et al. \(2017\)](#)). To separate the vorticity fluctuations from the acoustic ones, a characteristic

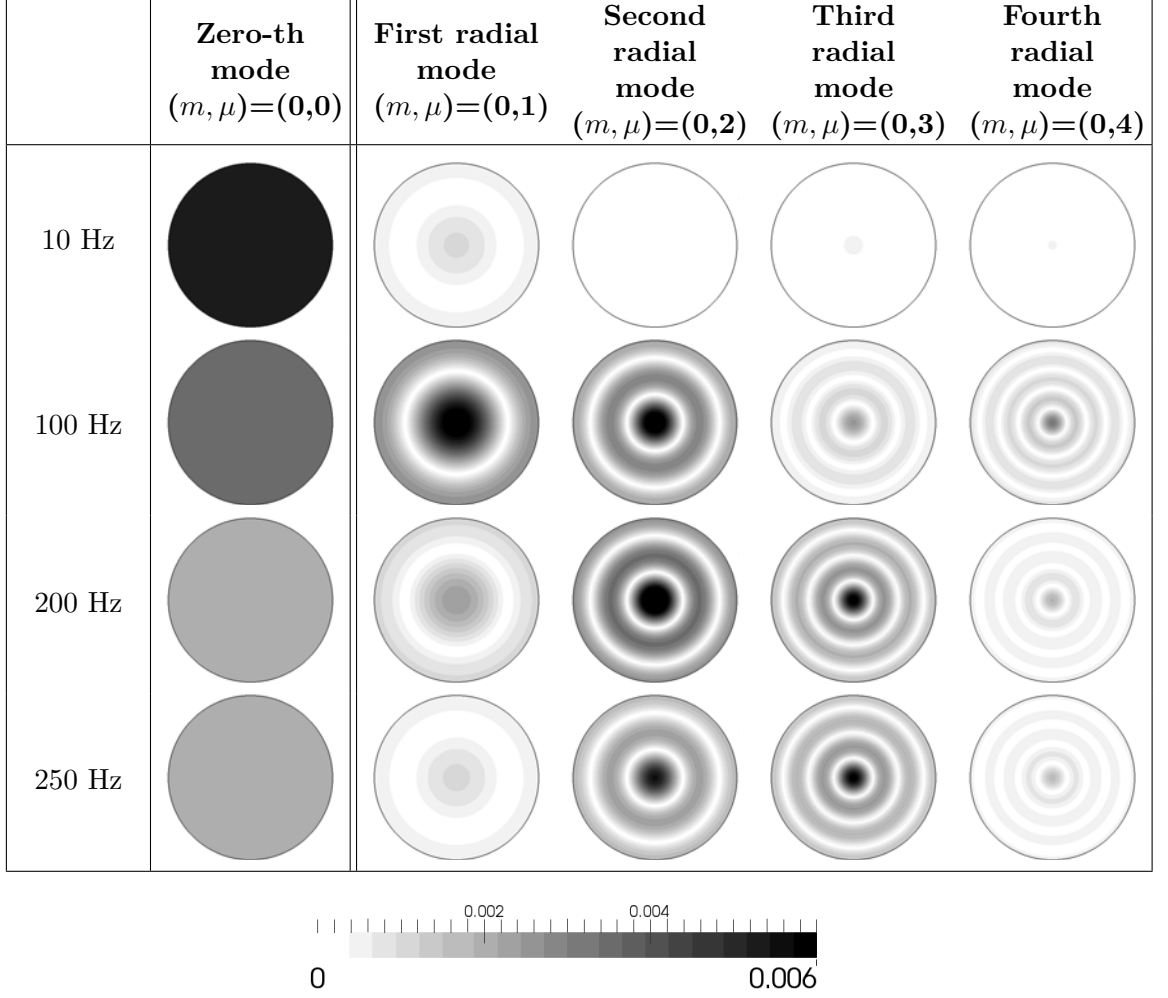


**Table 5.8** Modulus of the entropy wave extracted at the outlet plane of the nozzle ( $x_{N_{out}}$ ).

filtering (cf. [Kopitz et al. \(2005\)](#)) is applied in the downstream duct. [Figures 5.42](#) and [5.43](#) show the evolution of  $A^+$  and  $A^-$  acoustic waves respectively along the EWG upstream and downstream ducts. According to the distribution of acoustic and entropy waves shown in [Fig. 5.35](#), in the absence of an acoustic forcing, ingoing acoustic waves ( $A_0^+$  and  $A_1^-$ ) are reflections due to the non-reflective boundary conditions. Indeed, as shown by [Figs. 5.42](#) and [5.43](#),  $A_0^+$  and  $A_1^-$  have a small amplitude compared to the acoustic waves generated by the interactions with the nozzle (outgoing waves  $A_0^-$  and  $A_1^+$ ). These reflections can be confirmed computing the reflection coefficients of the boundary conditions using the low pass filter formulation of [Selle et al. \(2004\)](#) and comparing them to the reflection coefficient computed from the overall acoustic waves of the simulation. [Figures 5.44](#) and [5.45](#) confirm the good agreement between the theoretical reflection coefficient and the one computed with the overall acoustic waves, confirming that waves

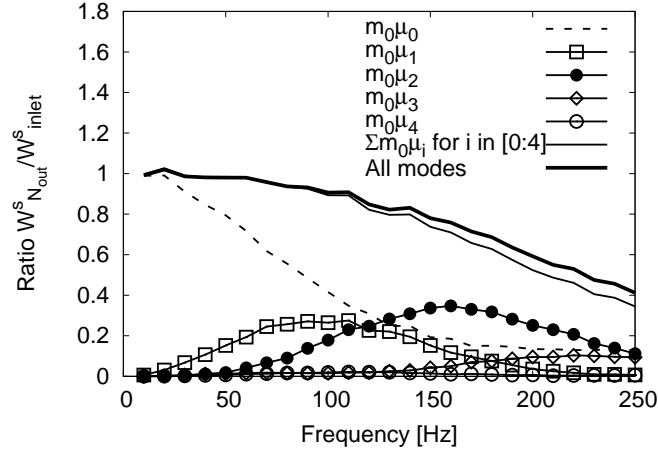


**Figure 5.41** Ratio of entropy fluxes between the outlet of the nozzle and the inlet of the CFD domain.

$A_0^+$  and  $A_1^-$  are effectively the result of reflections.

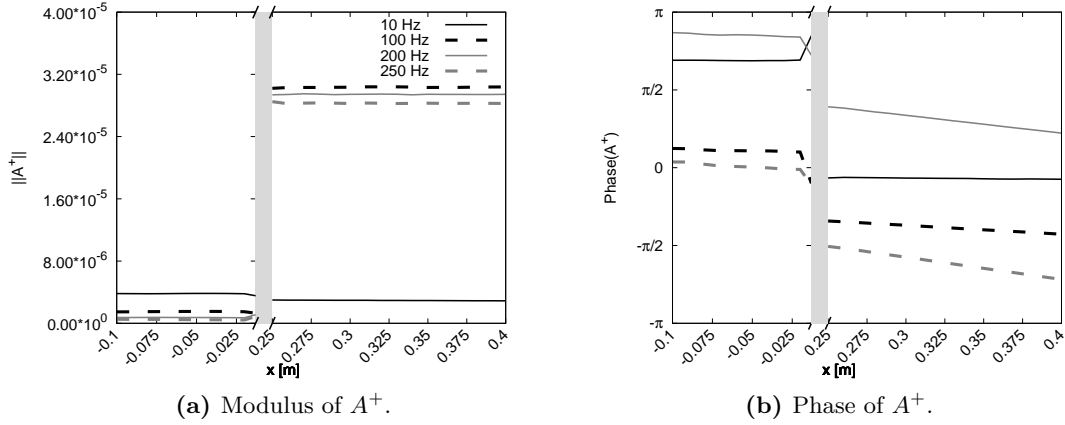


**Figure 5.42** Acoustic wave  $A^+$  in the upstream and downstream ducts of the nozzle. (Only harmonics 1, 10, 20 and 25 are presented).

To compute the entropy-acoustic transfer functions of the simulation and compare them to the analytical ones, a formalism to separate the generated acoustic waves from the entropy forcing (cf. Fig. 5.35) from the overall acoustic waves is however needed. To do this, the acoustic-acoustic transfer functions of the nozzle are needed and computed following the strategy described below.

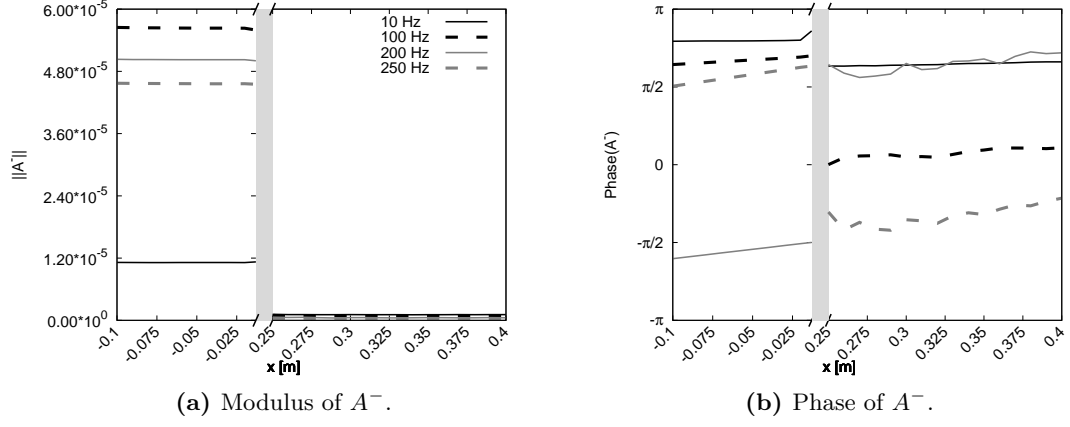


**Figure 5.43** Acoustic wave  $A^-$  in the upstream and downstream ducts of the nozzle. (Only harmonics 1, 10, 20 and 25 are presented).

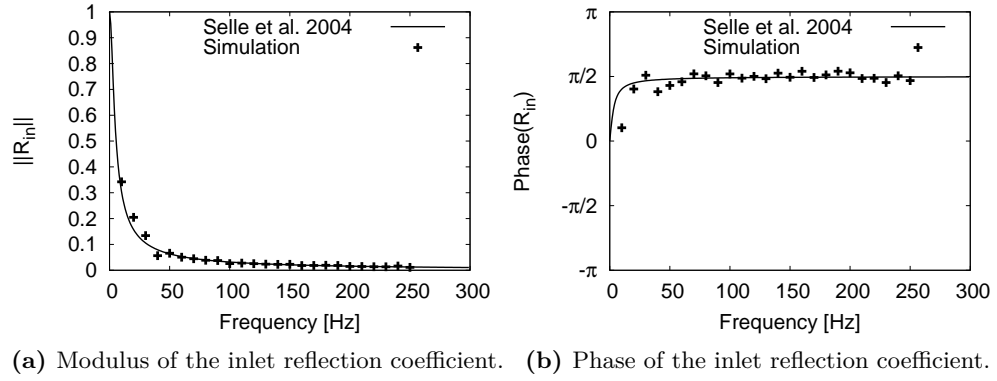
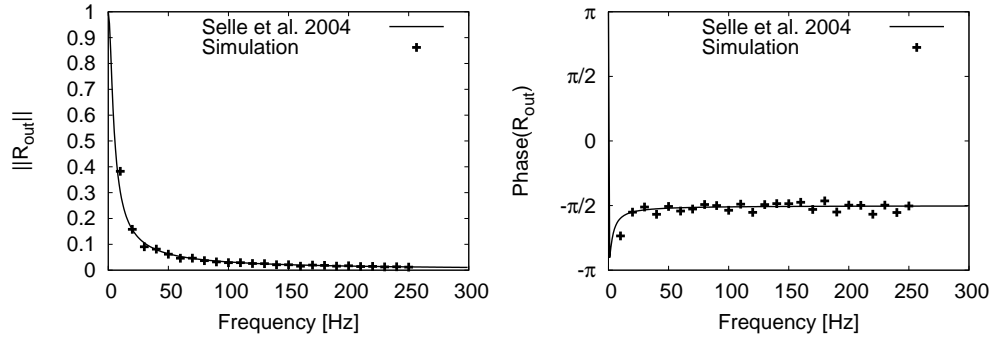


**Figure 5.44** Reflection coefficient computed from the extracted waves at the inlet boundary condition of the simulation.



(a) Modulus of the inlet reflection coefficient. (b) Phase of the inlet reflection coefficient.

**Figure 5.45** Reflection coefficient computed from the extracted waves at the outlet boundary condition of the simulation.

### 5.3.2.2 Upstream acoustic forcing simulation

The NSCBC acoustic forcing methodology used to introduce acoustics through the inlet boundary condition detailed in [Appendix A](#) is used in this section. The amplitude of the forced acoustic wave is chosen to be a very small velocity perturbation for which  $A = 0.75$  m/s (barely 7% of the baseline flow bulk velocity), to stay in the linear regime for acoustics. The system of waves generated by such a forcing can be described by [Fig. 5.46](#), where in the absence of reflections, only three waves remain inside the domain: the acoustic forced wave  $A_{0,f}^+$  and the response of the nozzle to this incoming disturbance, the reflected wave  $A_{0,r}^-$ , and the transmitted wave  $A_{1,t}^+$ . The system is more complex when the boundary conditions are reflective, since there is a coupling between the reflected waves and the already existing acoustic waves.

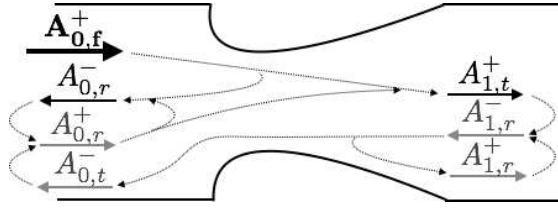


**Figure 5.46** Schematic view of acoustic waves formed by an upstream acoustic forcing with non-reflective boundary conditions.

Before computing acoustic waves and the transfer functions of the nozzle, it is important to retrieve the forcing signal from the simulation to understand the coupling between forced, reflected and transmitted waves. To do so, the velocity signal at the inlet boundary condition is compared with the velocity induced by the forcing signal  $0.75f_r(t)$  in [Fig. 5.47a](#). If the inlet boundary condition was perfectly non-reflecting, both signals should be equal. In the case of the present simulation this is however not satisfied because to maintain the target values at the boundary condition, a relaxation coefficient  $K = 20 \text{ s}^{-1}$  is found to be needed, making the boundary conditions to be partially reflecting. The velocity fluctuation extracted from the simulation in [Fig. 5.47a](#) (dark continuous line) is hence the result of the coupling of both upstream and downstream travelling acoustic waves in the upstream duct:

$$\begin{aligned} A_0^+ &= A_{0,f}^+ + A_{0,r}^+, \\ A_0^- &= A_{0,t}^- + A_{0,r}^-. \end{aligned} \quad (5.16)$$

The forced wave  $A_{0,f}^+$  can be isolated if the reflected wave  $A_{0,r}^+$  can be computed. To do so, the reflection coefficient must be known, allowing to write it as a function of the reflected wave ( $R_{in} = \frac{A_{0,r}^+}{A_0^+}$ ). Using [Selle et al.](#)'s formulation for the reflection coefficient with  $K = 20 \text{ s}^{-1}$ , the expression for  $R_{in}$  is known and the forced wave can be written



as a function of the overall acoustic waves and  $R_{in}$ :

$$A_{0,f}^+ = A_0^+ - R_{in}A_0^-. \quad (5.17)$$

The overall fluctuating velocity (cf. dark line from Fig. 5.47a) is computed subtracting the overall acoustic waves:  $u' = c(A_0^+ - A_0^-)$  (cf. acoustic wave definitions of Eq. (2.7)), whereas the forcing velocity is only the result of the forced wave  $A_{0,f}^+$  and should be computed as  $u'_f = cA_{0,f}^+$ . Figure 5.47b shows the fluctuating velocity  $u'_f$  computed from the simulation at the inlet boundary condition compared with the forcing signal. Note that, retrieving the forced velocity signal from the overall velocity fluctuation allows verifying whether the boundary condition is introducing correctly the intended forced signal.

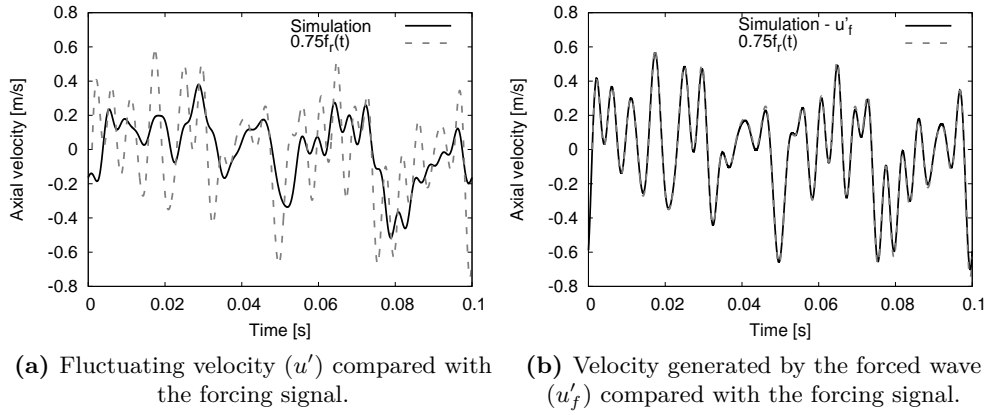


**Figure 5.47** Axial velocity extracted at the inlet boundary condition compared with the forcing signal.

Now, the reflection and transmission of the enforced acoustic waves through the nozzle is studied. To do so, the acoustic waves are computed in the temporal domain using the definitions of Eq. (2.7). Afterwards, a 3D field of waves corresponding to each harmonic of the forcing signal is obtained using a DFT (same sampling and signal length as used in the previous section). The acoustic waves are then averaged over the duct cross-sections and plotted against the stream-wise coordinate in Figs. 5.48 and 5.49. Thanks to such plots it is clear that the acoustic waves in the ducts obey the advection equations described by Eqs. (2.5a) and (2.5b) well (constant module and linear phase). The non compactness of the nozzle showed analytically in §4.4 is furthermore confirmed by the simulation, a phase shift appearing when waves are going through the nozzle.

Note that the use of partially-reflective boundaries infers that all the harmonics of the downstream travelling acoustic wave of the upstream duct  $A_0^+$  have different amplitudes (without reflections  $A_0^+ = A_{0,f}^+$ , which is constant, cf. Fig. 5.32b). In addition, these

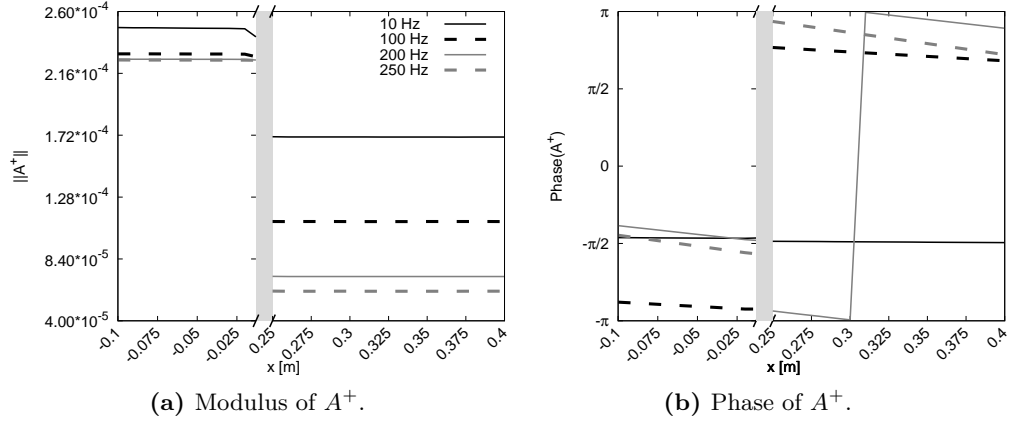


**Figure 5.48** Acoustic wave  $A^+$  in the upstream and downstream ducts of the EWG. (Only harmonics 1, 10, 20 and 25 are presented).

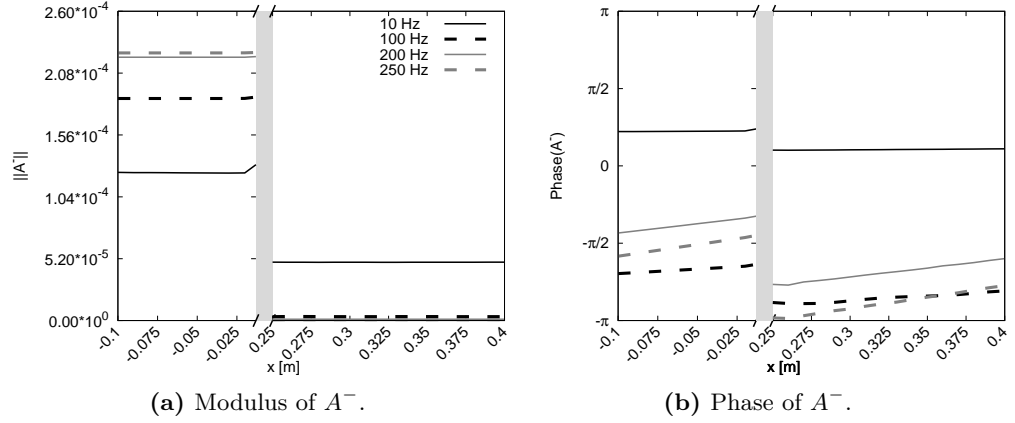


**Figure 5.49** Acoustic wave  $A^-$  in the upstream and downstream ducts of the EWG. (Only harmonics 1, 10, 20 and 25 are presented).

partially-reflective boundaries induce also the presence of a retrograde acoustic wave in the downstream duct  $A_1^-$  (cf. Fig. 5.49), when ideally (non-reflective case) this wave is absent. To verify that  $A_1^-$  are indeed reflected waves, the reflection coefficient at the outlet boundary condition  $R_{out} = \frac{A_1^-}{A_1^+}$  is computed and compared with the analytical expression of Selle et al. (2004) and shown in Fig. 5.50. As indicated by these results, the reflection coefficient of the simulation corresponds perfectly with the one computed with the analytical expression, which again confirms the diagnostics.

To finish, the acoustic transfer functions associated with the upstream acoustic forcing can be computed using the acoustic waves obtained in Figs. 5.48 and 5.49. However,

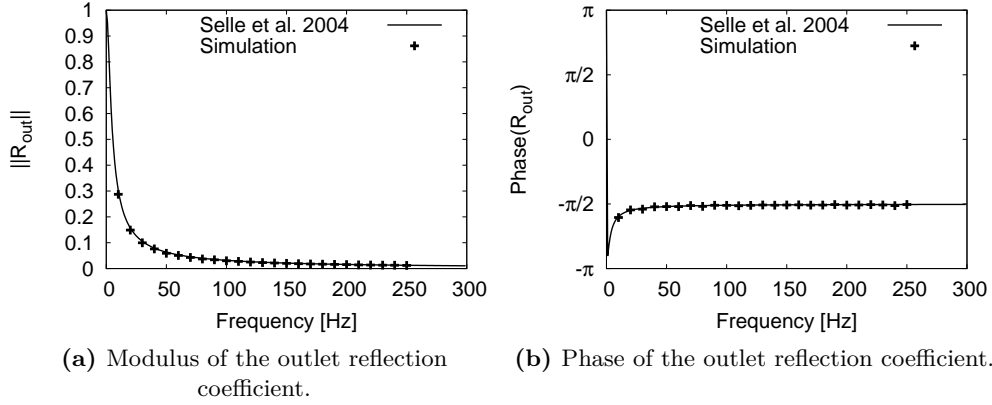


**Figure 5.50** Reflection coefficient computed from the extracted waves at the outlet boundary condition of the simulation.

the overall acoustic waves extracted from the simulation are polluted by reflections at the boundary conditions and need to be filtered from this contribution. In order to separate these reflections from the transmitted/reflected waves by the nozzle, the transfer functions associated with the downstream acoustic forcing are needed and computed in §5.3.2.4.

### 5.3.2.3 Downstream acoustic forcing simulation

The system of waves that forms after the introduction of an acoustic disturbance through the outlet boundary condition is very similar to the one described in the former section, and is shown in Fig. 5.51.

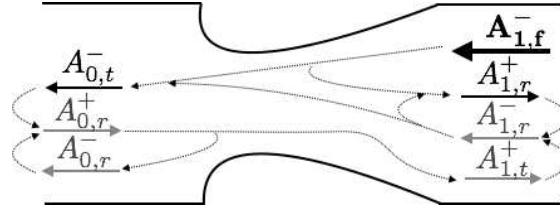


**Figure 5.51** Schematic view of acoustic waves formed by a downstream acoustic forcing with non-reflective boundary conditions.

The amplitude of the forcing disturbance has been set to 100 Pa (amplitude of the pressure fluctuation generated at the outlet by the upstream acoustic forcing). To verify the proper functioning of the outlet boundary condition, the forced signal is compared to the outlet static pressure signal in Fig. 5.52a as well as with the reconstruction of the forced acoustic pressure extracted from the simulation in Fig. 5.52b (as done for the inlet acoustic forcing in the former section). The overall fluctuating pressure (in

particular the one at the outlet boundary condition) is the addition of the two acoustic waves  $p' = \gamma p (A_1^+ + A_0^-)$ , whereas the pressure fluctuation generated by the forced wave depends only on the acoustic forced wave,  $p'_f = \gamma p A_{1,f}^-$ . To separate the forced wave from the overall downstream travelling acoustic wave  $A_1^-$ , the analytical expression of Selle et al. for the reflection coefficients is used to obtain  $A_{1,f}^- = A_1^- - R_{out} A_1^+$ .

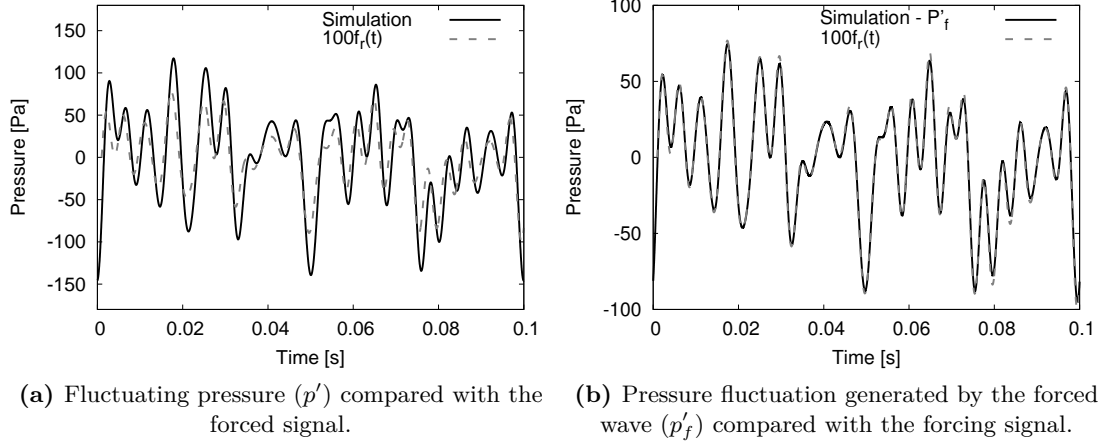


**Figure 5.52** Static pressure extracted at the outlet boundary condition compared with the forcing signal.

Comparison of the different contributors confirm the perfect match between the forced pressure disturbance and the forced signal, Fig. 5.52b. This again shows that the boundary condition introduces the right signal into the simulation. In the following, harmonic acoustic plane waves are computed using the same methodology used in §5.3.2.2. Figures 5.53 and 5.54 show the 1D fields of downstream and upstream travelling acoustic waves,  $A^+$  and  $A^-$  respectively, in the EWG ducts. From Fig. 5.52, one can already see that reflections at the outlet boundary condition are very small, which is confirmed by Fig. 5.54, where the amplitude of all the harmonics is found to be almost the same (like the forced signal in Fig. 5.32b). The amplitude of the upstream travelling acoustic wave in the upstream duct  $A_0^+$  is very small and should correspond to the reflections induced by the upstream boundary condition (there is only one wave  $A^+$  in the upstream duct, as represented in the schematic view of waves in Fig. 5.51). Therefore, using the overall acoustic waves in the upstream duct  $A_0^+$  and  $A_0^-$ , the inlet reflection coefficient of the simulation is computed and compared with its analytical formulation in Fig. 5.55, obtaining also a very good agreement for all harmonics.

Finally, the set of acoustic waves generated by the different forcings (acoustic and entropy) is complete. As explained in the preceding sections, these acoustic waves are polluted by reflections at the boundary conditions. In the following section, the noz-

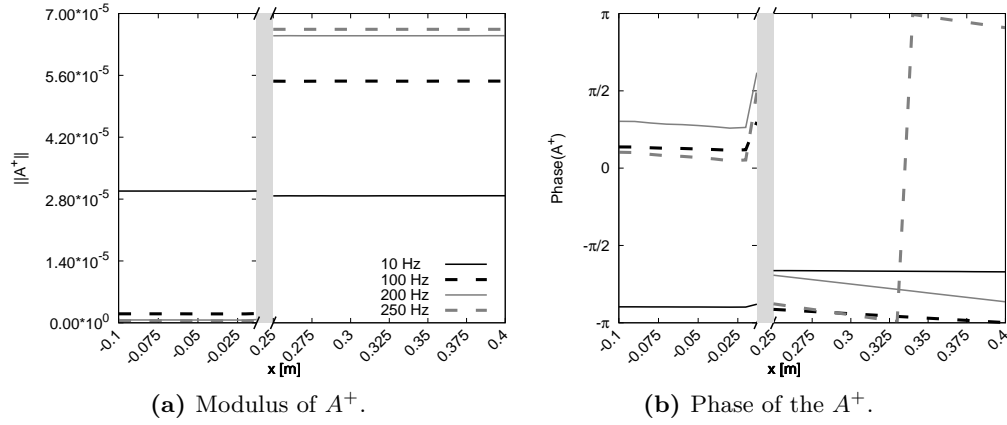


**Figure 5.53** Acoustic wave  $A^+$  in the upstream and downstream ducts of the EWG. (Only harmonics 1, 10, 20 and 25 are presented).

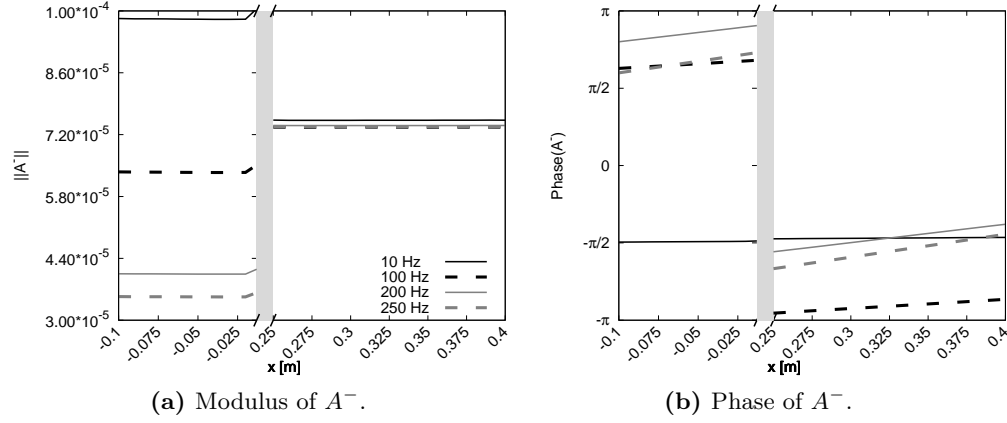
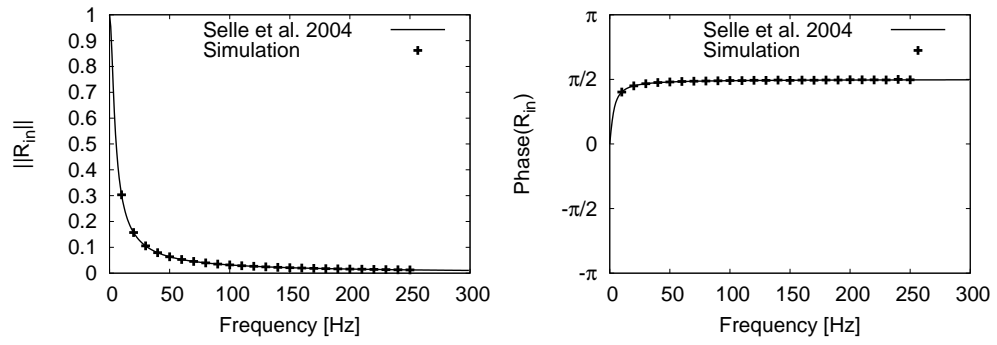


**Figure 5.54** Acoustic wave  $A^-$  in the upstream and downstream ducts of the EWG. (Only harmonics 1, 10, 20 and 25 are presented).

zle transfer functions are computed adopting a methodology to separate the boundary conditions reflected waves from the transmitted and reflected acoustic waves through the nozzle (methodology already adopted in the indirect combustion noise experimental study of the HAT nozzle of [Knobloch et al. 2015a](#)).



(a) Modulus of the inlet reflection coefficient. (b) Phase of the inlet reflection coefficient.

**Figure 5.55** Reflection coefficient computed from the extracted waves at the inlet boundary condition of the simulation.

#### 5.3.2.4 Euler nozzle transfer functions

A wave transfer function is a ratio of an outgoing wave to an ingoing wave. In this case, they are classified in two types: reflection and transmission, denoted by  $R$  and  $T$  respectively. Subscripts  $(\cdot)_{aa}$  and  $(\cdot)_{ea}$  are used to indicate the type of interaction between the generated waves as well as the ingoing wave and whose nature can be either acoustic-acoustic or entropy-acoustic interactions respectively. Finally, in the case of acoustic-acoustic interactions, the superscripts  $+$  and  $-$  indicate if the ingoing wave is a progressive or a regressive acoustic wave,  $A^+$  or  $A^-$  respectively. In the present study, as they are chosen at the inlet and outlet of the domain. This yields:

$$\text{For an upstream acoustic forcing} \begin{cases} R_{aa}^+ = \frac{A_{0,r}^-(x_{in})}{A_0^+(x_{in})}, \\ T_{aa}^+ = \frac{A_{1,t}^+(x_{out})}{A_0^+(x_{in})}. \end{cases} \quad (5.18a)$$

$$\text{For a downstream acoustic forcing} \begin{cases} R_{aa}^- = \frac{A_{1,r}^+(x_{out})}{A_1^-(x_{out})}, \\ T_{aa}^- = \frac{A_{0,t}^-(x_{in})}{A_1^-(x_{out})}. \end{cases} \quad (5.18b)$$

$$\text{For an entropy forcing} \begin{cases} R_{ea}^- = \frac{A_{ea-r}^-(x_{in})}{\sigma_0(x_{in})}, \\ T_{ea}^- = \frac{A_{ea-t}^+(x_{out})}{\sigma_0(x_{in})}. \end{cases} \quad (5.18c)$$

where acoustic waves are denoted as in Fig. 5.35. Furthermore, since the overall acoustic waves in the upstream and downstream ducts corresponds to the upstream and downstream forcings (cf. Figs. 5.46 and 5.51), they yield:

$$\begin{aligned} A_0^+|_u &= (A_{0,f}^+ + A_{0,r}^+)_u, & A_1^+|_u &= (A_{1,t}^+ + A_{1,r}^+)_u, \\ A_0^-|_u &= (A_{0,t}^- + A_{0,r}^-)_u, & A_1^-|_u &= (A_{1,r}^-)_u. \end{aligned} \quad (5.19)$$

$$\begin{aligned} A_0^+|_d &= (A_{0,r}^+)_d, & A_1^+|_d &= (A_{1,t}^+ + A_{1,r}^+)_d, \\ A_0^-|_d &= (A_{0,t}^- + A_{0,r}^-)_d, & A_1^-|_d &= (A_{1,f}^- + A_{1,r}^-)_d, \end{aligned} \quad (5.20)$$

where subscripts  $(\cdot)_u$  and  $(\cdot)_d$  indicate whether the forcing is from the upstream or the downstream boundary condition. Introducing relations from Eq. (5.19) into Eq. (5.18a), and Eq. (5.20) into Eq. (5.18b), the acoustic-acoustic transfer functions can be rewritten using only the overall acoustic waves and the other transfer functions,

$$R_{aa}^+ = \frac{A_0^- - A_{0,t}^-}{A_0^+} \Big|_u = \frac{A_0^-}{A_0^+} \Big|_u - \frac{A_1^-}{A_0^+} \Big|_u T_{aa}^-, \quad (5.21a)$$

$$T_{aa}^+ = \frac{A_1^+ - A_{1,r}^+}{A_0^+} \Big|_u = \frac{A_1^+}{A_0^+} \Big|_u - \frac{A_1^-}{A_0^+} \Big|_u R_{aa}^-, \quad (5.21b)$$

$$R_{aa}^- = \frac{A_1^+ - A_{1,t}^+}{A_1^-} \Big|_d = \frac{A_1^+}{A_1^-} \Big|_d - \frac{A_0^+}{A_1^-} \Big|_d T_{aa}^+, \quad (5.21c)$$

$$T_{aa}^- = \frac{A_0^+ - A_{0,r}^+}{A_1^-} \Big|_d = \frac{A_0^-}{A_1^-} \Big|_d - \frac{A_0^+}{A_1^-} \Big|_d R_{aa}^+. \quad (5.21d)$$

Finally, rearranging Eqs. (5.21a–5.21d), the acoustic-acoustic transfer functions can be written as a function of the overall acoustic waves only:

$$R_{aa}^+ = \frac{\frac{A_0^-}{A_1^-} \Big|_u - \frac{A_0^+}{A_1^-} \Big|_d}{\frac{A_0^+}{A_1^-} \Big|_u - \frac{A_0^-}{A_1^-} \Big|_d}, \quad (5.22)$$

$$T_{aa}^+ = \frac{\frac{A_1^+}{A_1^-} \Big|_u - \frac{A_1^-}{A_1^-} \Big|_d}{\frac{A_0^+}{A_1^-} \Big|_u - \frac{A_0^-}{A_1^-} \Big|_d}, \quad (5.23)$$

$$R_{aa}^- = \frac{\frac{A_1^+}{A_0^+} \Big|_u - \frac{A_1^-}{A_0^+} \Big|_d}{\frac{A_1^-}{A_0^+} \Big|_u - \frac{A_1^+}{A_0^+} \Big|_d}, \quad (5.24)$$

$$T_{aa}^- = \frac{\frac{A_0^-}{A_0^+} \Big|_u - \frac{A_0^+}{A_0^+} \Big|_d}{\frac{A_1^-}{A_0^+} \Big|_u - \frac{A_1^+}{A_0^+} \Big|_d}. \quad (5.25)$$

Acoustic-acoustic transfer functions from the acoustically forced numerical simulations presented in §5.3.2.2 and §5.3.2.3 are hence computed using Eqs. (5.22–5.25). They are compared with the transfer functions computed using the overall acoustic waves, and with the analytical transfer functions obtained by the analytical theory of Duran and Moreau (2013a) in Figs. 5.56–5.59. The latter formulation of the transfer functions (cf. Eqs. (5.22–5.25)) corrects the low frequency values, which results from the NSCBC low-pass filter reflection coefficients (low frequencies are reflected) and a very good agreement between the Euler and the analytical transfer functions is found. This result, where the exact analytical solution of the quasi-1D LEE equations of Duran and Moreau (2013a) is compared with the Euler simulation numerical results, allows to validate the proposed methodology to compute the acoustic-acoustic nozzle transfer functions associated with the numerical acoustic forcings.

The acoustic-acoustic transfer functions being studied, let's focus on the entropy-acoustic interactions. First, the overall acoustic waves generated by an entropy forcing in the upstream and downstream ducts yield (cf. Fig. 5.35):

$$\begin{aligned} A_0^+ \Big|_{ent} &= (A_{0,r}^+)_{ent} & , & \quad A_1^+ \Big|_{ent} = (A_{1,ea-t}^+ + A_{1,t}^+ + A_{1,r}^+)_{ent} , \\ A_0^- \Big|_{ent} &= (A_{0,ea-r}^- + A_{0,t}^- + A_{0,r}^-)_{ent} & , & \quad A_1^- \Big|_{ent} = (A_{1,r}^-)_{ent} . \end{aligned} \quad (5.26)$$



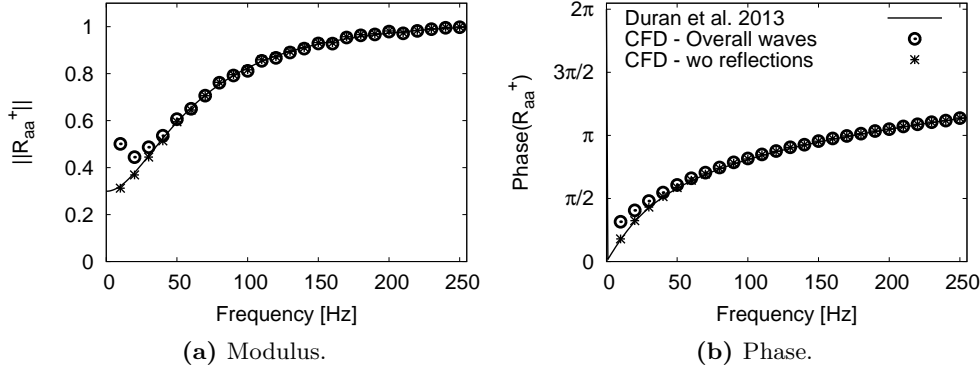


**Figure 5.56** Upstream reflecting coefficient  $R_{aa}^+$  filtered from the boundary conditions reflections.

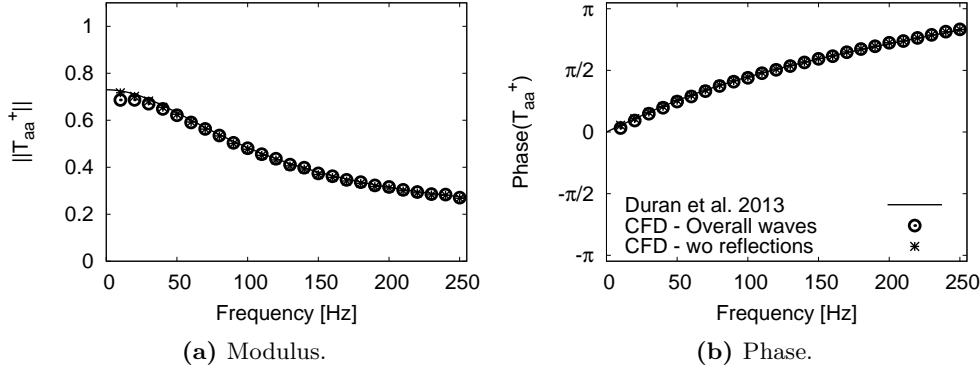


**Figure 5.57** Upstream transmission coefficient  $T_{aa}^+$  filtered from the boundary conditions reflections.

where the acoustic waves related to the entropy-acoustic transfer functions are the ones denoted with the subscript  $(\cdot)_{ea}$ . Introducing overall acoustic waves generated by an entropy forcing defined in Eq. (5.26) into Eq. (5.18c), and using the acoustic-acoustic transfer functions defined in Eqs. (5.18a) and (5.18b), the entropy-acoustic transfer functions can be written as a function of the overall acoustic waves of the entropy forced simulation as well as the acoustic-acoustic transfer functions, yielding:

$$T_{ea} = \frac{A_1^+}{\sigma_0} \bigg|_{ent} - \frac{A_0^+}{\sigma_0} \bigg|_{ent} T_{aa}^+ - \frac{A_1^-}{\sigma_0} \bigg|_{ent} R_{aa}^-, \quad (5.27a)$$

$$R_{ea} = \frac{A_0^-}{\sigma_0} \bigg|_{ent} - \frac{A_1^-}{\sigma_0} \bigg|_{ent} T_{aa}^- - \frac{A_0^+}{\sigma_0} \bigg|_{ent} R_{aa}^+. \quad (5.27b)$$

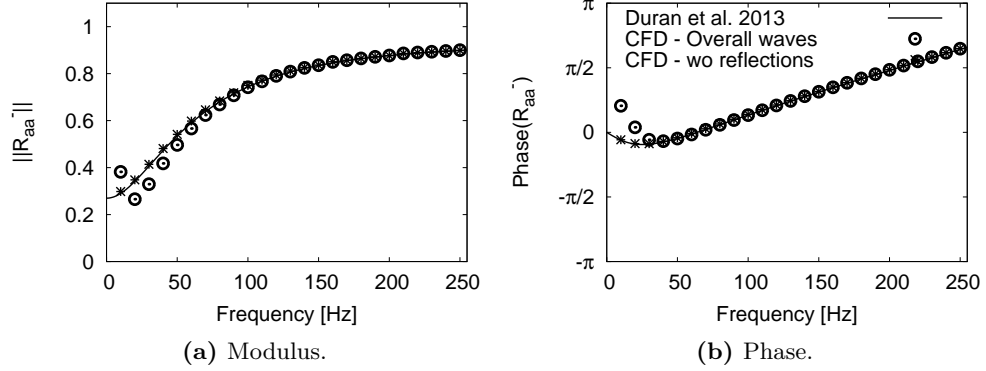


**Figure 5.58** Downstream reflecting coefficient  $R_{aa}^-$  filtered from the boundary conditions reflections.

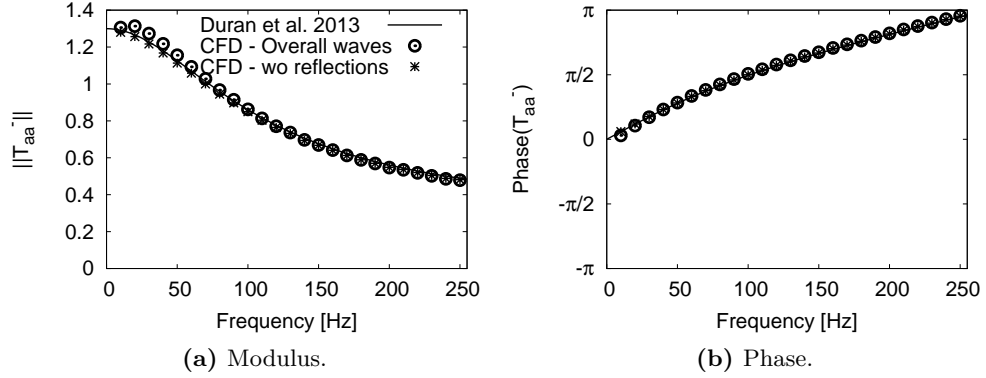


**Figure 5.59** Downstream transmission coefficient  $T_{aa}^-$  filtered from the boundary conditions reflections.

The entropy-acoustic transfer functions are presented in Figs. 5.60 and 5.61. Results match very well analytical expressions for frequencies lower than 100 Hz. For higher frequencies, the numerical simulation predicts a smaller amplitude in the transmitted and reflected waves. Indeed, the amplitude of the generated acoustic waves is known to be proportional to the amplitude of the entropy wave, therefore if the amplitude of the entropy plane wave decays through the nozzle (as highlighted by the entropy forced numerical simulation in §5.3.2.1, cf. Fig. 5.40), it is logical to expect an amplitude of the generated acoustic waves that decays with the attenuation of the entropy wave. However, recent studies published by Duran and Morgans (2015) in the framework of annular nozzle flows, show that the acceleration of an azimuthal entropy wave generates also vorticity waves. These vorticity waves, when accelerated by the nozzle also generate acoustic waves which interact with the already existing acoustic waves. In the case of the present study, no azimuthal entropy wave is forced. However, the distortion of the

plane entropy wave through the nozzle generates radial entropy fluctuations which may induce vorticity waves. To evaluate the magnitude of these vorticity waves, vorticity fluctuations may be written as:

$$\xi'_x = \frac{1}{2\pi f} \left[ \frac{1}{r} \left( \frac{\partial (r u'_\theta)}{\partial r} - \frac{\partial u'_r}{\partial \theta} \right) \right], \quad (5.28a)$$

$$\xi'_\theta = \frac{1}{2\pi f} \left[ \frac{\partial u'_r}{\partial x} - \frac{\partial u'_x}{\partial r} \right], \quad (5.28b)$$

$$\xi'_r = \frac{1}{2\pi f} \left[ \frac{1}{r} \frac{\partial u'_x}{\partial \theta} - \frac{\partial u'_\theta}{\partial x} \right]. \quad (5.28c)$$

Cross-sectional averaged values of vorticity are presented as a function of the axial coordinate. Note that here the amplitude of the axial and radial vorticity fluctuations is negligible compared to the amplitude of the azimuthal vorticity fluctuation (two orders of magnitude greater). [Figure 5.62](#) shows the amplitude of the azimuthal vorticity fluctuation plotted against the stream-wise coordinate, where the maximal amplitude is reached at the nozzle throat and is almost the same for all the harmonics computed. However, the greatest amplitude is reached at the lowest frequencies (as also observed by [Duran and Morgans 2015](#)), for which no significant differences in the entropy-acoustic transfer functions have been found in [Figs. 5.44](#) and [5.45](#) when comparing the analytical theory and the simulation. It is however noteworthy to stress that the entropy-acoustic transfer functions computed from the simulation take into account the sound generation of the coupled entropy and vorticity waves accelerated through the nozzle, the contribution of each process being not separable in the numerical simulation. Nevertheless, an estimation of the generated acoustic wave by the acceleration of a vorticity wave can be done using the compact relations from [Cumpsty and Marble \(1977a\)](#). In this process, the characteristics of the mean flow at the nozzle throat and the exit of the nozzle are used as jump conditions. It should be noted that the equivalent vorticity wave taken into account in [Cumpsty and Marble \(1977a\)](#) is the radial vorticity wave (obtained by the 2D flow considered in this study), whose vorticity-acoustic transfer function reads:

$$T_{va} = \frac{A_{xi}^+}{\xi'}, \quad (5.29)$$

Therefore, the vorticity generated acoustic wave through the nozzle yields  $A_{\xi'}^+ = T_{va}\xi'$ . To estimate the importance of the vorticity generated acoustic wave with respect to the entropy wave,  $A_{\xi'}^+$  is divided by the amplitude of the entropy wave introduced in the simulation to obtain an entropy-acoustic transfer function related to  $A_{\xi'}^+$ :

$$T_{ea-\xi'} = \frac{T_{va}\xi'}{\sigma}, \quad (5.30)$$

where  $T_{va}$  is a constant obtained from the compact relations of [Cumpsty and Marble \(1977a\)](#) and  $\xi'$  is replaced by the amplitude of the different vorticity waves computed at

the nozzle throat. Figure 5.63 shows the result of this estimation, where the amplitude of  $T_{ea-\xi'}$  is clearly negligible compared with the amplitude of the entropy-acoustic transfer function from Fig. 5.60. This result shows that the generated acoustic wave from the acceleration of vorticity waves through the nozzle diffuser is negligible and not responsible for the differences between the Euler numerical simulation and the analytical method from Fig. 5.60. Therefore, these high-frequency differences are attributed to the entropy plane wave attenuation through the nozzle.

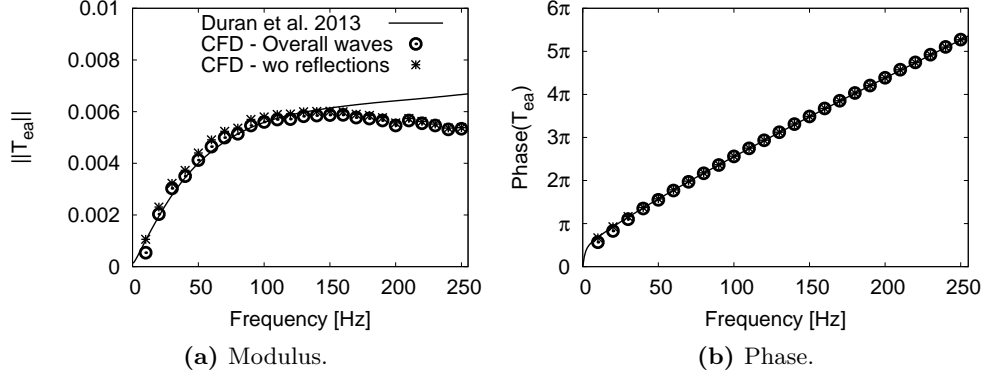


**Figure 5.60** Entropy-acoustic transmission coefficient  $T_{ea}$  filtered from the boundary conditions reflections.

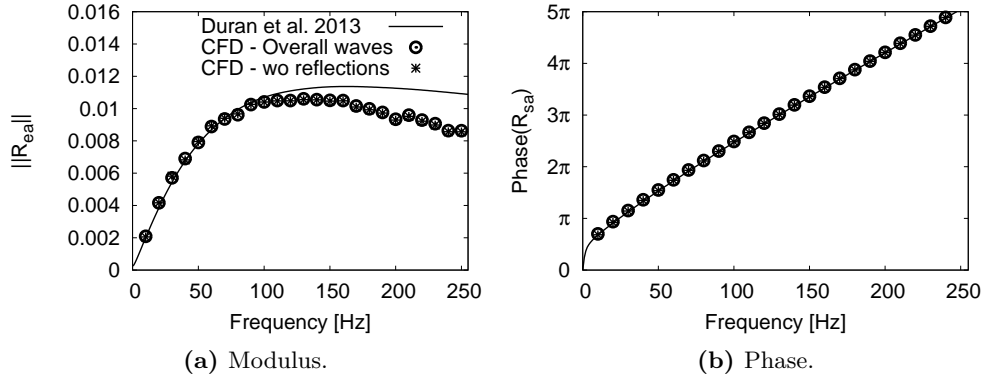


**Figure 5.61** Entropy-acoustic reflection coefficient  $R_{ea}$  filtered from the boundary conditions reflections.

### 5.3.2.5 Conclusion

In this subsection, a subsonic inviscid flow has been computed to study the EWG nozzle transfer functions. To do so, acoustic and entropy plane waves have been introduced

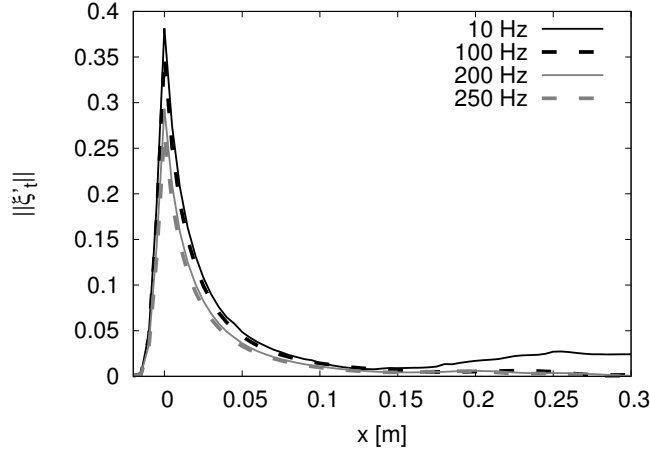


**Figure 5.62** Azimuthal vorticity fluctuations generated in the entropy forced Euler simulation for different harmonics (only harmonics 1, 10, 20 and 25 are presented).

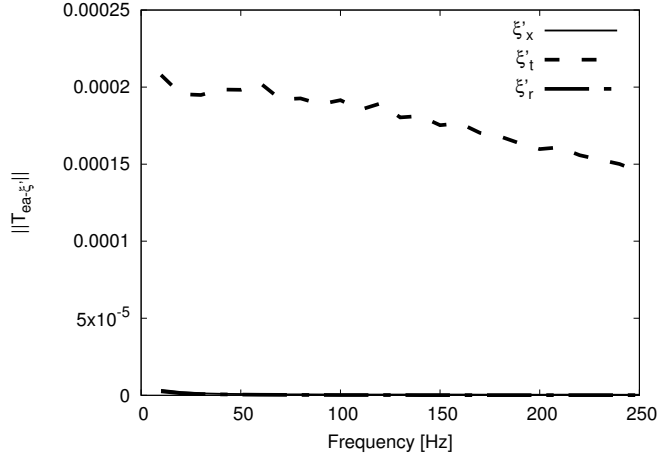


**Figure 5.63** Entropy-acoustic transfer function associated to the generated acoustic wave from a vorticity forcing.

through the boundary conditions using the NSCBC formalism. Particular attention has been taken to exclude the reflections due to the boundary conditions from the computed transfer functions, and a methodology to separate the various contributions has been proposed. The obtained transfer functions have been then compared with the analytical model of [Duran and Moreau \(2013a\)](#). Acoustic waves in the simulations are found to remain planar and a very good agreement between the numerical simulations and the acoustic-acoustic transfer functions is found whenever using analytical theory or numerical simulations. Before analysing the entropy-acoustic transfer functions, the convection of the entropy wave along the EWG configuration has been studied. It has been found that the entropy wave undergoes distortions due to the non-homogeneous flow through

the nozzle, which produces an attenuation of the entropy wave. The higher the frequency is, the higher the attenuation of the entropy wave is (as highlighted by [Morgans et al. 2013](#) and [Giusti et al. 2016](#)). This attenuation of the entropy wave is found to be responsible for the differences between the entropy-acoustic transfer functions of the nozzle computed from the numerical simulation and the analytical quasi-1D theory of [Duran and Moreau \(2013a\)](#) (in particular at the highest frequencies, where the attenuation is stronger). The analytical model proposed by [Zheng et al. \(2015\)](#), is capable of computing analytically the entropy-acoustic nozzle transfer functions while considering the attenuation of the entropy through a non-compact nozzle. In this model, acoustic waves are assumed as planar, which has been in agreement with the results obtained in this subsection. Finally, the generation of vorticity waves due to the acceleration of the distorted entropy wave (as explained by [Duran and Morgans 2015](#)) is highlighted by the numerical simulation. The process of generation of acoustic waves from the acceleration of these vorticity waves through the nozzle has been addressed using the 2D compact theory of [Cumpsty and Marble \(1977a\)](#), concluding that vortex sound in the entropy forced Euler simulation is negligible.

### 5.3.3 Navier-Stokes nozzle transfer functions

In the previous section, the methodology to force acoustic and entropy disturbances to study the nozzle transfer functions has been introduced. Thanks to the previous analysis, the acoustic-acoustic transfer functions between a Euler 360° simulation and the quasi-1D analytic theory were found to be equivalent. It furthermore showed that for the frequencies and the operation point studied, the acoustic-acoustic interactions remain 1D (as assumed by [Zheng et al. \(2015\)](#)). This is not the case for the entropy wave, which undergoes deformations caused by the non-homogeneous mean flow produced by the nozzle. Indeed, this non-homogeneous mean flow produces dispersion of the entropy wave, which increases with the frequency (smaller wavelength) and energy transfer from the low-order planar mode to higher order modes. In the present section, the methodology used to determine the nozzle transfer coefficients is applied to compute the Navier-Stokes transfer functions (NS-TF) of the same nozzle. The objective is to take into account the viscous effects absent in the Euler simulation, and which will induce turbulent mixing at the nozzle throat or the effects of wall boundary layers on the acoustic and entropy transfer functions.

The baseline flow used in this study is the one computed in the numerical mesh M2, which has been analysed in [§5.1](#). Now the results of the acoustic and entropy forced simulations are presented and compared with the Euler simulations as well as with the analytical theory of [Duran and Moreau \(2013a\)](#).

#### 5.3.3.1 Acoustic forcing Navier-Stokes simulations

The acoustic-acoustic transfer functions resulting from the upstream and downstream forcing of the LES simulation are presented in this section. To verify that the boundary condition introduces the correct forcing signal, the axial velocity and pressure forced signals from the inlet and outlet acoustic forcings are computed and presented in [Fig. 5.64](#). Similarly to previous computations, the velocity and pressure forced signals extracted from the simulation are in good agreement with the introduced forcing signals.

To compare with the analytical method, the 1D fields of acoustic waves are computed using the methodology described in [§5.3.2.2](#). Acoustic 1D waves computed from the acoustic forcing simulations are showed in [Figs. 5.65–5.68](#), where 1D wave fields from the Euler simulations are also showed for comparison. [Figures 5.65 and 5.66](#) show the acoustic waves extracted from the inlet acoustic forcing computation and [Figs. 5.67 and 5.68](#) the acoustic waves extracted from the outlet acoustic wave forcing. Globally, the resulting fields of amplitude and phase are very different whenever comparing the Euler and the LES computations. Concerning the comparison of the phase issued by the Euler and LES computations, it is worth noting that it is not the value of the phase which is important but its slope. Indeed, the value of the phase depends on the initial state  $t_0$  from which the DFT is computed, but its slope reflects the convection velocity of the wave. Regarding the amplitude of the waves, the amplitude of the forced acoustic

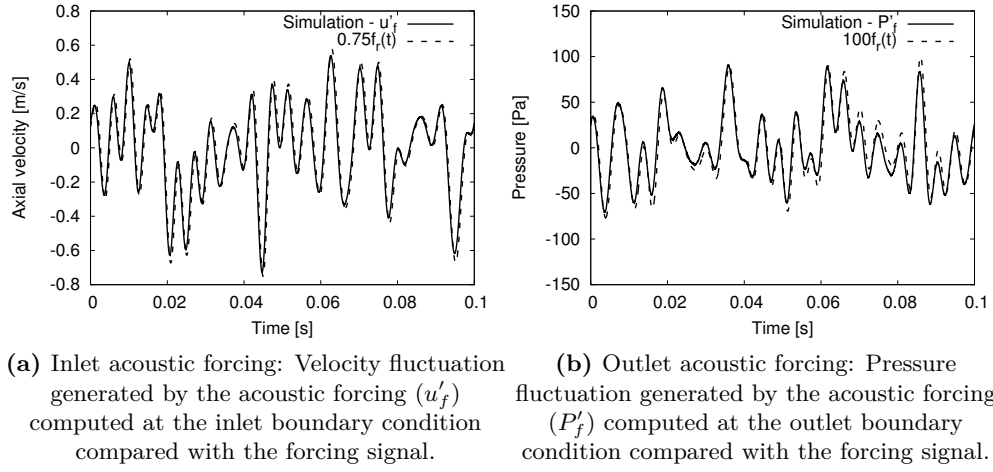


**Figure 5.64** Reconstruction of the forced signal from the information at the boundary conditions for the acoustic forced simulations.

waves ( $A_0^+$  of Fig. 5.65 and  $A_1^-$  of Fig. 5.68) remains constant, whereas the transmitted and reflected waves generated by the interaction with the nozzle oscillate around a mean value. In other words, the outgoing disturbances may contain a contribution of hydrodynamics perturbations caused by the nozzle jet (in the case of the downstream duct). However, looking closely at the amplitude of these oscillations around the mean value, they are not very important (the greatest is the case of  $A_1^+$  of the downstream acoustic forcing of Fig. 5.67). The slope of the phase remains furthermore constant, which means that the propagation velocity of the acoustic wave remains the same.

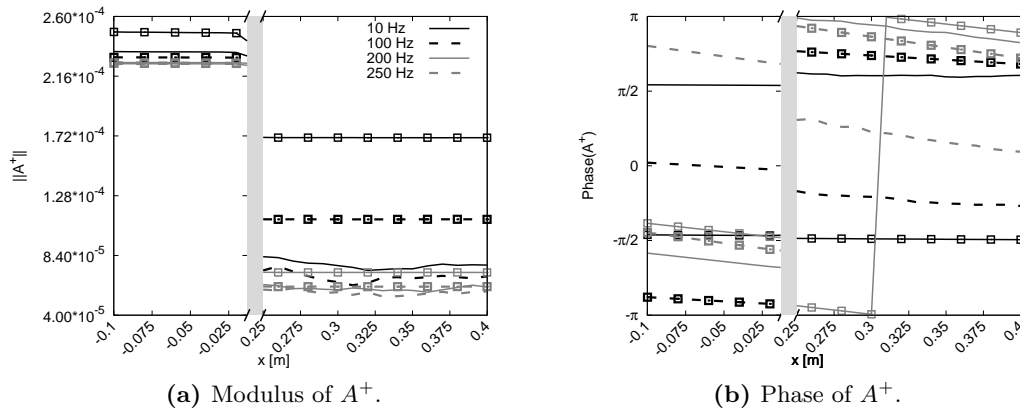


**Figure 5.65** Inlet acoustic forcing: Acoustic wave  $A^+$  in the upstream and downstream ducts of the EWG. Navier-Stokes simulation (lines), Euler simulations (lines with symbols). (Only harmonics 1, 10, 20 and 25 are presented).



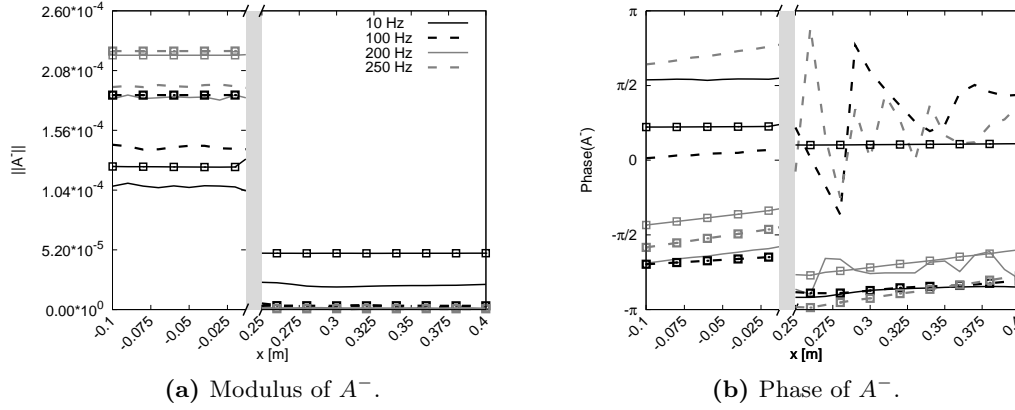


**Figure 5.66** Inlet acoustic forcing: Acoustic wave  $A^-$  in the upstream and downstream ducts of the EWG. Navier-Stokes simulation (lines), Euler simulations (lines with symbols). (Only harmonics 1, 10, 20 and 25 are presented).

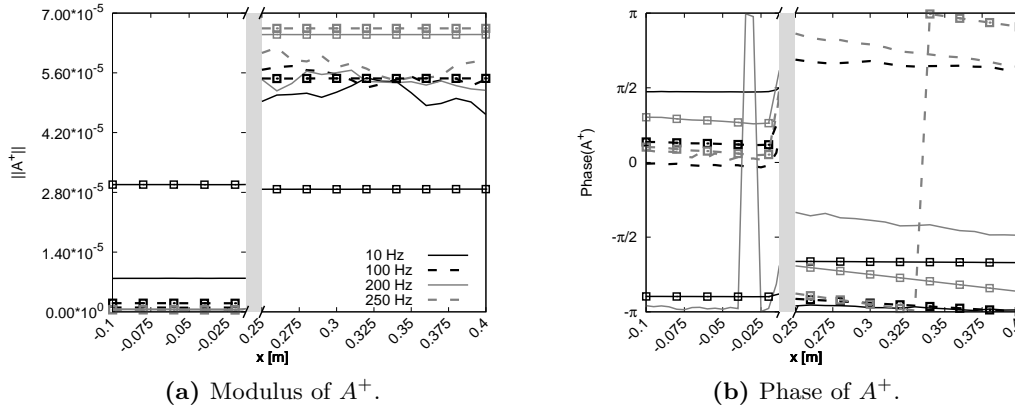


**Figure 5.67** Outlet acoustic forcing: Acoustic wave  $A^+$  in the upstream and downstream ducts of the EWG. Navier-Stokes simulation (lines), Euler simulations (lines with symbols). (Only harmonics 1, 10, 20 and 25 are presented).

The separation of acoustic from hydrodynamic perturbations has also been assessed for the computation of the nozzle transfer functions. Usually these methods are based on the convection velocity and wavelengths of the different disturbances. This is the case of the methodologies proposed by [Kopitz et al. \(2005\)](#) and [Bonneau et al. \(2014\)](#). [Kopitz et al.](#) consider the propagation of an acoustic wave as a characteristic wave. Therefore, an acoustic wave at an initial position  $x_0$  at the time  $t_0$  will be the same acoustic wave at the position  $x_0 + \Delta x$  with a time delay  $t_0 + \Delta t$ , the time delay being associated with the propagation velocity of the wave that is  $\Delta t = \frac{\Delta x}{u+c}$ . Using this property, the acoustic wave is computed at different axial positions and transported as a characteristic wave

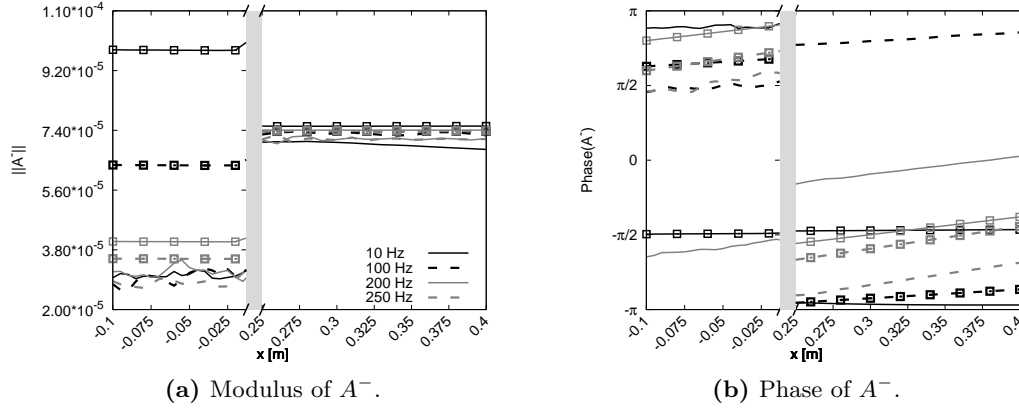


**Figure 5.68** Outlet acoustic forcing: Acoustic wave  $A^-$  in the upstream and downstream ducts of the EWG. Navier-Stokes simulation (lines), Euler simulations (lines with symbols). (Only harmonics 1, 10, 20 and 25 are presented).

to a position  $x_0$ . For a harmonic regime it yields:

$$\hat{A}(f, x_0) = \frac{1}{n} \sum_{i=0}^{n-1} A \exp \left( -i2\pi f \frac{\Delta x}{u + c} \right), \quad (5.31)$$

where  $A$  is the acoustic wave,  $\hat{A}$  is the filtered acoustic wave,  $\Delta x$  is the distance of the plane to the initial position  $x_0$  and  $n$  is the number of axial positions used for the filtering. It is worth noting that the number of planes  $n$  used for the filtering has an influence on the filtered frequencies since the number of planes per wavelength diminish with the frequency.

The methodology proposed by [Bonneau et al. \(2014\)](#) is based on the hydrodynamic convection wave number  $\mathcal{K}_c = \frac{2\pi f}{u}$ , where the hydrodynamic contribution is estimated as:

$$A(f, x_0)_{hydro} = \frac{\mathcal{K}_c}{2\pi} \int_{x_0 - \frac{\pi}{\mathcal{K}_c}}^{x_0 + \frac{\pi}{\mathcal{K}_c}} A(f, x) \exp(i\mathcal{K}_c x) dx. \quad (5.32)$$

From here on, it only remains to subtract the hydrodynamic contribution from the overall wave to obtain the filtered wave as:

$$\hat{A}(f, x_0) = A(f, x_0) - A(f, x_0)_{hydro} \exp(-i\mathcal{K}_c x_0). \quad (5.33)$$

To compute the acoustic transfer functions of the nozzle, the characteristic filtering of [Kopitz et al.](#) is used to filter the contribution of hydrodynamic fluctuations from the computed acoustic waves. Afterwards, the transfer functions are computed using [Eqs. \(5.22–5.25\)](#) to remove the contribution of reflections at the boundary conditions. The transmission and reflection coefficients corresponding to the acoustic forced simulations are shown in [Figs. 5.69–5.72](#). Regarding the upstream acoustic forcing: the forced

acoustic wave through the inlet boundary condition needs first to reach the nozzle to scatter itself into a reflected and a transmitted wave. The evaluation of this scattering into transmitted or reflected waves is represented by the transfer functions shown in Figs. 5.69 and 5.70. The amplitude of the transmitted wave appears to be diminished by the nozzle jet at low frequencies. In the case of the EWG experiment, it has been shown that the lowest frequencies are the most energetic (Fig. 4.15) and the transfer function  $T_{aa}^+$  is directly related to the transmission of direct noise, which has been found to be overestimated by the analytical evaluations in §4.4 when compared with the experimental measurements (all the comparisons with the analytical results obtained in §4.4 and the numerical simulations are related to the case with  $R_{in} = -1$ , cf. Fig. 4.11a). The decay in the amplitude of the transmitted acoustic wave found in the acoustic forced numerical simulation seems therefore coherent with the LES of the experiment presented in §5.2.2. The amplitude of the acoustic wave reflected by the nozzle (cf. Fig. 5.70) follows the same trend as the analytical one, whereas its phase indicates that the reflected acoustic wave is almost constant for the frequency range studied.

In the case of the downstream acoustic forcing: the acoustic wave that travels through the nozzle towards the upstream duct (Fig. 5.71) also has an amplitude decay at low frequencies, whereas for larger frequencies it follows the same trend as the analytical transfer function. Regarding the reflected wave by the nozzle, i.e. Fig. 5.72, its amplitude remains almost constant for the range of frequencies studied, and the low frequencies amplitude is larger for the LES computation. It should be noticed that turbulent vortices are produced at the nozzle throat, and that the acceleration of vortices is also a noise generation mechanism. The contribution of this supplementary noise source (that seems to affect the low frequencies) is taken into account in the NS computed nozzle transfer functions. Vorticity cross-section averaged fluctuations from the acoustic forced simulations are computed and plotted against the axial coordinate in Figs. 5.73 and 5.74, where the axial vorticity fluctuations are found to be negligible compared with the other two components of vorticity and therefore not shown. The amplitude of the computed 1D vorticity fields is found to be much higher than in the Euler case, not only concentrated at the nozzle throat and particularly significant at low frequencies, where from 10 to 100 Hz its amplitude decays by one order of magnitude. It is also worth noting that azimuthal and radial vorticity fluctuations are much larger in the NS simulation, while only the azimuthal component was relevant in the Euler simulation. According to this result, the differences in the acoustic-acoustic transfer functions shown in Figs. 5.69–5.72 at low frequencies may be attributed to the generated vortex noise. To estimate the contribution of the generated acoustic wave from a vorticity forcing in the acoustic-acoustic transfer functions, the methodology applied in §5.3.2.4 to compute the generated acoustic wave from a vorticity forcing is used here. Instead to be applied to the entropy forced wave, it is applied to the acoustic forced waves. In the case of the NS simulation and according to Figs. 5.73 and 5.74, the maximal vorticity fluctuations are reached at an axial position of approximately 5 mm from the nozzle throat (transition to turbulence, cf. Figs. 5.4b and 5.5). Therefore, Cumpsty and Marble (1977a)

jump conditions are applied between the axial positions  $x = 5$  mm and the outlet of the nozzle ( $x_{N_{out}} = 250$  mm). The resultant acoustic waves from the vorticity forcings ( $A_{\xi_t}^+$  and  $A_{\xi_r}^+$ ) are divided by the amplitude of the acoustic forcings ( $A_0^+$  for the inlet acoustic forcing and  $A_1^-$  for the outlet acoustic forcing) and represented in Figs. 5.69 and 5.72 respectively. This approximate result shows that the generated vortex sound is not negligible and is almost concentrated at the lowest frequencies, where the greater discrepancies between the analytical transfer functions and the Navier-Stokes transfer functions (NS-TF<sup>1</sup>) are located. Furthermore, the obtained vortex sound is at least of the same order of magnitude as the difference between the analytical transfer functions and the NS-TF, indicating that this noise mechanism may be a good candidate to explain these differences and highlight that this contribution should be taken into account.

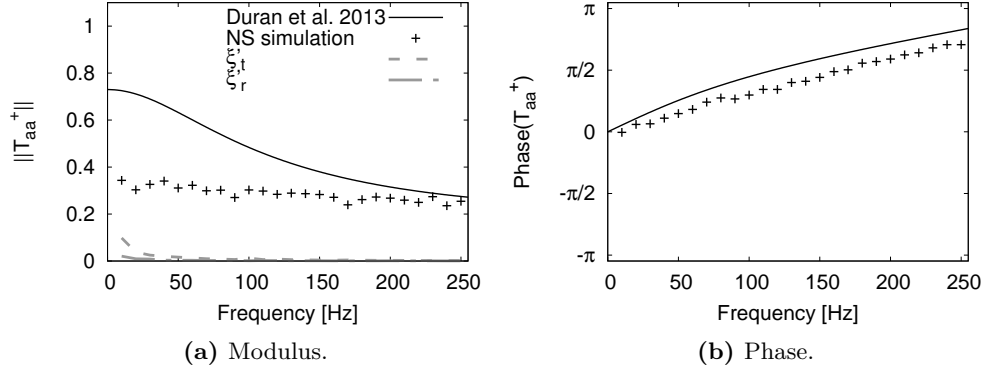


**Figure 5.69** Upstream transmission coefficient  $T_{aa}^+$  without the contribution of reflections.

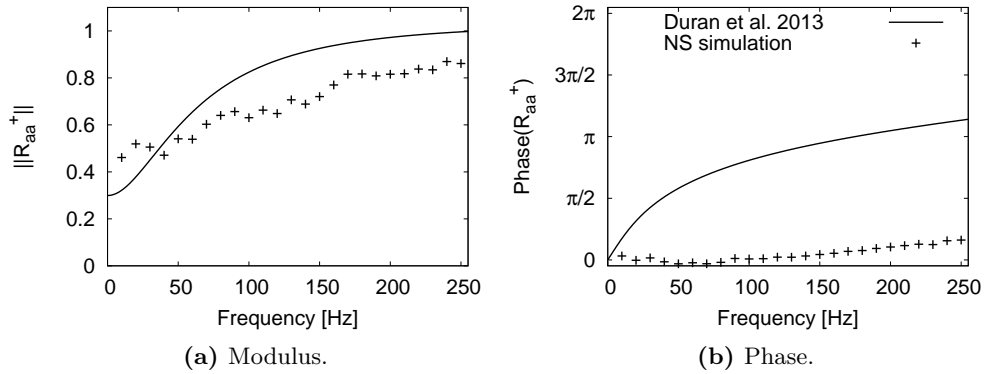


**Figure 5.70** Upstream reflecting coefficient  $R_{aa}^+$  without the contribution of reflections.

<sup>1</sup>In the present case NS or EU refers to the set of equations used for the LES computations.

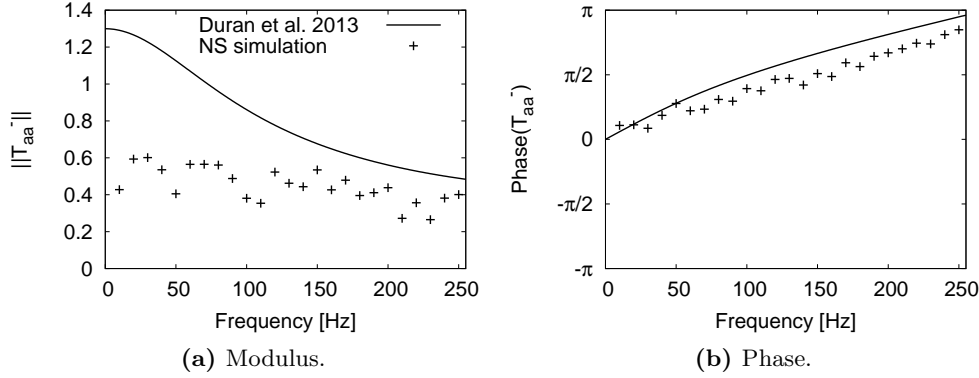


**Figure 5.71** Downstream transmission coefficient  $T_{aa}^-$  without the contribution of reflections.

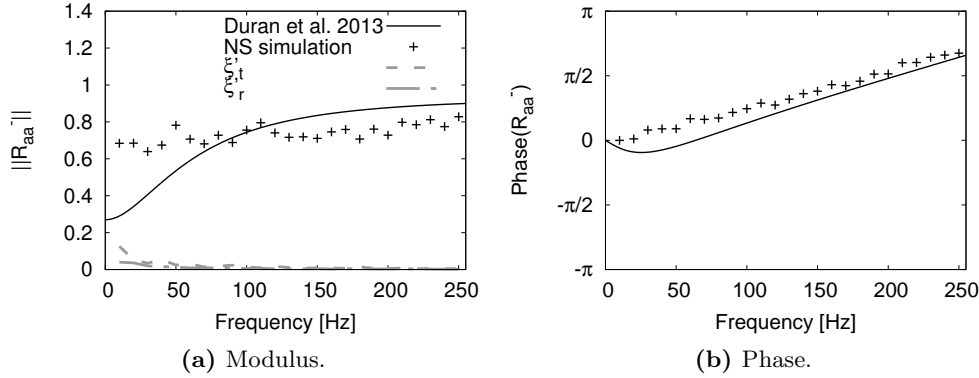


**Figure 5.72** Downstream reflecting coefficient  $R_{aa}^-$  without the contribution of reflections.

Acoustically forced LES simulations are found to be in a strong disagreement with the analytical acoustic-acoustic transfer functions at the low frequencies studied, and vortex sound seems to be a good candidate to explain these differences. To confirm this hypothesis, 1D vorticity waves have been computed along the nozzle and the compact theory of [Cumpsty and Marble \(1977a\)](#) has been used to estimate the generated vortex sound. The obtained results have shown that vortex sound is not negligible and may effectively explain the highlighted discrepancies between the analytical and NS acoustic-acoustic transfer functions. Furthermore, it has been found that direct noise produced in LES should be less than the one estimated by the analytical method or the Euler computations (cf. [Fig. 5.69](#)). It remains to evaluate the influence of the viscous effects on the noise generated by the acceleration of the entropy wave.

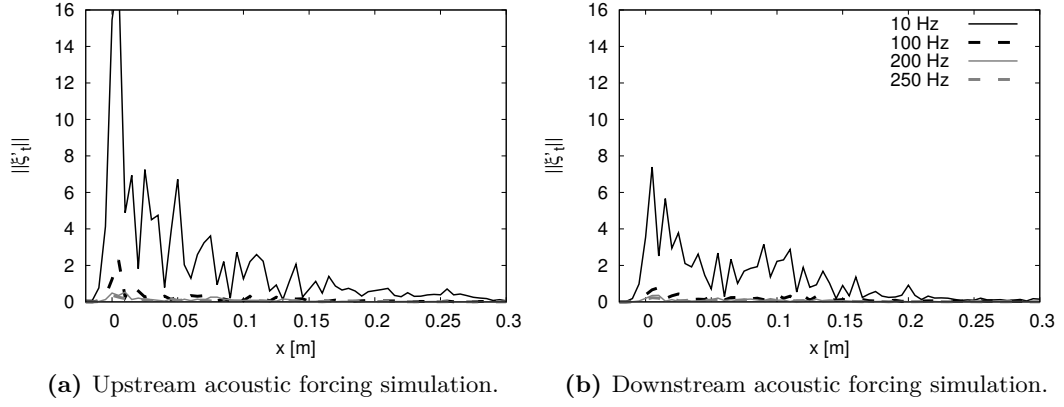


**Figure 5.73** Modulus of the azimuthal vorticity fluctuation  $||\xi'_\theta||$  for different harmonics along the axial coordinate.

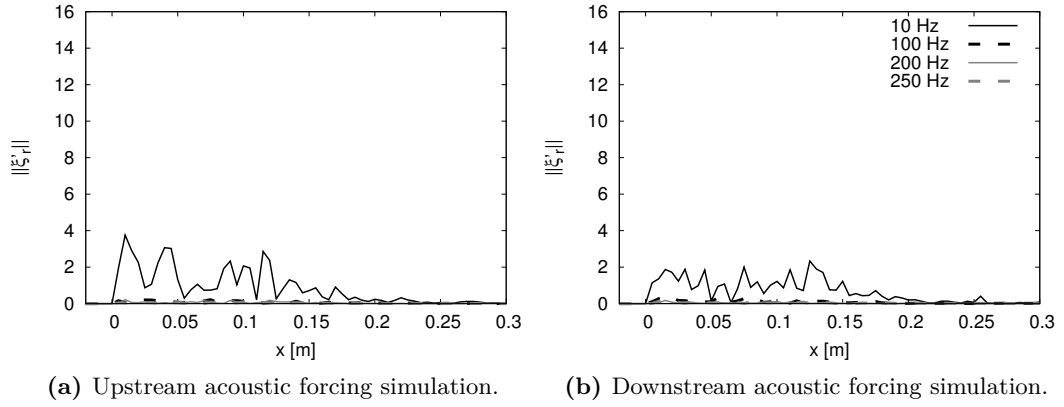


**Figure 5.74** Modulus of the radial vorticity fluctuation  $||\xi'_R||$  for different harmonics along the axial coordinate.

### 5.3.3.2 Entropy forcing Navier-Stokes simulation

In this last section of the EWG, the effects of the boundary layers and the nozzle jet on the entropy-entropy and entropy-acoustic transfer functions are studied. First, and as done for each forcing, the forced signal is compared to the temperature fluctuation at the inlet boundary condition to ensure that the correct signal is introduced by the boundary condition. Figure 5.75 shows that the temperature fluctuation extracted from the inlet boundary condition is in good agreement with the forced signal, which confirms the proper boundary condition setting.

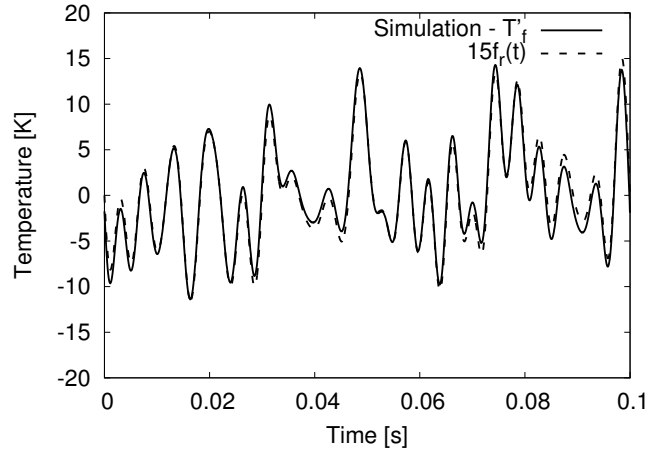


**Figure 5.75** Temperature fluctuation extracted from the numerical simulation compared with the forcing signal.

In the following, harmonic 3D fields of characteristic waves ( $A^+$ ,  $A^-$  and  $\sigma$ ) are computed using DFT. The real part of the entropy wave is compared with particle-lines traced from the inlet of the baseline flow simulation computed in M2 (cf. §5.1) and showed in Fig. 5.76. In the case of the NS simulation, the plane entropy wave introduced at the inlet is immediately deformed by the no-slip condition imposed at the walls, forming a thermal boundary layer (which is not the case of the Euler simulation where the entropy wave is convected as a plane wave through the inlet duct, cf. Fig. 5.37). Therefore, from the inlet of the configuration, the entropy plane mode energy is transferred to radial modes. In the inlet duct, the prediction of the entropy front deformation computed with the particle-lines is in good agreement with the real part of the entropy wave. However, when the entropy front travels through the nozzle, it undergoes the effects of the nozzle jet: turbulent mixing, the nozzle jet modulation, the azimuthal velocity produced by the conservation of the radial equilibrium (cf. Figs. 5.12 and 5.13), and the acceleration at the centreline of the nozzle. Attenuation of the entropy wave (highlighted in Fig. 5.76) in this case is due to strong 3D effects produced by the nozzle. These phenomena are not taken into account when considering only particle-lines from a 2D transverse (XY) mean field, which assumes an axisymmetrical flow. However, it

gives an idea of the distortion of the entropy front through the nozzle. Two particle-lines traced from the inlet of the configuration ( $x = -0.1$  mm) are shown in Fig. 5.77. The first particle-line represents a time lapse of 1 ms, where the entropy wave has already lost its planar shape. The second particle-line is traced at 18.5 ms and is seen to be stretched over the entire nozzle length. A large part this particle-line is found to be inside (or very close to) the boundary layer, where the largest gradients in the velocity profile responsible for the entropy attenuation are located.

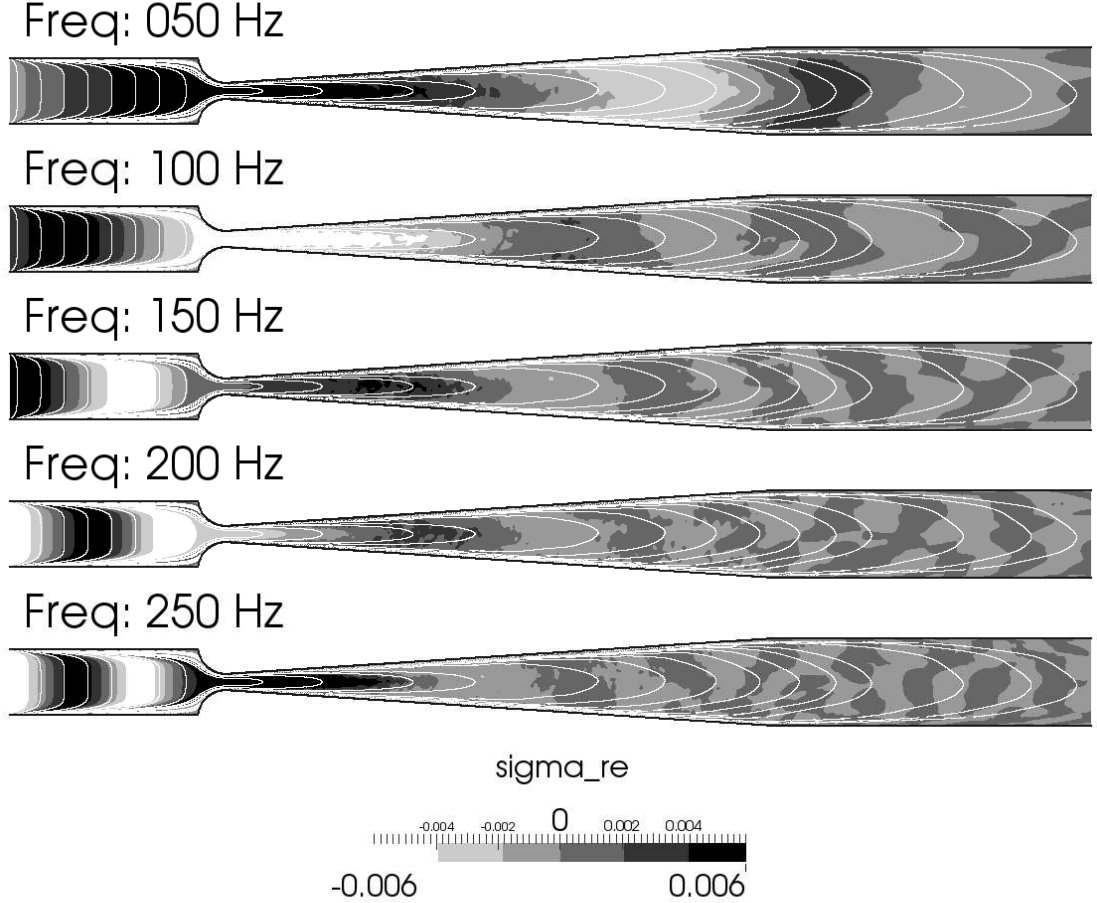


**Figure 5.76** Entropy wave real part compared with particle-lines traced from the inlet of the baseline flow.

The entropy wave in the inlet duct is decomposed into radial modes due to the boundary layer and the suction of the convergent, whereas in the downstream duct, azimuthal modes are generated due to the radial pressure gradient generated by the nozzle (radial equilibrium) as well as the motion of the nozzle jet. The five most important modes obtained by a modal decomposition (detailed in Appendix B) of the entropy fluctuation at the inlet and outlet of the nozzle are shown in Tables 5.9 and 5.10. Note that the



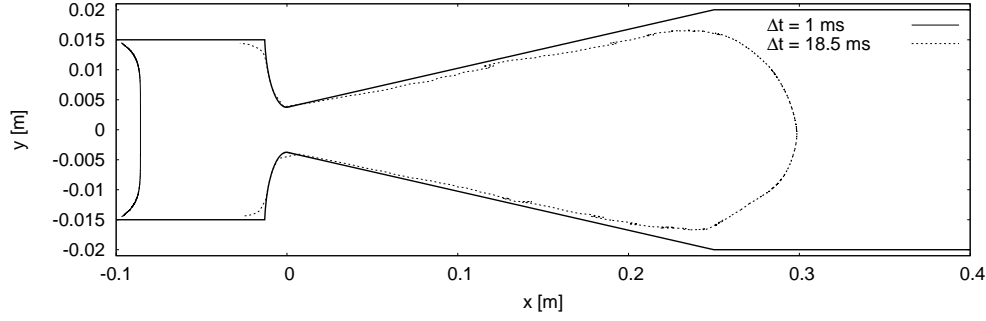


**Figure 5.77** Particles traced from the inlet of the baseline flow for two time lapses: 1 and 18.5 ms.

color scale in [Table 5.10](#) has been voluntarily saturated to see the shape of the different modes. At the inlet of the nozzle, the amplitude of the planar entropy mode is of the same order of magnitude as the second/third radial modes. However, the dominant mode is not planar but is instead the first radial mode (the planar mode dominates the low to mid frequencies in the Euler simulation, cf. [Tab. 5.7](#)). Moreover, the repartition of the energy between the different modes seems to be almost the same for all the frequencies. At the outlet of the nozzle, the energy scatters into radial modes, as in the inlet of the nozzle, but also into azimuthal and mixed modes. However, the amplitude of the different modes in the downstream ducts is highly attenuated after its passage through the nozzle. It is important to notice that the resultant modal decomposition between the Euler and Navier-Stokes (NS) nozzle outlet plane is completely different. In the case of the Euler simulation, the most important modes are only the planar and radial modes (cf. [Table 5.8](#)). In the NS simulation, the azimuthal modes at the outlet of the nozzle are dominant, which can be associated with the modal content of free jets ([Juve et al. 1979](#)).

To estimate the attenuation of the entropy harmonic fluctuations, the entropy flux is computed following [Eq. \(5.14\)](#) at different sections of the EWG: (1) the inlet of the mesh ( $x = -0.1$  mm), (2) the inlet of the nozzle ( $x = -0.013$  mm), (3) the outlet of the nozzle ( $x = 0.25$  mm), and (4) the outlet of the mesh ( $x = 0.4$  mm). Then the ratio between the entropy flux at these different sections is compared with the inlet entropy flux in [Fig. 5.78](#). The attenuation of an entropy wave in a turbulent channel flow has already been addressed by [Morgans et al. \(2013\)](#) and [Giusti et al. \(2016\)](#). In these works, dissipation of the entropy wave is found to be negligible, while its attenuation is almost solely due to shear dispersion issued by the mean velocity profile. In this case, no turbulence is present in the inlet duct, however turbulent structures are developed due to the turbulent vortices created near the nozzle throat. Attenuation due to the non-homogeneous mean velocity profile is also present everywhere in the domain. From [Fig. 5.78](#), it can be seen that a strong attenuation of the entropy wave has been induced by the nozzle (in comparison with the Euler simulation). The cumulative effect of the

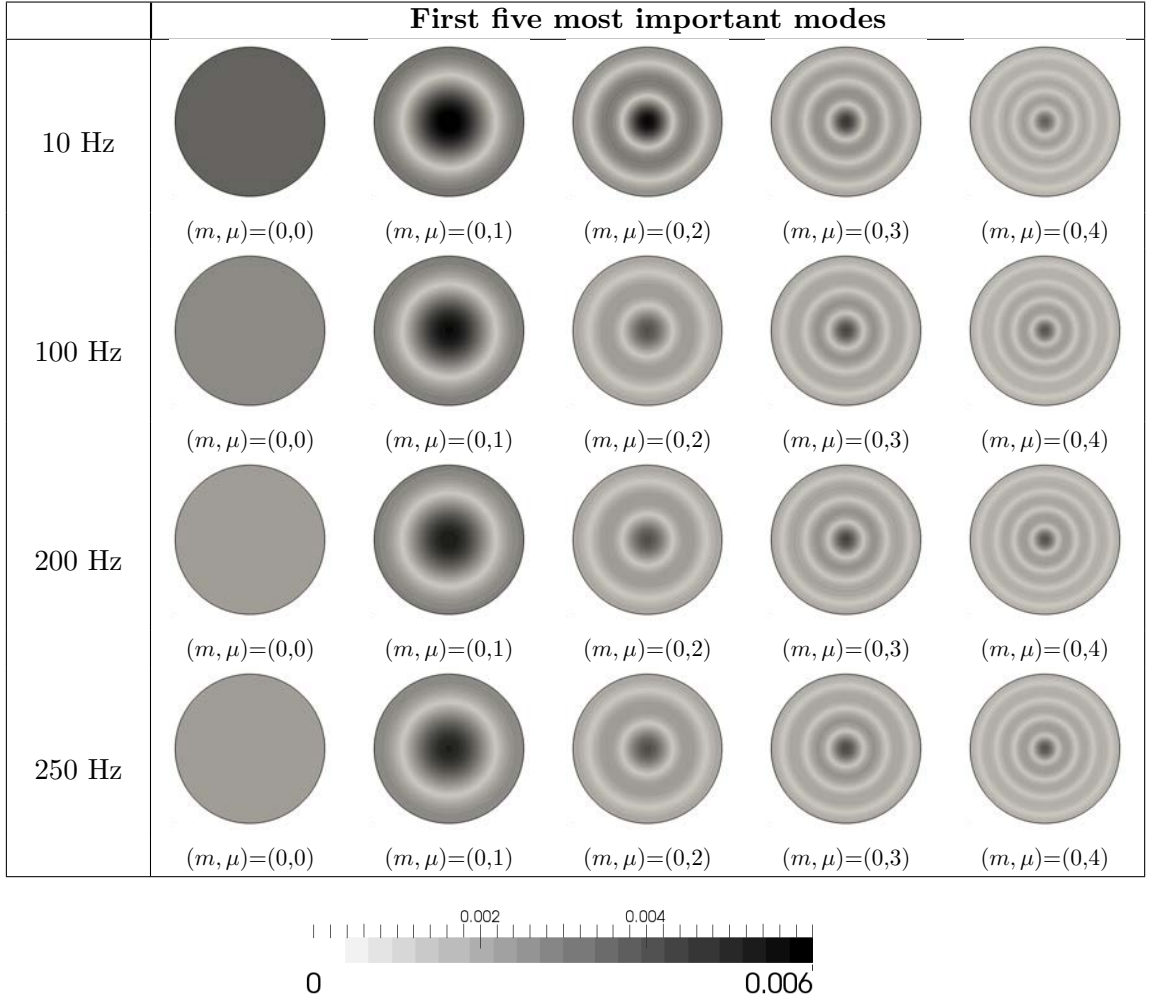


**Table 5.9** Modulus of the entropy wave modal decomposition extracted at the inlet plane of the nozzle ( $x_{N_{in}}$ ).  $m$ : order of the azimuthal mode,  $\mu$ : order of the radial mode.

strong acceleration of the entropy wave through the nozzle and the no-slip condition imposed at the walls produces a strong stretching of the entropy front (cf. Fig. 5.77). These two effects generate strong gradients in the velocity profile and therefore in the entropy front, resulting in a stronger attenuation if compared to the Euler simulation. However, even if the entropy fluctuation is found to be strongly attenuated (the ratio of the entropy flux between the outlet of the nozzle and the inlet of the domain is almost zero at high frequencies), the entropy wave is mainly scattered spatially and it is not really dissipated (cf. Appendix D).

To evaluate the importance of the attenuation of the different modes through the nozzle, the entropy flux ratio is computed between the outlet of the nozzle and the inlet

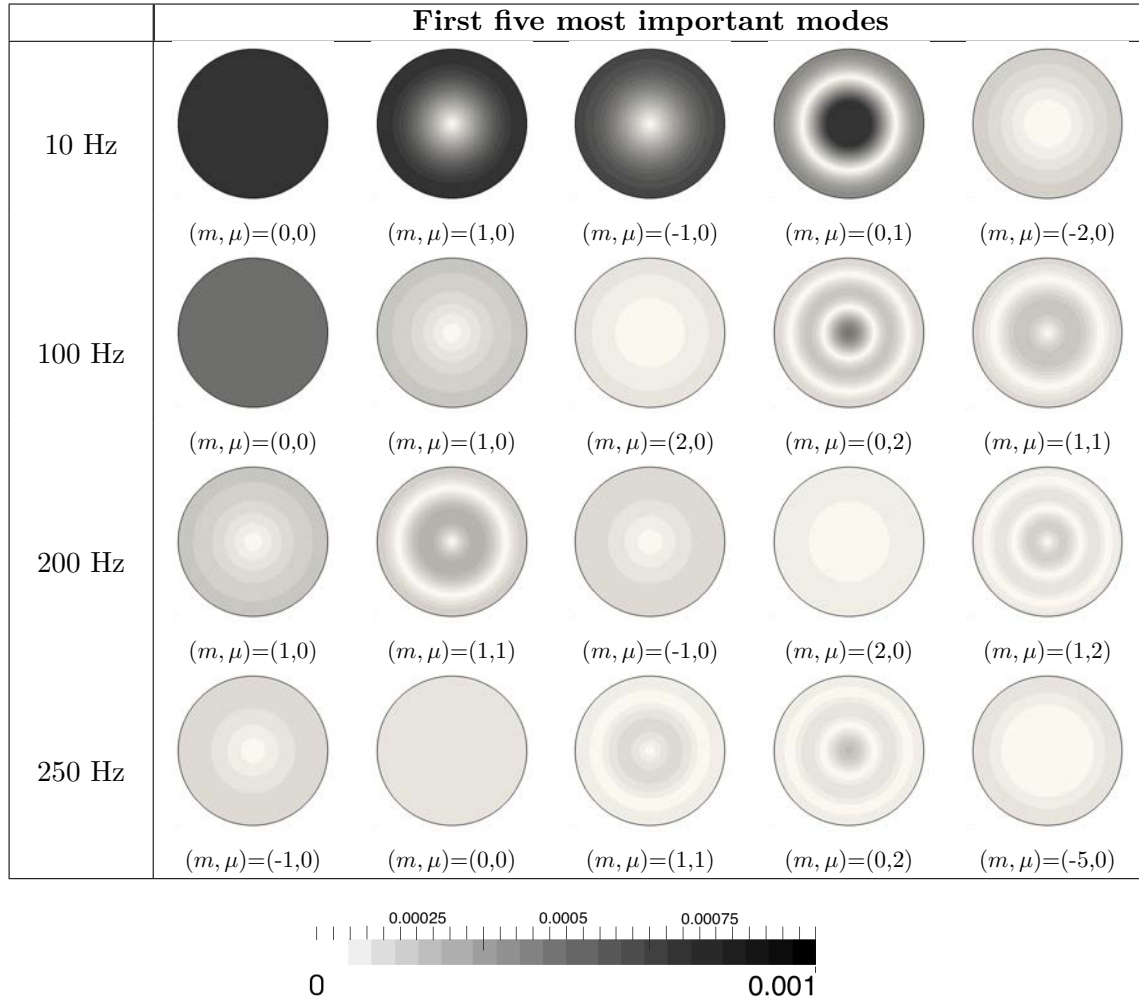


**Table 5.10** Modulus of the entropy wave modal decomposition extracted at the outlet plane of the nozzle ( $x_{N_{out}}$ ) ordered by the importance of its module.  $m$ : order of the azimuthal mode,  $\mu$ : order of the radial mode.

of the domain for the most energetic modes. In Fig. 5.79, the entropy flux contribution of the planar mode, the first three radial modes ( $(m, \mu)=(0,1)$ ,  $(0,2)$  and  $(0,3)$ ) and the first azimuthal mode ( $(m, \mu)=(-1,0)$  and  $(1,0)$ ) are compared with the inlet planar entropy mode flux. Up to about 60 Hz, the entropy planar mode appears to be the dominant mode. Afterwards, for higher frequencies, the contribution of the different modes (including the planar mode) is of the same order of magnitude and negligible compared to the amplitude of the inlet planar mode. One can hence conclude that after about 80 Hz, the entropy plane wave is almost fully attenuated through the nozzle. Furthermore, in comparison to the modal contribution obtained in the Euler simulation at the outlet of the nozzle (cf. Fig. 5.41), much more modes are needed to describe the

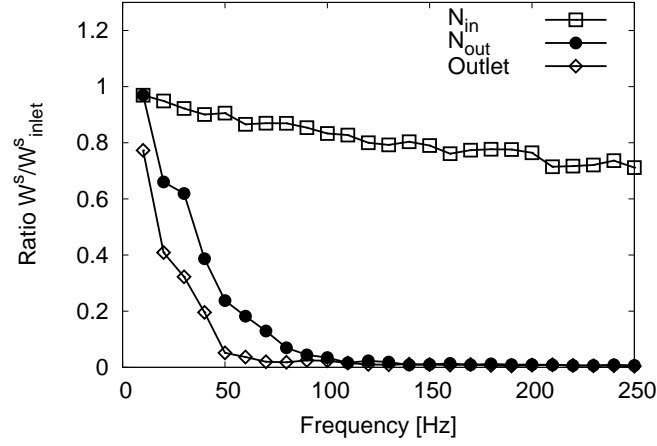


**Figure 5.78** Entropy flux ratio between different sections of the EWG (inlet and outlet of the nozzle and outlet of the domain) to the inlet of the domain.

total entropy flux.

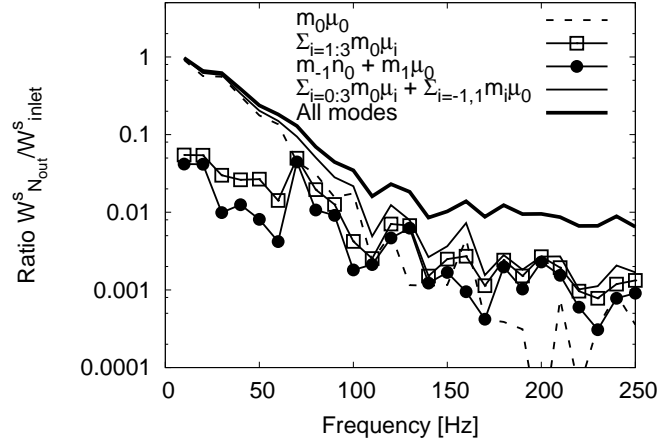


**Figure 5.79** Entropy flux of different modes at the outlet of the nozzle compared with the plane mode introduced at the inlet.

To compare with the analytical model presented in §2.2, only the planar mode is considered. The axial evolution of the entropy plane mode is shown in Fig. 5.80, where the amplitude of different harmonics is compared with the Euler simulation in Fig. 5.80a. For clarity, only the phase of the entropy plane wave computed in the LES is shown in Fig. 5.80b. The formation of a boundary layer by the NS simulation has an impact on the plane entropy mode, whose energy is transmitted into higher order modes immediately after its introduction through the inlet ( $x = -0.1$  m) making its amplitude decay. At

very low frequencies, the amplitude of the plane mode at the inlet of the nozzle is smaller than its amplitude at the outlet of the nozzle, which shows that the energy is not only transmitted into higher order modes but can also be redistributed into lower order modes. In the downstream duct, up to 100 Hz, the attenuation of the entropy planar mode seems to be almost linear along the stream-wise direction. For higher frequencies, the amplitude of the entropy plane wave is too attenuated to correctly estimate its attenuation in the stream-wise direction, as shown in [Tab. 5.10](#) and [Fig. 5.78](#).

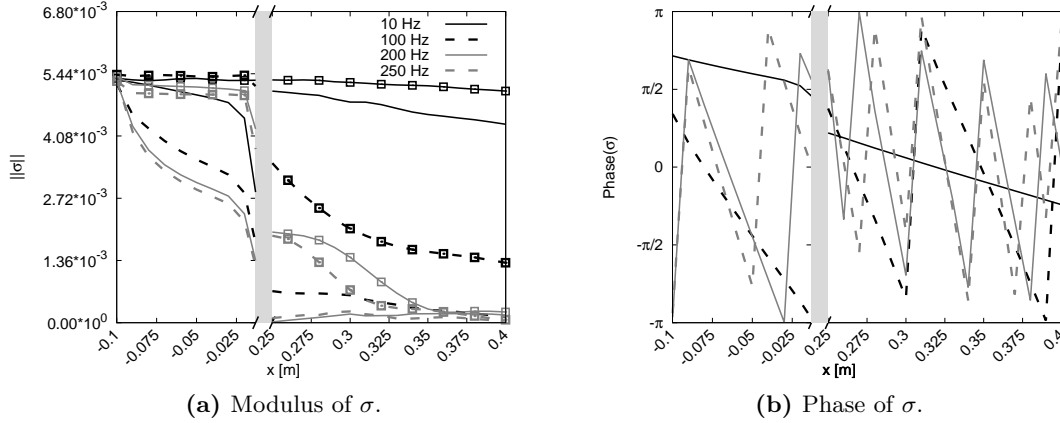


**Figure 5.80** Entropy wave  $\sigma$  in the upstream and downstream ducts of the EWG. Navier-Stokes simulation (lines). Euler simulation (lines with symbols). (Only harmonics 1, 10, 20 and 25 are presented).

The attenuation of the entropy plane wave can be estimated using the attenuation function of [Leyko et al. \(2010\)](#) (as done in the Euler numerical simulation in §5.3.2.1). In [Fig. 5.81](#), the entropy transmission coefficient computed between the inlet and the outlet of the LES domain is compared with [Leyko et al. \(2010\)](#) attenuation function and with the analytical transmission coefficient of the entropy wave computed by [Duran and Moreau \(2013a\)](#) methodology. The analytical method of [Duran and Moreau](#) assumes a quasi-1D flow, therefore no dispersion of the entropy wave due to transverse gradients of the mean flow can exist and the entropy wave is only convected through the nozzle (without attenuation). The attenuation function of [Leyko et al.](#) is the analytical solution of the convection of the entropy wave along a streamline computed from the baseline flow, therefore exact. In this case, the analytical evaluation of the attenuation of the entropy plane wave in 2D (performing an azimuthal average of the mean flow) and in 3D is found to be equivalent. However, this analytic evaluation underestimates the attenuation of the entropy plane wave obtained in the numerical simulation. This result is very important because it highlights that the attenuation of the entropy wave in this nozzle test case is not only due to the effects of the mean flow as found by [Morgans et al. \(2013\)](#) and [Giusti et al. \(2016\)](#), but it seems to be enhanced by other unsteady features of the flow like the turbulent mixing. However, this supplementary attenuation of the entropy plane

wave does not mean that the entropy wave is dissipated by the unsteady phenomena, the entropy wave is only scattered into higher modes as explained in [Appendix D](#). Finally, concerning the phase of the entropy-entropy transfer function (i.e. [Fig. 5.81b](#)), a good agreement is found between the LES and the analytic model. This result was however expected since the bulk velocity of the NS simulation and the isentropic velocity are found to be in very good agreement (cf. [Fig. 5.7](#)), as a consequence, the entropy plane wave is convected at the same velocity in both simulations.

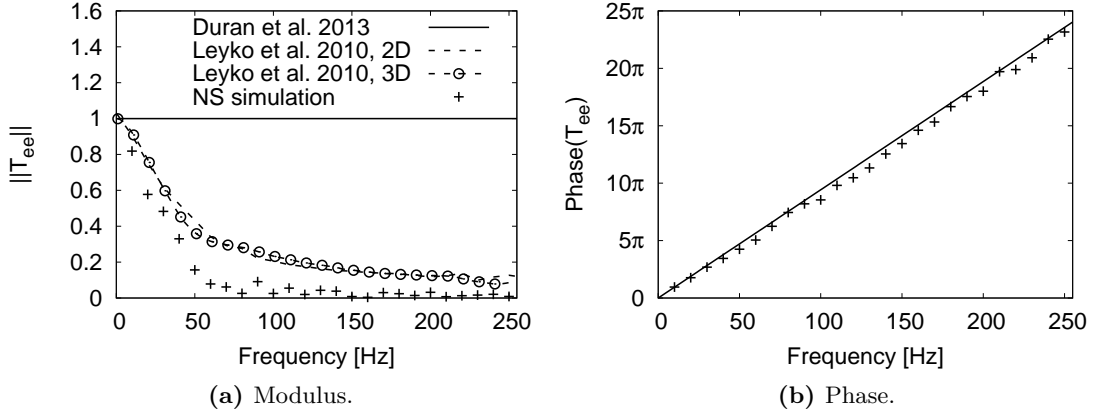


**Figure 5.81** Entropy-entropy transfer function  $T_{ee}$ .

Once the attenuation of the entropy wave in the NS simulation has been addressed, the generation of acoustic waves produced by the acceleration of this entropy wave through the nozzle can be studied. To do so, the characteristic acoustic plane waves are computed using the same methodology already explained in the previous sections. Then, the characteristic filtering of [Kopitz et al. \(2005\)](#) is applied to the acoustic waves to remove the contribution of hydrodynamic perturbation from the computed acoustic waves. Finally, the entropy-acoustic transfer functions of the nozzle are computed using [Eqs. \(5.27a\) and \(5.27b\)](#) to remove the reflected acoustic waves at the boundary conditions. [Figures 5.82 and 5.83](#) show the entropy-acoustic transfer functions of the nozzle computed from the compressible Navier-Stokes LES simulation. [Figure 5.82](#) shows the entropy-acoustic transmission coefficient, whose amplitude and phase are found to be in complete disagreement with results obtained at low frequencies with the analytical model. Yet, the amplitude of this transmission coefficient from mid to high frequencies ( $f \geq 120$  Hz) appears to be in better agreement with the Euler numerical simulation. Indeed, the numerical simulations take into account the dispersion/attenuation of the entropy wave through the nozzle, whose effect increases with frequency. The analytical model predicts an amplitude that increases monotonously with the frequency (where the compact solution is close to zero), whereas in the NS numerical simulation, the amplitude of the transmitted wave seems to decrease with the frequency (for the frequencies

of interest). Furthermore, the greater disagreement with the NS LES simulation is found to be at the lowest frequencies, where the Euler simulation and the analytical theory are found to be in good agreement. Therefore, the disagreement in the transfer functions found at low frequencies can only be attributed to viscous effects and will be discussed later in this section. Concerning the phase, the delay between the acoustic and the entropy wave of the numerical simulation seems to be smaller than the one predicted by the analytical method. Now, Fig. 5.83 shows the entropy-acoustic reflection coefficient, whose amplitude and phase are very similar to the transmission coefficient. The greater disagreement in the amplitude is found to be at the lowest frequencies, where the Euler simulation and the analytical model are in agreement and predict almost a nil amplitude of the reflection coefficient. For larger frequencies, the numerical simulations amplitude is in better agreement. Finally, the phase delay between the reflected acoustic wave and the entropy wave is smaller (lower slope) in the numerical NS simulation.

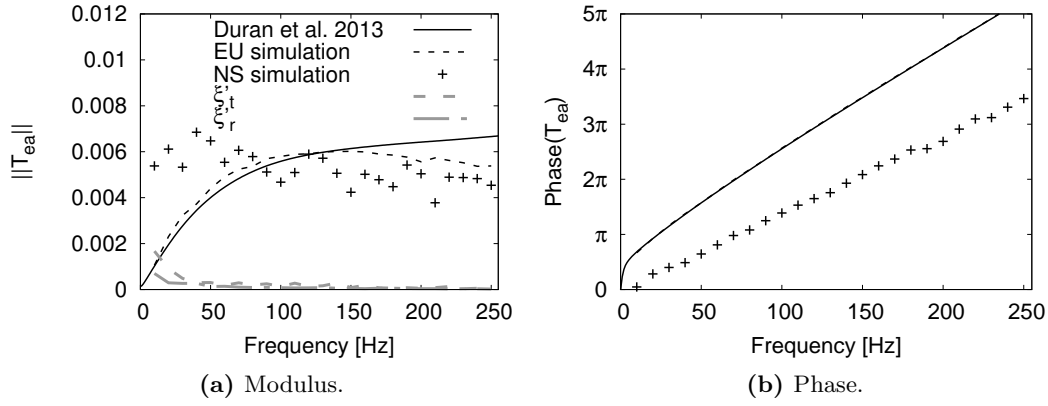


**Figure 5.82** Entropy-acoustic transmission coefficient  $T_{ea}$  filtered from boundary condition reflections.

In both entropy-acoustic transfer functions, the analytical solution of the Euler equations (cf. Duran and Moreau 2013a) predicts no (or almost zero) acoustic wave produced by the entropy disturbance close to the zero-frequencies. This result has also been confirmed by the transfer functions obtained in the Euler simulations of §5.3.2.4. It is important to remember that the experimental entropy spot characteristic time scale is 0.1 s ( $f = 10$  Hz). Therefore, according to the analytical and Euler entropy-acoustic transfer functions, almost no acoustic wave is generated at this frequency. On the contrary, the NS-TF show that it is at the very low frequencies that the amplitude of the generated acoustic waves is stronger. This result may explain the disagreement between the analytical modelling and the full compressible NS LES simulation of the EWG subsonic test case shown in Fig. 4.11a. Indeed, the indirect noise at low frequencies was strongly underestimated by the analytical modelling. It has been shown in the above paragraphs that the acceleration of vorticity waves created near the nozzle

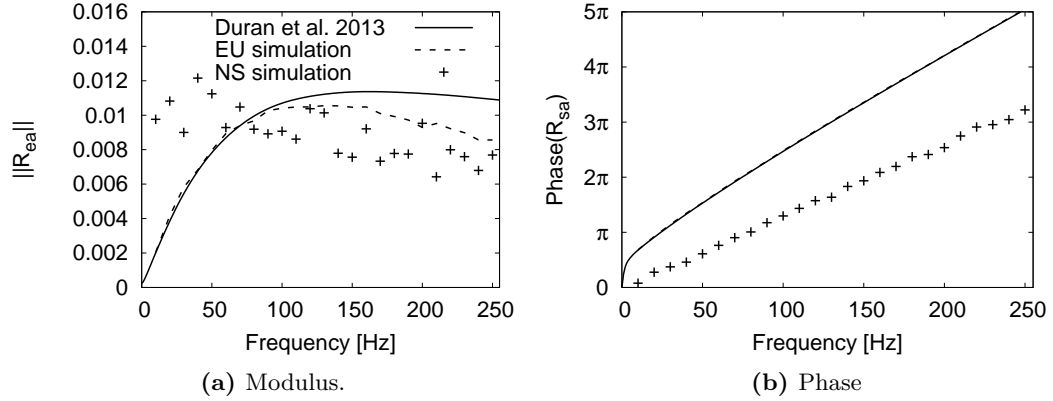


**Figure 5.83** Entropy-acoustic reflection coefficient  $R_{ea}$  filtered from the boundary conditions reflections.

throat produces an additional noise source particularly important at the low frequencies. Furthermore, according to [Duran and Morgans \(2015\)](#) (and highlighted in the entropy forced Euler simulations of §5.3.2.4) the acceleration of an azimuthal entropy wave produces a vorticity wave. Therefore, following the methodology already used in §5.3.2.4 and §5.3.3.1, the entropy-acoustic transmission coefficient associated to the generated acoustic wave from a vorticity forcing is estimated using the compact theory of [Cumpsty and Marble \(1977a\)](#). To do so, 1D vorticity fields are computed and compared to the ones obtained in the entropy forced Euler simulation. These 1D vorticity fields are represented in [Figs. 5.84](#) and [5.85](#), where the axial vorticity is found to be negligible in comparison to the other vorticity components. The amplitude of the obtained vorticity fluctuations is at least one order of magnitude higher than the one obtained in the Euler simulations and decreases more slowly in the NS simulation. The azimuthal vorticity fluctuation is found to be the dominant component. The radial vorticity component in the case of the NS simulation is however of the same order of magnitude and 1000 times stronger than the one computed in the Euler simulation. The effect of vorticity seems to be concentrated at the low frequencies, for higher frequencies their amplitude decreases rapidly (as already found in the acoustic forced simulations). The maximal vorticity fluctuation is located at approximately  $x = 5$  mm from the nozzle, where [Cumpsty and Marble \(1977a\)](#) jump conditions are computed between this position and the nozzle outlet ( $x_{N_{out}} = 250$  mm). From here, an entropy-acoustic transmission coefficient associated to the acoustic wave generated by a vorticity forcing can be computed. These transmission coefficients (associated to each vorticity wave) are illustrated in [Fig. 5.82a](#), where their amplitude at low frequencies is not negligible and of the same order of magnitude as the entropy-acoustic transmission coefficient. This result confirms that vortex sound is responsible for the differences highlighted in the entropy-acoustic transfer functions at low frequencies and that vortex sound should be taken into account in the computation of these transfer functions. The study of [Howe \(2010\)](#), describes



the influence of vorticity on the sound emitted by the acceleration of an entropy wave enunciating that vortex sound is strongly correlated to the entropy noise and can reduce the overall sound level (specially at higher subsonic Mach numbers). However, in the present study, vorticity waves computed from the entropy forced simulation seem to be coupled with the entropy wave (generation of vorticity wave) in a constructive way so that it generates more acoustic waves and this at low frequencies.

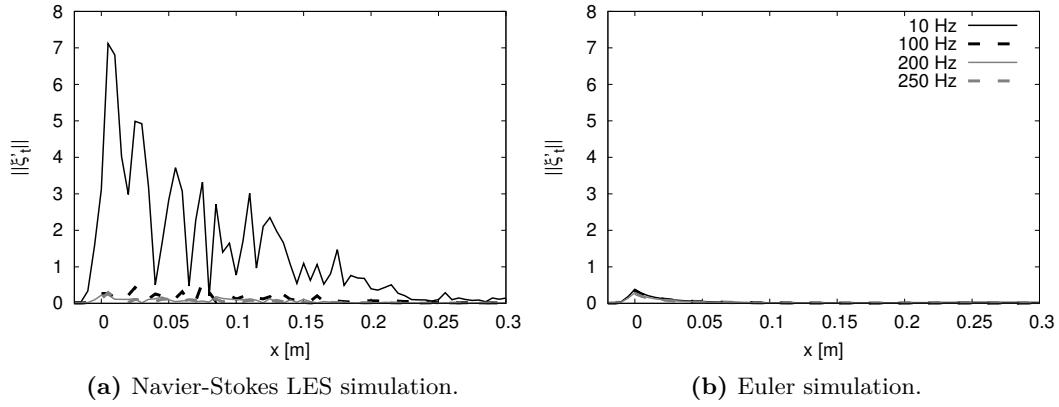


**Figure 5.84** Amplitude of the azimuthal vorticity wave ( $||\xi'_t||$ ) along the stream-wise coordinate for different harmonics.

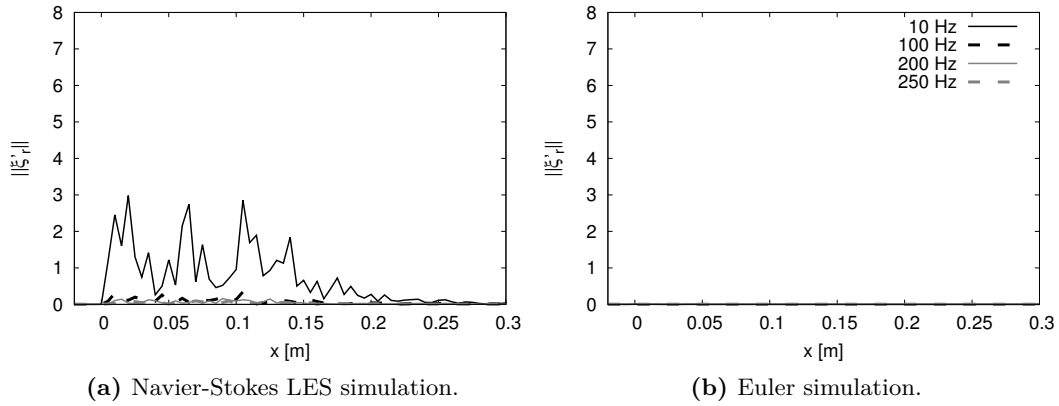


**Figure 5.85** Amplitude of the radial vorticity wave ( $||\xi'_r||$ ) along the stream-wise coordinate for different harmonics.

The transfer functions of the EWG nozzle were computed by LES using the Euler and the NS equations, allowing to determine the influence of the viscous effects. In the next section, these nozzle transfer functions are introduced in the analytical modelling of the EWG presented in §4.4. The main objective is to verify if these nozzle transfer functions,

that consider acoustic plane waves only are capable of retrieving the numerical results of the EWG LES simulation (cf. §5.2).

### 5.3.3.3 Application of the LES nozzle transfer functions into an analytical model

In this final section of combustion noise in nozzle flows, the NS-TF are introduced into the analytical propagation model described in §4.4. Indeed, replacing the analytical transfer functions obtained by the analytical resolution of the LEE (cf. Duran et al. 2013b) by the NS-TF should allow to retrieve the full compressible LES simulation presented in §5.2. To do so, the transfer functions need to be extrapolated to 0 Hz and interpolated. Instead of the classical approach of interpolation between points, it has been chosen to fit a polynomial through the computed points to obtain continuous functions rather than a piece-wise function. The interpolated transfer functions are represented in Figs. 5.86–5.91. These interpolated transfer functions, which resulted to be very different from the analytical ones can be directly introduced in the analytical model presented in §4.4. Doing this, viscous and geometry effects taken into account in the NS-TF can be introduced artificially in the analytical model of §4.4 to first compare the experiment LES simulation described in §5.2.2 to the new analytical result and then study different shapes and amplitudes of entropy forcings, different acoustic impedances, duct length and other parameters to study the generation of indirect combustion noise. To do so, the bulk temperature fluctuation measured in the numerical simulation of the EWG experiment is used as the reference temperature fluctuation ( $\Delta T_{bulk} \approx 16$  K) instead of the mean temperature indicated in the experimental data ( $\Delta T_{mean} = 13.4$  K). The same relaxation coefficients of the simulation are used to model the reflection coefficients in the analytical method, namely  $K_{in} = 50000$  and  $K_{out} = 160 \text{ s}^{-1}$ . Finally, the pressure traces extracted at the fourth microphone position ( $x_{mic_4} = 1150.5$  mm) obtained by the different approaches used in this manuscript are compared in Fig. 5.92. The viscous transfer functions (NS-TF), the inviscid analytical transfer functions (Invariants-TF) and the numerical simulation (LES) are compared. The numerical simulation and the analytical approach with the NS-TF are in very good agreement in terms of shape and amplitude of the signal. In Fig. 5.93, the analytical pressure signal obtained using the Invariants-TF and the NS-TF are decomposed into direct and indirect noise, showing (as already demonstrated by the LES analysis in §5.2) that direct noise in this simulation is negligible. The dissociation of direct and indirect noise shows (in the present test case) that direct noise is overestimated (as already highlighted by the amplitude of the acoustic transmission coefficient, i.e. Fig. 5.69) and indirect noise has been underestimated by the analytical solution of the LEE. These results show that viscous effects taken into account in the LES simulation, in particular the generation of vorticity fluctuations in the low frequency limit (Euler vorticity fluctuations being almost solely around the azimuthal direction and negligible compared to the NS vorticity fluctuations, cf. Figs. 5.84 and 5.85), have an important influence in the acoustic response of the nozzle to entropy and acoustic disturbances. Away from the low frequency limit, the generated vorticity fluctuation amplitude is negligible and the attenuation of the entropy wave through

the nozzle (taken into account in both the Euler and NS simulations) is responsible for the differences highlighted with the analytical model entropy-acoustic transfer functions. The use of the 2D methodology proposed by [Zheng et al. \(2015\)](#) computes the nozzle transfer functions taking into account the attenuation of the entropy waves through the nozzle, while considering acoustic generated waves as planar waves. This analytical methodology seems to be the most physical representation to describe the mid-to-high frequencies studied in this case. Nevertheless, the generation of vorticity waves is not taken into account and is found to have an important acoustic contribution at low frequencies. The methodology proposed by [Duran and Morgans \(2015\)](#), is capable of taking into account vorticity waves without the compact assumption used in this manuscript and could be a first step to better explain the differences found in the low frequency limit in the nozzle transfer functions.

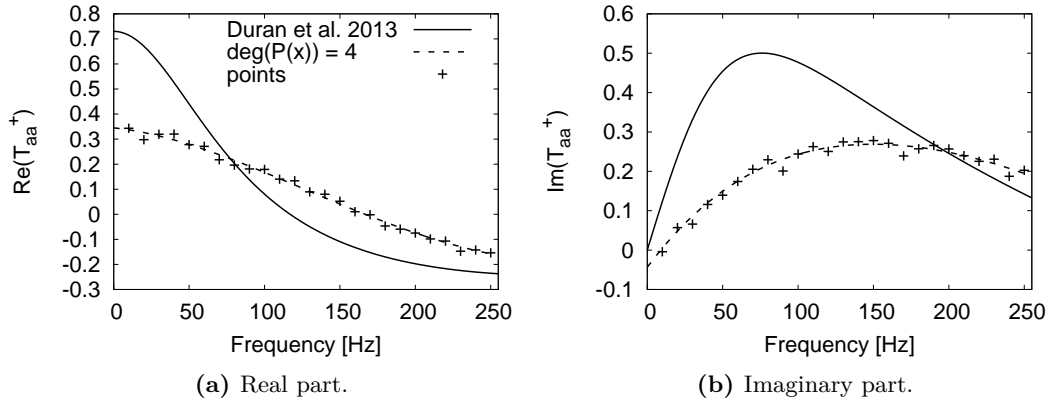


**Figure 5.86** Interpolated Navier-Stokes upstream acoustic-acoustic transmission coefficient  $T_{aa}^+$ .

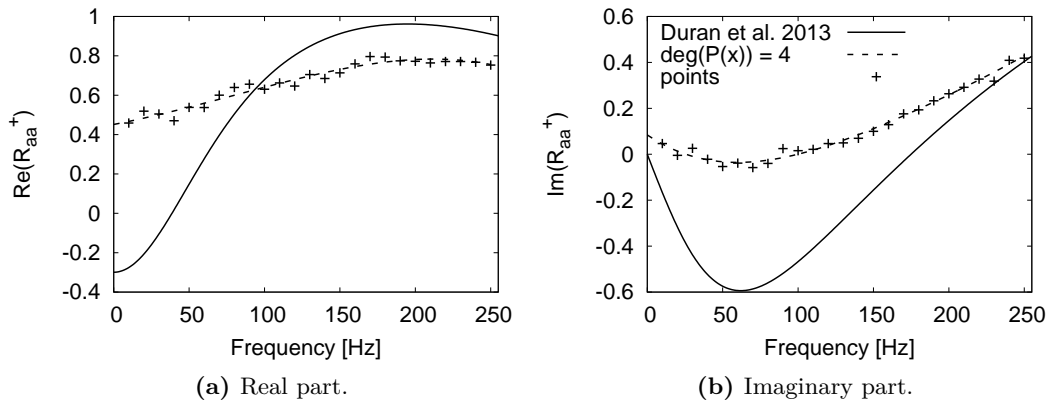


**Figure 5.87** Interpolated Navier-Stokes upstream acoustic-acoustic reflection coefficient  $R_{aa}^+$ .

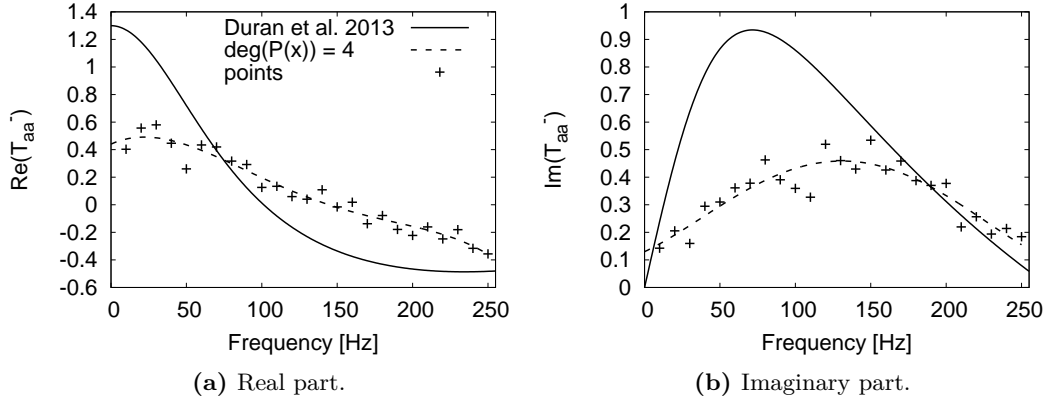


**Figure 5.88** Interpolated Navier-Stokes downstream acoustic-acoustic transmission coefficient  $T_{aa}^-$ .

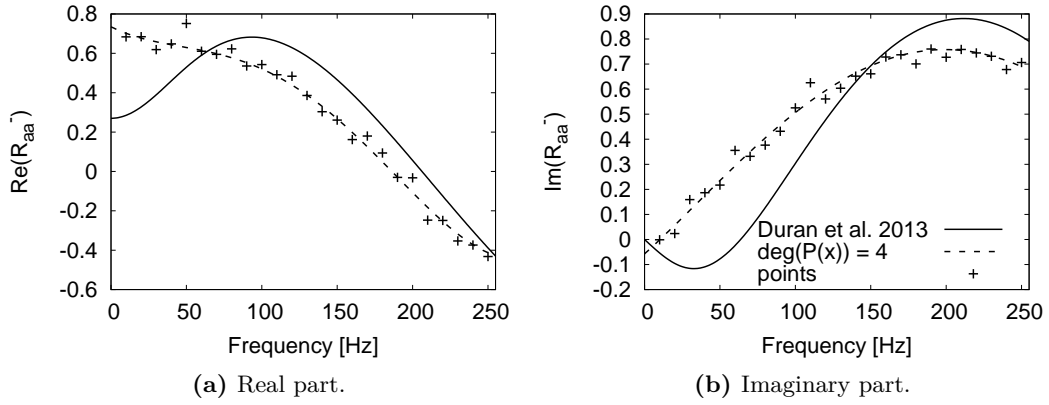


**Figure 5.89** Interpolated Navier-Stokes downstream acoustic-acoustic reflection coefficient  $R_{aa}^-$ .

To conclude this chapter, the noise peak evolution investigated analytically in [Chapter 4](#), [Fig. 4.16](#), that has pushed the scientific community to understand why indirect combustion noise saturates for Mach numbers close to the choked condition is plotted again in [Fig. 5.94](#). This time, the new point that corresponds to the LES of the experiment conducted in [§5.2](#) and the analytical model developed in [Chapter 4](#) with the NS-TF is added. This plot allows to illustrate multiple characteristics of the generation of indirect combustion noise in this experiment: First, the different analytical curves (Invariants-TF and [Duran et al. 2013b](#)) show the strong variability of the generated noise issued by the effect of the inlet acoustic impedance. Second, the viscous effects taken into account in the LES simulation and the NS-TF, have also a very important role in the generated peak noise, where for strictly the same configuration the NS-TF

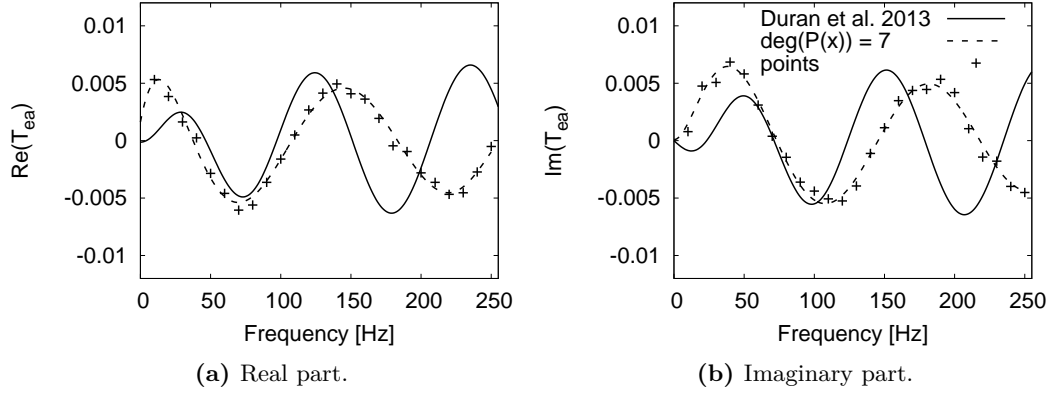


**Figure 5.90** Interpolated Navier-Stokes upstream entropy-acoustic transmission coefficient.  $T_{ea}$ .

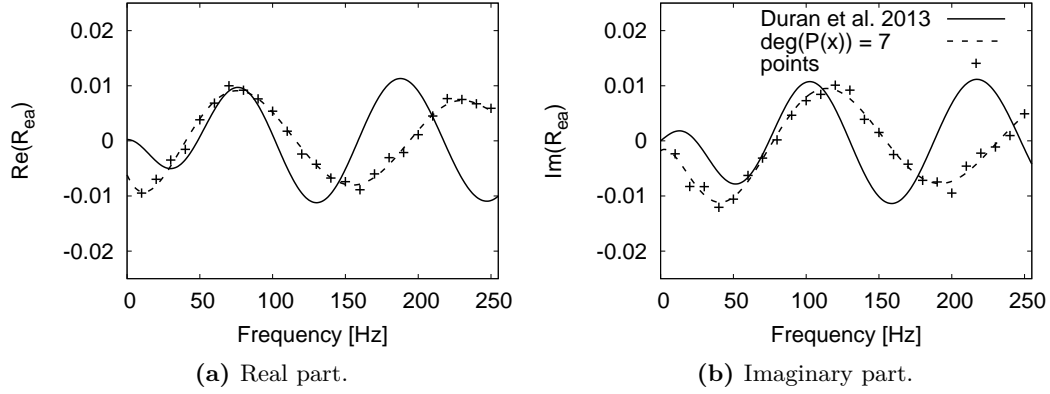


**Figure 5.91** Interpolated Navier-Stokes upstream entropy-acoustic reflection coefficient  $R_{ea}$ .

predicts a peak noise twice as big as the one predicted with the Invariants-TF. And third, that noticeable progress in the understanding of the indirect combustion noise generation mechanism has been achieved.

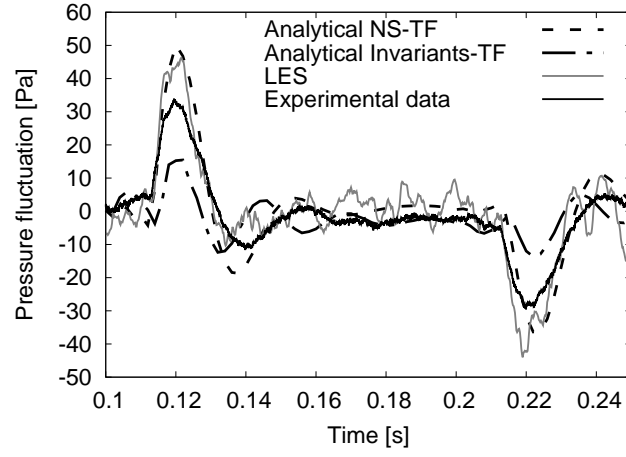


**Figure 5.92** Pressure traces measured at the fourth microphone ( $x_{mic_4} = 1150.5$  mm) for the different analytical approaches, the numerical LES simulation and the experimental data.

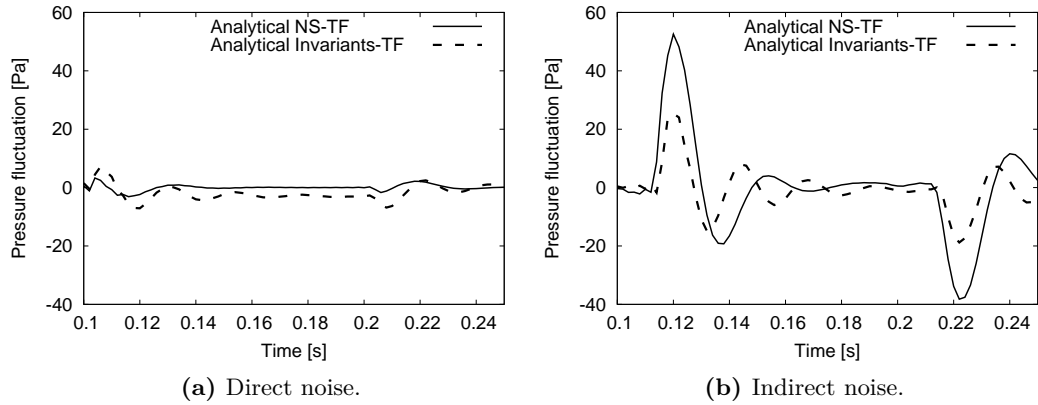


**Figure 5.93** Contribution of direct/indirect noise on the pressure traces measured at the fourth microphone ( $x_{mic_4} = 1150.5$  mm).

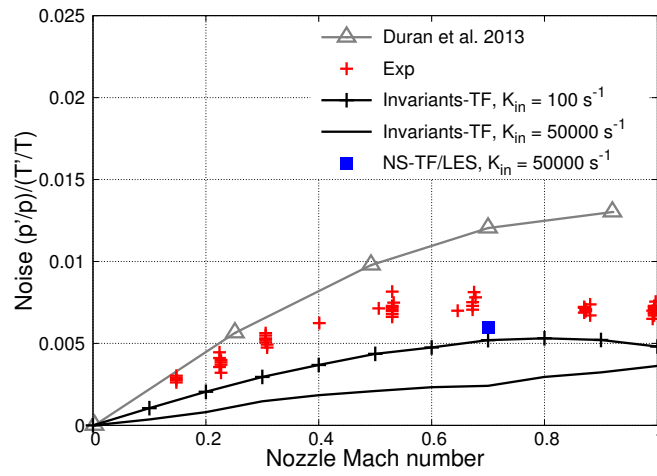


**Figure 5.94** Evaluation of the noise peak pressure at the outlet of the EWG as a function of the throat Mach number.

## 5.4 Conclusions

Within this chapter, the EWG experiment by [Bake et al. \(2009\)](#), designed to study the generation and transmission of indirect combustion noise has been studied using different approaches: from the analytical modelling to the numerical simulation using the Euler and the NS set of equations. First, the analytical compact studies carried out by [Leyko et al. \(2011\)](#) in the framework of the choked nozzle with a shock and by [Duran et al. \(2013b\)](#) in the framework of a subcritical nozzle flow ( $M_{N_{th}} = 0.7$ ) have been recomputed. This time, the non-compact frequencies have been taken into account solving analytically the LEE using the invariants methodology of [Duran and Moreau \(2013a\)](#). The operating points studied showed that two parameters have a strong influence on the generated pressure signals: the shape of the temperature fluctuation and the acoustic impedances (boundary conditions). The shape of the temperature fluctuation is controlled by the model describing the heating device. Therefore, the model proposed by [Leyko et al. \(2011\)](#) has been extended to consider individually each of the heated rings composing the heating device and the experimental ignition sequence. As for the acoustic impedances, the outlet acoustic impedance was measured and [Leyko et al. \(2011\)](#), using NSCBC boundary conditions, fitted the relaxation coefficient  $K_{out}$  numerically to be the closest as possible to the experimental value. However, the inlet acoustic impedance has not been measured and it is found to have an important influence on the generated pressure signals, especially for the subsonic test case. Indeed, analytical results obtained for the supersonic test case have small variability when considering an inlet reflection coefficient between -1 and 0, taking into account the different heating rings or the compact/non-compact solution. However, the inlet acoustic impedance, the ignition sequence of the heating device and the non-compact solution have a strong influence on the generated pressure signals of the subsonic test case. The heating device is found to be compact for acoustics but non-compact for the convection of the entropy wave. Therefore, the ignition sequence of the heating device is important and needs to be taken into account. The inlet acoustic impedance has also a strong variability in the results of the generated pressure fluctuations, where the closest results to the experimental data were found to be with a reflection coefficient between -1 and 0. The non-compactness of the nozzle has also been demonstrated, and for  $R_{in} = -1$ , the compact solution predicts almost solely direct noise, while the non-compact solution predicts an indirect noise dominance. Finally, the analytical study of the EWG subsonic test case did not succeed to find a correct agreement with the experimental data. However, guidelines about the influence of the different parameters have been found.

To obtain better insight in the indirect noise generation phenomena, the subsonic test case, in which the analytical methodology seems to lack understanding to reproduce the experimental results, has been chosen to be studied with LES. Indeed, other studies like the ones conducted by [Muhlbauer et al. \(2009\)](#) and [Lourier et al. \(2014\)](#), in which an URANS methodology has been used to reproduce the EWG subsonic test case have found good agreement with the experiment. Therefore, viscous effects, at least on the



mean flow (RANS do not give any turbulent fluctuations), can be a key element in the acoustic response of the nozzle to entropy disturbances. With this in mind, the EWG subsonic test case has been computed using a LES methodology. Following the analytical guidelines, a reliable model to describe the heating device has been proposed and the inlet acoustic reflection coefficient has been set to  $R_{in} = -1$ . For the heating device, it has been chosen to introduce an energy source term to model the heating produced by each heated ring. Doing so, direct noise is generated when the temperature rises or decreases and indirect noise is generated with the acceleration of the hot spot through the nozzle (as in the experiment). The results of the LES simulation are in good agreement with the experimental values, even if the exact inlet acoustic impedance is not known. In parallel, in order to study the generation of only indirect noise, the 2D temperature field generated next to the heating device has been extracted and introduced as a temperature fluctuation by the inlet boundary condition of a new LES prediction. Doing so, no direct noise is generated. This simulation showed that the experiment produces almost solely indirect noise (which is in agreement with the analytical study using the same acoustic impedances and the non-compact solution of the LEE). Finally, the convection of the entropy hot slug through the EWG configuration has been studied. An analytical method based on the energy transport equation has been proposed to follow the position of the hot slug along the EWG without dissipation (as assumed by the analytical model of [Duran and Moreau 2013a](#)). Comparing the shape of the entropy hot slug at different positions and times between the numerical LES simulations and the analytical transport of the same hot slug allowed to estimate the dispersion undergone by the hot slug through the EWG configuration. Conclusions are that the hot slug shape is conserved through the nozzle and only dispersed by non-homogeneous mean flow in the downstream duct, in agreement with the previous DNS of [Morgans et al. \(2013\)](#) and [Giusti et al. \(2016\)](#).

In order to understand why the results obtained in the LES simulation are in better agreement with the experiment, the acoustic response of the nozzle to ingoing harmonic acoustic and entropy disturbances has been computed. First, the transfer functions of the nozzle have been computed neglecting the viscous effects (using Euler equations). This step, allowed to validate the methodology to compute the nozzle transfer functions in the framework of quick and low storage simulations. Furthermore, since the characteristics of the flow are almost the same as the ones assumed by the solution of the quasi-1D LEE used for the analytical model ([Duran and Moreau 2013a](#)), similar transfer functions should be obtained. The methodology has been validated and the acoustic-acoustic transfer functions of the nozzle Euler simulation are superimposed with the analytical model of [Duran and Moreau \(2013a\)](#). However, when computing the entropy-entropy transmission coefficient, the scattering of the entropy plane wave into radial modes, and the generation of vorticity waves due to the acceleration of a radial entropy disturbance through the nozzle are highlighted. The attenuation of the entropy plane wave at higher frequencies is found to be responsible for the differences between the entropy-acoustic transfer functions computed in the Euler simulation compared with the analytical theory. Concerning the vorticity generated waves produced by the acceleration of a radial entropy

disturbance, which should affect the lowest frequencies, no significant differences with the simulation and the analytical theory have been found.

Finally, the transfer functions of the nozzle have been computed taking into account viscous effects (using compressible NS equations). These transfer functions are found to have significant differences at the low frequency range compared with the analytical theory and the computed Euler transfer functions, where vortex sound may be responsible for these discrepancies. Indeed, the vorticity waves amplitude generated in the Euler simulations is found to be negligible compared to the amplitude of vorticity wave in the NS simulations. The influence of the generated acoustic waves due to the acceleration of a vorticity wave has been estimated using the compact theory of [Cumpsty and Marble \(1977a\)](#), finding that vortex sound can not be neglected from the computation of the nozzle transfer functions. Concerning the convection of entropy disturbances, the entropy plane wave is highly attenuated through the nozzle. The coupling of the no-slip boundary condition applied at the walls and the strong acceleration of the flow produced by the nozzle make the entropy front to be strongly stretched through the nozzle (the front occupies the total nozzle length), generating strong gradients that attenuate the entropy wave. Furthermore, in the LES simulation, the scattering of the entropy wave into radial, azimuthal and even mixed modes produced by the unsteadiness of the nozzle jet has been highlighted. In this case, the entropy transfer function has been computed using the attenuation model of [Leyko et al. \(2010\)](#), where an azimuthal average of the flow has been performed to compute 2D streamlines and compared to the attenuation function obtained using 3D streamlines. Both attenuation functions are found to be equivalent (in the NS simulation) and both underestimate the attenuation of the entropy plane wave extracted from the simulation. This result suggests that the unsteady features of the flow as turbulent mixing improve the attenuation of the entropy plane wave. Finally, the entropy generated noise is found to be coupled to vorticity generated noise in a constructive way. This observation contradicts the results found by [Howe \(2010\)](#), where vorticity generated noise attenuates entropy generated noise.

Differences found between the NS and the analytical entropy-acoustic transfer functions are attributed to two effects: in the low frequency range, where the vorticity fluctuations are the strongest, the interaction between vortex sound and entropy noise is responsible for the increased generated acoustics. For higher frequencies, it has been found that it is the deformation of the entropy wave through the nozzle that is responsible for the decay of the amplitude of the generated indirect noise. Finally, in the last part of this chapter, the analytical nozzle transfer functions used in §4.4 to carry out the analytical study of the EWG subsonic test case are replaced by the transfer functions obtained by the LES simulations and compared with the numerical simulation of the experiment described in §5.2.2. The generated pressure signal obtained by the analytical modelling using the transfer functions obtained in LES is found to be in very good agreement with the numerical simulation pressure signal at the fourth microphone position. Using this analytical methodology, the contribution of direct and indirect noise on

the overall pressure signal can be obtained, showing that the transmitted noise in the experiment is almost solely resulting from the indirect noise generation mechanism.

Some perspectives for this work are: for the entropy-acoustic transfer functions at high frequencies, the attenuation of the entropy wave should be taken into account. This can be done by the 2D analytical model of [Zheng et al. \(2015\)](#). Another proposition should be by extending the invariants methodology of [Duran and Moreau \(2013a\)](#) to consider the attenuation of the entropy wave using the attenuation function of [Leyko et al. \(2010\)](#), which in accordance with the presented results is very reliable. Nonetheless, none of these methods is capable to consider azimuthal fluctuations as vorticity, which has been found to have an important influence in transfer functions at low frequency. The first step to improve these developments could be to use the [Cumpsty and Marble \(1977a\)](#) compact assumptions (as done in this manuscript) or its non-compact extension proposed [Duran and Morgans \(2015\)](#). However, the vorticity generation at the nozzle due to the transition to turbulence throat is still to be computed.

In the next part of this thesis, combustion noise is studied in a more realistic configuration, i.e. a high pressure, transonic turbine stage. In this turbine case, the nature of the flow makes that a quasi-1D model as the one used in this section is no longer valid and more advanced modelling is necessary. Indeed, the turbine blades induce a strong tangential deviation of the flow, the annular duct cross-section is rarely constant, which induce a variation in the radial component of the velocity and the presence of secondary flows make the topology of the turbine flow strongly 3D. However, for its analytical study, the strong assumption of a 2D flow is done considering only the axial and azimuthal components of the velocity vector. Furthermore, other difficulties as the rotation of the rotor, flow separation and the presence of shock waves will render the analysis of combustion noise more realistic and complicated.



## Part II

# Towards a better understanding of combustion noise: Study of noise generation in a turbine stage



# Table of Contents

---

<b>6</b>	<b>Study of indirect combustion noise in a high-pressure turbine stage</b>	<b>169</b>
6.1	Introduction . . . . .	169
6.2	The MT1 turbine stage indirect combustion noise analysis . . . . .	171
6.2.1	Numerical methodology . . . . .	172
6.2.2	The MT1 baseline flow simulation . . . . .	174
6.2.3	The MT1 entropy forced simulation . . . . .	186
6.2.4	Comparison of the numerical results to the analytical compact actuator disk theory . . . . .	199
6.3	Conclusions . . . . .	210

---





## Chapter 6

# Study of indirect combustion noise in a high-pressure turbine stage

### 6.1 Introduction

The study of combustion noise generation and transmission in an aeronautical engine is quite complex. The heat release fluctuations responsible for the direct noise generation mechanism are indeed generated by a turbulent reacting flow, where turbulence and combustion alone are already complex phenomena to describe (very small characteristic lengths and time scales). Temperature and pressure fluctuations (acoustic waves) generated by these heat release fluctuations are then transported through the combustion chamber and the turbine stages, where indirect combustion noise generation takes place (transport of temperature fluctuations through a non-homogeneous flow). To better understand the responsible phenomena of combustion noise generation, each problematic is usually subdivided into more fundamental independent problems. In [Part I](#), the generation and transmission of indirect combustion noise has been addressed in the framework of temperature fluctuations generated by a heating device and accelerated through a nozzle. This studied test case involved multiple simplifications of the initial complex geometry problem: no combustion, a globally axisymmetrical flow (without deviation produced by the turbine blades), no rotating parts and a shape and frequency of the induced temperature fluctuations that were controlled by a heating device and not just the result of the interaction between turbulence and flames. In this [Part II](#), the combustion chamber and combustion itself are still not taken into account. Instead, the heat release fluctuations responsible for direct and indirect noise generation produced by a burner are chosen to be modelled using a cylindrical fluctuating energy source term. The temperature fluctuations generated by this fluctuating energy source term are then convected through a high pressure turbine stage and the resulting entropy noise is analysed. It is worth noting that the study of this entropy forced turbine test case involves different phenomena not taken into account in the test case studied in [Part I](#).

First of all, the entropy fluctuation size, in comparison with the nozzle test case, the introduced temperature fluctuation in the turbine is very small compared to the annular cross-section. Second, a strong azimuthal flow is induced by the turbine blades. Third, interactions with shocks and wakes are present. Finally, a rotating part (the turbine rotor) is taken into account in the simulations. All these differences make the study of the generation of indirect noise much more complex. However, this study is more realistic and represents the flow in a real turbo-engine better. It also generalizes the prior works of [Papadogiannis et al. \(2016\)](#) and [Wang et al. \(2016\)](#) to more realistic temperature spots as was done in the RECORD EU-project (cf. [Gaetani et al. 2015](#) and [Gaetani and Persico 2017](#)).

The configuration chosen for this specific study is the transonic high-pressure turbine stage MT1 (32 stator and 60 rotor blades) designed by Rolls-Royce. The experiment has been conducted by [Beard et al. \(2009, 2011\)](#), RANS numerical simulations by [Hosseini et al. \(2011\)](#) and [Salvadori et al. \(2011\)](#), while LES results have been obtained by [Wang et al. \(2013, 2014a, 2016\)](#) and [Papadogiannis et al. \(2014, 2016\)](#). The converged baseline flow computed in the work of [Papadogiannis et al. \(2016\)](#) and [Wang et al. \(2016\)](#) is here used to investigate the generation of indirect noise by non-planar entropy waves.

This final chapter is divided in four sections: In [§6.2.1](#) the numerical methodology adopted for the computation of the moving domain is explained. The second section, [§6.2.2](#), describes the numerical simulation of the non forced baseline flow. [§6.2.3](#) describes the numerical simulation in which a volumetric cylindrical energy source term is introduced to generate polychromatic temperature fluctuations. Note that, the generated temperature fluctuations are of the same magnitude as the temperature fluctuations produced in a real combustor engine ( $T' \approx 100\text{ K}$ ). Finally in [§6.2.4](#), the results of the entropy forced simulation are compared with the compact actuator disc theory of [Cumpsty and Marble \(1977b\)](#), which is the basis of the CHORUS analytical tool ([Leyko 2010](#), [Duran 2013](#) and [Livebardon et al. 2015, 2016](#)) developed at CERFACS dedicated to the study of the propagation of combustion noise through turbine stages.

## 6.2 The MT1 turbine stage indirect combustion noise analysis

MT1 is an unshrouded, single stage, high-pressure turbine stage configuration studied in the framework of the European project "Turbine Aero-Thermal External Flows 2" (TATEF-II). Experimental measurements have been conducted at the Oxford Turbine Research Facility (OTRF) (a sketch is illustrated in Fig. 6.1) by Beard et al. (2011). The OTRF is a short duration, isentropic light piston turbine facility used for representative engine aerodynamics and heat transfer investigation of single-stage (stator/rotor) or  $1\frac{1}{2}$  stage (high-pressure (HP) stage and intermediate-pressure(IP) or low-pressure (LP) vane) turbines. In the present study the OTRF was operated using the MT1 HP turbine stage. A classical test sequence operated in the OTRF is described by the following steps: Prior to a test the working section is evacuated, allowing the rotating assembly to be spun to the turbine design speed by an air motor. The test gas is contained within the piston tube (cf. Fig. 6.1) and is separated from the working section by a fast-acting plug valve. When the correct turbine speed is achieved, high-pressure air is injected into the piston tube behind the light free piston, causing the piston to travel down the piston tube, compressing and heating the working gas ahead of it. When the correct conditions of test gas pressure and temperature are reached, the plug valve is opened and the working gas is allowed to pass through the turbine and into the dump tank. The turbine pressure ratio is set by an adjustable choked throat downstream of the stage. The run ends as the piston reaches the end of the piston tube. The quasi-steady run time with the MT1 turbine is approximately 400 ms. The operating point of interest to this study is summarized in Table 6.1.

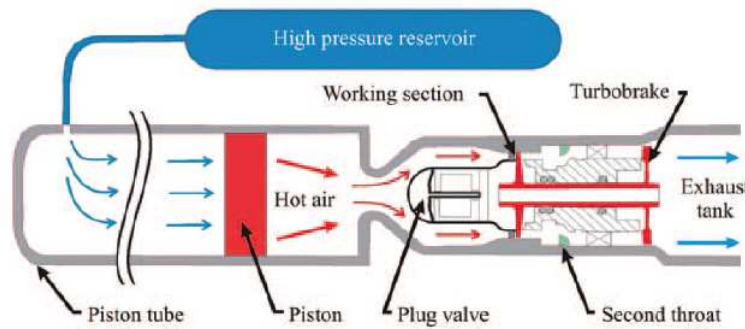


Figure 6.1 Sketch of the Oxford Turbine Research Facility.

Experimental results were afterwards compared with RANS numerical simulations performed by Beard et al. (2011), Hosseini et al. (2011) and Salvadori et al. (2011) as well as LES simulations performed by Wang et al. (2013, 2014a, 2016) and Papadogiannis et al. (2014, 2016). In this work, the LES baseline flow obtained in the study of Papadogiannis et al. (2016) and Wang et al. (2016) is used to perform a new entropy

Parameter	Exp. value	Wang et al. (2013, 2014a)	LES
Rotational speed (r/min)	9500 $\pm 1\%$	9500	9500
Inlet total pressure (bar)	4.6 $\pm 1\%$	4.5	4.5
Inlet total temperature (K)	444 $\pm 1\%$	444	444
Outlet static pressure (bar)	1.428 $\pm 1\%$	1.428	1.428
Pressure ratio ( $p_{T_{in}}/p_{x_{Pnear,hub}}$ )	3.22	3.15	3.17
Blade wall temperature (K)	—	288.5	288.5

**Table 6.1** MT1 operating conditions.

forced LES in which a cylindrical fluctuating energy source term is introduced to model the behaviour of more realistic entropy spots generated by a flame and study the radiated noise. Note that in this latter study, the reduced blade count technique of [Mayorca et al. \(2011\)](#) has been used to scale the number of blades in the stator from 32 to 30 blades allowing to reduce the computational cost. This scaling indeed allows to reduce the domain to a periodic sector of 12 degrees (instead of 90 degrees from the initial configuration with 32 stator and 60 rotor blades). [Hosseini et al. \(2011\)](#), studied the effect of the number of blades in the MT1 turbine by means of RANS simulations, concluding that the impact of the scaling on the mean flow is minimal (as long as the solidity<sup>1</sup> and the blade angles are maintained). However, it should be noted that the unsteady flow is impacted as the blade passing frequency (BPF) is modified and hence the associated unsteady flow dynamics.

In the following sections, the numerical methodology employed to simulate the coupling of the static and rotating parts of the HP turbine stage is first described in §6.2.1. Then, the unperturbed flow characteristics are briefly detailed (work published by [Papadogiannis et al. 2016](#) and [Wang et al. 2016](#)). Finally, the entropy harmonic forcing of the MT1 turbine stage is analysed.

### 6.2.1 Numerical methodology

The numerical simulation of a turbomachine needs a special treatment for the moving and static parts of the domain. In this work, the Multi Instances Solver Coupled on Overlapping Grids (MISCOG) methodology (cf. [Wang et al. 2014a,b](#), [Papadogiannis et al. 2014, 2016](#), [Bonhomme et al. 2014](#), [Labarrere et al. 2016](#) and [de Laborderie et al. 2016](#)) is used. In MISCOG, two or more instances of the same LES solver (namely AVBP), each with their own computational domain, are coupled through the parallel coupler OpenPALM ([Piacentini et al. 2011](#); [Duchaine et al. 2013](#)). To handle the interface between the different instances, an overset grid method (overlapping between meshes) is introduced along with the use of interpolation of the conservative variables wherever needed. To do so, an efficient distributed search algorithm is implemented in

<sup>1</sup>Solidity: Geometrical parameter defined as the ratio of the chord length to pitch.

the OpenPALM coupler to locate the points in the partitioned mesh blocks and a Hermitian interpolation (3rd order interpolation) is used for the data exchange, ensuring low dissipation and dispersion. Issues of numerical stability of the coupled solution and convergence of this coupled problem are directly linked to the size of the overlapped region as well as the stencil of the numerical schemes used (Wang et al. 2014a). The MISCOG methodology has been validated extensively in different test cases and configurations: Bonhomme et al. (2014) studied the turbulent flow generated in a closed vessel stirred by six fans coupling seven AVBP instances, Labarrere et al. (2016) computed an experimental device dedicated to the study of the constant volume combustion in which two rotating valves close and open the combustion chamber. Furthermore, it has been extensively used to simulate with success turbo-machinery flows for the study of aero-acoustics and combustion noise in compressor and turbine configurations. Some examples of this applications are the works of Wang et al. (2014b) and de Laborderie et al. (2016) in compressor applications, Leonard et al. (2016) simulating a scale-model turbofan and Wang et al. (2013, 2014a, 2016) and Papadogiannis et al. (2014, 2016) simulating the present MT1 turbine stage configuration together with validation test cases of acoustic propagation, vortex convection and even a turbulent pipe flow to validate the low dispersion and dissipation between the instances.

For the MT1 turbine stage simulation described in this chapter, the domain is divided into two AVBP instances: one corresponding to the static part (AVBP01) and another to the rotating part (AVBP02). For the rotating parts, the code uses the moving-mesh approach in the absolute reference frame, while the remaining unit simulates the flow in the stationary part in the same coordinate system. Figure 6.2 shows a radial cut of the stator/rotor instances composing the MT1 configuration. The stator and rotor meshes are composed of 9.4 and 21 million cells respectively, where 10 prismatic layers surround the blades to improve the resolution of boundary layers. The numerical set-up employed for the LES numerical simulations are summarized in Tab. 6.2.

Boundary conditions	
Stator inlet	NSCBC total pressure and total temperature.
Rotor outlet	NSCBC static pressure.
Blades	Wall law iso-temperature.
Walls	Wall law adiabatic.
Numerical parameters	
Governing equations	Navier-Stokes
Numerical scheme	TTG4A
LES model	WALE
Time step	0.025 $\mu s$

**Table 6.2** Numerical set-up of the MT1 numerical simulations.

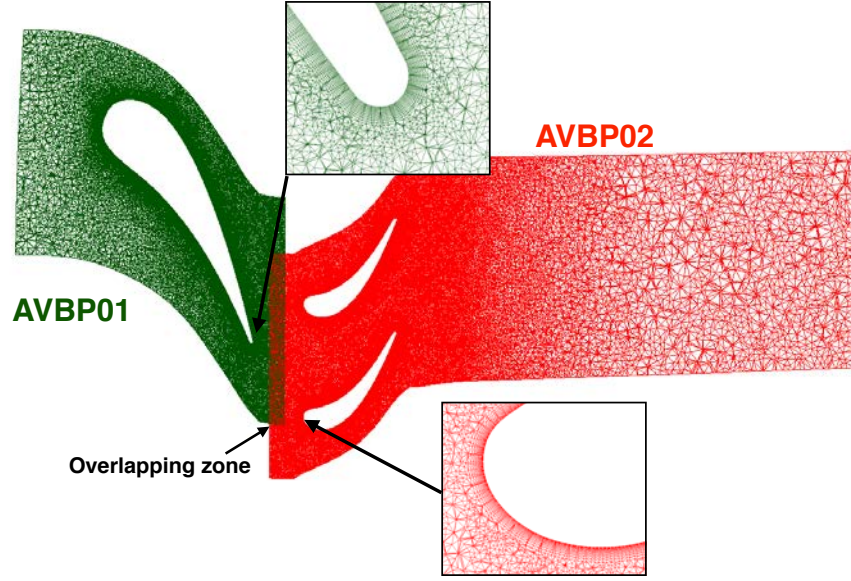


**Figure 6.2** Numerical domains corresponding to each AVBP instance.

### 6.2.2 The MT1 baseline flow simulation

The baseline flow of the MT1 turbine stage has been analysed and compared with the experiment by Wang et al. (2013, 2014a). However, the mesh used in Wang et al. (2013, 2014a) studies is coarser (5 and 8 million cells for the stator and rotor domains respectively) than the one employed here. Therefore, the different mean variables measured in the experiment are extracted from this LES and compared with the experimental and Wang et al. (2013, 2014a) data. The principal elements (probes and planes) locations used for the comparisons are detailed in Fig. 6.3 and Tab. 6.3, where extraction planes are illustrated in blue and probes by black squares. The radial position of the probes is  $r_0 = 0.284$  m and all of them are set in a fixed reference frame. Figure 6.4a shows the isentropic Mach number profile of the stator blade and Fig. 6.4b the mean static pressure of the rotor blade, both extracted at 50% span. For both blades, results are very similar to the ones already obtained by Wang et al. (2013, 2014a) with the coarser mesh, and very close to the experimental data. Small differences are highlighted on the pressure side of the stator blade that can be attributed to the position of the shock wave. Azimuthally averaged total pressure, absolute Mach number and yaw angle profiles at the rotor exit near and far planes are plotted against the percentage rotor vane height in Fig. 6.5. LES results are compared with the experimental data and with Wang et al. (2013, 2014a) coarser simulation. For all the profiles, the present LES reproduces the experimental results better, showing that this LES is better resolved. Furthermore, mean quantities used to ensure that the correct operating point has been reached are

summarized in [Tab. 6.1](#). All of these quantities are imposed by the boundary conditions, except the pressure ratio, which in this case and when compared to the experimental value, is an indicator of the pressure loss, which is better captured in the present LES. Finally, the flow topology is analysed using an iso-surface of the Q-criterion (second invariant of the velocity gradient tensor) coloured by the absolute Mach number of an instantaneous solution in [Fig. 6.6](#). The Q-criterion iso-surface selected allows to identify different secondary flow structures:

**W:** The region of the stator wake, which goes across the stator/rotor interface without interference and impinges the rotor blades.

**H:** In the vicinity of the rotor leading-edge and the hub, the span-wise pressure gradient generates a vortex roll-up called horseshoe vortex (cf. [Praisner and Smith \(2005a,b\)](#)). This vortex is composed of two legs, one on the pressure-side of the blade and the other one on the suction-side.

**C:** The suction-side leg of the horseshoe vortex interacts with the stator wake turning into a corner vortex.

**I, L and S:** Are a group of structures studied by [You et al. \(2007\)](#), the induced vortex (I), the tip-leakage vortex (L) and the tip-separation vortex (S). All of these structures are considered as the tip secondary structures.

**P :** Tip-passage vortex that joins the tip-leakage vortex in the suction of the rotor blade.

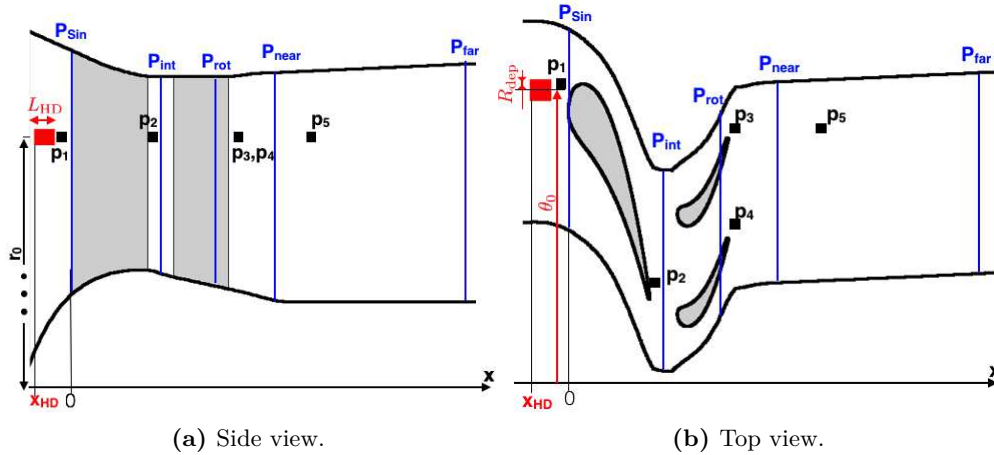


**Figure 6.3** MT1 elements positions.

All of these structures have already been identified in the works of [Wang et al. \(2014a\)](#) (with the coarser mesh) and [Wang et al. \(2016\)](#) (with the present mesh). However, secondary flows are not the only structures that characterize the flow in a transonic turbine stage. Shock waves are also present in this kind of configuration, and have an



Element	Symbol	Axial position
Stator domain inlet	$x_{in}$	-0.21 m
Rotor domain outlet	$x_{out}$	0.202 m
Stator inlet plane	$x_{P_{Sin}}$	0 m
Inter-blade plane	$x_{P_{int}}$	0.047 m
Rotor blade plane	$x_{P_{rot}}$	0.07 m
Rotor exit near plane	$x_{P_{near}}$	$\approx 0.091$ m
Rotor exit far plane	$x_{P_{far}}$	$\approx 0.198$ m
Probe 1	$x_{p_1}$	-0.0035 m
Probe 2	$x_{p_2}$	0.040 m
Probe 3	$x_{p_3}$	0.083 m
Probe 4	$x_{p_4}$	0.083 m
Probe 5	$x_{p_5}$	0.12 m

**Table 6.3** Summary of the axial positions of the different elements of the MT1 numerical domain.

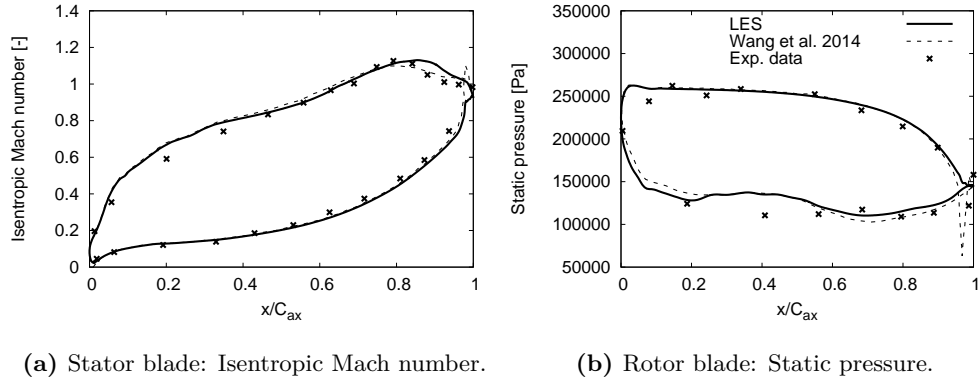


**Figure 6.4** Mean profiles extracted at 50% span: LES predictions compared with the numerical simulations of Wang et al. (2013, 2014a) and experimental data.

important impact in the flow dynamics and acoustics. To visualize the shock structures in the MT1 transonic stage, the reduced norm of the density gradient ( $||\nabla\rho/\rho||$ ) is computed and shown in Fig. 6.7, where shock waves are represented with red lines. It should be noticed that these shock waves are not static and interact with the blades (producing reflected shock waves) and flow. Figure 6.7 also reveals the propagation of acoustic waves from the trailing edge of the stator and the leading of the rotor blades, as well as the wakes generated by the bluntness of the trailing edges. All of these mechanisms are sources of noise generation that should be taken into account (filtered) when the generation of acoustics by an entropy wave is studied. The spectral content of the baseline flow has been studied by means of local probes in the stator and rotor domains as well as by Dynamic Mode Decomposition (DMD) analysis by Wang et al. (2016) and



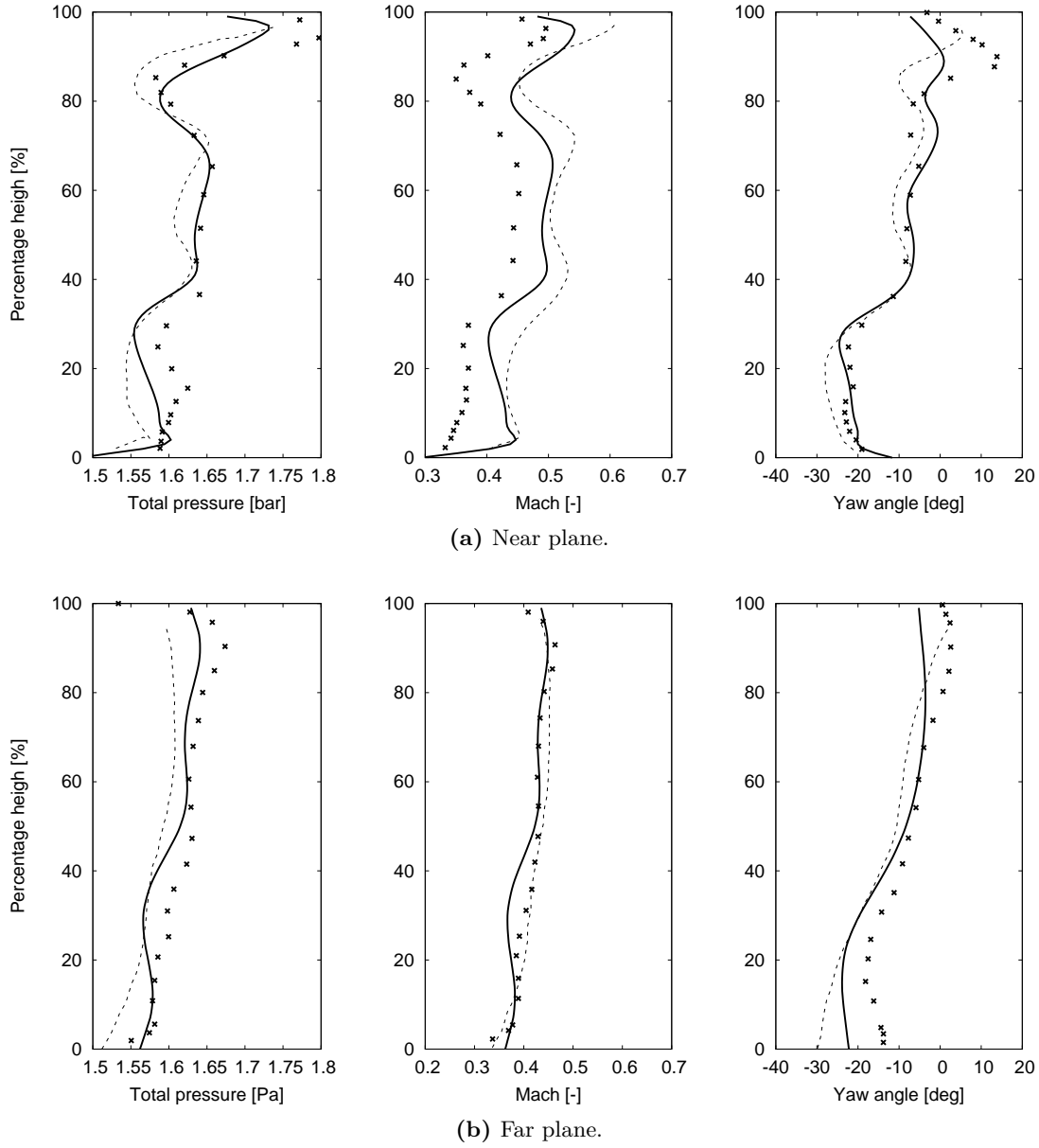


**Figure 6.5** Azimuthal mean profiles. LES predictions (—). Wang et al. (2013, 2014a) predictions (---). Experimental data (\*).

Papadogiannis et al. (2016). Both analyses have shown the same spectral features: stator and rotor BPFs at 9.5 kHz and 4.75 kHz respectively, the BPFs harmonics over the full frequency range and the signature of the stator and rotor vortex shedding. However, something that has not been addressed by any study is the "ability" of the baseline flow to generate entropy noise. Indeed, strong temperature fluctuations are generated

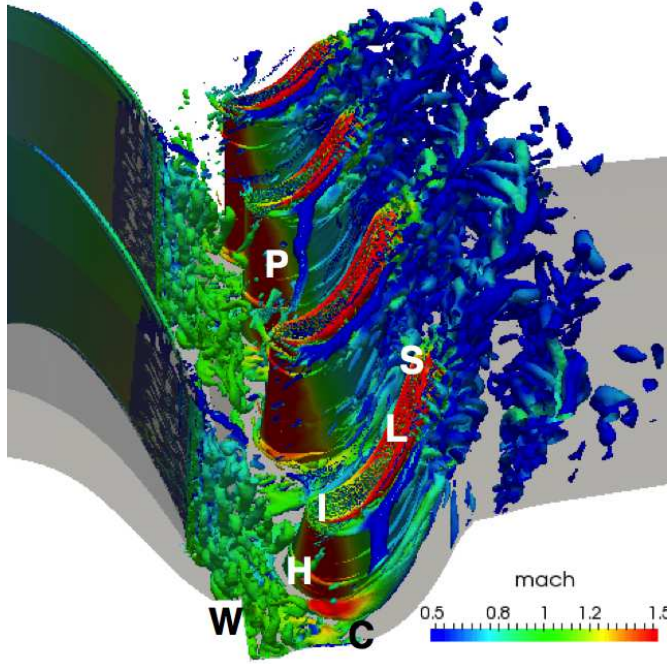


**Figure 6.6** Iso-surface of the Q criterion coloured by the absolute Mach number.

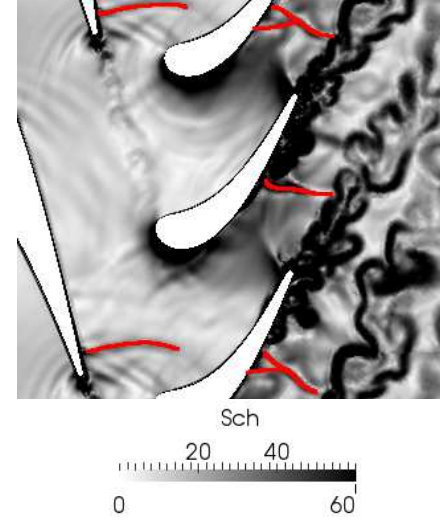


**Figure 6.7** Field of  $||\nabla\rho||/\rho$  of an instantaneous field at  $R = 0.284$  mm.

mostly in the wake regions due to the sheared flow (conversion of vorticity modes into entropy modes) and the isothermal boundary condition applied to the stator and rotor blades. Temperature instantaneous fluctuations are shown in a blade to blade view at  $R = 0.284$  m in Fig. 6.8. It is found that the amplitude of the temperature fluctuations in the rotor domain is at least three times greater than in the stator. Furthermore, the temperature fluctuations generated in the rotor domain are due to the strong shock present in the suction side of the rotor blades (cf. Fig. 6.7). To quantify the amount of the fluctuating temperature, probes in the fixed reference frame shown in Fig. 6.3 are used to register the temperature fluctuations signals, which are plotted against time in Fig. 6.9. No temperature fluctuation is registered in the upstream section of the stator blade (cf.  $p_1$ , Fig. 6.9a). In the inter-stage vane,  $p_2$  shows a maximal temperature fluctuation of  $\approx 5$  K (cf. Fig. 6.9b), even though the probe is not located in the wake trajectory. Then, near the rotor blades trailing edge ( $p_3$  and  $p_4$ ) the temperature fluctuation increases up to  $\approx 40$  K (cf. Figs. 6.9c and 6.9d) due to the shock wave before being attenuated by the mixing of the wakes to about 15 K as shown in Fig. 6.9e.

All of the above discussed features (shock waves, secondary flows, flow separation and turbulence), make the analysis of the MT1 forced flow difficult to study. Uncorrelated events as turbulence need to be filtered from the harmonic forcing. Such a concern will nonetheless be treated by the use of Fourier analysis, as detailed in Papadogiannis et al.

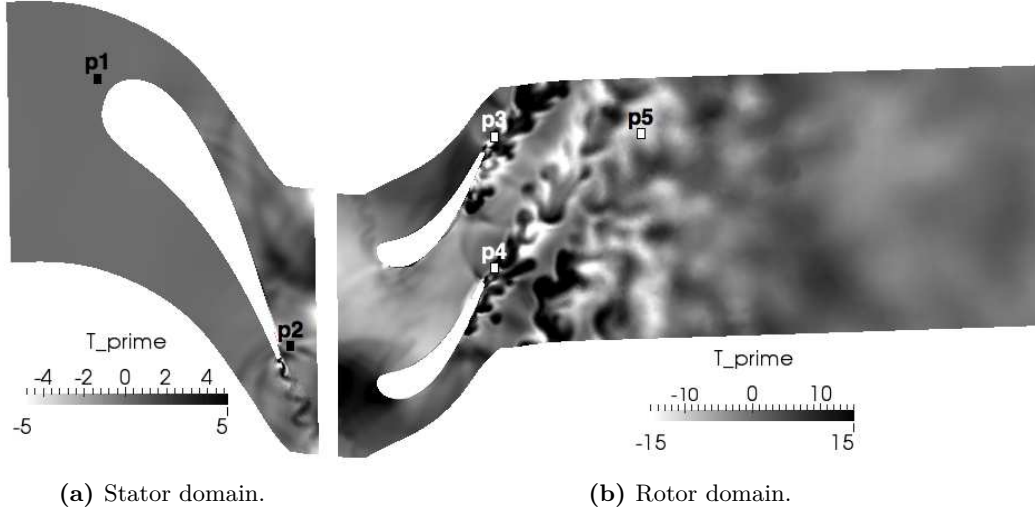


**Figure 6.8** Temperature fluctuations instantaneous fields. Radial cut at  $r_0 = 0.284$  m.

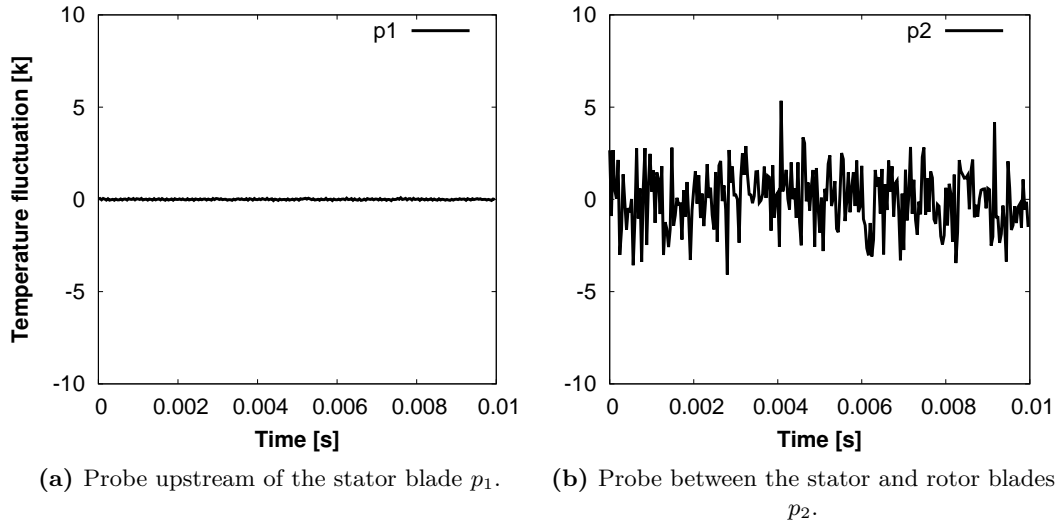


**Figure 6.9** Temperature fluctuations registered at different probes inside the MT1 baseline flow simulation.

(2016). In their work, DMD analysis was used to identify a harmonic entropy planar wave forced through the MT1 inlet. Results of this study show that at least six periods (and up to ten periods) of the entropy forcing wave (2000 Hz) are needed to correctly retrieve the BPFs and forced frequency peaks in the DMD spectrum. Indeed, adding more snapshots to the treated signal increases the signal length, which improves the spectral resolution decreasing the amplitude of the irrelevant modes (a better signal to noise ratio is obtained). The present study is not focused on the whole range of fre-

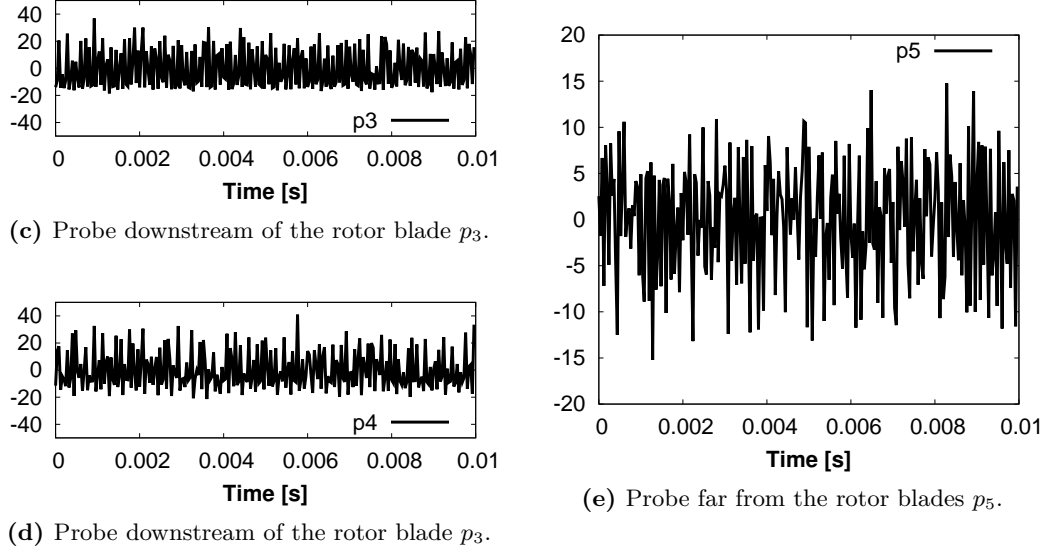


**Figure 6.9** Temperature fluctuations registered at different probes inside the MT1 baseline flow simulation.

quencies already addressed by Wang et al. (2016) and Papadogiannis et al. (2016). Only a reduced range of frequencies, where harmonic entropy perturbations are introduced ( $f \in [100; 3000]$ ) is of interest. Since the contribution of different phenomena present in the baseline flow to the overall spectrum is unknown, DMD analysis is an ideal tool to identify their signature without having a multiple of the sampling frequency. Therefore, DMD analysis is performed in planes at the interstage region and near the rotor blades trailing edge,  $P_{int}$  (in the stator domain) and  $P_{near}$  (in the rotor domain) respectively. The velocity magnitude and temperature spectra of the stator and rotor planes are represented in Figs. 6.10a and 6.10b respectively. A hump in the velocity magnitude and the temperature appears between 1500 Hz and 3000 Hz in the plane extracted at the stator wake ( $P_{int}$ , Fig. 6.10a). To understand the phenomena taking place at this frequency range, the most important modes are extracted ( $f = 2185$  Hz and  $f = 2500$  Hz) and reconstructed in the temporal space to be compared with the corresponding instantaneous field in Figs. 6.11 and 6.12. Note that fluctuations are represented in both figures and that the mode at 2500 Hz is present in both stator and rotor wakes. As evidenced by the instantaneous velocity fluctuations in Fig. 6.11, flow separation occurs earlier in the near hub region. This is due to the presence of a second shock wave located approximatively at the half of the axial chord of the stator blade and highlighted by the dilatation representation in Fig. 6.11. Both extracted modes show strong velocity fluctuations in the wake region, particularly near the hub, where the flow separation generates the strongest fluctuations. The temperature fluctuation of the instantaneous flow and the reconstructed temperature fluctuation from both extracted modes are represented in Fig. 6.12. A temperature fluctuation pattern is more difficult

to identify in the instantaneous temperature field, where temperature fluctuations are present almost everywhere. However, the separation zone, the stator wake and the shock can be identified. The DMD reconstruction for the first extracted mode ( $f = 2185$  Hz), which is located in the middle of the stator hump DMD spectrum, shows a clear conversion of vorticity to entropy modes. The second mode however is less correlated with the velocity fluctuations (as shown by the DMD stator spectrum, cf. Fig. 6.10a) and exhibits temperature fluctuations near the hub. Note that this temperature mode is also present in the rotor DMD spectrum. The rotor relative velocity and temperature fluctuations are shown in Figs. 6.13 and 6.14. In this case, fluctuations generated by the instantaneous flow are too strong to be compared directly with the DMD most energetic mode reconstruction ( $f = 1250$  and  $2500$  Hz). Therefore, two color scales are used for the comparison. Relative velocity fluctuations computed at  $x_{P_{near}}$  in the rotor domain wake are shown in Fig. 6.13. The instantaneous velocity fluctuation field shows that almost all the activity takes place in the wake regions. However, reconstructing the first extracted mode ( $f = 1250$  Hz) shows that strong velocity fluctuations take place in the wakes and near the tip, where tip vortical structures are generated and convected. The second extracted mode, which according to the DMD spectrum (cf. Fig. 6.10b) is a temperature mode, shows mostly structures generated by the wakes. The temperature fluctuation fields computed in the rotor wake are shown in Fig. 6.14. As in the stator DMD instantaneous fields, it is difficult to identify the source of the temperature fluctuations. However, once again, the first mode shows a strong correlation between the velocity and the temperature mode, particularly in the tip region, where the mode conversion is clearly evidenced. The second extracted mode, however, once again seems to be a temperature mode alone and shows temperature fluctuations with sources almost everywhere.

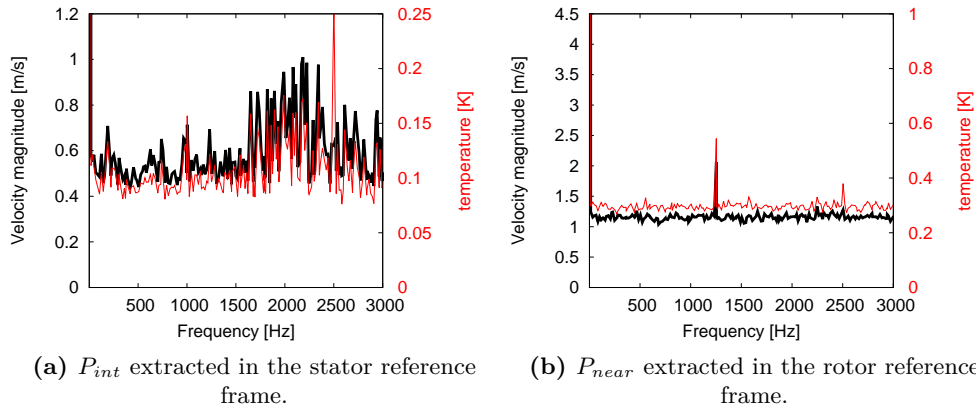


**Figure 6.10** DMD spectra of the velocity magnitude and the temperature inside the stator and rotor wakes.

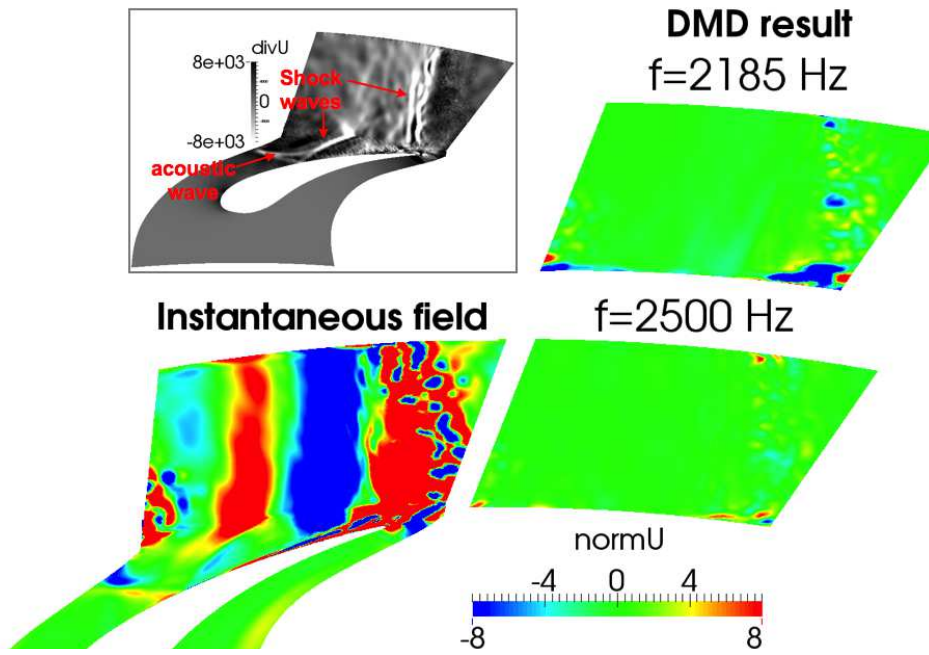


**Figure 6.11** Strongest velocity fluctuation modes in the DMD analysis of the stator wake extracted in plane  $P_{int}$ .

The objective of this last analysis is to highlight the generation of entropy by the baseline flow and therefore the difficulty to dissociate the entropy generation source, whether it is coming from the baseline flow or the entropy forced wave. In the following section, the MT1 baseline flow here described is used to introduce harmonic temperature fluctuations and study the entropy radiated noise. Then, the LES flow field upstream of the stator blades is used as input to compute acoustic and entropy waves and then propagate them with the analytical tool CHORUS to the outlet of the turbine.

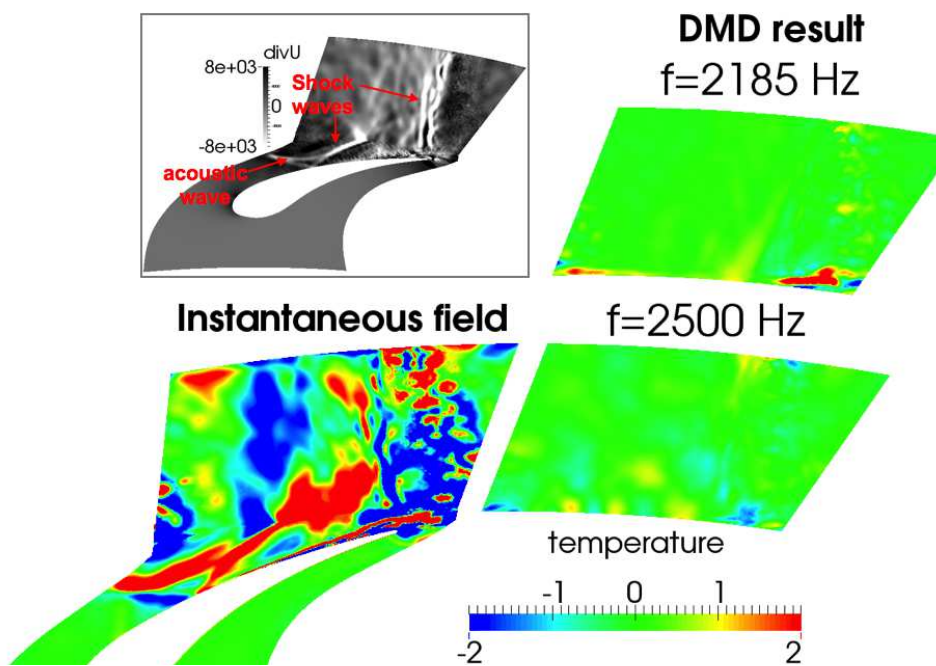


**Figure 6.12** Strongest temperature fluctuation modes in the DMD analysis of the stator wake extracted in plane  $P_{int}$ .



## Instantaneous field    DMD result

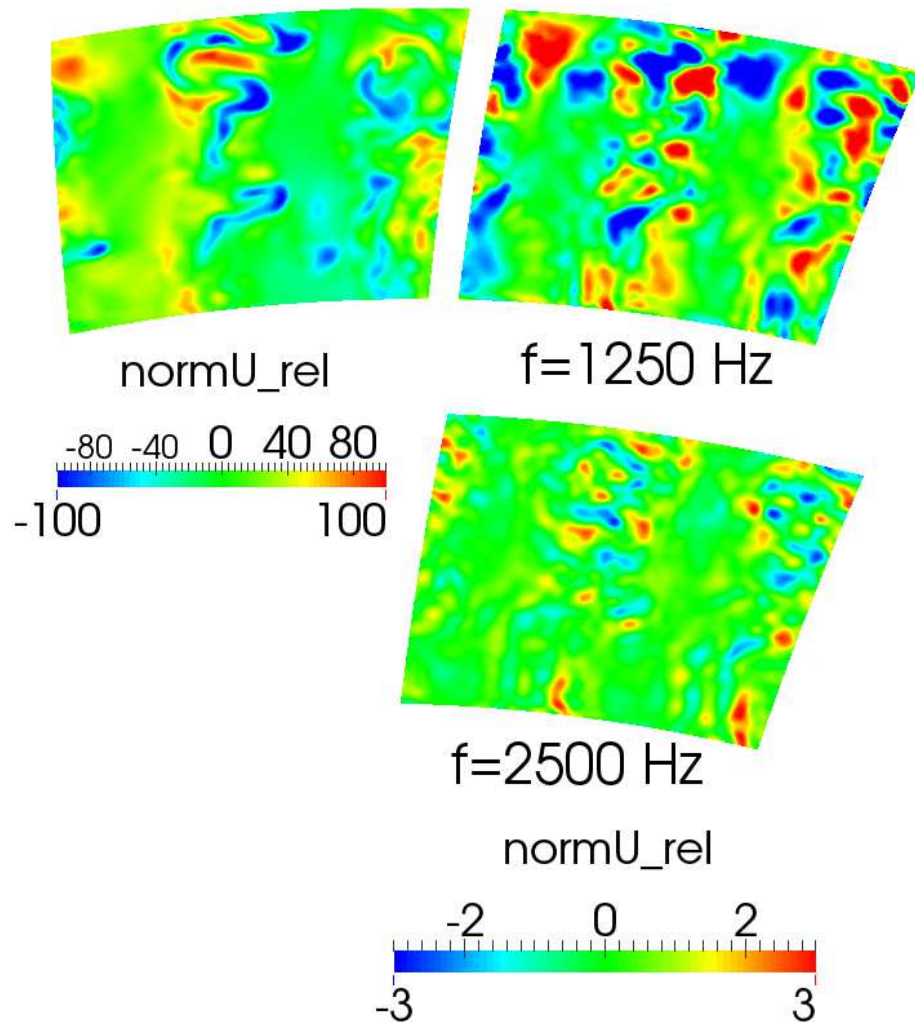


**Figure 6.13** Strongest velocity fluctuation (relative velocity) modes in the DMD analysis of the rotor wake extracted in plane  $P_{near}$ .



## Instantaneous field    DMD result

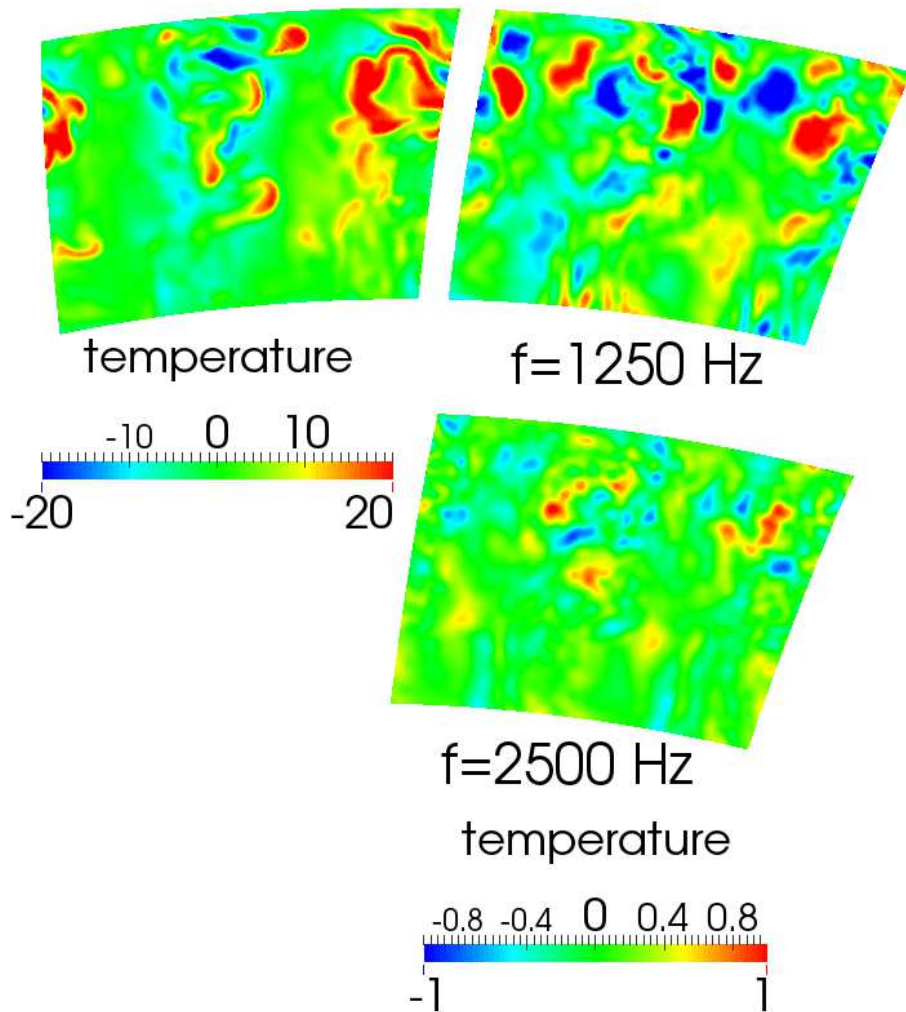


**Figure 6.14** Strongest temperature fluctuation modes in the DMD analysis of the rotor wake extracted in plane  $P_{near}$ .

### 6.2.3 The MT1 entropy forced simulation

Noise generation mechanisms and propagation in a turbine have been studied widely by different authors. For example, 2D numerical simulations of a turbine stage at mid-span have been performed by [Leyko et al. \(2010\)](#), [Leyko et al. \(2014\)](#), [Duran et al. \(2011, 2013a\)](#) and [Duran and Moreau \(2013b\)](#). In these works, the study of noise generation due to acoustic and entropy disturbances has been first carried in a stator alone configuration by [Leyko et al. \(2010, 2014\)](#). Then, [Duran et al. \(2011, 2013a\)](#) studied the same mechanism of sound generation but in an isolated rotor configuration. Finally, it was [Duran and Moreau \(2013b\)](#) and [Bauerheim et al. \(2016\)](#) that complemented these early studies addressing the propagation and generation of acoustic waves by an entropy and acoustic forcing in the full stator/rotor configuration. All of these 2D numerical simulations allowed to validate the analytical core-noise propagation tool in turbine configuration CHORUS (which is discussed later in this section) developed at CERFACS. Then, 3D full-compressible LES simulations of the forcing of a 2 kHz entropy plane wave through the inlet of the MT1 12° periodic sector configuration were performed by [Papadogiannis et al. \(2016\)](#) and [Wang et al. \(2016\)](#). Results of these simulations have been compared to the 2D numerical simulations and analytical results of [Duran and Moreau \(2013b\)](#). This time, the conclusions of these works were multiple: first of all, the generation of acoustic waves by the acceleration of an entropy wave (indirect entropy noise) has been highlighted with a visible peak in the temperature and pressure spectrum (DMD analysis of the forced flow) at the forcing frequency, even though no acoustic wave has been introduced with the entropy wave forcing. Second, the number of snapshots used to perform the DMD has an important influence on the positions of the peaks of the  $\text{BPF} \pm 2000$  kHz (the entropy forced wave frequency). For this study, convergence of the DMD in terms of number of periods of the entropy forced wave is found to be at least 10. Third, the compact theory results are dependent on the frequency due to the phase shift applied to the waves when travelling through the inter-stage zone (not considered as compact). It is important to notice that this assumption does not mean that the compact theory is valid for larger frequencies. In this case, good agreement between the 2D numerical simulations and the compact theory has been found up to 1000 Hz. Results between the 2D and 3D simulations are very close when considering the entropy-acoustic transfer functions. Finally, the entropy wave in the 3D simulation is found to be more attenuated than in the 2D simulations and in the analytical model. This result can be explained by the presence of walls (generation of a boundary layer) as well as secondary flows in the 3D simulation. Both generate an increase of the inhomogeneity of the flow and mixing, resulting in a higher attenuation of the entropy wave.

In the present study, the generation of noise produced by a non-planar entropy perturbation is studied. A cylindrical pulsating energy source term is introduced in the energy transport equation (strategy similar to the one used in §5.2.1 for the EWG heating device) to model the heat release fluctuations generated by an aeronautical burner. It is worth noting that the introduction of an energy source term results in the generation of direct noise, which will be coupled to indirect noise generation once the entropy streak

is convected through the stator vanes and rotor blades. Therefore, acoustic-acoustic and entropy-acoustic transfer functions will be difficult to compute without a model to separate the contribution of each noise source to the overall acoustic waves (cf. computing the EWG nozzle transfer functions in §5.3.2.4 and §5.3.3). However, this is the real behaviour of an aero-engine: both direct and indirect noise mechanisms interact together. Experimental studies of this kind of temperature forcing have been carried by [Gaetani and Persico 2017](#), in which hot air is injected (steadily) in a subsonic HP turbine stage. The influence of the position of the injectors with respect to the stator blade leading edge (clocking) was studied. It has been found that the temperature forcing may enhance the generation of secondary flows, which will play an important role in the dispersion of the hot streak.

The formulation of the introduced energetic source term is composed of two spatial functions,  $f(x)$  and  $g(y, z)$  as well as one temporal function  $f_r(t)$ , which yield:

$$\dot{Q} = \frac{E_0}{\iiint f(x) \cdot g(y, z) \cdot dV} \cdot f(x) \cdot g(y, z) \cdot f_r(t), \quad (6.1)$$

$$f(x) = \begin{cases} 1 & \text{if } x \in [x_{HD}; x_{HD} + L_{HD}] \\ 0 & \text{if } x \notin [x_{HD}; x_{HD} + L_{HD}] \end{cases} \quad (6.1a)$$

$$g(y, z) = \begin{cases} \sum_{i=1}^{n_{cyl}} \cos\left(\frac{\pi d_i(y, z)}{2R_{dep}}\right) & \text{if } d_i \leq R_{dep} \\ 0 & \text{if } d_i > R_{dep} \end{cases} \quad (6.1b)$$

$$d_i(y, z) = \left[ (y - r_0 \cos(\theta_0 + (i-1)\Delta\theta))^2 + (z - r_0 \sin(\theta_0 + (i-1)\Delta\theta))^2 \right]^{1/2},$$

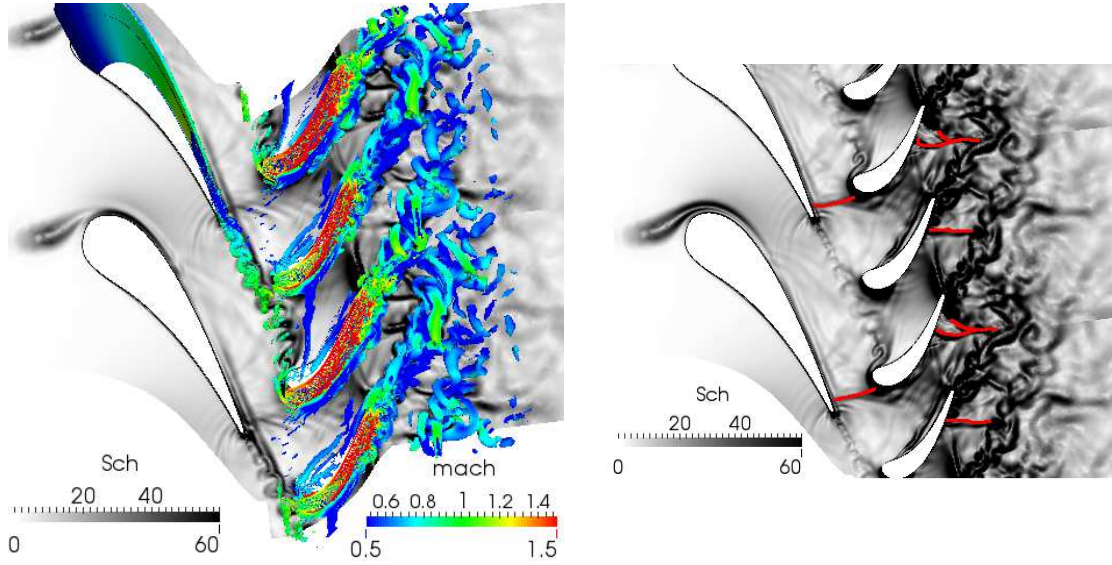
$$\iiint f(x) \cdot g(y, z) \cdot dV = \frac{(\pi^2 - 4)}{2\pi} R_{dep}^2 L_{HD} n_{cyl}, \quad (6.1c)$$

where  $f(x)$  limits the energy of the deposition into a volume contained between  $x_0$  and  $x_0 + L_{HD}$ ;  $g(y, z)$  scatters the energy into  $n_{cyl}$  cylindrical source terms, each one located at  $[r_0; \theta_0 + (i-1)\Delta\theta]$ . Inside these cylindrical source terms, the spatial distribution of the energy in the x-normal plane is a bell shape, with its maximum at the center of the disc. Finally,  $f_r(t)$  is the temporal forcing signal, defined in [Eq. \(5.13\)](#). In the 12° periodic test case studied, only one burner is modelled by a cylindrical source term located next to the stator blade leading edge. An illustration of the geometrical position of the energy source term is illustrated in [Fig. 6.3](#) by the red rectangle. [Table 6.4](#) summarizes the different parameter values for the heating deposition model. The choice in the energy deposition location can be compared to the leading edge injection of hot fluid in the study of [Gaetani and Persico \(2017\)](#).

Function	Parameter	Value
$f(x)$	$x_0$	-0.0185 m
	$L_{HD}$	0.01 m
$g(y, z)$	$r_0$	0.284 m
	$\theta_0$	-1.658 rad
	$R_{dep}$	3 mm
	$\Delta\theta$	0
	$n_{cyl}$	1
$f_r(t)$	$f_0$	100 Hz
	$N_{harm}$	29

**Table 6.4** List of values for the energy deposition model of the MT1 entropy forced simulation.

Prior to the harmonic analysis of the temperature fluctuations generated by the energy deposition and its attenuation through the turbine stage, the instantaneous fields are analysed using the reduced norm of the density gradient ( $||\nabla\rho||/\rho$ ) and the Q-criterion colored by the Mach number magnitude in Fig. 6.15. A blade to blade view at  $R = 0.284$  m is used for this analysis (same one used for the prior analysis of the baseline flow). In comparison with the baseline flow topology, the forced flow exhibits the same characteristics in terms of shock waves and secondary flows. However, the path taken by the temperature streak and its deformation is revealed by the reduced norm of the density gradient. First, at the inlet of the stator, the temperature streak is entrained by the suction side of the stator blade and travels close to the blade wall. Then, the temperature streak is found to be trapped in the stator wake, where it follows a strong deformation (the streak seems to wrap the wakes as it is convected by them, cf. Fig. 6.15a). It should be noticed that the temperature spot is in the trajectory of the wake, as in the experimental study of Gaetani and Persico (2017) when the injection of hot fluid takes place next to the stator blade leading edge. Afterwards, the deviation of the flow caused by the stator blade makes the streak to be spread in the azimuthal direction before entering the rotor domain, where the non-homogeneous flow distorts the streak. Indeed, the flow is faster on the suction side of the blade and slower on the pressure side. Then, the deformed streak travels close to the tip passage vortex (cf. Fig. 6.15a), which should contribute to the dispersion of the streak. After this zone, the streak is no more visible and most likely deformed and mixed by the tip-leakage, separation vortices as well as the rotor wakes. In Fig. 6.15b, another instant is chosen to look further in the path followed by the temperature streak, where shock waves are highlighted by red lines. From Figs. 6.15a and 6.15b, one can conclude that the stator downstream shock does not have an important influence on the trajectory or the shape of the temperature streak and it arrives almost "unaltered" to the stator wake. In Fig. 6.15b, the trace of the temperature streak can be followed up to the rotor wakes, where in this case, the trace of the temperature streak close to the suction side is lost after the shock and its trace on the suction side is lost when the streak arrives in the rotor wakes.



(a) Iso-surface of Q-criterion coloured by the absolute Mach number.

(b) Visualisation of shock structures.

**Figure 6.15** Instantaneous fields of  $||\nabla\rho||/\rho$  at  $r_0 = 0.284$  m.

Figure 6.15 shows a global view of the temperature-fluctuation field. To quantify the amount of temperature fluctuations generated, the temperature fluctuations are extracted at the probes illustrated in Fig. 6.3. Temperature fluctuations registered at these probes are compared with the temperature-fluctuation envelope (maximal and minimal values represented by horizontal lines) generated by the baseline flow alone (cf. Fig. 6.9) in Fig. 6.16. For probes located before the rotor blades ( $p_1$  and  $p_2$ ), the temperature fluctuation generated by the energy source term can be easily identified (as already shown by Fig. 6.15). However, when the temperature spot traverses the rotor blades (probes  $p_3$ ,  $p_4$  and  $p_5$ ), the streak has already been dispersed by the stator and rotor wakes, as well as the secondary flows and shocks. Here, it becomes difficult to distinguish the contribution of the temperature forcing and the temperature fluctuation produced by the baseline flow. However, this information is still useful to be compared with experimental studies, as the one realised by Schuster et al. (2015). In this experiment, the Honeywell TECH977 engine<sup>1</sup>, which is a realistic aeronautical turbo-engine is equipped with temperature and pressure probes before and after each turbine stage to study combustion noise. In this experiment, the maximum temperature registered at the outlet of the combustion chamber is about 110 K, while in the present MT1 forced simulation it reaches (between the energy deposition and the stator blade, at  $p_1$ ) about 150 K, which represents about 30% of the mean temperature value. Then, the temperature fluctuation registered after the first HP turbine stage in the experiment is  $\approx 10$  K, which is of the

<sup>1</sup>The Honeywell TECH977 is a 7000 lb thrust class engine with a two stage high pressure turbine and a three stage low pressure turbine

same order of magnitude at  $p_5$  in the MT1 configuration. In both cases it represents an attenuation of one order of magnitude of the initial value.

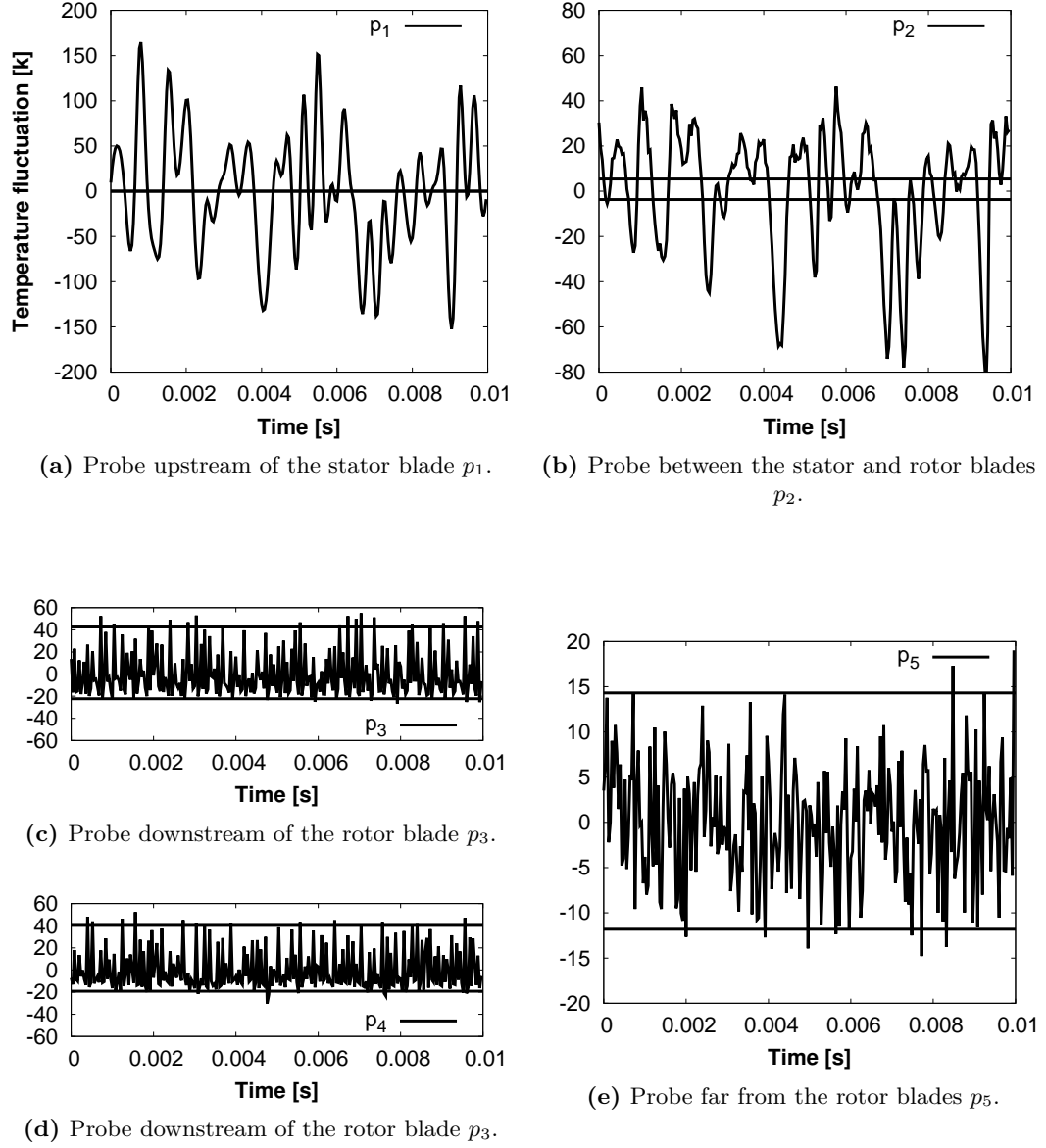


**Figure 6.16** Temperature fluctuations registered at different probes inside the MT1 domain.

Now that the global characteristics of the generated temperature fluctuation have been studied, DMD analysis is performed in  $P_{int}$  and  $P_{near}$  planes. DMD spectra of the velocity magnitude and the temperature in the extracted planes is represented in Fig. 6.17, where the baseline flow spectrum is added for comparison in dashed lines.



Note that the absolute velocity magnitude is computed in the stator reference frame ( $P_{int}$ ) and the relative velocity magnitude in the rotor reference frame ( $P_{near}$ ). In the stator reference frame (cf. Fig. 6.17a), the velocity magnitude spectrum is very similar to the one computed in the baseline flow simulation, with a hump in between 1500 and 3000 Hz. Concerning the computed temperature spectrum, each harmonic of the entropy forcing signal is correctly retrieved by its corresponding peak (every 100 Hz). In the rotor domain computed DMD (cf. Fig. 6.17b), relative velocity fluctuations are of the same order of magnitude, except for the peak at 1250 Hz, which doubles its amplitude. In the temperature spectrum computed in the rotor domain plane, the harmonic peaks are difficult to visualise. Indeed, temperature fluctuations generated by the baseline flow are of the same order of magnitude as the temperature forcing at this position, making difficult to visualise their contribution and are shown as broadband oscillations. However, an increase in the temperature fluctuation amplitudes is perceived, due to the temperature forcing. Furthermore, the maximum temperature amplitude modes shown in the baseline flow analysis ((peaks at 1250 and 2500 Hz) are still at the same positions in the forced flow DMD spectrum. This latter result (the temperature peaks at the same position) shows that the same mechanisms of entropy generation are still present in the entropy forced simulation.

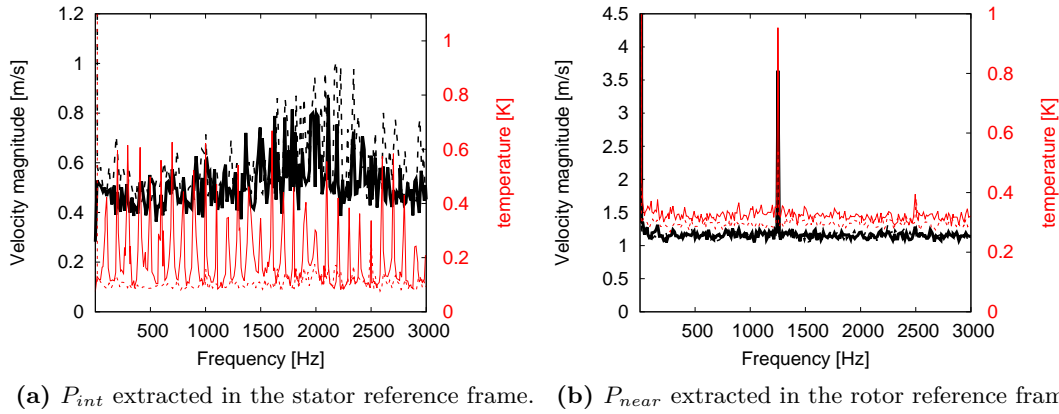


**Figure 6.17** DMD spectra of the velocity magnitude and the temperature inside the stator and rotor wakes. (—) Forced flow. (---) Baseline flow.

The global characteristics of the baseline flow are shown to be present in the forced flow. To push this analysis further, Fourier analysis is performed over the 3D instantaneous fields of the MT1 forced simulation. Knowing that the fundamental forced frequency is 100 Hz, the temporal signal to capture this frequency needs to be at least 0.01 s (one period). The last forced harmonic is 3000 Hz, which is the largest frequency of interest in the present study. From Shannon-Nyquist theorem, a sampling of  $\Delta t = 0.16$  ms is at least needed to solve the whole frequency range of interest. The signal sampling is therefore chosen to be  $\Delta t = 40$   $\mu$ s (equivalent to eight points over

the highest frequency period). Afterwards, DFT analysis is applied over the complete 3D stator and rotor instantaneous fields. The convergence of the DFT fields is studied varying the length of the studied signal (as already done in the previous study of Papadogiannis et al. 2016). According to the EWG nozzle transfer functions analysis performed in §5.3.3, quantities like the temperature fluctuations are the last to converge and are very sensitive to turbulence. The highest wavelength to be resolved is the one corresponding to the highest entropy forcing frequency. According to the bulk velocity and the characteristic cell length, this harmonic entropy wave contains at least 18 points per wavelength, that is to say three times more than the minimal required by the numerical scheme to correctly convect the waves without dispersion or dissipation (cf. Appendix C). In the following the temperature fluctuation is used to assess the convergence of the DFT analysis carried in this study. Figures 6.18–6.26 show the modulus of the temperature fluctuation computed by DFT in the stator and rotor attached reference frames for different frequencies and run time lengths. Only three frequencies are shown for three different run time lengths: 100 Hz (the fundamental frequency), 1500 Hz (a mid-range frequency) and 3000 Hz (the last forced harmonic) for one, five, nine and ten periods of the fundamental frequency. In these figures, different types of cuts are used to illustrate the path and deformation followed by the temperature streak: radial cuts at  $R = 0.284$  m, which corresponds to the radius where the energy source term is located, as well as axial cuts located at  $x_{P_{sin}} = 0$  m (stator inlet),  $x_{P_{int}} = 0.047$  m (inter-stage vane) and  $x_{P_{near}} \approx 0.091$  m (experimental plane near the rotor blades). Figures 6.18–6.20 show a blade to blade view of some of the frequencies of interest (100, 1500 and 3000 Hz). For the stator DFT (Figs. (6.18–6.20)(a)), results are found to be very similar when comparing the influence of the run time length. The only difference is found to be in the stator wake, where DFT carried over 9 and 10 periods filter the non-correlated structures showing a more continuous wake in cone shaped form. This filtering effect can be seen as a phase average of the fields where a temporal signal is decomposed into three contributions (when harmonic regime is assumed):

$$\phi(t, x) = \bar{\phi}(x) + \phi'_{det}(t, x) + \phi'_{stoc}(t, x) \quad (6.2)$$

where  $\bar{\phi}$  is the mean value of the signal,  $\phi'_{det}$  is the deterministic part of the signal (function  $f_r(t)$  in Eq. (6.1)) and  $\phi'_{stoc}$  is the stochastic part, which is assumed to be non correlated to the deterministic part and should be considered here as noise. Therefore, adding more periods to the studied signal improves the spectral resolution of the DFT increasing the signal to noise ratio and so filtering the stochastic contribution. This filtering effect is more visible in the rotor domain DFT field view, where the amplitude of the temperature fluctuation in the wakes decreases strongly with the number of periods considered. Furthermore, the shape of the entropy streak can be better visualised considering more periods. In the stator (Figs. (6.18–6.20)(a)) the temperature streak is continuous, its radius changes along its passage through the stator domain being spread in the azimuthal direction when arriving to the stator wake (cf. axial cuts in Figs. 6.21, 6.23 and 6.25 allow a better insight). Before the stator blade, the streak has a radius equal to the deposition radius  $R_{dep}$  in Eq. (6.1). During its passage through the stator



vane the radius is contracted and when it reaches the stator wake it is spread by the wakes. In this zone, the streak traverses the stator shock wave, which seems to have small influence in the shape, or the trajectory of the streak, and this for all the frequencies studied. Concerning the attenuation of the entropy wave, the temperature fluctuation magnitude is observed to decrease during the passage of the streak and the attenuation is more important when the frequency increases. This attenuation is mostly due to dispersion of the hot streak due to the non-homogeneous flow. The higher the frequency is, the stronger the attenuation of the streak is, as described by [Leyko et al. \(2010\)](#), [Morgans et al. \(2013\)](#) and [Giusti et al. \(2016\)](#) and evidenced in [Chapter 5](#) in the EWG nozzle. In the rotor domain, the entropy streak is spread into the azimuthal direction (cf. [Figs. \(6.18–6.20\)\(b\)](#)). Indeed, the rotor DFT is computed in the rotor moving reference frame. Therefore, the rotor domain sees an entropy fluctuation that is introduced at different azimuthal positions as time marches. It is also noted that the entropy streak is found to be discontinuous at the stator/rotor interface, and some stripes are perceived. Those stripes may be related to an insufficient sampling to recover a continuous signal in the rotor. Indeed, the rotating speed of this operating point is 9500 rpm ( $57000^\circ/\text{s}$ ) while the chosen frequency of sampling  $40\text{ }\mu\text{s}$ . It results that the entropy streak will be effectively seen by the  $12^\circ$  periodic rotor domain approximatively 5.3 times per passage, generating the observed stripes. Afterwards, when the streak arrives near the rotor blade trailing edge, supplementary temperature fluctuations are generated at the separation zone induced by the shock highlighted in [Fig. 6.15b](#). Furthermore, the shock wave and secondary flows present in the rotor vane disrupt completely the streak and no more stripes are perceived after this position. [Figures 6.21–6.26](#) show axial planes for the different harmonics and run times. [Figures 6.21, 6.23 and 6.25](#) show axial cuts of the DFT performed in the stator fixed reference frame at the inlet and outlet planes ( $x_{P_{S_{in}}}$  and  $x_{P_{int}}$ ). The entropy streak enters the stator with a well defined circular shape (as defined by [Eq. \(6.1\)](#)) and leaves the stator with an oval form. This dispersion into an oval form is mostly due to the flapping modulation by the vortex shedding of the stator wake as seen in [Fig. 6.6](#). Furthermore, an attenuation of the maximum value of the temperature magnitude is observed along the stator. This attenuation is even stronger for the case at 3000 Hz, where the maximum temperature value is already diminished at the entrance of the stator (cf. [Fig. 6.25a](#)), even though the energy is equally distributed into all the harmonics. One can furthermore compare the attenuation of the entropy streak through the stator to the experimental study carried by [Gaetani and Persico \(2017\)](#). To make a fair comparison between these studies, the modulus of the total temperature fluctuation at 100 Hz (considering that the attenuation followed by a 100 Hz temperature disturbance can be compared to the one followed by a steady hot inflow) is computed at the inlet and outlet planes of the stator. Then, the reduced total temperature fluctuation is computed (total temperature fluctuation of the forced flow over the mean total temperature of the baseline flow) and the maximum values between the inlet and outlet planes are compared. An attenuation from 0.042 to 0.015, that is to say almost 3 times the initial spot temperature is obtained, which is in the same order of magnitude as the one obtained experimentally by [Gaetani and Persico \(2017\)](#) from 0.2 to 0.05 (for a bigger

characteristic injection length). Moving on to the passage of the temperature streak from the stator to the rotor, axial cuts from Figs. (6.21, 6.23, 6.25)(b) and Figs. (6.22, 6.24, 6.26)(a) are located at the same axial position ( $x_{P_{int}}$ ) but extracted in the stator and rotor reference frames respectively. Since the DFT in the rotor is computed in its own reference frame, the entropy streak is no more seen as a circle but as a band located at a mean radius  $R = 0.284$  m, which covers the complete azimuthal length of the sector. However, this band is found to be discontinuous and exhibiting several streaks most likely produced by the sampling of the signal (as already highlighted in the radial cuts). As expected, the amplitude of the temperature fluctuation in the stator reference frame is much higher than the one computed in the rotor reference frame due to the spreading of the streak along the azimuthal direction of the rotor. Another axial cut is extracted near the rotor blades leading edge and close to the rotor shock wave position ( $x_{P_{rot}}$ ) in Figs. (6.22, 6.24, 6.26)(b). Here, the signature of secondary flows appears near the suction side of the rotor blades. The hub passage vortex moves towards the tip and the tip-leakage vortex seems to push the streak towards the hub. Afterwards, in Figs. (6.22, 6.24, 6.26)(c), the axial position  $x_{P_{near}}$  is represented. Here, the entropy streak remains in the upper part (close to the tip), where the tip-leakage vortex grows and intensifies, which result in a mixing of the entropy streak. At this point, the entropy streak has already been attenuated by different phenomena along the turbine stage and it is difficult to identify the original circular pattern, which remains visible for the smallest frequencies). Considering more periods of the forced signal clearly enhance the filtering of turbulent structures, rendering the visualisation of the temperature streak possible. However, convergence of the DFT results is only reached with 9 and 10 periods, where the DFT fields are equivalent (c.f. Figs. 6.18–6.26). Furthermore, convergence yields the typical chequerboard pattern downstream caused by mixing of stator and rotor wakes.

Figures (6.18–6.26) show a global view of the temperature fluctuation harmonics composing the forcing signal of the MT1 entropy forced simulation. To quantify the evolution of the entropy wave through this high pressure turbine stage, several  $\vec{x}$  normal planes along the MT1 domain are extracted every millimetre from the inlet to the outlet of the complete configuration. The acoustic and entropy waves are computed following Eq. (2.7) and the surface integral weighted by the mass flow rate is computed for each plane. The axial evolution of the entropy wave through the MT1 turbine is shown in Figs. 6.27–6.29 for the entropy forced flow and the baseline flow. Gray zones represent the positions of the stator and rotor vanes. The comparison of the entropy wave between the entropy forced flow and the baseline flow is all the more important here as entropy waves are also generated by the unsteady wakes of the entropy forced flow and are not yet completely been filtered by the DFT computation. Therefore, computing the axial evolution of the entropy wave in the baseline flow allows quantifying the entropy fluctuations not coming from the forcing, which from results shown in Figs. (6.27–6.29)(b) might not be negligible. Computing the entropy generated by the baseline flow allows to confirm that: the supplementary generation of entropy waves is indeed in the wake

Freq: 100 Hz

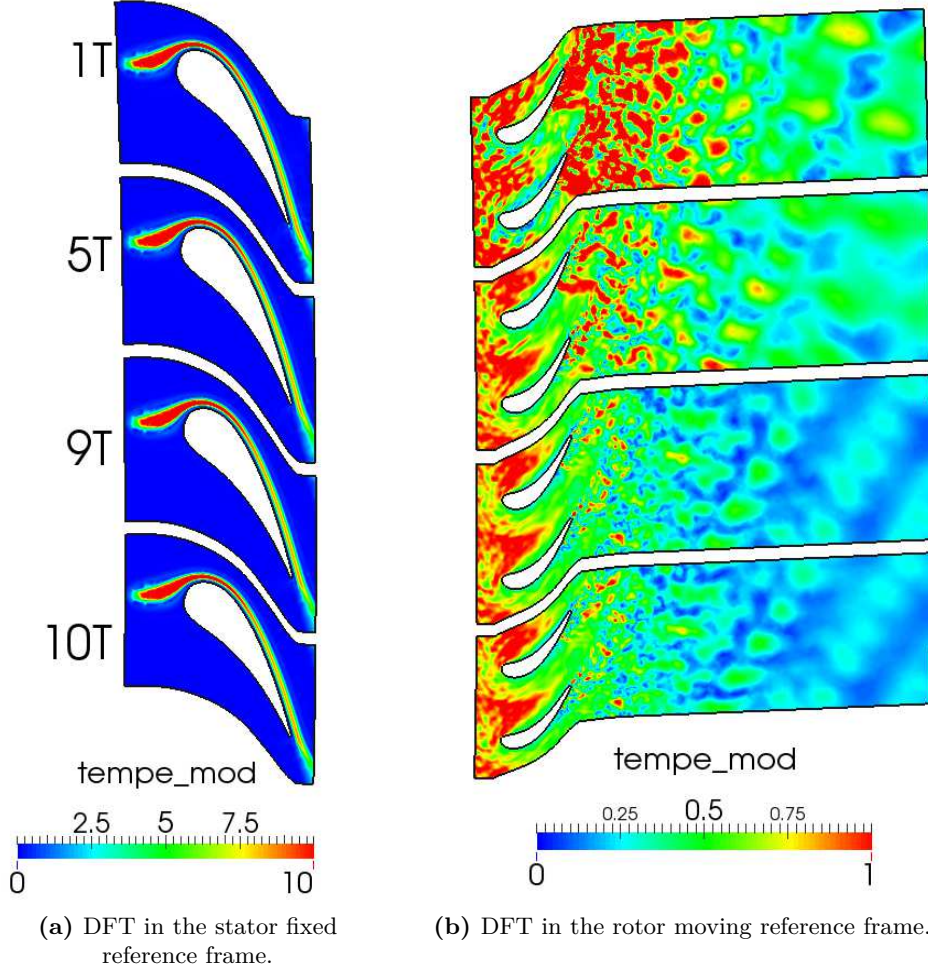


**Figure 6.18** DFT of the MT1 instantaneous fields computed for different run time lengths. Extraction of the fundamental forcing frequency: 100 Hz. Radial cut at  $r_0 = 0.284$  m.

and shock regions and that the stochastic part of Eq. (6.2) is not correlated to the deterministic part (its amplitude decreases with the number of periods taken into account in the DFT). However, it is clear that convergence of the baseline flow has not been reached and this result should only be seen as an estimation of the entropy produced by the baseline flow. Concerning the evolution of the entropy wave in the forced flow (cf. Figs. (6.27, 6.28, 6.29)(a)), the zone where the energy deposition takes place is evidenced by the rapid increase in entropy before the stator blades. After the deposition zone and up to the exit of the stator blade, the entropy streak seems to be almost constant and

Freq: 1500 Hz

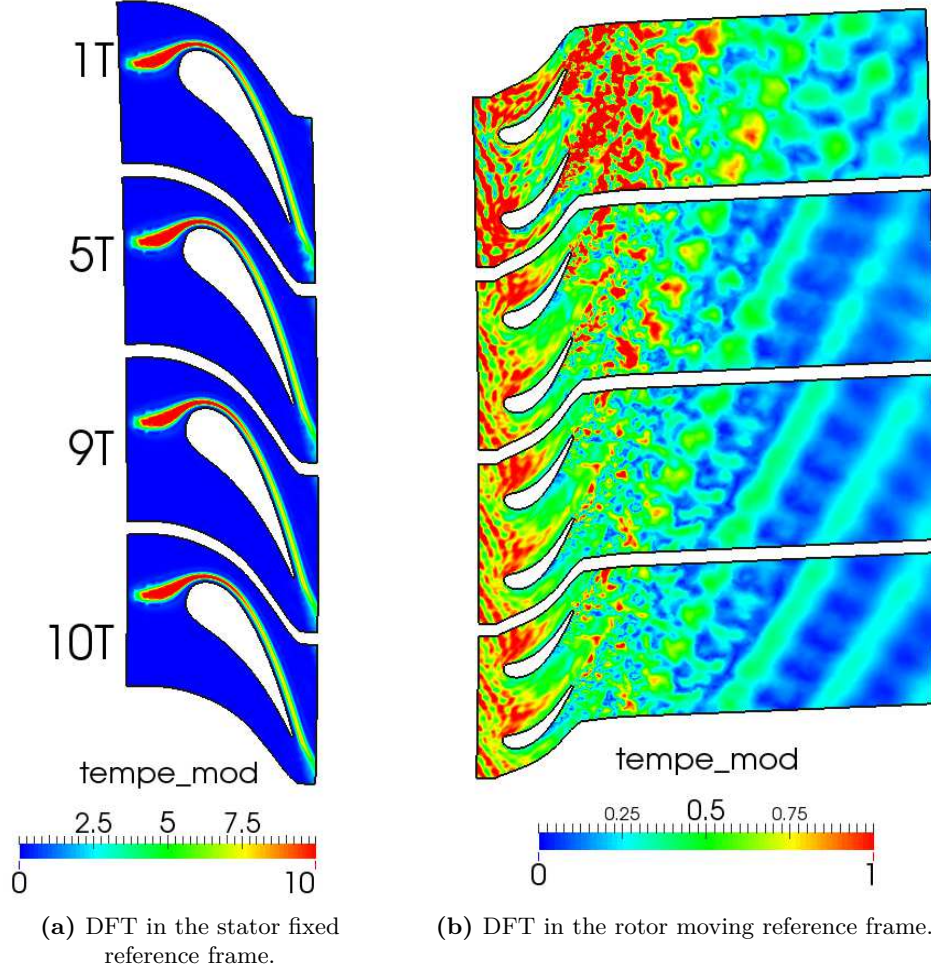


**Figure 6.19** DFT of the MT1 instantaneous fields computed for different run time lengths. Extraction of the harmonic at 1500 Hz. Radial cut at  $r_0 = 0.284$  m.

transported with almost no attenuation. Indeed, since the entropy forcing is not a planar wave it is less sensitive to the dispersion produced by the heterogeneous flow. Instead it acts as a passive scalar that follows the streamlines of the flow without (or less) deformation. In this case, the smaller its characteristic length is (in this case  $R_{dep}$ ), the less sensitive to the mean flow dispersion the streak is. Nevertheless, when the frequency of the forcing is high, the dispersion effect is stronger and attenuates the entropy wave as highlighted by Morgans et al. (2013) and Giusti et al. (2016) (cf. Fig. 6.29a). Afterwards, when the streak arrives in the rotor domain, it is attenuated due to the mixing



Freq: 3000 Hz

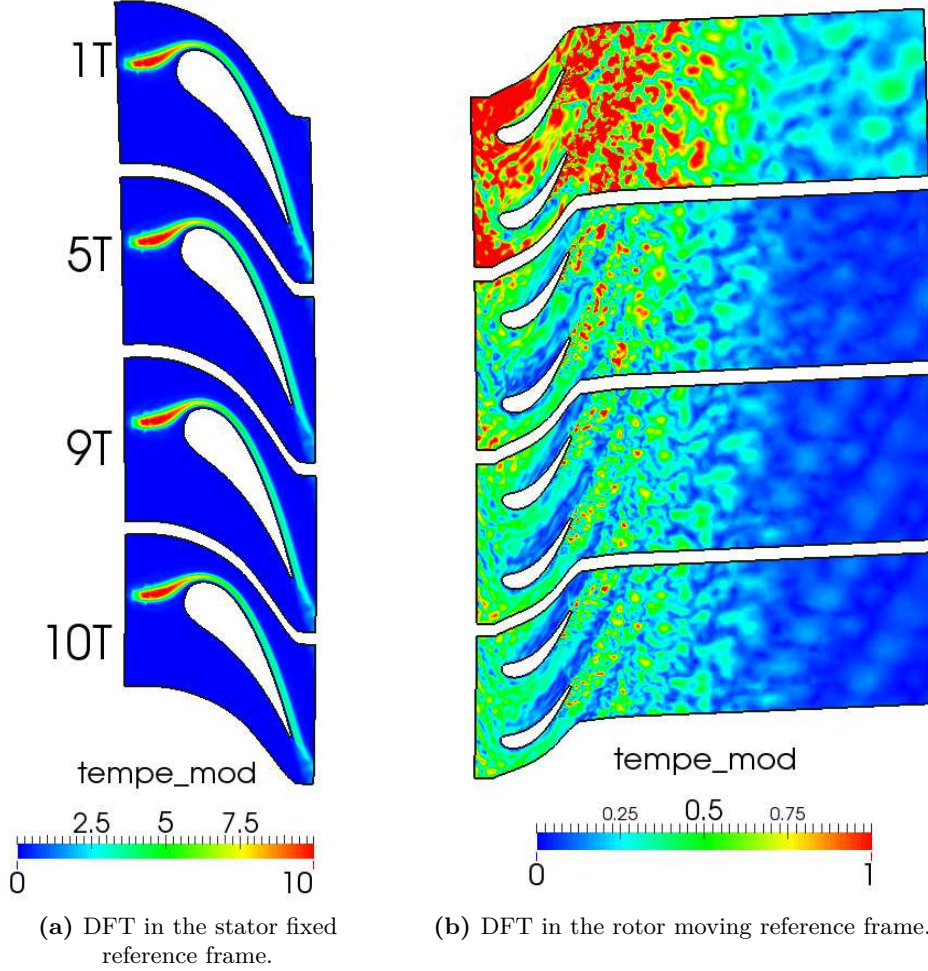


**Figure 6.20** DFT of the MT1 instantaneous fields computed for different run time lengths. Extraction of the harmonic at 3000 Hz. Radial cut at  $r_0 = 0.284$  m.

induced by the natural rotational velocity of the rotor. It is worth noting that once the entropy wave traverses the rotor and assuming that no energy can be transmitted between modes, no entropy gain can exist (besides the one caused by the rotor wakes and shocks) and the entropy wave shall be attenuated or remain constant after the rotor wake. For this reason and the fact that the entropy plane wave evolution against the axial coordinate remains almost the same between 9 and 10 periods, one can conclude that the DFT results are converged and representative of the evolution of the entropy wave in this MT1 configuration.

Freq: 100 Hz

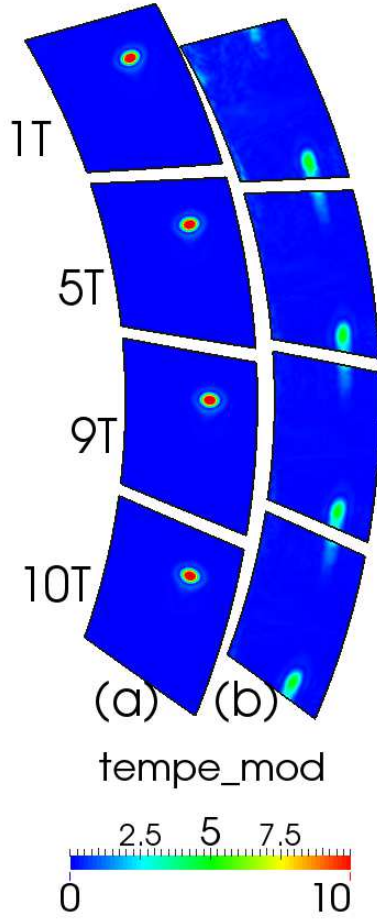


**Figure 6.21** DFT in the stator reference frame, extraction of the fundamental frequency: 100 Hz. Axial cuts at positions  $x_{P_{sin}}$  and  $x_{P_{int}}$  for different run time lengths.

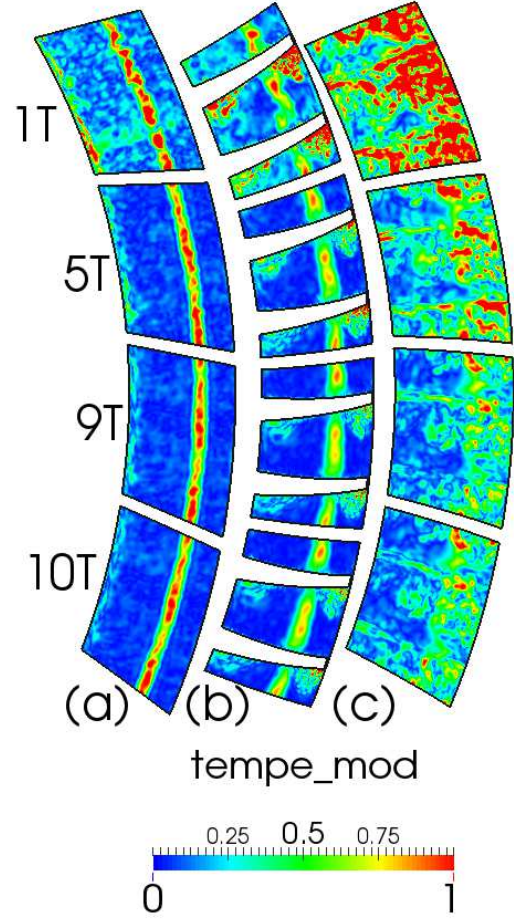


**Figure 6.22** DFT in the rotor reference frame, extraction of the fundamental forcing frequency: 100 Hz. Axial cuts at positions: (a)  $x_{P_{sin}}$ , (b)  $x_{P_{rot}}$  and (c)  $x_{P_{near}}$  for different run time lengths.

In the following section, the results of the numerical simulation are compared with the analytical methodology CHORUS (Leyko 2010, Duran 2013 and Livebardon et al. 2015, 2016) developed at CERFACS, which is based on the compact actuator disk theory of Cumpsty and Marble (1977a). This analysis allows to evaluate the limitations of this reduced model on the prediction of combustion noise in the framework of a realistic industrial configuration.

Freq: 1500 Hz

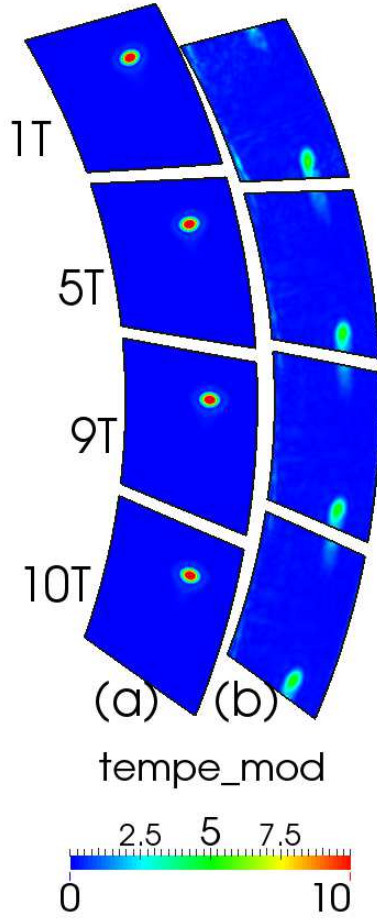


**Figure 6.23** DFT in the stator reference frame, extraction of the harmonic at 1500 Hz. Axial cuts at positions  $x_{P_{sin}}$  and  $x_{P_{int}}$  for different run time lengths.

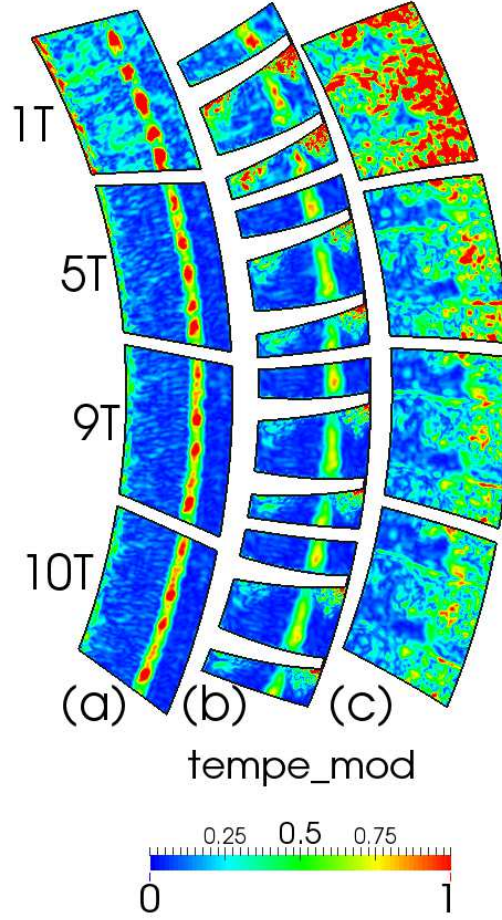


**Figure 6.24** DFT in the rotor reference frame, extraction of the harmonic frequency: 1500 Hz. Axial cuts at positions: (a)  $x_{P_{sin}}$ , (b)  $x_{P_{rot}}$  and (c)  $x_{P_{near}}$  for different run time lengths.

#### 6.2.4 Comparison of the numerical results to the analytical compact actuator disk theory

In this section, the analytical methodology CHORUS is used to extract the acoustic and entropy waves at the inlet of the MT1 configuration and then analytically compute the transmitted noise at the outlet of the turbine stage. In the general case, this methodology starts with a LES computation of the combustor alone to correctly predict entropy, vorticity and acoustic waves generated by the turbulent combustion process. The next step is the extraction of several planes perpendicular to the engine axis at the outlet of



Freq: 3000 Hz

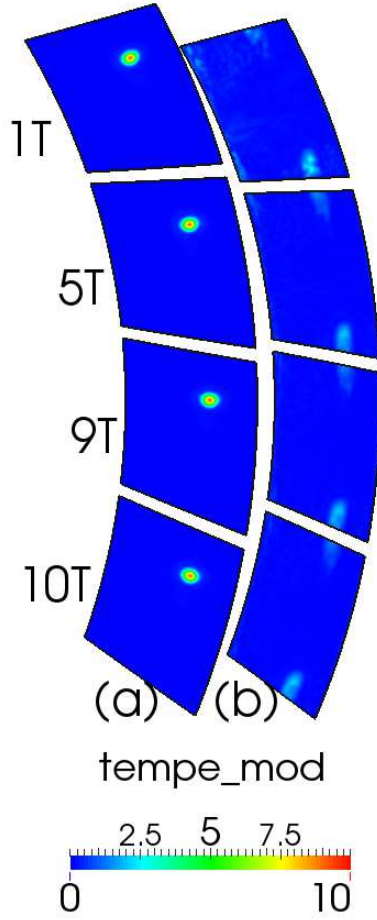


**Figure 6.25** DFT in the stator reference frame, extraction of the harmonic at 3000 Hz. Axial cuts at positions  $x_{P_{sin}}$  and  $x_{P_{int}}$  for different run time lengths.

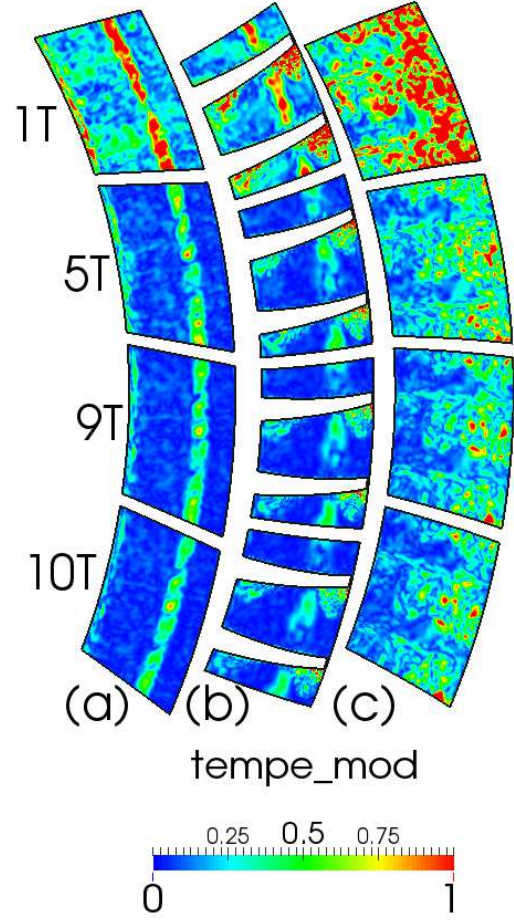


**Figure 6.26** DFT in the rotor reference frame, extraction of the harmonic frequency: 3000 Hz. Axial cuts at positions: (a)  $x_{P_{sin}}$ , (b)  $x_{P_{rot}}$  and (c)  $x_{P_{near}}$  for different run time lengths.

the combustion chamber. In these planes, primitive variables are used to compute the upstream and downstream propagating waves (namely the entropy wave  $\sigma$ , the vorticity wave  $\xi'$  and the upstream and downstream acoustic waves,  $A^-$  and  $A^+$  respectively) used in the 2D actuator disk theory of [Cumpsty and Marble \(1977a\)](#) model. However, the passage from primitive variables to waves is not direct and several steps are needed:

1. Radial averaging is performed to extract the zero-th radial mode from the unsteady fields extracted at the different outlet planes of the combustion chamber to be consistent with the 2D model of [Cumpsty and Marble \(1977a\)](#).



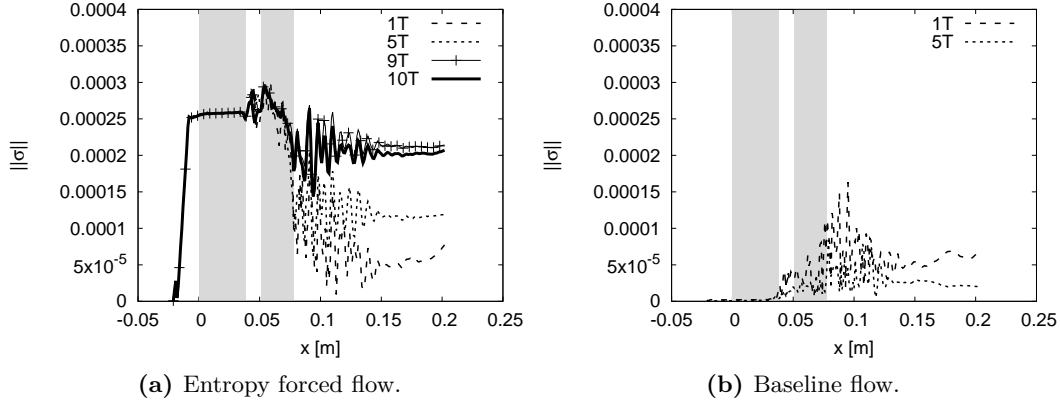


**Figure 6.27** Axial evolution of the entropy wave at frequency  $f = 100$  Hz.

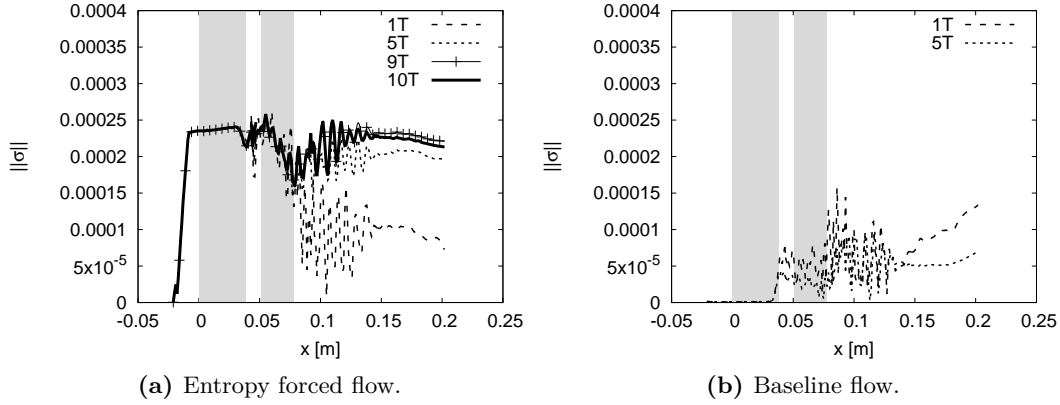


**Figure 6.28** Axial evolution of the entropy wave at frequency  $f = 1500$  Hz.

2. Temporal Fourier transform is performed over the radial averaged primitive variables.
3. Spatial Fourier transform over the azimuthal direction bounded by the angular extrema of the domain (in the present MT1 simulation it is a  $12^\circ$  sector) allows performing an azimuthal modal decomposition.
4. Dispersion relations derived from the 2D LEE are used to transform the primitive variables into the wave formulation.

Then, the different planes extracted at the outlet of the combustion chamber are used to filter the set of waves using a characteristic filtering (cf. [Kopitz et al. 2005](#)). Filtered waves are afterwards propagated through the different turbine stages using the analytical compact model of [Cumpsty and Marble \(1977a\)](#) for each blade row. Therefore, matching conditions are applied to determine the interactions produced between waves. For an

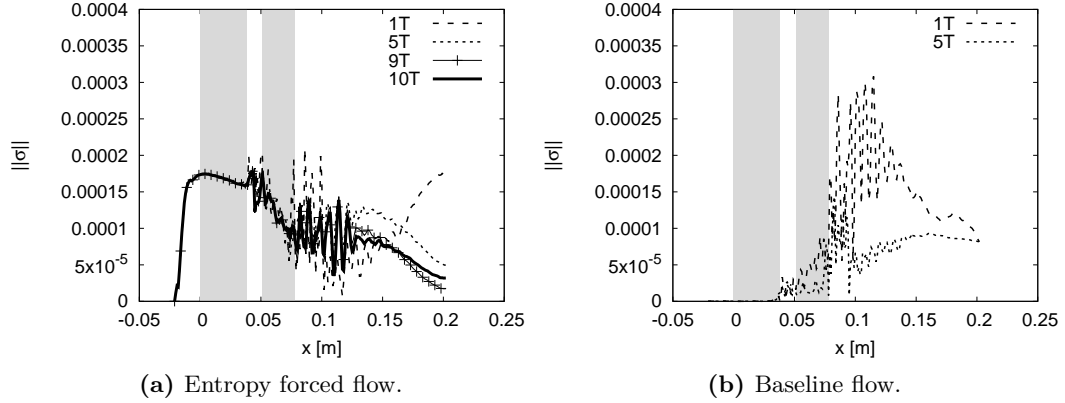


**Figure 6.29** Axial evolution of the entropy wave at frequency  $f = 3000$  Hz.

incident wave, the transmission and reflection coefficients are obtained as well as the generation of new waves (e.g. an azimuthal entropy wave produces a vorticity wave, cf. §5.3.2.4). The convection of waves between two consecutive rows is taken into account by introducing a phase shift based on the wave convection time. Finally, a simplified attenuation function for the entropy plane wave (according to findings presented by Leyko et al. 2010, 2014) based on the characteristic pitch of a blade row can be applied at each compact row. Regarding this matter, Bauerheim et al. (2016) proposes the modelling of the velocity profile through the blades using an asymmetric power law, allowing to estimate the entropy attenuation function of Leyko et al. (2010) analytically. The attenuation of the entropy wave when estimating entropy noise is an important matter. The amount of entropy noise generated is proportional to the amplitude of the entropy wave, which is attenuated at each blade row passage. Therefore, entropy noise is mostly generated in the first stages, where the amplitude of the entropy wave is stronger.

Here, CHORUS is used to evaluate analytically the direct and indirect noise contributions, discriminating noise generated by entropy, vorticity and acoustic waves through any number of turbine stages. However, it is important to notice that this methodology neglects several phenomena naturally present in the numerical simulation, e.g. the generation of entropy and vorticity modes in the stator and rotor wakes, the generation of entropy due to the isothermal boundary conditions applied to the stator and rotor blades and the entropy and vorticity modes generated by the unsteady shock waves.

In the case of the present simulation, the application of CHORUS is slightly different from the one described in the above paragraphs. Here, neither combustion chamber, nor turbulent combustion process has been simulated. The heat release fluctuations are generated by the introduction of a fluctuating energy source term in the upstream annular section (see Fig. 6.3). Eight extraction planes are located between the energy deposition and the leading edge of the stator blades, from  $x = -8$  mm to  $x = -1$  mm,

with a spacing of 1 mm between each plane. As only one sector of the MT1 complete geometry has been computed, only plane waves are considered in this study, which is sufficient to describe the pressure field. However, the entropy field is a composition of several modes, even if only the plane mode is considered. However, even if circumferential modes were to be considered, acoustic waves generated by higher entropy modes cannot be propagated through the turbine stages because the first circumferential mode available is the one corresponding to the first multiple of the number of sectors (here  $m = 30$ ), with a cut-off frequency far beyond the frequency range of interest. Let us first compute the entropy-entropy transfer function for the planar entropy mode between the outlet of the MT1 domain and the last extracted plane ( $x = -1$  mm) in the stator domain. [Figure 6.30](#) shows the comparison of the entropy transfer function computed by the analytical model (cf. attenuation function of [Leyko et al. 2010](#) using the parabolic axial velocity profile of [Livebardon 2015](#)) and the ones computed within the simulation using different run times as well as the one obtained by [Papadogiannis et al. \(2016\)](#) pulsating a 2000 Hz entropy plane wave. The first remark concerning the entropy transfer function computed in the present study is that the variability of the DFT results is very sensitive to the number of periods used and that convergence of the result is only reached between 9 and 10 periods. The numerical transfer function shows characteristics not shown in the prior study of the EWG nozzle (cf. [§5.3.3](#)), where the entropy wave is almost completely attenuated through the passage of the nozzle (at 50 Hz only 20% of the entropy plane wave reaches the outlet of the EWG). In this turbine case study, the conversion of vorticity into entropy modes and the entropy generated waves due to the isothermal boundary condition applied to the blades seems to compensate the attenuation of the entropy wave through the turbine stage. For some cases the entropy wave amplitude at the outlet of the MT1 is even greater than the one introduced at the inlet. Furthermore, the fact that the entropy forcing was not a plane wave from the beginning but a small deposition radius makes the entropy streak less sensitive to attenuation. This effect is clearly highlighted when comparing the 2000 Hz harmonic with the numerical simulation of [Papadogiannis et al. \(2016\)](#) (entropy plane wave forcing), where the amplitude of the entropy wave in the present simulation is twice as big. Furthermore, when comparing to the attenuation function computed by the CHORUS methodology, a good agreement is found up to  $\approx 900$  Hz. It should be noticed that the attenuation of the entropy plane wave estimated by CHORUS is only taken into account at the stator and rotor vanes and not in the annular ducts, as taken into account in the numerical computed attenuation function. In order to estimate the attenuation of the entropy plane wave by the mean flow effects only, the methodology of [Leyko et al. \(2010\)](#) is applied, where 3D streamlines are traced from the inlet of the MT1 configuration. This procedure is done in three different steps: first, streamlines are traced in the stator domain using the absolute velocity vector. Second, streamlines are traced at the rotor moving parts domain (the blades and the hub) using the relative velocity vector (subtracting the rotational speed of the blades). Finally, in the last part of the rotor domain, streamlines are traced using the absolute velocity. [Figure 6.31](#), shows the resultant streamlines for each sub-domain of the MT1 configuration. Notice that only a part of the whole set of the generated

streamlines is represented for an easier visualisation of the mean flow characteristics. In the stator domain, where no secondary flows are highlighted by the Q-criterion shown in Fig. 6.15a, the streamlines bypass the stator blade and go through the stator domain smoothly leaving almost with a straight trajectory. In the rotor vane, some streamlines are captured by the secondary flows: some travel in the tip region from the pressure to the suction side of the blade and then roll in the tip vortices and others are seen to be absorbed by the hub passage vortex. Finally, in the outlet annular section of the rotor domain, streamlines are again smooth and almost straight. However, in the upper part of the duct the flow is found to be dominated by the axial velocity, whereas in the bottom part of the duct a strong contribution of the tangential velocity deviates the streamlines. To compute the attenuation function of the entropy plane wave, the elapsed time of a particle seeded from the inlet of each sub-domain to reach the outlet (of the sub-domain) of all the traced streamlines are needed. The spatial distribution of this elapsed time at the outlet of each sub-domain is what Leyko et al. (2010) defines as the function  $t_d(r, \theta)$  and is shown in Fig. 6.32. At the outlet of the stator and rotor vanes (cf. Figs. 6.31a and 6.31c), the wakes are clearly visualised by the regions with the longest particle times. At the outlet of the rotor annular duct (cf. Fig. 6.31c) streamlines deviated by the tangential velocities are the ones taking the longest to reach the outlet. Once the function  $t_d(r, \theta)$  is known, the entropy plane wave attenuation function of each sub-domain can be computed using Eq. (C.1b) and compared with the one estimated by CHORUS. Figure 6.33 shows the different attenuation functions of each MT1 sub-domain compared with the analytical estimations of CHORUS. A fair estimation of the entropy plane wave attenuation is done by CHORUS at the stator and rotor vanes. However, this result shows the entropy plane wave suffers a strong attenuation in the rotor outlet duct (a similar result has been found in the EWG configuration studied in Chapter 5). This is not very important, since in the entropy wave is only convected and does not generate acoustic waves. However, this attenuation should be taken into account if the inter-stage vane is too long. Finally, the global attenuation function is shown in Fig. 6.30, where it seems to be in a very good agreement with the forced numerical simulation up to  $\approx 500$  Hz. Afterwards, one can consider that the discrepancies between the forced simulation and the 3D streamline dissipation function methodology are due to the conversion of vorticity modes into entropy modes. It should be noticed that the attenuation function based on the 3D streamlines methodology superimposes the dot at 2000 Hz, where the reference simulation of Papadogiannis et al. (2016) shows a greater attenuation. This result may be due to the surface integration formulation used in this manuscript, where mass weighted integration is used. However, this result has its bigger influence on the entropy waves, which are not only planar (as already shown in Chapter 5) and less on the acoustic waves which still can be considered as plane waves (when properly filtered from the hydrodynamic contributions).

Up to now, this study was focused on the evolution, distortion and attenuation of the entropy wave. Now, CHORUS is used to estimate the contribution of each wave (computed at the extracted planes) to the overall noise emission radiated at the outlet

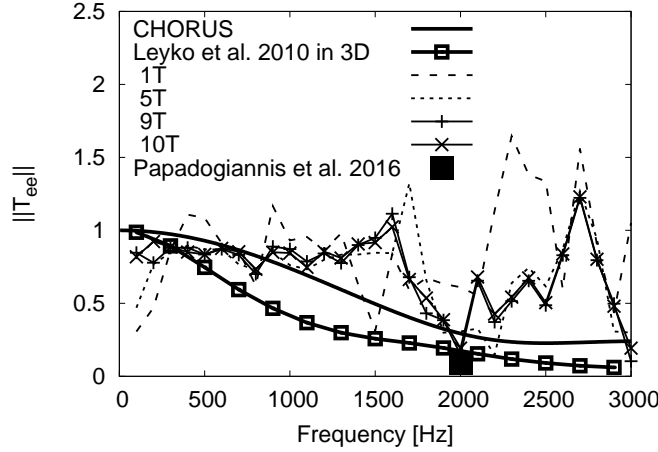


**Figure 6.30** Comparison of the entropy-entropy transmission coefficient between the analytical model (CHORUS), the numerical simulation using different run times and [Papadogiannis et al. \(2016\)](#) entropy forced simulation.

of the MT1 configuration. To do so, the acoustic power ( $\mathcal{P}$ ) at the outlet of the MT1 turbine is computed using the [Bretherton and Garrett \(1968\)](#) formula, which takes into account the convective terms,

$$\mathcal{P}(m, \omega)_{\text{out}} = [(M \cos \theta + \cos \nu) (1 + M \cos (\theta - \nu))]_{\text{out}} \left( A_{\text{out}}^+ \right)^2 (\gamma p c A)_{\text{out}}, \quad (6.3)$$

and measures the outgoing acoustic power per propagating mode. In this equation  $m$  is the order of the azimuthal mode;  $\omega$  is the angular frequency;  $M$  represents the absolute Mach number,  $\theta$  and  $\nu$  are respectively the flow angle and the angle of the wave vector;  $p$  and  $c$  are the mean pressure and sound velocity of the flow;  $\gamma$  is the ratio of specific heat capacities and  $A$  is the section of the turbine outlet. To make a proper comparison between the simulation and the analytical model, one should evaluate the validity limit of the analytical results within the compact theory. To do so, the 3D numerical simulation of [Papadogiannis et al. \(2016\)](#), in which the entropy plane wave has been introduced without the generating acoustics (direct noise) is used as reference simulation to compare the entropy-acoustic transmission coefficient obtained by CHORUS. In this case, and unlike the transfer functions presented by [Papadogiannis et al. \(2016\)](#), the transfer functions are computed using the 3D mean flow characteristics of the MT1 simulation and not the 2D flow of [Duran and Moreau \(2013b\)](#). [Figure 6.34](#) shows the entropy-acoustic transmission coefficient of the MT1 stator/rotor configuration. It is worth noting that to be coherent with the definition of the acoustic waves used in this manuscript (cf. [Eq. \(2.7\)](#)), the entropy-acoustic transfer result obtained by [Papadogiannis et al. \(2016\)](#) has been multiplied by 2. The vertical dashed line in [Fig. 6.34](#) represents the compactness theoretical limit (Helmholtz number computed using the length of the stator blade axial chord and the mean velocity at the inlet of the MT1). A good agreement is found between the entropy-acoustic transmission coefficient computed by the

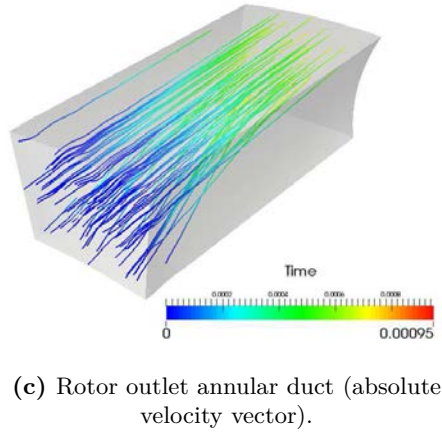
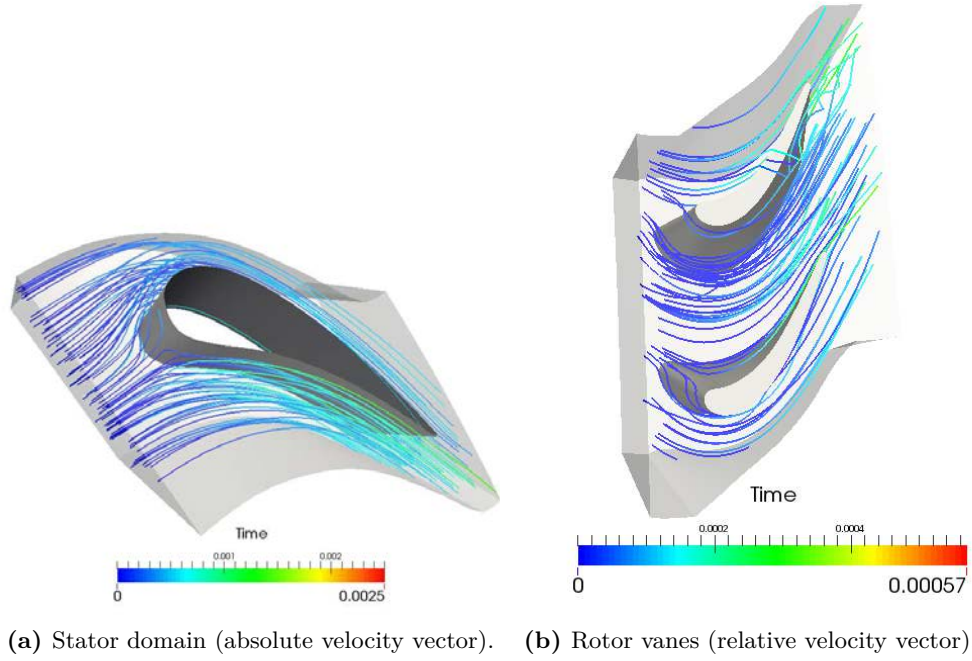


**Figure 6.31** MT1 baseline mean flow streamlines coloured by the elapsed time of a particle over the streamline.

analytical model using the MT1 3D mean flow data and the numerical simulation of [Papadogiannis et al. \(2016\)](#). Assuming that the compact results for the entropy-acoustic transmission coefficient are still valid up to at least 2000 Hz (even though no information has been acquired between 0 and 2000 Hz), the acoustic power can be evaluated and considered as a good approximation up to this limit. Furthermore, the entropy-acoustic

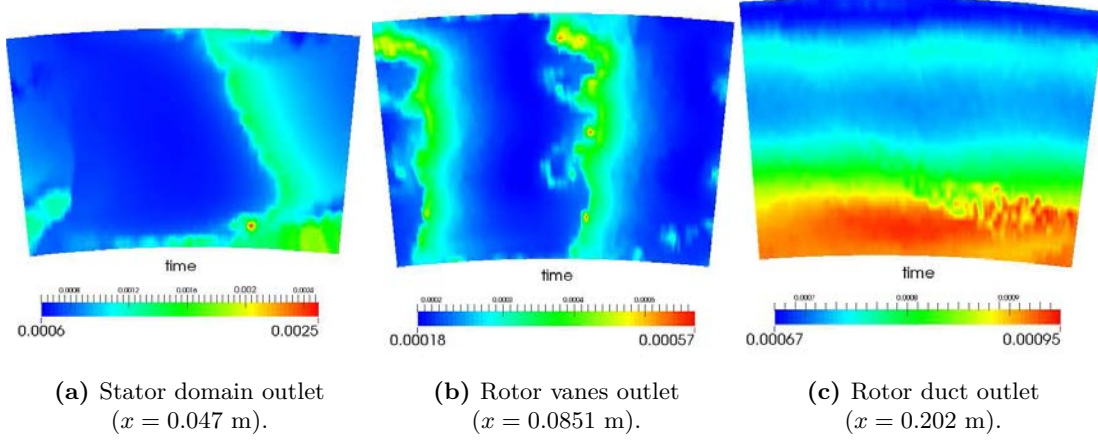


**Figure 6.32** MT1 elapsed time spatial distribution at the outlet of the MT1 sub-domains (function  $t_d(r, \theta)$ ).

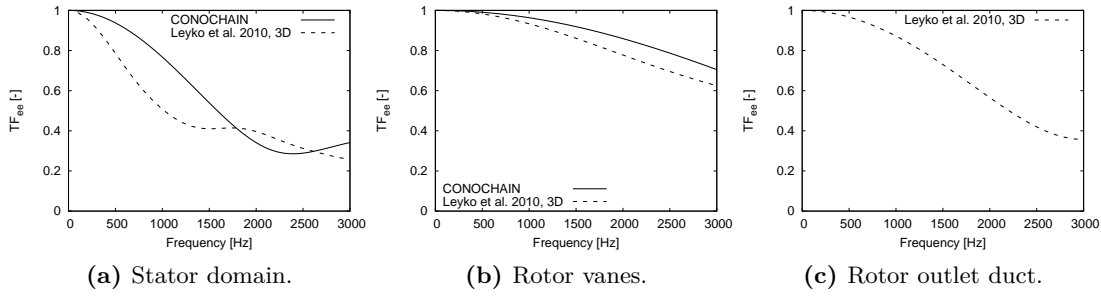


**Figure 6.33** Attenuation functions of each MT1 sub-domain.

transfer function computed numerically within the simulation is added for comparison. It is worth noting that this numerical computed transfer function is an estimation of the real one, in which multiple assumptions are done. Indeed, the entropy wave at the inlet of the configuration (in this case taken next to the energy deposition) is not a purely plane wave and is the result of a mass weighted integration at this axial position. The second strong approximation made is that the acoustic wave considered at the outlet of the configuration is an overall acoustic wave and not the purely acoustic wave generated by the entropy forcing alone. Therefore, the numerical entropy-acoustic transfer function is representative of all the generated acoustic waves at the outlet of the configuration:

- reflected acoustic waves at the boundary conditions and the rotor blades,
- acoustic waves generated by the acceleration of the entropy forcing,
- acoustic waves generated by the energy source term (direct noise),



- acoustic waves generated by the acceleration of entropy waves generated by the wakes and shocks,
- acoustic waves generated by the acceleration vorticity waves,

compared to the inlet entropy plane wave. In this case, the separation of each contribution is not possible (as done in §5.3.3), since the complete set of transfer functions is unknown to build the system described in Eqs. (5.22–5.25). However, some characteristics found in the EWG analysis are also found in this complex case geometry. In the low frequency range (up to  $\approx 1500$  Hz), where according to the DMD spectrum of the baseline flow computed in the stator wake (cf. Fig. 6.10a), the generation of supplementary entropy waves is less important and compensates only the attenuation of the entropy wave, the generation of indirect noise decreases with the increasing frequency (cf. EWG entropy-acoustic transfer function in Fig. 5.82). In this case, since the attenuation of the entropy wave is compensated by the generation of new entropy modes, the generation of acoustic waves is also stronger compared with the analytical theory. It is worth noting that with all of the assumptions made for this entropy-acoustic transfer function, a very good agreement between the analytical and the simulation result is found below 1500 Hz and the same trend is retrieved. For higher frequencies (1500 Hz to 3000 Hz), strong modes conversion from vorticity to entropy modes have been highlighted and a hump in the generation of acoustic waves also appears in Fig. 6.34 at this frequency range. The strong disagreement between the analytical model and the numerical simulation is due to the lack of a model to predict the generation of new entropy modes in the wakes and shocks regions, which enhances the production of more entropy noise.

Finally, once the limitations of the compact theory assessed, the total acoustic power can be computed. Figure 6.35a shows the total acoustic power at the outlet of the MT1 forced simulation when considering 10 periods of the entropy forced signal for the DFT computation compared with its analytical estimation using the CHORUS methodology. As expected, the generated noise in the LES simulation is greater than the one estimated by CHORUS. However, the global trend of the acoustic power estimated by CHORUS is also obtained in the numerical results, where the maximal acoustic power is radiated by the smallest frequencies. The contribution of the different noise sources to the overall radiated acoustic power in the numerical simulation cannot be computed. In the CHORUS methodology, which considers linear acoustics, the contribution of each noise source is computed and shown in Fig. 6.35b. According to CHORUS, the generation and propagation of direct noise by the introduction of the energy source term is negligible compared with the generation and propagation of entropy noise. However, since this study is only limited to the propagation of plane waves, the convection of an entropy plane wave does not generate vorticity waves which generate vorticity noise (as highlighted in Chapter 5 and explained by Duran and Morgans 2015). Furthermore, CHORUS is not capable of computing vortex noise when no vorticity wave is captured at the extraction planes (which is the case in this simulation) and no model allows to estimate the vorticity waves generated in the wakes. For all of these reasons it is normal



to obtain an underestimation of the generated acoustic power by the CHORUS methodology. However, the global trend and the order of magnitude obtained by the analytical estimation is in a very good agreement with the 3D-full compressible LES simulation.

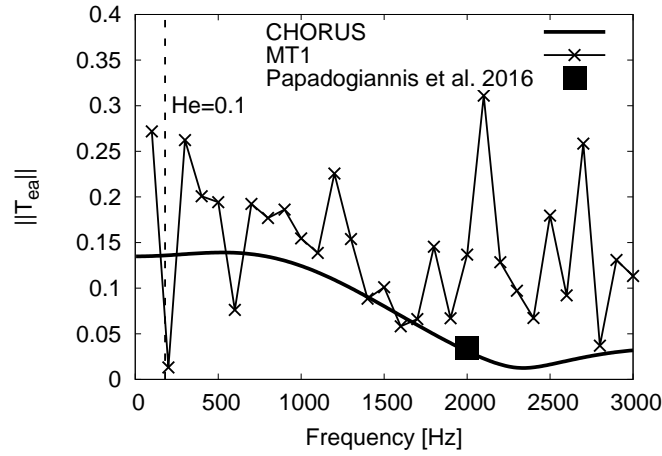


**Figure 6.34** Entropy-acoustic transmission coefficient computed numerically compared with CHORUS and [Papadogiannis et al. \(2016\)](#) 3D MT1 simulation.

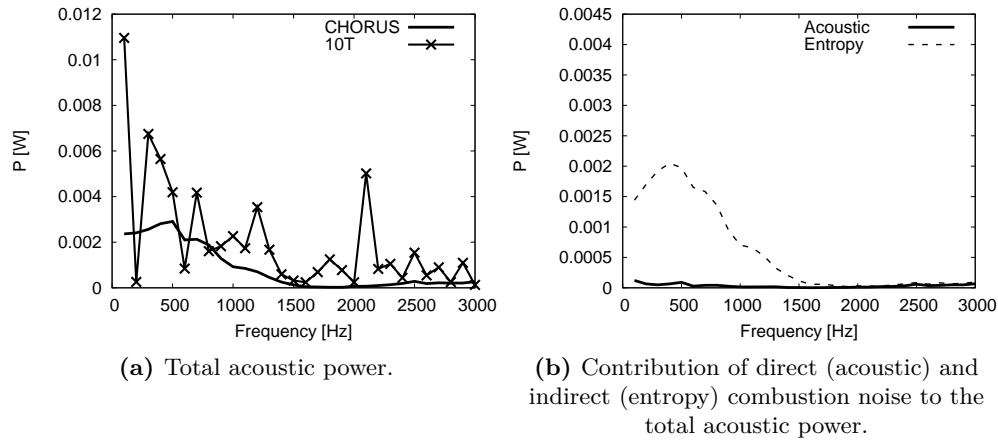


**Figure 6.35** Acoustic power at the outlet of the MT1 turbine.

## 6.3 Conclusions

In this second part of the manuscript, combustion noise generation is studied within a high pressure transonic turbine stage. In this case, the flow cannot be considered as axisymmetrical, as done in [Part I](#) due to a strong azimuthal deviation of the flow produced by the stator and rotor blades as well as the rotational velocity of the rotor. Due to the different flow topology (in comparison with the nozzle flow studied in [Chapter 5](#)), different combustion noise tools prediction need to be developed based on equations taking into account the azimuthal deviation of the flow (cf. [Cumpsty and Marble 1977a](#)). For this study in combustion noise generation, the numerical simulation performed by [Wang et al. \(2016\)](#) and [Papadogiannis et al. \(2016\)](#), where an entropy plane wave is introduced at the inlet of MT1 turbine stage is revisited. In this case, to be more realistic with the actual production of hot streaks in a real aero-engine, a cylindrical energy source term is introduced in the upstream annular section of the domain to generate harmonic temperature fluctuations. The path followed by this temperature streak, its attenuation and the interactions between the streak, shock waves and secondary flows are studied. An energy deposition model based on the one proposed in [Chapter 5](#) is adapted to generate a cylindrical harmonic pulsating temperature fluctuation. The generated temperature fluctuation is transported by the flow and is found to be absorbed by the suction side of stator blade, where it follows its path close to the blade wall. Close to the blade leading edge, the streak traverses a shock wave, which seems to have little influence on the trajectory and the shape of the streak. Then, the streak trajectory is found to be in the wake, in accordance with [Gaetani and Persico \(2017\)](#) measurements. In this wake zone, the streak follows its first important deformation, where the streak is wrapped around the vortex shedding. Furthermore, the attenuation of the maximal value of the temperature is also in good agreement with [Schuster et al. \(2015\)](#) and [Gaetani and Persico \(2017\)](#) measurements. Inside the rotor, the streak is strongly deformed by the non-homogeneous flow and interacts with the secondary flows and shock waves. Here again, the attenuation of the temperature maximum value is in agreement with [Schuster et al. \(2015\)](#) measurements.

The analysis of noise generation and entropy attenuation has been carried in the frequency domain to be compared with prior studies and analytical methods. In this case, the numerical simulation of [Papadogiannis et al. \(2016\)](#) and [Wang et al. \(2016\)](#) has been taken as reference entropy forced simulation, while the analytical methodology (CHORUS) used for the comparison is based in the actuator disc theory of [Cumpsty and Marble \(1977a\)](#). To do so, DFT of the complete 3D fields is performed and its convergence is evaluated using different sampling lengths. The convergence of the DFT analysis has been evaluated using the temperature fluctuation fields and has been reached using 10 periods of the fundamental forcing frequency (100 Hz). In order to be rigorous and compare with the analytical methodology, a radial average must be done before computing the DFT followed by a modal decomposition into azimuthal modes. However, since the numerical simulation considers only a  $12^\circ$  periodic sector, the corresponding

first azimuthal mode is the 30<sup>th</sup> mode, for which the cut-off frequency should be far beyond the combustion noise generation frequency range. Thanks to this fact, only the planar mode is considered and its evolution along the MT1 configuration is obtained by a successive surface (mass-weighted) integration at different axial positions of each DFT field. Doing so, the evolution of the entropy plane wave and therefore its attenuation can be followed along the complete stator/rotor. It has been highlighted that the separation of the flow produced by the shock waves on the suction side of the stator vane and rotor blades is an entropy source. This feature has been identified in the forced and unforced flow and corresponds to a transfer of energy between vorticity to entropy modes. In the low frequency range (between 100 and  $\approx 1500$  Hz), where the entropy mode is less submitted to dispersion produced by the heterogeneous flow (cf. [Morgans et al. \(2013\)](#) and [Giusti et al. \(2016\)](#)), this entropy source is sufficient to compensate the attenuation of the entropy wave, leaving its entropy-entropy transfer function to be  $\approx 1$ . For higher frequencies (between 1500 and 3000 Hz), a strong generation of entropy and velocity fluctuations is identified by DMD analysis at the stator wake region of the baseline flow. In this frequency range, the generation of entropy by the wakes and shocks is strong enough to not only compensate the attenuation of the entropy plane wave, but to be stronger than the generated entropy wave at the inlet of the configuration (entropy-entropy transfer function  $> 1$ ). Comparing the attenuation of this cylindrical entropy forcing with the reference plane wave forcing carried by [Papadogiannis et al. \(2016\)](#) and [Wang et al. \(2016\)](#), it has been found that the cylindrical forcing (non-planar wave) is less sensitive to the attenuation of the non-homogeneous flow: in this case the attenuation of the 2000 Hz entropy plane wave is divided by two compared with [Papadogiannis et al. \(2016\)](#) plane wave forcing simulation. Indeed, since the cylindrical forcing is not a plane wave, it acts as a passive scalar that follows the streamlines of the flow, where its attenuation should be dependent on its characteristic length (in this case the radius): the bigger the radius is, the closer to a plane wave the forcing is and therefore the stronger the dispersion of the wave due to the non-homogeneous flow is. Afterwards, the generation of acoustic waves in the simulation has been compared with the analytical generation and propagation of acoustic waves due to a planar entropy forcing using the CHORUS methodology. It has been found that more acoustic waves are generated in the simulation, where up to 1500 Hz both results follow the same trend: maximum generation of acoustics at low frequencies and then decreasing of the generation of acoustics, as already found in [Chapter 5](#). Afterwards, for larger frequencies, the generation of supplementary entropy modes make the generation of acoustic waves stronger and therefore in disagreement with the analytical findings. Indeed, the analytical methodology neither takes into account the entropy sources located in the wakes and shocks, nor the vortex noise generated at the wakes. Finally, the radiated acoustic power at the outlet of the MT1 has been computed. The same trend as in the entropy-acoustic transfer function has been obtained, where the maximum production of acoustics is found to be in the lowest frequencies and the numerical simulation shows a stronger acoustic power generated. The advantage of the analytical methodology is that the contribution of each noise source can be split, showing that acoustic waves generated by the heating produced by

the energy source term (direct noise) are negligible compared with the entropy generated acoustic waves (indirect noise). However, the contribution of vortex noise is not taken into account in the analytical model due to the fact that no vorticity wave is present in the extraction planes in the CHORUS methodology and there is no model that takes into account vorticity sources in the wakes. In the case of the numerical simulation, the overall acoustic waves are taken into account in the radiated acoustic power: vortex noise, entropy noise, direct noise and even reflected waves at the boundary conditions, which are very small and concentrated only in the very small frequencies ( $\leq 300$  Hz).

Finally the last conclusion of this chapter is that the CHORUS methodology gives a very good estimation of the propagated noise in this case. Even though, one of the strongest assumptions is the compact limit, a good agreement has been found in all the presented results up to 3000 Hz, while the compact limit has been estimated to be at  $\approx 250$  Hz. However, a model to take into account the vorticity and entropy generated at the wakes is needed to improve the predictions.

# General conclusions and perspectives

Over the years, the constant increase in air traffic led to the public awareness of the associated consequences that are fuel consumption, pollutant emissions, and other disturbances. To control the outcome of this traffic growth, international regulations were enforced. One of these impacts the specific phase of aircraft in the near zone airports. Indeed, in this usually busy environment, perceived noise is of importance. Due to the different governmental constraints put in place over the years, all of the noise identified sources of an aircraft have been considerably reduced with the exception of combustion noise, which becomes today a potentially limiting factor for further reduction. In this PhD work, our objectives were to: 1) review and understand the limits of reduced models whenever applied to combustion noise predictions, 2) rely on high-fidelity LES simulations to improve our understanding and 3) address a complex geometry application.

To ease the understanding and assess numerical methods to predict indirect noise generation, neither the combustion chamber nor the combustion process have been considered. In [Part I](#) combustion noise generation is studied in the simplest configuration: a subsonic nozzle flow. Indeed, the flow can be considered axisymmetric and isentropic, allowing a strong simplification of the governing equations. Throughout this present work, numerical results are compared or guided by analytical methods presented in [Chapter 2](#). For this specific study and adequate validation, the chosen configuration is a well defined nozzle flow called the Entropy Wave Generator (EWG) introduced in [Chapter 3](#), and for which experimental data is available. For this configuration, the analytical methods presented in [Chapter 2](#) are used to make a parametric study of the influence of the inlet acoustic boundary condition and the modelling of the introduced temperature fluctuation in [Chapter 4](#). It is concluded that the correct modelling of the experimental heating device allows to retrieve the correct shape of the temperature fluctuation as well as the correct timing of the pressure fluctuation signal (which was not the case in the prior studies carried by [Duran et al. 2013b](#)). The inlet acoustic boundary condition plays an important role on the generation of entropy noise and without an accurate evaluation of its experimental value, an exact reproduction of the experiment by numerics or analytics is very difficult. Overall analytical results show disagreement between the predicted pressure signals and the measurements. To obtain a better insight in the mechanisms re-

sponsible for combustion noise generation and understand why the analytical modelling fails to reproduce the subsonic experiment, full compressible Large Eddy Simulations (LES) are detailed in [Chapter 5](#) for the EWG. Here, special care is taken to model correctly the two important parameters identified in the analytical analysis of the nozzle (i.e. the heating device and the inlet acoustic impedance). The electrical resistances of the experiment are taken into account in the CFD simulation by the introduction of an energetic source term in the energy transport equation while the inlet reflection coefficient is set to the most physical value, i.e.  $R_{in} = -1$  due to the upstream settling chamber. The EWG LES pressure signals agree very well with the measurements, which highlights the lack of physics in the reduced models. To get an improved understanding on the effects missing in the analytical models, the nozzle transfer functions are computed by LES and compared with the analytical ones. First, in order to respect as much as possible the hypothesis made by the analytical model (i.e. isentropic flow) and validate the numerical methodology to compute the nozzle transfer functions, the Euler set of governing equations is used. The acoustic-acoustic transfer functions of the nozzle are found to be equivalent between the non-compact analytical method of [Duran and Moreau \(2013a\)](#) and the Euler 3D simulation. However, the entropy-acoustic transfer functions and the entropy-entropy transmission coefficient are found to disagree for the range of frequencies between 100 and 250 Hz. This reveals a geometry effect not taken into account by the analytical quasi-1D theory. Indeed, the distortion of the entropy plane wave through the nozzle causes this disagreement. The entropy plane wave is scattered into higher order modes (mostly radial modes in the case of Euler simulation) due to the flow distortion and streamlines curvature at the nozzle. This attenuation of the entropy plane wave can be taken into account by models like [Leyko et al. \(2010\)](#) and [Zheng et al. \(2015\)](#). The attenuation model of [Leyko et al. \(2010\)](#) is found to be very precise when comparing to the results obtained in the Euler numerical simulation and other exact models like the one proposed by [Giusti et al. \(2016\)](#). Second, the LES based Navier-Stokes (NS) equations are used to take into account all the physics of the problem (specially the viscous effects neglected by the isentropic model) and the nozzle transfer functions are re-obtained. This time, all the nozzle transfer functions at low frequency (below 100 Hz approximatively) are found to be in disagreement with the analytical predictions. The transition to turbulence at the nozzle throat generates vorticity, which produces vorticity waves that generate more acoustic waves. The generation of vorticity and its associated noise is another phenomenon neglected by the analytical model and seems to be an important contributor of the generated acoustics at low frequency as already found by [Howe \(2010\)](#). Finally, the analytical model presented in [Chapter 4](#) is used together with the LES NS transfer functions, to reproduce the results obtained by the EWG LES. This time, the resulting pressure signals are in good agreement with the EWG LES, which confirms the importance of viscous and geometry effects naturally present in the LES NS transfer functions. For this final case, and although the entropy wave is found to be scattered into higher order modes, only plane waves have been considered to reproduce the results of the EWG LES. This result confirms that acoustic waves remain 1D, as proposed in the analytical model of [Zheng et al. \(2015\)](#).

In [Part II](#), combustion noise is studied in a more realistic framework: a high pressure turbine stage by use of LES. The selected configuration is the MT1 turbine stage, whose baseline flow topology is first studied in [§6.2.2](#). Then, in order to better represent the physics in a real aero-engine, the temperature fluctuations generated by a burner are modelled by the introduction of a cylindrical fluctuating energy source term. For this specific simulation, particular attention has been taken to introduce temperature fluctuation amplitudes of the same order magnitude as the ones measured in real aero-engines (cf. [Schuster et al. 2015](#)). To get further insight in the attenuation of the generated temperature fluctuation and the generation of combustion noise, Fourier analysis is carried based on the unsteady simulations. For this complex geometry flow, the analysis is found to be much more complex due to the presence of secondary flows, shock waves, wakes and rotor motion. It has been found that the baseline flow generates entropy modes by two mechanisms, the motion of the unsteady shock waves and the conversion of vorticity modes into entropy modes. The attenuation of the entropy plane wave in the simulation is compared with the 3D entropy dissipation function computed using the model of [Leyko et al. \(2010\)](#), which has been proven to give precise results in nozzle flows. However this time, since only the velocity mean field is used to estimate the attenuation of the entropy plane wave, only the effects of the mean flow are taken into account, neglecting the generation of entropy waves by the unsteady baseline flow, thereby underestimating the entropy transmission coefficient. The results of the numerical simulation are also compared to an analytical model, the CHORUS methodology developed at CERFACS, which is based on the 2D compact model of [Cumpsty and Marble \(1977a\)](#). Once again, important features such as strong 3D effects as well as viscous effects are neglected by the analytical model. Therefore, and as expected, the acoustic generation due to the introduction and acceleration of temperature fluctuations is underestimated (cf. [Figs. 6.30 and 6.34](#)). This is mostly due to the lack of a model taking into account the generation of entropy modes and vorticity waves (as already found in the nozzle flow analysis) by the unsteady baseline flow. It is also highlighted that entropy noise is the dominant noise source (cf. [Fig. 6.35](#)) for this configuration and a reliable model to take into account the attenuation of the entropy wave needs to be developed. However, despite the fact that the generation of acoustic waves by the analytical model is underestimated, CHORUS is capable of predicting the generated noise and this using the compact assumption.

A first perspective of the present PhD work is to improve analytical models and the understanding of combustion noise generation and propagation. The invariants methodology of [Duran and Moreau \(2013a\)](#) should be first extended to take into account the attenuation of the entropy wave through the nozzle, using for example the attenuation function of [Leyko et al. \(2010\)](#). New models are needed to be developed to take estimate the vorticity waves generated by the unsteadiness of the flow (eg. transition to turbulence or wakes). A model is also needed to take into account the conversion of vorticity modes into entropy modes as well as the generation of entropy modes by shock waves. To further improve the understanding in combustion noise generation in a turbine stage, the same analysis carried for the EWG nozzle to compute the transfer functions

is needed. To do so, instead of introducing an energy source term, acoustic and entropy plane waves need to be introduced properly through the boundary conditions, and this taking particular care to the reflections at boundary conditions. Finally, in this study of the MT1 turbine stage, only planar waves were considered in the diagnostics. This is justified by the simplification of the full geometry into a  $12^\circ$  periodic sector, for which the first azimuthal mode corresponds to the 30<sup>th</sup> azimuthal mode of the full annular configuration. In real engines, the first azimuthal mode could appear as a strong contributor in the total acoustic power, as shown by [Livebardon et al. \(2015\)](#). In such a case, the acoustic planar mode representation is not sufficient to describe the pressure field and the full geometry needs to be taken into account. Such an exercise is today quite CPU intensive and although possible, basic fundamental questions seem to be addressed first for a viable exploitation of such a LES.



# Appendices



# Table of Contents

---

<b>A</b>	<b>Characteristic Boundary Conditions</b>	<b>221</b>
A.1	NSCBC general formalism . . . . .	221
A.2	NSCBC extension for forcing waves . . . . .	223
A.2.1	Upstream acoustic forcing methodology . . . . .	224
A.2.2	Downstream acoustic forcing methodology . . . . .	224
A.2.3	Entropy forcing methodology . . . . .	225
<b>B</b>	<b>Spectral and modal decomposition</b>	<b>227</b>
B.1	Spectral decomposition . . . . .	227
B.2	Azimuthal mode decomposition . . . . .	228
B.3	Radial mode decomposition . . . . .	228
<b>C</b>	<b>Numerical dissipation/dispersion of the entropy wave</b>	<b>231</b>
<b>D</b>	<b>Conservation of the entropy wave through a nozzle flow</b>	<b>239</b>

---



## Appendix A

# Characteristic Boundary Conditions

Usually, numerical codes solve equations for conservative or primitive variables inside a numerical grid bounded by boundary conditions. When the equations solved by numerical code are compressible, the propagation of acoustic waves is possible and the code needs to handle these acoustic waves properly. A decomposition from conservative/primitive variables to waves is hence usually done at the boundary conditions to handle properly the acoustics separately from other waves. To do so, the characteristic decomposition is used. Although the characteristic method works for hyperbolic systems (as the Euler equations) as described by [Thompson \(1987\)](#) who developed the Euler Characteristic Boundary Conditions (ECBC), this method can not be directly applied in the Navier-Stokes equations. [Poinsot and Lele \(1992\)](#) extended the ECBC methodology to Navier-Stokes Characteristic Boundary Conditions (NSCBC) adding the contribution of viscous dissipation and thermal diffusion with supplementary relations. [Baum et al. \(1994\)](#); [Moureau et al. \(2005\)](#) then extended the NSCBC formalism to reacting flows while [Yoo and Im \(2007\)](#); [Lodato et al. \(2008\)](#) developed the transverse terms of NSCBC to take into account three dimensional effects that were usually neglected.

### A.1 NSCBC general formalism

The main step of the NSCBC formalism consists in decomposing flow variables into characteristic variables (waves) in the reference frame of the boundary condition. The obtained waves are two acoustic waves ( $\mathcal{L}^1$  and  $\mathcal{L}^2$ ), two vorticity waves ( $\mathcal{L}^3$  and  $\mathcal{L}^4$ ) and one entropy wave ( $\mathcal{L}^5$ ). Some of these waves are ingoing while others are outgoing depending on their nature, flow (whether subsonic or supersonic), and the local position with respect to the computational domain: inlet or outlet. Outgoing waves are waves computed by the numerical code at the end of a time iteration. Ingoing waves are waves that have to be imposed by the NSCBC strategy. For example, [Fig. A.1](#) shows the wave decomposition for a subsonic inflow and outflow. For the inlet, four waves must be imposed ( $\mathcal{L}^1$ ,  $\mathcal{L}^3$ ,  $\mathcal{L}^4$  and  $\mathcal{L}^5$ ) and for the outlet only the ingoing acoustic wave  $\mathcal{L}^2$  needs to be imposed.

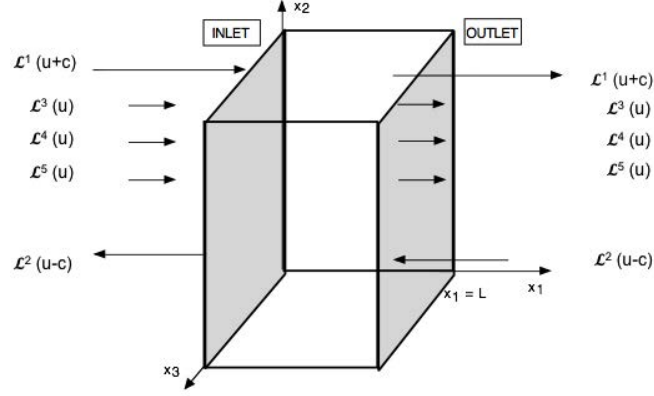


**Figure A.1** NSCBC waves decomposition for a subsonic inflow and outflow.

For a single-species flow (no chemical reaction), the variations of characteristic variables in terms of primitive variables read:

$$\partial \mathcal{L}^1 = \partial u_n + \frac{1}{\rho c} \partial p, \quad (\text{A.1a})$$

$$\partial \mathcal{L}^2 = -\partial u_n + \frac{1}{\rho c} \partial p, \quad (\text{A.1b})$$

$$\partial \mathcal{L}^3 = \partial u_{t_1}, \quad (\text{A.1c})$$

$$\partial \mathcal{L}^4 = \partial u_{t_2}, \quad (\text{A.1d})$$

$$\partial \mathcal{L}^5 = \frac{\rho(\gamma-1)}{2c} (\partial \mathcal{L}^1 + \partial \mathcal{L}^2) - \frac{\rho}{T} \partial T, \quad (\text{A.1e})$$

where subscripts  $n$ ,  $t_1$  and  $t_2$  represent the normal and tangential components attached to the reference frame of the boundary condition and " $\partial$ " indicates a fluctuation between the specified value at the boundary condition (called target value) and the value computed at the end of the iteration (called state value).

Let's take the example of a subsonic inflow where the velocity and the temperature fields are imposed. For a subsonic inflow, four ingoing waves are needed: the upstream acoustic travelling acoustic wave  $\mathcal{L}^1$ , the two vorticity waves  $\mathcal{L}^3$  and  $\mathcal{L}^4$  and the entropy wave  $\mathcal{L}^5$  (cf. [Fig. A.1](#)). Therefore, [Eq. \(A.1\)](#) should be written in terms of the known variables (outgoing acoustic wave  $\mathcal{L}^2$ , velocity field and temperature):

$$\partial \mathcal{L}^1 = 2\partial u_n + \partial \mathcal{L}^2, \quad (\text{A.2a})$$

$$\partial \mathcal{L}^3 = \partial u_{t_1}, \quad (\text{A.2b})$$

$$\partial \mathcal{L}^4 = \partial u_{t_2}, \quad (\text{A.2c})$$

$$\partial \mathcal{L}^5 = \frac{\rho(\gamma-1)}{c} (\partial u_n + \partial \mathcal{L}^2) - \frac{\rho}{T} \partial T. \quad (\text{A.2d})$$

If these conditions are applied directly (in particular Eq. (A.2a)), the boundary condition will act as acoustically fully reflective, which in some cases will end in a physically and/or numerically unstable problem. To introduce an acoustic wave and avoid reflections, the relaxed formulation is used. To do so, the dependence on the outgoing wave  $\mathcal{L}^2$  need to be dropped from incoming waves  $\mathcal{L}^1$  and  $\mathcal{L}^5$  and fluctuations are written as the difference between the "target" and the "state" values.

$$\partial \mathcal{L}^1 = 2K_{u_n} (u_n^t - u_n^s) \Delta t, \quad (\text{A.3a})$$

$$\partial \mathcal{L}^3 = K_{u_{t_1}} (u_{t_1}^t - u_{t_1}^s) \Delta t, \quad (\text{A.3b})$$

$$\partial \mathcal{L}^4 = K_{u_{t_2}} (u_{t_2}^t - u_{t_2}^s) \Delta t, \quad (\text{A.3c})$$

$$\partial \mathcal{L}^5 = \frac{\rho^s (\gamma - 1)}{c^s} [K_{u_n} (u_n^t - u_n^s) \Delta t] - \frac{\rho^s}{T^s} K_T (T^t - T^s) \Delta t, \quad (\text{A.3d})$$

where superscripts  $t$  and  $s$  stand for target and state values respectively,  $K$  is the relaxation coefficient related to the different variables in the reference frame of the boundary condition and  $\Delta t$  is the time step of the iteration. Note that this formulation acts like a spring, where the stiffness of the spring is controlled by the relaxation coefficient  $K$ . The greater the value of  $K$ , the greater the correction of the system (the ingoing wave introduced). Therefore, the value of  $K$  is directly related to the reflection coefficient of the boundary condition (as explained by Selle et al. (2004)).

A subsonic outflow is easier to treat, since the only ingoing wave is the downstream travelling acoustic wave  $\mathcal{L}^2$ . When static pressure is imposed and using the relaxed formulation, the expression for  $\partial \mathcal{L}^2$  reads:

$$\partial \mathcal{L}^2 = \frac{2K_p}{\rho^s c^s} (p^t - p^s) \Delta t. \quad (\text{A.4})$$

This formalism for boundary conditions is used for the inlet and outlet for every numerical simulation computed with AVBP in the present work. For the acoustically and entropy forced simulations, an extension of the above presented NSCBC formalism is needed for the introduction of the disturbances while keeping the same acoustic impedances.

## A.2 NSCBC extension for forcing waves

In the present section a methodology to introduce acoustic and entropy disturbances through the boundary conditions adding a forcing term in the NSCBC formalism is detailed. The forcing signal is a user defined function that depends only on time  $f(t)$ . In the next paragraphs, the extended NSCBC forcing methodology is briefly explained for three cases:

1. Acoustic forcing through a subsonic inlet boundary condition where the velocity and temperature are imposed.

2. Entropy forcing through a subsonic inlet boundary condition where the velocity and temperature are imposed.
3. Acoustic forcing through a subsonic outlet boundary condition where the static pressure is imposed.

### A.2.1 Upstream acoustic forcing methodology

The forcing of an acoustic perturbation through the inlet boundary condition is added to the expression of the acoustic ingoing wave  $\partial\mathcal{L}^1$  (cf. Eq. (A.1a)). The NSCBC formalism was formulated in terms of fluctuations, therefore the forced signal is introduced as a time derivative  $\mathcal{A}\frac{df(t)}{dt}$  source term, where  $\mathcal{A}$  is the amplitude of the forcing and  $f(t)$  the forcing signal. However, the introduction alone of this source term in the expression of  $\partial\mathcal{L}^1$  reacts as a modification of the target value, modifying therefore the value of the ingoing wave and therefore the reflection coefficient of the boundary condition. To avoid this effect, a term is needed to compensate the introduction of the forcing term, in other words the velocity perturbations generated by the introduction of the forced wave written:  $\mathcal{A}K_{u_n}f(t)$ . Following these steps, the set of resulting waves yields (when imposing velocity and temperature):

$$\partial\mathcal{L}^1 = 2K_{u_n} \left( u_n^t - u_n^s \right) \Delta t + \underbrace{2\mathcal{A} \left[ K_{u_n} f(t) + \frac{df(t)}{dt} \right] \Delta t}_{\text{Acoustic forcing contribution}}, \quad (\text{A.5a})$$

$$\partial\mathcal{L}^3 = K_{u_{t_1}} \left( u_{t_1}^t - u_{t_1}^s \right) \Delta t, \quad (\text{A.5b})$$

$$\partial\mathcal{L}^4 = K_{u_{t_2}} \left( u_{t_2}^t - u_{t_2}^s \right) \Delta t, \quad (\text{A.5c})$$

$$\begin{aligned} \partial\mathcal{L}^5 = & \frac{\rho^s(\gamma-1)}{c^s} \left[ K_{u_n} \left( u_n^t - u_n^s \right) \Delta t \right] - \frac{\rho^s}{T^s} K_T \left( T^t - T^s \right) \Delta t - \\ & \underbrace{\mathcal{A} \frac{\rho^s}{T^s} K_T f(t) \Delta t}_{\text{Temperature fluctuation generated by the forced acoustic wave}}, \end{aligned} \quad (\text{A.5d})$$

It should be noticed that the acoustic forced wave generates an entropy wave coming from Eq. (A.1e). If no temperature fluctuation is introduced in  $\partial\mathcal{L}^5$ , extra entropy waves will be generated at the same time, due to the NSCBC conditions trying to fix the temperature to the target value  $T^t$ .

### A.2.2 Downstream acoustic forcing methodology

The forcing of an acoustic perturbation through the outlet boundary condition is added in the expression of the acoustic ingoing wave  $\partial\mathcal{L}^2$  (cf. Eq. (A.1b)). The principle is the same as in the inlet acoustic forcing: two source terms are added, one to introduce the forcing signal and one that compensate (in the present case) the pressure fluctuations generated by the introduction of the forcing. Therefore, the expression of an acoustic



forcing through the outlet boundary condition extended from Eq. (A.4), leads to (when imposing static pressure):

$$\partial \mathcal{L}^2 = \frac{2K_p}{\rho^s c^s} (p^t - p^s) \Delta t + \underbrace{\frac{2\mathcal{A}}{\rho^s c^s} \left[ K_p f(t) + \frac{df(t)}{dt} \right] \Delta t}_{\text{Acoustic forcing contribution}}, \quad (\text{A.6})$$

### A.2.3 Entropy forcing methodology

The forcing of an entropy perturbation through the inlet boundary condition is added in the expression of the entropy ingoing wave  $\partial \mathcal{L}^5$ . The forcing signal is introduced in Eq. (A.3d), resulting in the following set of equations (when imposing velocity and temperature):

$$\partial \mathcal{L}^1 = 2K_{u_n} (u_n^t - u_n^s) \Delta t, \quad (\text{A.7a})$$

$$\partial \mathcal{L}^3 = K_{u_{t_1}} (u_{t_1}^t - u_{t_1}^s) \Delta t, \quad (\text{A.7b})$$

$$\partial \mathcal{L}^4 = K_{u_{t_2}} (u_{t_2}^t - u_{t_2}^s) \Delta t, \quad (\text{A.7c})$$

$$\begin{aligned} \partial \mathcal{L}^5 = & \frac{\rho^s (\gamma - 1)}{c^s} \left[ K_{u_n} (u_n^t - u_n^s) \Delta t \right] - \frac{\rho^s}{T^s} K_T (T^t - T^s) \Delta t - \\ & \underbrace{\mathcal{A} \frac{\rho^s}{T^s} \left[ K_T f(t) + \frac{df(t)}{dt} \right] \Delta t}_{\text{Entropy forcing contribution}}, \end{aligned} \quad (\text{A.7d})$$



## Appendix B

# Spectral and modal decomposition

The spectral decomposition methods are used to separate the contribution of different harmonics from a signal. Once in the spectral space, a modal decomposition can be furthermore done into azimuthal and radial modes. In the case of nozzle flows for example, due to the axi-symmetric nature of the studied flow, it could be interesting to study the radial modes. In the case of the LES simulation, azimuthal modes can be triggered due to the nozzle jet, and an azimuthal decomposition can be helpful to study their importance.

### B.1 Spectral decomposition

In the present study, the harmonics that compose the forcing signal are well known. Hence, the transformation of the temporal forced signal into a Fourier's series can be simply done by a Discrete Fourier Transform (DFT). The DFT consists in decomposing a periodic signal  $S$  containing  $N$  discrete points into a sum of complex numbers through the relation:

$$S_k = \sum_{n=-\infty}^{\infty} s_n \exp(i\omega_n k/N), \quad (\text{B.1})$$

where  $S_k$  is the  $k^{th}$  point of the discrete signal  $S$ ,  $s_n$  is the  $n^{th}$  Fourier's coefficient (corresponding to the  $n^{th}$  harmonic) and  $\omega_n = 2\pi n$  is the angular frequency. The Fourier coefficients  $s_n$  are computed by the following relation:

$$s_n = \frac{1}{N} \sum_{k=0}^{N-1} S_k \exp(-i\omega_n k/N). \quad (\text{B.2})$$

This expression is used in each node of the numerical grid using a total of  $N$  instantaneous solutions. The result is a 3D field of each harmonic composing the forcing signal.

## B.2 Azimuthal mode decomposition

For each harmonic, a decomposition into azimuthal modes can be done. The azimuthal decomposition of a ring of radius  $r$ , discretised by  $N_t$  points from  $-\pi$  to  $\pi$  into the Fourier space can be written:

$$s_{nk}(r, \theta, x) = \sum_{m=-\infty}^{\infty} s_{nm}(r, x) \exp(-im\theta), \quad (\text{B.3})$$

where the azimuthal Fourier coefficients  $s_{nm}$  are given by the relation:

$$s_{nm}(r, x) = \frac{1}{N_t} \sum_{k=1}^{N_t} s_{nk}(r, \theta, x) \exp(im\theta_k). \quad (\text{B.4})$$

It is important to notice that the azimuthal mode of order  $m$  has  $m$  lobes and its angular rotation speed is of  $\omega/m$ .

## B.3 Radial mode decomposition

It is possible to decompose each azimuthal mode into radial modes. Nevertheless, there is no periodicity over the radius and a different formalism for the radial modes decomposition is applied.

The radial mode decomposition for a cylindrical duct of constant section is issued from the wave equation ([Rienstra and Hirschberg 2003](#), Chap. 7 - Duct acoustics):

$$\frac{\partial^2 A}{\partial x^2} + \frac{\partial^2 A}{\partial r^2} + \frac{1}{r} \frac{\partial^2 A}{\partial \theta^2} + \omega^2 A = 0, \quad (\text{B.5})$$

where  $A$  is a wave. Using the method of separation of variables for the wave  $A(r, \theta, x) = A_r(r)A_\theta(\theta)A_x(x)$ , it can be shown that the radial component  $A_r(r)$  satisfies the equation:

$$r^2 \frac{d^2 A_r}{dr^2} + r \frac{dA_r}{dr} + (r^2 k^2 - m^2) A_r = 0, \quad (\text{B.6})$$

where, imposing the boundary condition  $\frac{\partial A}{\partial r}|_{r=R} = 0$  (rigid wall), the proper solutions of [Eq. \(B.6\)](#) are written in the form:

$$E_{m\mu}(r) = \mathcal{A}_{m\mu} J_m(\chi_{m\mu} r), \quad (\text{B.7})$$

with  $J_m$  the ordinary Bessel function (corresponding to the azimuthal order  $m$ ) of the first kind,  $\mu$  the order of the radial mode and  $\mathcal{A}_{m\mu}$  and  $\chi_{m\mu}$  the modal coefficients of the cylindrical duct which are determined using the boundary conditions.

In order to express each azimuthal mode as the sum of radial modes, the proper solutions  $E_{m\mu}(r)$  are normalised such that the norm of the scalar product defined as:

$$\langle f|g\rangle = \int_0^R r f(r)g(r)dr, \quad (\text{B.8})$$

is equal to 1 ( $\langle E_{m\mu}(r)|E_{m\mu}(r)\rangle = 1$ ). In that case, the azimuthal modes yield:

$$A_{nm}(r) = \sum_{\mu=0}^{+\infty} A_{nm\mu} E_{m\mu}(r) = \sum_{\mu=0}^{+\infty} \langle A_{nm}(r)|E_{m\mu}(r)\rangle E_{m\mu}(r). \quad (\text{B.9})$$



## Appendix C

# Numerical dissipation/dispersion of the entropy wave

Before introducing any perturbation in the numerical simulation, it is important to choose a numerical scheme capable of transporting without dissipation and dispersion the different disturbances. AVBP classical numerical schemes are: LW, TTGC and TTG4A. In the work of [Lamarque \(2007\)](#), the numerical dissipation and dispersion properties of AVBP numerical schemes were studied. The dissipation of the numerical scheme is given by the amplification coefficient of the scheme  $|G|$  and corresponds to an error on the amplitude of the convected waves. [Figures C.1a](#) and [C.2a](#) show the dissipation introduced by the different numerical schemes for CFL=0.1 and CFL=0.7 ( $\Delta$  being the characteristic length of a mesh element) respectively. TTGC scheme shows performances close to a compact numerical scheme of 6th order, being the best AVBP scheme to convect disturbances without dissipation. Dispersion of the scheme is a phase error that changes according to the wavelength. Indeed, the oscillations are transported with a wrong velocity. The study of the dispersion of a scheme is done analysing the phase velocity and the real part of the modified wave number ( $\mathcal{K}_R^*$ ). [Figures C.1b](#) and [C.2b](#) show the real part of the modified dimensionless wave number ( $\mathcal{K}_R^*\Delta$ ) compared with the dimensionless wave number for different values of CFL (0.1 and 0.7). A value of  $\mathcal{K}_R^* > \mathcal{K}$  indicates that the scheme has a phase in advance, whereas  $\mathcal{K}_R^* < \mathcal{K}$  indicates a phase in retard. LW and TTG4A schemes dissipate more than TTGC. However, LW and TTG4A schemes disperses less, in particular when the CFL number increases.

For a given CFL, the number of points per wavelength needed to avoid dispersion is considered to be the maximum value of  $\mathcal{K}\Delta$  allowing to have less then 5% of error in the phase velocity. This number of points per wavelength can be computed from [Figs. C.1b](#) and [C.2b](#). [Table C.1](#) summarizes the maximum wave numbers and wavelengths to obtain less than 5% of error in the phase velocity. The best result is obtained for TTGC scheme with 5.37 points per wavelength. It remains to know the minimum wavelength to be resolved in the numerical simulations to construct a numerical mesh that respect at least 6 points per wavelength. Knowing that 250 Hz is the highest computed frequency and

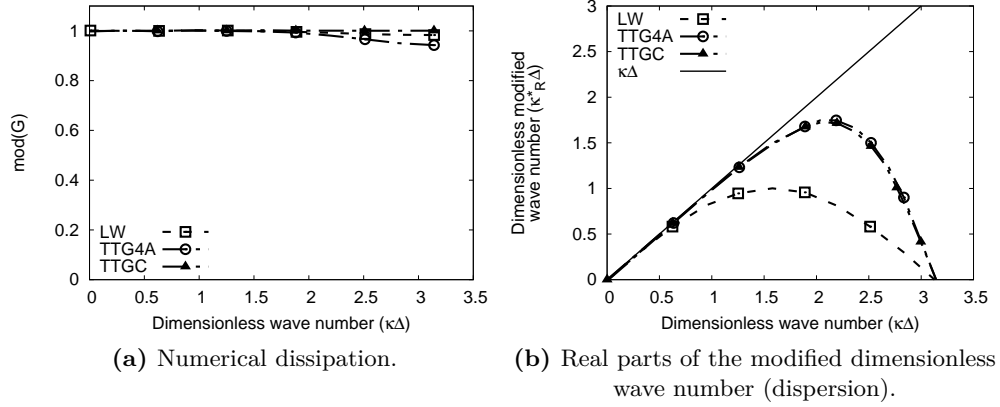


**Figure C.1** Numerical dissipation and dispersion introduced by the different numerical schemes of AVBP computed with a CFL=0.1.

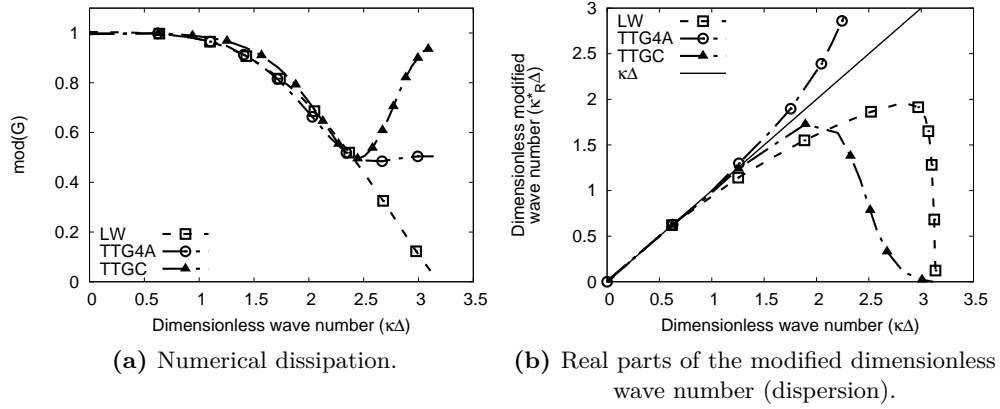


**Figure C.2** Numerical dissipation and dispersion introduced by the different numerical schemes of AVBP computed with a CFL=0.7.

the convection velocity of the different transported waves, the different wavelengths can be computed:  $\lambda_\sigma = \frac{|u|}{250}$ ,  $\lambda_{A+} = \frac{|u+c|}{250}$  and  $\lambda_{A-} = \frac{|u-c|}{250}$ . Using the isentropic relations, an estimation of the bulk quantities inside the nozzle (velocity and sound velocity) can be obtained. Figure C.3 shows the evolution of the different wavelengths along the axial coordinate. The wavelength is proportional to the wave convection velocity, therefore, it is the entropy wave which determines the smallest wavelength and the limiting factor of the characteristic element size of the mesh. According to the bulk quantities computed using the isentropic relations, the convection velocity of the entropy wave reaches its minimum in the upstream and downstream ducts of the EWG. The wavelengths inside each duct are of about 45 and 25 mm respectively, and according to Tab. C.1, the characteristic length of the mesh elements inside the upstream and downstream ducts



should be of about 8 and 5 mm respectively.

Scheme	CFL = 0.7	
	$k\Delta$	$\lambda$
LW	0.46	$13.66\Delta$
TTG4A	1.099	$5.72\Delta$
TTGC	1.17	$5.37\Delta$

**Table C.1** Wave numbers and wavelengths to obtain less than 5% error in the phase velocity.

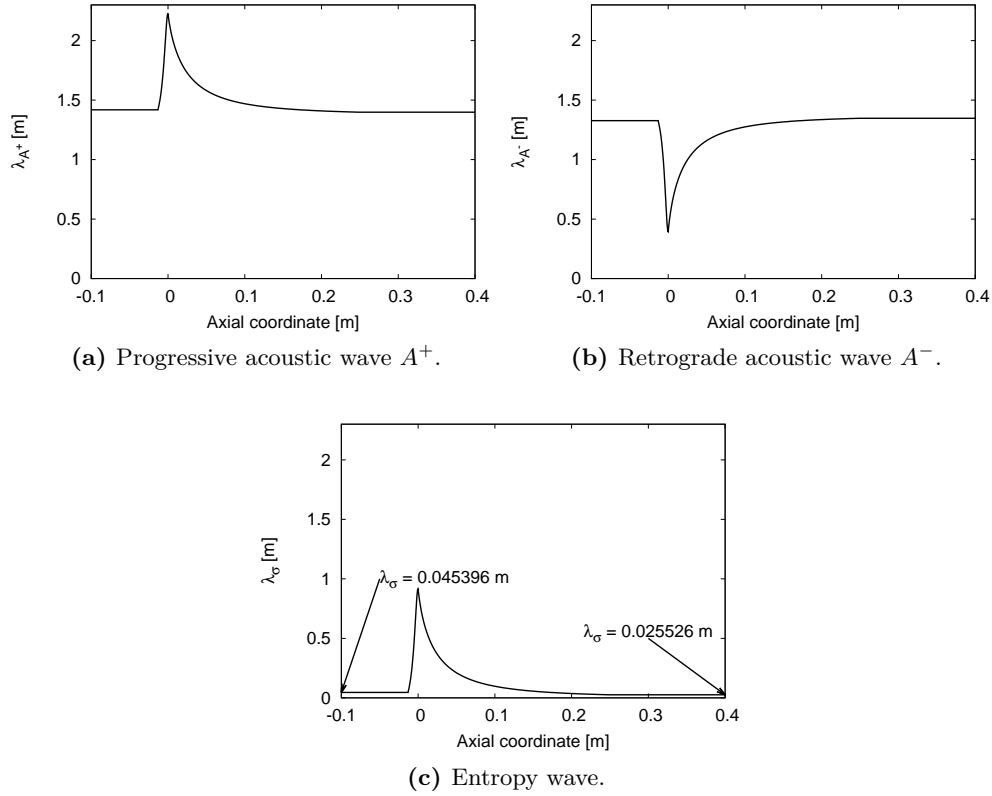


**Figure C.3** Wavelengths of the disturbances at 250 Hz along the EWG numerical domain.

It has been shown that the characteristic element length of the mesh for the study of the acoustic transfer functions of the nozzle depends on the smallest entropy wavelength convected, which corresponds to the highest frequency studied. Therefore, a series of test cases to evaluate the capability of the numerical scheme to properly convect entropy waves without dissipation and dispersion along the domain are carried out. The test cases consist in the introduction of an entropy perturbation of 15 K of amplitude (5%

of the mean temperature of the flow at the inlet) in a cylindrical straight duct of 15 mm of radius (inlet duct of the EWG) and 0.5 m of length (total length of the domain considered for this study). The fluid is considered to be inviscid (Euler equations are solved) and the walls of this cylindrical duct are considered to be adiabatic slip walls (only the velocity normal to the wall is zero). The test cases are:

1. Convection of a sinusoidal entropy plane wave of 250 Hz of frequency by a flat velocity profile.
2. Convection of a sinusoidal entropy plane wave of 250 Hz of frequency by a non-flat velocity profile imposed at the boundary condition.
3. Convection of an entropy impulsion by a non-flat velocity profile imposed at the inlet boundary condition.

The first test case evaluates the capability of the numerical scheme to properly convect the entropy wave without dissipation and dispersion produced by the numerical scheme. The second test case assesses the distortion of the entropy plane wave by a non-homogeneous mean flow. Finally, the third test case evaluates the conservation of an entropy perturbation. Second and third test cases should demonstrate that the entropy wave is not dissipated but only redistributed in space by the non-homogeneous flow (conclusion of the of work [Morgans et al. 2013](#) in the framework of a fully developed turbulent channel flow).

The numerical scheme chosen is TTGC, two meshes are constructed with only tetrahedral elements: M1 with characteristic element length 3.75 mm (12 points per wavelength) and M2 with characteristic element length of 2.2 mm (20 points per wavelength). [Figure C.4](#) shows the fluctuations of the temperature along the central line of the cylindrical domain ( $R=0$ ) for the first test case (flat velocity profile imposed at the inlet), where  $smu_2$  and  $smu_4$  are coefficients that control the  $2^{nd}$  and  $4^{th}$  dissipation operators for artificial viscosity. In the cases where no artificial viscosity is added, the convection of the entropy wave produces artificial noise that exceeds the amplitude of the introduced wave (15 K). Adding more points convects the temperature wave generating much less artificial noise. Note that for both meshes, if no artificial viscosity is present the simulation crashes. Artificial viscosity is needed to stabilize the computations, however artificial viscosity consequently dissipates the entropy wave. Therefore, the artificial viscosity introduced needs to have the smallest possible value. After multiple computations, this value seems to be  $smu_2 = 0$  and  $smu_4 = 0.007$ , which allows convecting the wave properly. In the case of the coarser mesh M1, 63% of the introduced amplitude fluctuation reaches the outlet of the duct, whereas in M2 90% of the initial amplitude reaches the outlet of the duct.

In the second test case, only M2 is used. The velocity profile imposed at the inlet boundary condition obeys the law:

$$u_x(r) = A + B \cos(2\pi Cr),$$

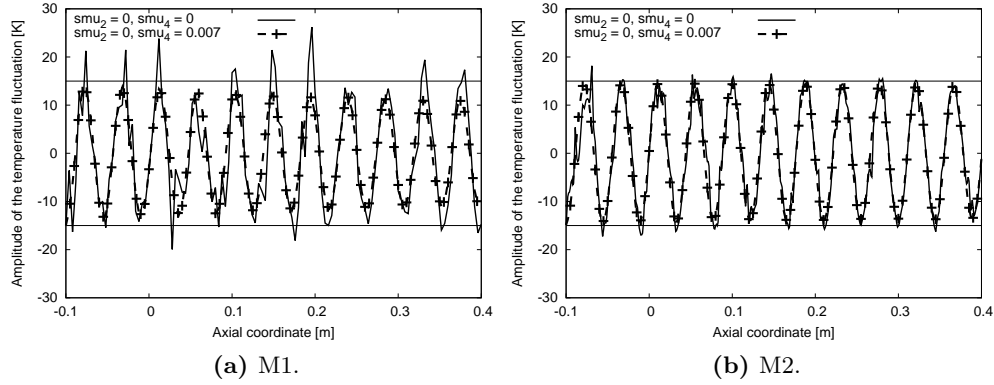


**Figure C.4** Temperature fluctuations extracted at the central line ( $R=0$ ) of the cylindrical duct domain with and without artificial viscosity.

where  $A = 11.95$ ,  $B = 2.5$ , and  $C = \frac{200\pi}{3}$  are coefficients chosen to conserve the mass flow rate imposed in the isentropic baseline flow computed in §5.1, and provide an axial velocity fluctuation of about 5 m/s between the wall and the centreline. In Fig. C.5, the velocity profile is plotted against the radius at three different positions of the duct: the inlet, the middle and the outlet of the duct. Ideally, in the simulation of a straight cylindrical duct with constant section following only the Euler equations, the radial velocity profile should remain the same through the duct. In the present simulation, even though the artificial viscosity added in the simulation is fixed to the smallest possible value, it has an effect on the velocity profiles, smoothing them (the velocity profile loses 10% of its maximal value). In Fig. C.6, the evolution of the real part of the entropy wave is showed. The plane entropy wave is first distorted by the velocity profile and then it is highly attenuated. This attenuation has been studied by different authors: Sattelmayer (2003) and Leyko et al. (2013) introduced a dissipation function of the entropy wave in the framework of a cylindrical duct flow and turbine rows respectively. Morgans et al. (2013) and Giusti et al. (2016) carried out DNS and LES studies respectively of a fully-developed turbulent flow in which an entropy wave was convected. It has been found that for small values of the Helmholtz number, the decay on the entropy wave magnitude is mostly due to shear dispersion arising from the non-uniform mean velocity profile. For larger values of the Helmholtz number, turbulent mixing and diffusion become more important. In the case of the present simulation, the effects of turbulence are not present, therefore the attenuation is solely due to the non-homogeneities in the velocity profile. Perturbations in the middle of the duct move faster compared to the perturbations close to the walls. The hot and cold spots collide with each other losing the planar form imposed at the inlet boundary. This also generates gradients in the radial direction, leading to radial diffusion that further contributes to the mixing between hot and cold spots. These effects are expected to increase with the residence time and with the decrease of the entropy wavelength. A smaller wavelength of the entropy perturbation leads to higher gradients making the diffusion process faster. To

illustrate the attenuation of the entropy wave, different attenuation models describing the ratio of the entropy wave along the stream-wise coordinate  $\sigma(x)$  to the entropy wave introduced at the boundary condition  $\sigma_0$  are compared in Fig. C.7. The results are showed against the Helmholtz number  $St = x \frac{f}{u_b}$ . The formulations of the different models are:

$$\left. \frac{\sigma(x)}{\sigma_0} \right|_{Sattelmayer} = \exp(-i\omega\tau) \frac{\sin(-i\omega K\tau)}{\omega K\tau}, \quad (\text{C.1a})$$

$$\left. \frac{\sigma(x)}{\sigma_0} \right|_{Leyko} = \frac{1}{R^2} \int_0^R r \exp(-i\omega t_d(r)) dr, \quad (\text{C.1b})$$

$$\left. \frac{\sigma(x)}{\sigma_0} \right|_{Morgans} = \exp\left(-\frac{\omega^2}{4\pi A_{IR}^2}\right) \exp(-i\omega\tau), \quad (\text{C.1c})$$

$$\left. \frac{\sigma(x)}{\sigma_0} \right|_{Giusti} = \frac{2}{R^2 u_b} \int_0^R r u_x(r) \exp\left(-i\omega \frac{x}{u_x(r)}\right) dr, \quad (\text{C.1d})$$

where  $\tau = \frac{x}{u_b}$  is the characteristic convection time of the entropy wave,  $K$  is a constant measuring the dispersion rate of the entropy wave,  $t_d$  is a function measuring the time lapse of a particle over a streamline to go from the inlet to  $x$ , and  $A_{IR}$  is a model parameter found from a Gaussian model of the amplitude of the impulse response (e.g. obtained from the probability density function of the residence time of the entropy wave) that depends on the axial position and the bulk velocity. Giusti et al. (2016) introduced a constant  $A'$  to replace  $A_{IR}$  that depends only on the shape of the mean velocity profile, where  $A' = \frac{x A_{IR}}{\sqrt{\pi} u_b}$ . It is worth noting that all the models, except the one proposed by Leyko et al. are only valid for a constant duct section. The most representative of the physical phenomena are the ones proposed by Leyko et al. and Giusti et al., where no constant needs to be fitted and correspond to the direct resolution of the entropy conservation equation. Besides, they are the ones that reproduce better the numerical results in terms of shape and amplitude.

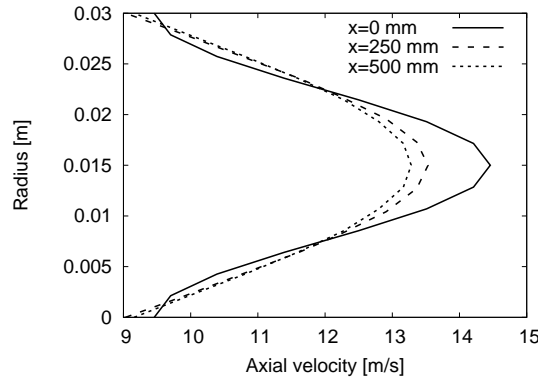


**Figure C.5** Axial velocity profiles along the axial coordinate of the cylindrical test case with a velocity profile.

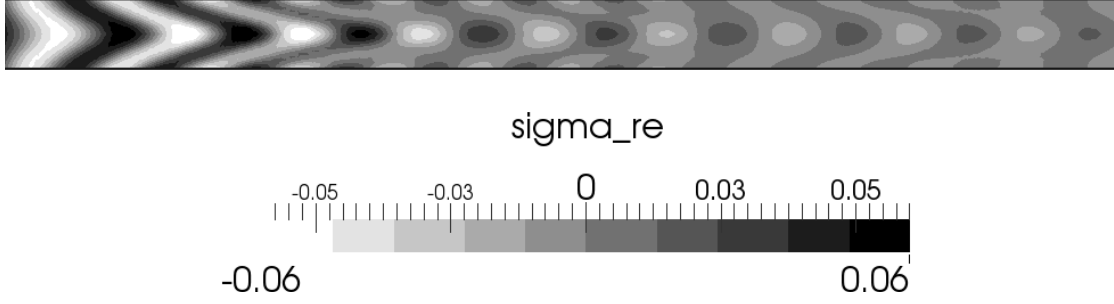
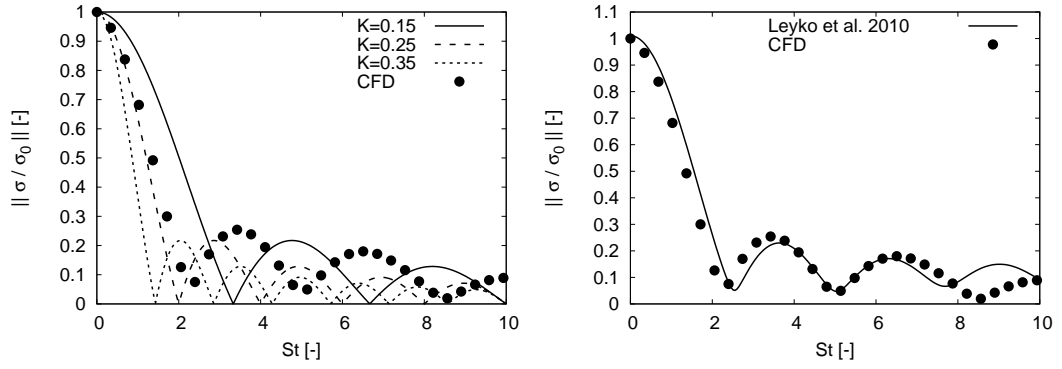
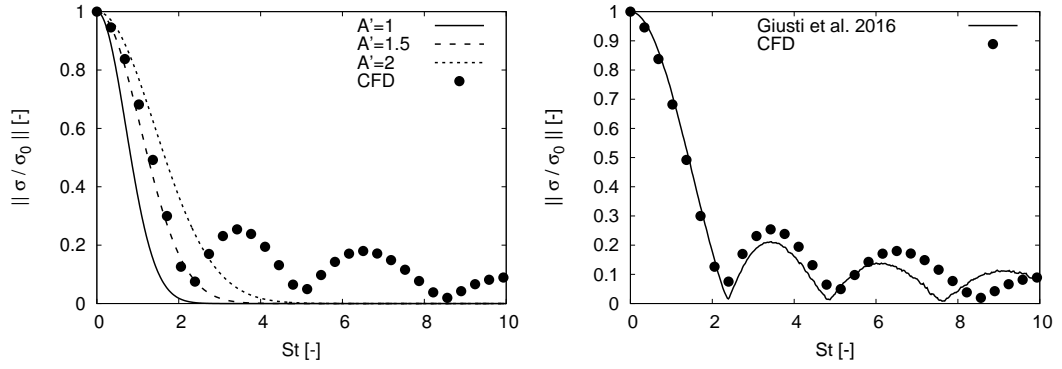


**Figure C.6** Real part of the entropy wave of the cylindrical test case with a velocity profile.

Finally, in third test case, only M2 and the same velocity profile used for the second test case are used. An impulsion of 15 K of amplitude corresponding to a half period of a sinusoidal wave of 250 Hz is introduced through the inlet boundary condition ( $f(t) = 15 \sin(2\pi 250t)$  for  $t \in \left[\frac{1}{2(250)}; \frac{1}{250}\right]$ ). The temporal evolution of the averaged value of  $T'/\bar{T}$  over the cylindrical duct cross-section along time for different axial positions is shown in [Fig. C.8a](#). The relative entropy integral of each axial position to the inlet are plotted in [Fig. C.8b](#). The entropy amplitude of the impulse is attenuated as it is convected along the duct, but its integral remains constant, which demonstrate that the entropy wave is not dissipated but only redistributed in space (in agreement with [Morgans et al. 2013](#)).

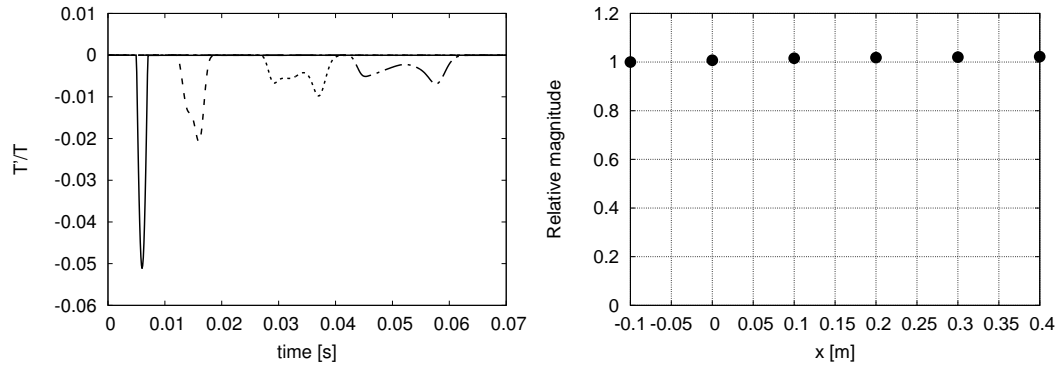


(a) Attenuation function of Sattelmayer (2003). (b) Attenuation function of Leyko et al. (2010).



(c) Attenuation function of Morgans et al. (2013) (d) Attenuation function of Giusti et al. (2016).

**Figure C.7** Attenuation functions of the entropy wave based on the mean flow compared with the entropy attenuation extracted from the numerical simulation.



(a) Variation of  $T'/\bar{T}$  at different axial positions against the time. (b) Relative magnitude of the temperature fluctuation as it advects in the cylindrical duct.

**Figure C.8** Convection of an entropy impulsion along a straight cylindrical duct by a non-homogeneous flow.

## Appendix D

# Conservation of the entropy wave through a nozzle flow

In this section the dissipation of an entropy pulse through the EWG nozzle configuration is studied following the methodology already proposed by [Morgans et al. \(2013\)](#). An entropy pulse is introduced into the domain through the inlet boundary condition and is convected by the flow. This study is realised for two cases: using the Euler and the NS set of equations to model the flow. The corresponding converged mean flows used to convect the entropy pulse are the ones described in §5.3.2 (for the Euler simulation) and §5.1 on M2 (for the NS simulation). The entropy pulse corresponds to half a period of a sinusoidal temperature wave of 15 K amplitude ( $f(t) = 15 \sin(2\pi 250t)$  for  $t \in [\frac{1}{2(250)}; \frac{1}{250}]$ ) introduced as a plane wave through the inlet boundary condition. [Figure D.1](#) shows the convected entropy pulse at different instants, where the upper half of each sub-figure represents the Euler numerical simulation and the lower part the NS numerical simulation. From the firsts instants after the introduction of the entropy pulse, the entropy front is distorted from its planar shape in the NS simulation, while it remains planar in the Euler simulation. Indeed, the velocity profile developed in NS simulation induces this deformation, where the velocity is zero at the walls and reaches its maximal value at the centreline of the duct. After traversing the nozzle, the amplitude of the entropy pulse in the NS simulation is more attenuated than in the Euler simulation. This is due to strong 3D effects present in the NS simulation like the turbulent mixing that induces the mixing of the spot. Finally, when the entropy fluctuation is convected through the downstream duct, the Euler slug is found to be strongly attenuated, while this attenuation seems to have less importance in the NS simulation.

To estimate the dissipation of the entropy pulse, the temperature fluctuations mass-weighted cross-section average trace at different axial positions of the domain is extracted and shown in [Fig. D.2](#). The key positions are: 1. the inlet of the domain, 2. the inlet of the nozzle, 3. the outlet of the nozzle and 4. the outlet of the domain. Clearly, the entropy fluctuation is strongly attenuated in both simulations (as already highlighted

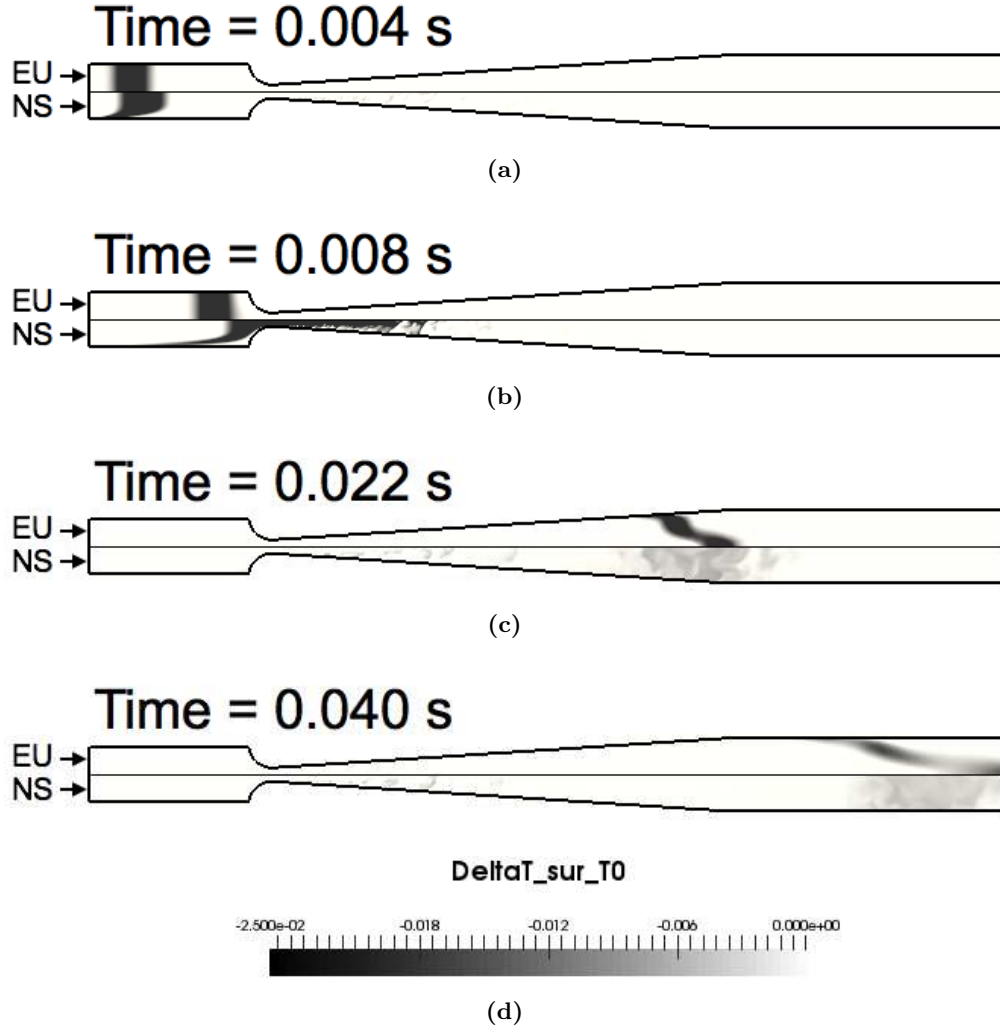


**Figure D.1** Progression of the entropy pulse through a nozzle viscous and inviscid flow.

in Fig. D.1). However, the attenuation followed in both simulations is not the same. According to Morgans et al. (2013) and Giusti et al. (2016) dispersion generated by the non-homogeneous velocity profile is the responsible for this attenuation. To illustrate this, the absolute value of the radial gradient of the axial velocity ( $||\partial U_x / \partial R||$ ) is shown in Fig. D.3. This field is representative of the radial deformation of the velocity profile, where clearer zones represent a flat velocity profile, while darker zones are representative of strong velocity gradients. As already illustrated by Figs. D.1 and D.2, the entropy gust is almost convected without attenuation in the upstream duct in the Euler simulation, where the entropy fluctuation keeps its planar shape, the attenuation in this duct is caused by the curvature of the streamlines near the convergent. In the NS simulation, the attenuation in the upstream duct is due to the non-homogeneous mean profile caused by



the wall boundary layers. The presence of the nozzle generates strong velocity gradients, where also the entropy spot is strongly attenuated in both simulations. Finally, in the downstream duct strong gradients of velocity are present in the Euler simulation, where the entropy wave is also strongly attenuated, while almost no gradients are shown in the NS simulation and the attenuation is found to be negligible in the downstream duct. Therefore, in agreement with [Morgans et al. \(2013\)](#) and [Giusti et al. \(2016\)](#), inhomogeneities in the velocity profile are responsible of attenuation by shear dispersion of the entropy wave.

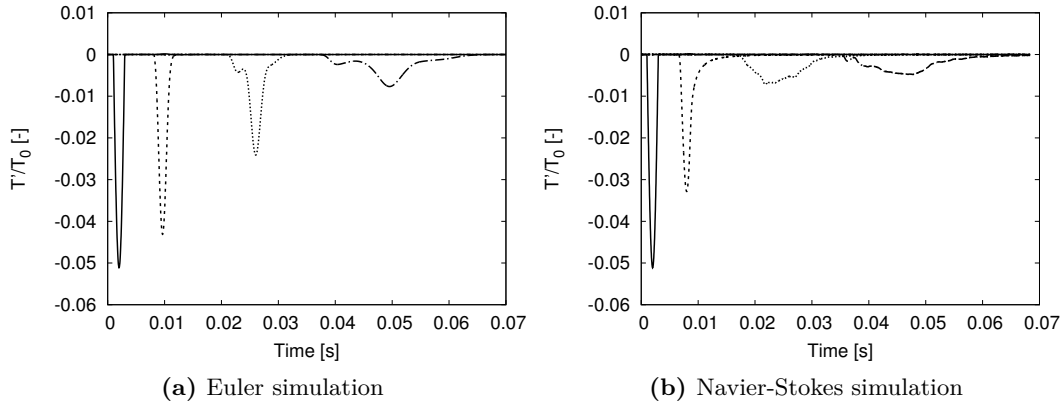


**Figure D.2** Variation of  $T'/T_0$  along the EWG configuration against time.

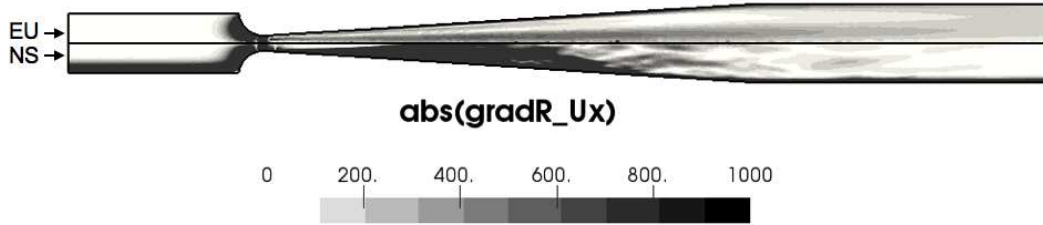


**Figure D.3** Absolute value axial velocity radial gradient ( $||\partial U_x / \partial R||$ ) computed from the baseline flow of the numerical simulations.

[Figs. D.1–D.3](#) have highlighted the attenuation of the entropy wave. However, to verify if the entropy wave is dissipated or only redistributed in space, the relative integral (to the inlet of the configuration) of the temperature fluctuations registered at different sections in [Fig. D.2](#) is computed and shown in [Fig. D.4](#). This results reveals that even through a nozzle, where strong 3D effects are taken into account by the numerical simulation, the dissipation of the entropy wave is negligible during its advection (in agreement with the turbulent channel flow study of [Morgans et al. 2013](#)).

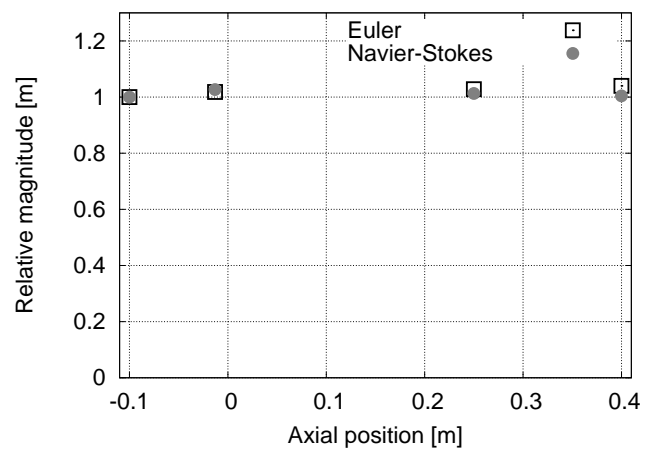


**Figure D.4** Relative magnitude of the temperature fluctuation as it is advected through the EWG configuration.

# Bibliography

- A380, 2017. URL <http://www.airbus.com/aircraftfamilies/passengeraircraft/a380family/innovation/>. 2
- ACARE, 2016. URL <http://www.acare4europe.com/>. 2
- Bailly, C., Bogey, C., and Candel, S. Modelling of sound generation by turbulent reacting flows. *International Journal of Aeroacoustics*, 9(4):461–490, 2010. 7, 15
- Bake, F., Richter, C., Muhlbauer, B., Kings, N., Rohle, I., Thiele, F., and Noll, B. The entropy wave generator (ewg): a reference case on entropy noise. *J. Sound Vib.*, pages 574–598, 2009. xxi, 7, 37, 38, 41, 43, 44, 55, 65, 82, 91, 101, 160
- Bauerheim, M., Duran, I., Livebardon, T., Wang, G., Moreau, S., and Poinso, T. Transmission and reflection of acoustic and entropy waves through a stator–rotor stage. *Journal of Sound and Vibration*, 374:260–278, 2016. 96, 98, 109, 186, 202
- Baum, M., Poinso, T., and Thévenin, D. Accurate boundary conditions for multicomponent reactive flows. *J. Comput. Phys.*, 116:247–261, 1994. 221
- Beard, P. F., Povey, T., and Chana, K. S. Turbine efficiency measurement system for the qinetiq turbine test facility. *Journal of Turbomachinery*, 132(1):011002–011002–13, 09 2009. URL <http://dx.doi.org/10.1115/1.3066271>. 170
- Beard, P. F., Smith, A. D., and Povey, T. Experimental and computational fluid dynamics investigation of the efficiency of an unshrouded transonic high pressure turbine. *Proceedings of the Institution of Mechanical Engineers, Part A: Journal of Power and Energy*, 225(8):1166–1179, 2017/04/24 2011. doi: 10.1177/0957650911407979. URL <http://journals.sagepub.com/doi/abs/10.1177/0957650911407979>. 170, 171
- Becerril, C., Moreau, S., Bauerheim, M., Gicquel, L.Y.M., and Poinso, T. Numerical investigation of combustion noise: The entropy wave generator. In *22nd AIAA/CEAS Aeroacoustics Conference*, Lyon, France, 30 May - 1 June 2016. doi: 10.2514/6.2016-2830. URL <http://dx.doi.org/10.2514/6.2016-2830>. 9, 44
- Blanes, S., Casas, F., Otero, J. A., and Ros, J. The magnus expansion and some of its applications. *Physics Reports*, 470(5-6):151–238, January 2009. 31

- Bohn, M. S. *Noise produced by the interaction of acoustic waves and entropy waves with high-speed nozzle flows*. PhD thesis, 1976. 7, 37
- Bohn, M.S. Response of a subsonic nozzle to acoustic and entropy disturbances. *J. Sound Vib.* , 52(2):283 – 297, 1977. ISSN 0022-460X. doi: 10.1016/0022-460X(77)90647-2. URL <http://www.sciencedirect.com/science/article/pii/0022460X77906472>. 7
- Bonhomme, A., Duchaine, F., Wang, G., Selle, L., and Poinso, T. A parallel multidomain strategy to compute turbulent flows in fan-stirred closed vessels. *Computers & Fluids*, 101:183–193, 2014. 172, 173
- Bonneau, V., Polacsek, C., Barrier, R., and Lévy, S. Prediction of harmonic sound power generated by a modern turbofan with heterogeneous ogv and internal bifurcations. In *20th AIAA/CEAS Aeroacoustics Conference*, Atlanta, GA, 16-20 June 2014. doi: 10.2514/6.2014-3054. URL <http://dx.doi.org/10.2514/6.2014-3054>. 137, 138
- Brès, G., Nichols, J., Lele, S. K., Ham, F., Schlinker, R., Reba, R., and Simonich, J. Unstructured large eddy simulation of a hot supersonic over-expanded jet with chevrons. In *18th AIAA/CEAS Aeroacoustics Conference (33rd AIAA Aeroacoustics Conference)*, Colorado Springs, CO, 4-6 June 2012. doi: 10.2514/6.2012-2213. URL <http://dx.doi.org/10.2514/6.2012-2213>. 63
- Bretherton, F. P. and Garrett, C. J. R. Wavetrains in inhomogeneous moving media. *Proceedings of the Royal Society of London*, 302(1471):529–554, 1968. 205
- Chang, C. T., Lee, C.-M., Herbon, J. T., and Kramer, S. K. Nasa environmentally responsible aviation project develops next-generation low-emissions combustor technologies (phase i). *Journal of Aeronautics & Aerospace Engineering*, 2013, 2013. 5
- Chiu, H. H. and Summerfield, M. Theory of combustion noise. *Acta Astronautica* , 1: 967–984, 1974. 4, 6
- Colin, O. and Rudgyard, M. Development of high-order taylor-galerkin schemes for unsteady calculations. *J. Comput. Phys.* , 162(2):338–371, 2000. 66
- Cumpsty, N. A. and Marble, F. E. The interaction of entropy fluctuations with turbine blade rows; a mechanism of turbojet engine noise. *Proc. R. Soc. Lond. A* , 357: 323–344, 1977a. 4, 5, 131, 134, 139, 141, 152, 162, 163, 198, 200, 201, 210, 215
- Cumpsty, N. A. and Marble, F. E. Core noise from gas turbine exhausts. *J. Sound Vib.* , 54(2):297–309, 1977b. 5, 170
- de Laborderie, J., Duchaine, F., Vermorel, O., Gicquel, L., and Moreau, S. Application of an overset grid method to the large eddy simulation of a high-speed multistage axial compressor. Number 49712, pages V02CT39A015–, Seoul, South Korea, 13–17 June 2016. URL <http://dx.doi.org/10.1115/GT2016-56344>. 172, 173

- Dowling, A. P. and Mahmoudi, Y. Combustion noise. *Proceedings of the Combustion Institute*, 35(1):65–100, 2015. [8](#)
- Duchaine, F., Jaure, S., Poitou, D., Quemerais, E., Staffelbach, G., Morel, T., and Gicquel, L. Y. M. High performance conjugate heat transfer with the openpalm coupler. In *V International Conference on Coupled Problems in Science and Engineering*, Ibiza, Spain, 17-19 June 2013. [172](#)
- Ducros, F., Nicoud, F., and Poinso, T. Wall-adapating local eddy-viscosity models for simulations in complex geometries. In *ICFD*, pages 293–300. Baines M. J., 1998. [67](#)
- Duran, I. *Prediction of combustion noise in modern aero-engines combining large eddy simulations and analytical methods - th/cfd/13/83*. PhD thesis, Université de Toulouse - Institut National Polytechnique de Toulouse, MEGeP, 2013. [10](#), [105](#), [170](#), [198](#)
- Duran, I. and Moreau, S. Analytical and numerical study of the entropy wave generator experiment on indirect combustion noise. In *17th AIAA/CEAS Aeroacoustics Conference - AIAA-2011-2829*, Portland, Oregon, 2011. [26](#), [39](#), [40](#)
- Duran, I. and Moreau, S. Study of the attenuation of waves propagating through fixed and rotating turbine blades. In *18th AIAA/CEAS Aeroacoustics Conference (33rd AIAA Aeroacoustics Conference)*, number AIAA2012-2133 paper, Colorado Springs, USA, June 4-6 2012. [96](#), [98](#), [109](#)
- Duran, I. and Moreau, S. Solution of the quasi-one-dimensional linearized euler equations using flow invariants and the magnus expansion. *J. Fluid Mech.*, 723:190–231, 4 2013a. ISSN 1469-7645. doi: 10.1017/jfm.2013.118. [20](#), [23](#), [28](#), [29](#), [31](#), [32](#), [35](#), [41](#), [43](#), [97](#), [102](#), [104](#), [107](#), [113](#), [128](#), [133](#), [134](#), [135](#), [149](#), [151](#), [160](#), [161](#), [163](#), [214](#), [215](#)
- Duran, I. and Moreau, S. Numerical simulation of acoustic and entropy waves propagating through turbine blades. In *19th AIAA/CEAS Aeroacoustics Conference*, pages AIAA 2013–2102, Berlin, Germany, May 27-29 2013b. [186](#), [205](#)
- Duran, I. and Morgans, A. On the reflection and transmission of circumferential waves through nozzles. *Journal of Fluid Mechanics*, 773:137–153, 2015. [35](#), [115](#), [130](#), [131](#), [134](#), [152](#), [155](#), [163](#), [208](#)
- Duran, I., Leyko, M., Moreau, S., Nicoud, F., and Poinso, T. Computing combustion noise by combining Large Eddy Simulations with analytical models for the propagation of waves through turbine blades. In *3rd Colloquium INCA*, Toulouse (France), November 17-18 2011. [186](#)
- Duran, I., Leyko, M., Moreau, S., Nicoud, F., and Poinso, T. Computing combustion noise by combining Large Eddy Simulations with analytical models for the propagation of waves through turbine blades. *C. R. Acad. Sci. - Mécanique*, 341(1-2):131–140, January 2013a. [186](#)

- Duran, I., Moreau, S., and Poinso, T. Analytical and numerical study of combustion noise through a subsonic nozzle. *AIAA Journal*, 51(1):42–52, 2013b. 8, 28, 31, 37, 39, 40, 41, 43, 44, 47, 48, 49, 56, 57, 59, 61, 63, 64, 83, 154, 156, 160, 213
- Eckstein, J., Freitag, E., Hirsch, C., and Sattelmayer, T. Experimental study on the role of entropy waves in low-frequency oscillations for a diffusion burner. In Paper, ASME, editor, *ASME Turbo Expo*, Vienna, Austria, 2004. 37
- EIA, 2016. URL <http://www.eia.gov/totalenergy/data/monthly>. 1
- Emmanuelli, A., Huet, M., Le Garrec, T., and Ducruix, S. Caa study of entropy noise in nozzle flow for the validation of a 2d semi-analytical model. In *ASME Turbo Expo 2017: Turbomachinery Technical Conference and Exposition*, pages V02CT43A006–V02CT43A006, North Carolina, USA, 26-30 June 2017. American Society of Mechanical Engineers. 115
- Férand, M., Livebardon, T., Moreau, S., Sensiau, C., Bouty, E., Sanjose, M., and Poinso, T. Numerical investigation of far-field combustion noise from aeronautical combustors. 2016. 8
- Gaetani, P. and Persico, G. Hot streak evolution in an axial hp turbine stage. *International Journal of Turbomachinery, Propulsion and Power*, 2(2):6, 2017. 170, 187, 188, 193, 210
- Gaetani, P., Persico, G., Spinelli, A., Sandu, C., and Niculescu, F. Entropy wave generator for indirect combustion noise experiments in a high-pressure turbine. In *Proceedings of the ETC*, Madrid, Spain, 23-27 March 2015. 7, 170
- Giauque, Alexis, Huet, Maxime, and Clero, Franck. Analytical analysis of indirect combustion noise in subcritical nozzles. In *Proceedings of ASME TURBO EXPO*, number x, pages 1–16, 2012. 28
- Giret, J.C., Sengissen, A., Moreau, S., Sanjosé, M., and Jouhaud, J.C. Prediction of the sound generated by a rod-airfoil configuration using a compressible unstructured les solver and a fw-h analogy. In *18th AIAA/CEAS Aeroacoustics Conference (33rd AIAA Aeroacoustics Conference)*, Colorado Springs, CO, 4-6 June 2012. doi: 10.2514/6.2012-2058. URL <http://dx.doi.org/10.2514/6.2012-2058>. 63, 64
- Giret, J.C., Sengissen, A., Moreau, S., and Jouhaud, J.C. Prediction of lagoon landing-gear noise using an unstructured les solver. In *19th AIAA/CEAS Aeroacoustics Conference*, Berlin, Germany, 27-29 May 2013. doi: 10.2514/6.2013-2113. URL <http://dx.doi.org/10.2514/6.2013-2113>. 63, 64
- Giusti, A., Worth, N. A., Mastorakos, E., and Dowling, A. P. Experimental and numerical investigation into the propagation of entropy waves. *AIAA Journal*, pages 1–13, 2016. 63, 95, 96, 98, 101, 110, 112, 113, 134, 145, 149, 161, 193, 196, 211, 214, 235, 236, 238, 240, 241

- Goh, C. S. and Morgans, A. S. Phase prediction of the response of choked nozzles to entropy and acoustic disturbances. *Journal of Sound and Vibration*, pages 1–15, June 2011a. ISSN 0022460X. doi: 10.1016/j.jsv.2011.05.016. URL <http://linkinghub.elsevier.com/retrieve/pii/S0022460X11004019>. 34
- Goh, Chee Su and Morgans, Aimee S. The effect of entropy wave dissipation and dispersion on thermoacoustic instability in a model combustor. In *17th AIAA/CEAS Aeroacoustics Conference - AIAA-2011-2914*, Portland, 2011b. 23, 27, 28
- Griffiths, J. W. R. The spectrum of compressor noise of a jet engine. *J. Sound Vib.* , 1 (2):127–140, 1964. 4
- Harper-Bourne, M., Moore, A., and Siller, H. A study of large aero-engine combustor noise. *AIAA Paper* , 2942, 2008. 5, 37
- Hassan, H. Scaling of combustion generated noise. *J. Fluid Mech.* , 49:445–453, 1974. 4, 5
- Hosseinalipour, S. M., Fattahi, A., Afshari, H., and Karimi, N. On the effects of convecting entropy waves on the combustor hydrodynamics. *Applied Thermal Engineering*, 110:901–909, 2017. 63, 98
- Hosseini, S. M., Fruth, F., Vogt, D. M., and Fransson, T. H. Effect of scaling of blade row sectors on the prediction of aerodynamic forcing in a highly-loaded transonic turbine stage. (54662):1297–1307, 2011. URL <http://dx.doi.org/10.1115/GT2011-45813>. 170, 171, 172
- Howe, M. S. Indirect combustion noise. *J. Fluid Mech.* , 659:267–288, Aug 2010. ISSN 1469-7645. doi: 10.1017/S0022112010002466. URL [http://journals.cambridge.org/article\\_S0022112010002466](http://journals.cambridge.org/article_S0022112010002466). 8, 40, 41, 63, 152, 162, 214
- Huet, M. Nonlinear indirect combustion noise for compact supercritical nozzle flows. *Journal of Sound and Vibration*, 374:211–227, 2016. 28
- Huet, M. Budgets of disturbances energy for nozzle flows at subsonic and choked regimes. In *ASME Turbo Expo 2017: Turbomachinery Technical Conference and Exposition*, pages V02CT43A005–V02CT43A005, North Carolina, USA, 26-30 June 2017. American Society of Mechanical Engineers. 110
- Huet, M and Giaume, A. A nonlinear model for indirect combustion noise through a compact nozzle. *J. Fluid Mech.* , 733:268–301, September 2013. 28, 46
- Hultgren, L. S. Core noise: Implications of emerging n+ 3 designs and acoustic technology needs. 2011. 5
- Hurle, I. R., Price, R. B., Sugden, T. M., and Thomas, A. Sound emission from open turbulent premixed flames. *Proc. R. Soc. Lond. A* , 303(409), 1968. 5

- ICAO. <http://www.icao.int>. 2013. 3
- Ihme, M. Combustion and engine-core noise. *Ann. Rev. Fluid Mech.* , 49(1), 2017. 4
- Ihme, M. and Pitsch, H. On the generation of direct combustion noise in turbulent non-premixed flames. *International Journal of Aeroacoustics*, 11(1):25–78, 2012. URL [http://www-personal.umich.edu/~mihme/Site/Publications\\_files/IntJAeroAcoustics.pdf](http://www-personal.umich.edu/~mihme/Site/Publications_files/IntJAeroAcoustics.pdf). 8
- Ihme, M., Bodony, D., and Pitsch, H. Towards the prediction of combustion-generated noise in non-premixed turbulent flames using large-eddy simulation. *CTR Annual Research Briefs*, pages 311–323, 2005. URL [http://www-personal.umich.edu/~mihme/Site/Publications\\_files/mihmeBodonyPitschARB2005.pdf](http://www-personal.umich.edu/~mihme/Site/Publications_files/mihmeBodonyPitschARB2005.pdf). 8
- Jameson, A., Schmidt, W., and Turkel, E. Numerical solution of the euler equations by finite volume methods using runge-kutta time stepping schemes. In 81-1259, AIAA paper, editor, *14th Fluid and Plasma Dynamic Conference*, Palo Alto, 1981. 107
- Jiménez, J. and Moin, P. The minimal flow unit in near-wall turbulence. *J. Fluid Mech.* , 225:213–240, 1991. doi: 10.1017/S0022112091002033. 68
- Juve, D., Sunyach, M., and Comte-Bellot, G. Filtered azimuthal correlations in the acoustic far field of a subsonic jet. *AIAA Journal*, 17(1):112–113, 1979. 145
- Kings, N., Enghardt, L., and Bake, F. Indirect combustion noise: experimental investigation of the vortex sound generation in a choked convergent-divergent nozzle. In *Société Française d’Acoustique, Acoustics 2012*, Nantes, France, 23-27 April 2012. 7
- Knobloch, K., Lahiri, C., Enghardt, L., Bake, F., and Peitsch, D. Hot-acoustic-testrig (hat): A unique facility for thermoacoustic research. In *ASME Turbo Expo 2015: Turbine Technical Conference and Exposition*, number 54679, pages 1023–1032, Montreal, Quebec, Canada, 6-10 June 2011. URL <http://dx.doi.org/10.1115/GT2011-45705>. 7
- Knobloch, K., Werner, T., and Bake, F. Noise generation in hot nozzle flow. In *ASME Turbo Expo 2015: Turbine Technical Conference and Exposition*, number 56642, pages V02BT41A012–, Montreal, Quebec, Canada, 15-19 June 2015a. URL <http://dx.doi.org/10.1115/GT2015-43702>. 7, 125
- Knobloch, K., Werner, T., and Friedrich, B. Entropy Noise Generation and Reduction in a Heated Nozzle Flow. In *AIAA*, pages 1–13, April 2015b. 7, 70
- Kopitz, J., Huber, A., Sattelmayer, T., and Polifke, W. Thermoacoustic stability analysis of an annular combustion chamber with acoustic low order modeling and validation against experiment. In *Int’l Gas Turbine and Aeroengine Congress & Exposition*, number ASME GT2005-68797 , Reno, NV, U.S.A., 2005. 116, 137, 138, 150, 201



- Kotake, S. On combustion noise related to chemical reactions. *J. Sound Vib.* , 42: 399–410, 1975. 6
- Kumar, R. N. Further experimental results on the structure and acoustics of turbulent jet flames. *AIAA Paper* , 1975. 6
- Labarrere, L., Poinso, T., Dauphin, A., Duchaine, F., Bellenoue, M., and Boust, B. Experimental and numerical study of cyclic variations in a constant volume combustion chamber. *Combustion and Flame*, 172:49–61, 2016. 172, 173
- Lamarque, N. *Schémas numériques et conditions limites pour la simulation aux grandes échelles de la combustion diphasique dans les foyers d’hélicoptère*. Phd thesis, INP Toulouse, 2007. 231
- Leonard, T., Sanjose, M., Moreau, S., and Duchaine, F. Large eddy simulation of a scale-model turbofan for fan noise source diagnostic. In *22nd AIAA/CEAS Aeroacoustics Conference*, Lyon, France, 30 May - 1 June 2016. American Institute of Aeronautics and Astronautics. doi: doi:10.2514/6.2016-3000. URL <http://dx.doi.org/10.2514/6.2016-3000>. 173
- Leyko, M. *Mise en oeuvre et analyse de calculs aéroacoustiques de type SGE pour la prévision du bruit de chambres de combustion aéronautiques - th/cfd/10/88*. PhD thesis, Institut de Mathématiques et de Modélisation de Montpellier - UM2, 2010. URL [http://www.cerfacs.fr/~cfdbib/repository/TH\\_CFD\\_10\\_88.pdf](http://www.cerfacs.fr/~cfdbib/repository/TH_CFD_10_88.pdf). 10, 170, 198
- Leyko, M., Nicoud, F., Moreau, S., and Poinso, T. Numerical and analytical investigation of the indirect noise in a nozzle. In *Proc. of the Summer Program* , pages 343–354, Center for Turbulence Research, NASA AMES, Stanford University, USA, 2008. 6
- Leyko, M., Nicoud, F., and Poinso, T. Comparison of direct and indirect combustion noise mechanisms in a model combustor. *AIAA Journal* , 47(11):2709–2716, 2009. 28, 37
- Leyko, M., Moreau, S., Nicoud, F., and Poinso, T. Waves transmission and generation in turbine stages in a combustion-noise framework. In *16th AIAA/CEAS AeroAcoustics Conference*, 2010. 28, 96, 98, 109, 112, 113, 149, 162, 163, 186, 193, 202, 203, 204, 214, 215, 238
- Leyko, M., Moreau, S., Nicoud, F., and Poinso, T. Numerical and analytical modelling of entropy noise in a supersonic nozzle with a shock. *J. Sound Vib.* , 330(16, 1): 3944–3958, 2011. 8, 39, 43, 44, 48, 49, 50, 51, 52, 59, 63, 82, 83, 86, 88, 101, 160
- Leyko, M., Duran, I., Moreau, S., Nicoud, F., and Poinso, T. Simulation and modelling of the waves transmission and generation in a stator blade row in a combustion-noise framework. *JSV*, submitted, 2013. 235, 236

- Leyko, Matthieu, Duran, Ignacio, Moreau, Stephane, Nicoud, Franck, and Poinso, Thierry. Simulation and modelling of the waves transmission and generation in a stator blade row in a combustion-noise framework. *J. Sound Vib.* , 333(23):6090–6106, November 2014. 105, 186, 202
- Lighthill, M. J. On sound generated aerodynamically. i. general theory. *Proc. R. Soc. Lond. A , Mathematical and Physical Sciences*, 211(1107):564–587, 1952. 4, 6, 7, 15
- Livebardon, T. *Modeling of combustion in helicopter engines*. Phd thesis, Université de Toulouse - Ecole doctorale MEGeP Dynamique des Fluides, 9 2015. 10, 203
- Livebardon, T., Moreau, S., Poinso, T., and Bouty, E. Numerical investigation of combustion noise generation in a full annular combustion chamber. In *21st AIAA/CEAS Aeroacoustics Conference*, Dallas, TX, 22-26 June 2015. American Institute of Aeronautics and Astronautics. doi: doi:10.2514/6.2015-2971. URL <http://dx.doi.org/10.2514/6.2015-2971>. 170, 198, 216
- Livebardon, T., Moreau, S., Gicquel, L. Y. M., Poinso, T., and Bouty, E. Combining LES of combustion chamber and an actuator disk theory to predict combustion noise in a helicopter engine. *Combustion and Flame*, 165:272–287, 2016. 8, 96, 98, 170, 198
- Lodato, G., Domingo, P., and Vervisch, L. Three-dimensional boundary conditons for direct and large-eddy simulation of compressible viscous flow. *J. Comput. Phys.* , 227(10):5105–5143, 2008. 221
- Lourier, J.-M., Huber, A., Noll, B., and Aigner, M. Numerical Analysis of Indirect Combustion Noise Generation Within a Subsonic Nozzle. *AIAA Journal* , 52(10): 2114–2126, October 2014. 40, 63, 82, 83, 92, 93, 94, 95, 160
- Magnus, W. On the exponential solution of differential equations for a linear operator. *Communications on pure and applied mathematics*, 7(4):649–673, November 1954. 31
- Magri, L., O’Brien, J., and Ihme, M. Compositional inhomogeneities as a source of indirect combustion noise. *J. Fluid Mech.* , 799:R4, 2016. 5, 6
- Marble, F. E. and Candel, S. Acoustic disturbances from gas nonuniformities convected through a nozzle. *J. Sound Vib.* , 55:225–243, 1977a. 29, 37, 39
- Marble, F. E. and Candel, S. Acoustic disturbances from gas nonuniformities convected through a nozzle. *J. Sound Vib.* , 55:225–243, 1977b. 4, 5, 7, 8, 19, 20, 28, 32, 34
- Martin, C., Benoit, L., Sommerer, Y., Nicoud, F., and Poinso, T. LES and acoustic analysis of combustion instability in a staged turbulent swirled combustor. *AIAA Journal* , 44(4):741–750, 2006. 64
- Mayorca, M. A., De Andrade, J. A., Vogt, D. M., Mårtensson, H., and Fransson, T. H. Effect of scaling of blade row sectors on the prediction of aerodynamic forcing in a highly loaded transonic compressor stage. *Journal of turbomachinery*, 133(2):021013, 2011. 172

- Moan, P. C. and Niesen, J. Convergence of the Magnus series. Technical Report 0316, La Trobe University, 2006. [32](#)
- Moase, W. H., Brear, M. J., and Manzie, C. The forced response of choked nozzles and supersonic diffusers. *Journal of Fluid Mechanics*, 585:281–304, 2007. ISSN 0022-1120. doi: 10.1017/S0022112007006647. URL [http://journals.cambridge.org/abstract\\_S0022112007006647](http://journals.cambridge.org/abstract_S0022112007006647). [23](#), [34](#)
- Morfey, C. L. Amplification of aerodynamic noise by convected flow inhomogeneities. *J. Sound Vib.* , 31:391–397, 1973. [7](#)
- Morgans, A. S., Goh, C. S., and Dahan, J. A. The dissipation and shear dispersion of entropy waves in combustor thermoacoustics. *J. Fluid Mech.* , 733, September 2013. [41](#), [63](#), [95](#), [96](#), [98](#), [101](#), [113](#), [134](#), [145](#), [149](#), [161](#), [193](#), [196](#), [211](#), [234](#), [235](#), [237](#), [238](#), [239](#), [240](#), [241](#)
- Moureau, V., Lartigue, G., Sommerer, Y., Angelberger, C., Colin, O., and Poinso, T. Numerical methods for unsteady compressible multi-component reacting flows on fixed and moving grids. *J. Comput. Phys.* , 202(2):710–736, 2005. [221](#)
- Muhlbauer, B., Noll, B., and Aigner, M. Numerical investigation of the fundamental mechanism for entropy noise generation in aero-engines. *Acta Acustica united with Acustica* 95, 95(3):470–478, 2009. [40](#), [48](#), [63](#), [82](#), [160](#)
- NIST. Nist chemistry webbook. URL <http://webbook.nist.gov/chemistry/>. [1](#)
- Papadogiannis, D., Duchaine, F., Sicot, F., Gicquel, L. Y. M., Wang, G., and Moreau, S. Large eddy simulation of a high pressure turbine stage: Effects of sub-grid scale modeling and mesh resolution. In *ASME turbo expo 2014: turbine technical conference and exposition*, number 45615, pages V02BT39A018–V02BT39A018, Düsseldorf, Germany, 16-20 June 2014. URL <http://dx.doi.org/10.1115/GT2014-25876>. [170](#), [171](#), [172](#), [173](#)
- Papadogiannis, D., Wang, G., Moreau, S., Duchaine, F., Gicquel, L. Y. M., and Nicoud, F. Assessment of the indirect combustion noise generated in a transonic high-pressure turbine stage. *Journal of Engineering for Gas Turbines and Power*, 138(4):041503, 2016. [xxviii](#), [63](#), [170](#), [171](#), [172](#), [173](#), [177](#), [178](#), [180](#), [186](#), [192](#), [203](#), [204](#), [205](#), [206](#), [209](#), [210](#), [211](#)
- Phillips, O. M. On the generation of sound by supersonic turbulent shear layers. *J. Fluid Mech.* , 9:1–28, 1960. [6](#), [7](#)
- Piacentini, A., Morel, T., Thévenin, A., and Duchaine, F. O-palm: An open source dynamic parallel coupler. In *Proceedings of the IV International Conference on Computational Methods for Coupled Problems in Science and Engineering–Coupled Problems*, Kos Island, Greece, 20-22 June 2011. [172](#)

- Poinsot, T. and Lele, S. Boundary conditions for direct simulations of compressible viscous flows. *J. Comput. Phys.*, 101(1):104–129, 1992. doi: 10.1016/0021-9991(92)90046-2. 64, 221
- Praisner, T. J. and Smith, C. R. The dynamics of the horseshoe vortex and associated endwall heat transfer—part i: Temporal behavior. *Journal of Turbomachinery*, 128(4):747–754, 02 2005a. URL <http://dx.doi.org/10.1115/1.2185676>. 175
- Praisner, T. J. and Smith, C. R. The dynamics of the horseshoe vortex and associated endwall heat transfer—part ii: Time-mean results. *Journal of Turbomachinery*, 128(4):755–762, 02 2005b. URL <http://dx.doi.org/10.1115/1.2185677>. 175
- Price, R. B., Hurle, I. R., and Sugden, T. M. Optical studies of the generation of noise in turbulent flames. *Symposium (International) on Combustion*, 12(1):1093–1102, 1969. doi: [http://dx.doi.org/10.1016/S0082-0784\(69\)80487-X](http://dx.doi.org/10.1016/S0082-0784(69)80487-X). URL <http://www.sciencedirect.com/science/article/pii/S008207846980487X>. 5
- Rienstra, S. W. and Hirschberg, A. *An introduction to acoustics*. Eindhoven University of Technology, 2003. 228
- Salas, P. and Moreau, S. Aeroacoustic simulations of a simplified high-lift device accounting for some installation effects. *AIAA Journal*, pages 1–16, 2016. 64
- Salvadori, S., Montomoli, F., Martelli, F., Adami, P., Chana, K.S., and Castillon, L. Aerothermal study of the unsteady flow field in a transonic gas turbine with inlet temperature distortions. *Journal of Turbomachinery*, 133(3):031030, 2011. 170, 171
- Sanjose, M., Pouangue, A., Fosso, Moreau, S., Wang, G., and Padois, T. Unstructured les of the baseline exejet dual-stream jet. In *20th AIAA/CEAS Aeroacoustics Conference*, Atlanta, GA, 16-20 June 2014. doi: doi:10.2514/6.2014-3037. URL <http://dx.doi.org/10.2514/6.2014-3037>. 63, 64
- Sattelmayer, T. Influence of the combustor aerodynamics on combustion instabilities from equivalence ratio fluctuations. *J. Eng. Gas Turb. and Power*, 125:11–19, 2003. 112, 235, 238
- Schønfeld, T. and Poinsot, T. Influence of boundary conditions in LES of premixed combustion instabilities. In *Annual Research Briefs*, pages 73–84. Center for Turbulence Research, NASA Ames/Stanford Univ., 1999. 64
- Schønfeld, T. and Rudgyard, M. Steady and unsteady flows simulations using the hybrid flow solver avbp. *AIAA Journal*, 37(11):1378–1385, 1999. 39
- Schuster, B., Gordon, G., and Hultgren, L. S. Dynamic temperature and pressure measurements in the core of a propulsion engine. *AIAA Paper*, 2819, 2015. 7, 189, 210, 215

- Selle, L., Nicoud, F., and Poinso, T. The actual impedance of non-reflecting boundary conditions: implications for the computation of resonators. *AIAA Journal* , 42(5): 958–964, 2004. 51, 56, 87, 116, 120, 122, 124, 223
- Selle, L., Benoit, L., Poinso, T., Nicoud, F., and Krebs, W. Joint use of compressible large-eddy simulation and Helmholtz solvers for the analysis of rotating modes in an industrial swirled burner. *Combust. Flame* , 145(1-2):194–205, 2006. 64
- Sinai, Y. L. The generation of combustion noise by chemical inhomogeneities in steady, low-Mach-number duct flows. *Journal of Fluid Mechanics*, 99, 1980. URL [http://journals.cambridge.org/abstract\\_S0022112080000663](http://journals.cambridge.org/abstract_S0022112080000663). 6
- Smith, T. J. B. and Kilham, J. K. Noise generation by open turbulent flames. *J. Acous. Soc. Am.* , 35(5):715–724, 1963. 5
- Stow, S. R., Dowling, A. P., and Hynes, T. P. Reflection of circumferential modes in a choked nozzle. *Journal of Fluid Mechanics*, 467:215–239, 2002. ISSN 0022-1120. doi: 10.1017/S0022112002001428. URL [http://journals.cambridge.org/abstract\\_S0022112002001428](http://journals.cambridge.org/abstract_S0022112002001428). 23, 27, 28, 34
- Strahle, W. C. On combustion generated noise. *J. Fluid Mech.* , 49:399–414, 1971. 6
- Strahle, W. C. Some results in combustion generated noise. *J. Sound Vib.* , 23(1): 113–125, 1972. 4, 6
- Strahle, W. C. Refraction, convection, and diffusion flame effects in combustion-generated noise. *Symposium (International) on Combustion*, 14(1):527–535, 1973. doi: [http://dx.doi.org/10.1016/S0082-0784\(73\)80051-7](http://dx.doi.org/10.1016/S0082-0784(73)80051-7). URL <http://www.sciencedirect.com/science/article/pii/S0082078473800517>. 6
- Thompson, K. W. Time dependent boundary conditions for hyperbolic systems. *J. Comput. Phys.* , 68:1–24, 1987. 221
- Truffin, K. and Poinso, T. Comparison and extension of methods for acoustic identification of burners. *Combust. Flame* , 142(4):388–400, 2005. 64
- Tsien, H. S. The transfer functions of rocket nozzles. *J. American Rocket Society* , 22(3):139–143, 1952. 5
- Tyler, J. M. and Sofrin, T. G. Axial flow compressor noise studies. Technical report, SAE Technical Paper, 1962. 4
- Ullrich, W. and Sattelmayer, T. Transfer functions of acoustic, entropy and vorticity waves in an annular model combustor and nozzle for the prediction of the ratio between indirect and direct combustion noise. In *21st AIAA CEAS Aeroacoustics Conference*, pages 1–19, April 2015. 40

- Ullrich, W. C., Gikadi, J., Jörg, C., and Sattelmayer, T. Acoustic-entropy coupling behavior and acoustic scattering properties of a laval nozzle. In *20th AIAA/CEAS Aeroacoustics Conference*, Atlanta, GA, 16-20 June 2014. doi: doi:10.2514/6.2014-3193. URL <http://dx.doi.org/10.2514/6.2014-3193>. 40, 63
- Ullrich, W. C., Bake, F., Kings, N., and Sattelmayer, T. Numerical investigation of indirect noise generation by accelerated vorticity. In *21st AIAA/CEAS Aeroacoustics Conference*, Dallas, TX, 22-26 June 2015. doi: doi:10.2514/6.2015-2382. URL <http://dx.doi.org/10.2514/6.2015-2382>. 8, 63
- Wang, G., Papadogiannis, D., Duchaine, F., Gourdain, N., and Gicquel, L. Y. M. Towards massively parallel large eddy simulations of turbine stages. San Antonio, USA, June 3-7 2013. Proceedings of the ASME TURBO EXPO 2013 Gas Turbine Technical Congress and Exposition. xxvii, 170, 171, 172, 173, 174, 176, 177
- Wang, G., Duchaine, F., Papadogiannis, D., Duran, I., Moreau, S., and Gicquel, L. Y. M. An overset grid method for large eddy simulation of turbomachinery stages. *Journal of Computational Physics*, 274:333–355, 2014a. xxvii, 170, 171, 172, 173, 174, 175, 176, 177
- Wang, G., Moreau, S., Duchaine, F., de Laborderie, J., and Gicquel, L. Les investigation of aerodynamics performance in an axial compressor stage. In *22nd Annual Conference of the CFD Society of Canada*, pages 1–4, Toronto, Canada, June 2014b. 1-4 June. 172, 173
- Wang, G., Sanjose, M., Moreau, S., Papadogiannis, D., Duchaine, F., and Gicquel, L. Noise mechanisms in a transonic high-pressure turbine stage. *International Journal of Aeroacoustics*, 15(1-2):144–161, 2016. 63, 170, 171, 172, 173, 175, 176, 180, 186, 210, 211
- Williams, J. E. F. and Howe, MS. The generation of sound by density inhomogeneities in low Mach number nozzle flows. *Journal of Fluid Mechanics*, 70(3):605–622, 1975. URL [http://journals.cambridge.org/abstract\\_S0022112075002224](http://journals.cambridge.org/abstract_S0022112075002224). 8
- Yoo, C.S. and Im, H.G. Characteristic boundary conditions for simulations of compressible reacting flows with multi-dimensional, viscous, and reaction effects. *Combust. Theory and Modelling*, 11:259–286, 2007. 221
- You, Donghyun, Wang, Meng, Moin, Parviz, and Mittal, Rajat. Large-eddy simulation analysis of mechanisms for viscous losses in a turbomachinery tip-clearance flow. *J. Fluid Mech.*, 586:177–204, 2007. 175
- Zheng, J., Huet, M., Cléro, F., Giauque, A., and Ducruix, S. A 2d-axisymmetric analytical model for the estimation of indirect combustion noise in nozzle flows. In *21st AIAA/CEAS Aeroacoustics Conference*, Dallas, TX, 22-26 June 2015. doi: doi:10.2514/6.2015-2974. URL <http://dx.doi.org/10.2514/6.2015-2974>. 96, 98, 109, 113, 114, 134, 135, 155, 163, 214

Zukoski, E. E. and Auerbach, J. M. Experiments concerning the response of supersonic nozzles to fluctuating inlet conditions. *Journal of Engineering for Power*, 98(1):60–64, 1976. [7](#), [37](#)